# Isolated and Deposited

# Metal Clusters

**Dissertation**

## Denitsa Alamanova

Saarbrücken, 2006

# Acknowledgment

# Contents

# Abstract

The present work deals with the application of different semiempirical potentials to the global optimization of transition and noble metal clusters. The three energetically lowest isomers of gold and silver clusters with up to 150 atoms have been determined. For structural and energetical comparison, additional computations have been performed on nickel and copper systems. The results confirm the applicability of the embedding functions even to the smallest metal particles. In order to determine general cluster properties, we have introduced structural and energetical descriptors such as stability function, moments of inertia, radial distribution of distances, similarity function quantifying the similarity to different *fcc* and icosahedral fragments, and how much a cluster of $N$ atoms can be considered as made of a $N - 1$ - atom cluster plus one additional atom. When possible, comparison was made to *ab initio* and experimental results. While copper, nickel and silver clusters show very similar structural and energetical properties, gold clusters differ markedly from those systems. In contrast to the regular icosahedral cluster growth observed for Ni and Cu, and the decahedral for Ag, the gold particles show irregular growth with predominant low-symmetric lowest-energy isomers, and no preferred structural pattern.

The second part of this study concerns dynamical processes of deposition of clusters on metal surfaces. The cluster-cluster interactions were followed from the Low Energy Cluster Beam, using a newly developed Molecular Dynamics algorithm, simulating the experimental procedure. It was found that applying even little kinetic energy to the clusters leads to the formation of diverse (meta)stable products. The cluster molecules emerged from the collision processes had relatively short lifetimes, and were crucially dependent on the initial orientation of the impacting clusters.

Deposition of clusters on substrates was carried out using particularly stable and particularly unstable copper cluster structures. The results showed that at low impact energies the structure of the smallest deposited cluster, $Cu_{13}$, remained preserved on the surface up to relatively high impact energy of 0.5 eV/atom, where it collapsed on the surface forming a monolayer. Similar behavior was observed for the particularly unstable $Cu_{18}$. The final products of the cluster deposition depended on all parameters of the deposition process, i.e., impact energy, cluster size, relative orientation and position.

# Abstrakt

Die vorliegende Arbeit beschäftigt sich mit der Anwendung verschiedener semiempirischer Potentiale zur globalen Optimierung von Übergangs- und Edelmetal-Clustern. Es wurden die drei energetisch niedrigsten Isomere von Gold- und Silber-Clustern mit bis zu 150 Atomen bestimmt. Um die Strukturen und Energien vergleichen zu können, wurden zusätzliche Berechnungen mit Nickel- und Kupfer-Systemen durchgeführt. Die Ergebnisse bestätigen die Anwendbarkeit der Embedding-Funktionen auf kleinste Metallpartikel. Um allgemeine Cluster-Eigenschaften bestimmen zu können, wurden strukturelle und energetische Deskriptoren eingeführt, wie zum Beispiel Stabilitätsfunktion, Massenträgheitsmoment, Radiale Verteilungsfunktion oder Ähnlichkeitsfunktion, welche die Ähnlichkeit von verschiedenen fcc und ikosaedrischen Fragmenten quantifiziert und inwiefern ein Cluster (bestehend) aus $N$ Atomen als ein Cluster aus $N-1$ Atomen plus ein zusätzliches Atom betrachtet werden kann. Wenn möglich wurde mit *ab initio* und experimentellen Ergebnissen verglichen.

Während Cu-, Ni-, und Ag-Cluster sehr ähnliche strukturelle und energetische Eigenschaften zeigen, unterscheiden sich Au-Cluster erheblich von diesen Systemen. Im Gegensatz zu dem regelmäßigen ikosaedralen Cluster-Wachstum, welches für Ni und Cu beobachtet wurde, und dem dekaedralen Wachstum für Ag zeigen die Au-Partikel unregelmäßiges Wachstum, das zu vorwiegend niedrigsymmetrischen Isomeren führt. In diesem Fall bevorzugen die Au-Partikel keine bestimmten Wachstumsmuster.

Der zweite Teil dieser Arbeit bezieht sich auf dynamische Prozesse der Deponierung von Clustern auf metallenen Oberflächen. Die Cluster-Cluster-Wechselwirkungen wurden dem *Low Energy Cluster Beam*-Experiment (LECB) nachgeahmt, in dem man einen *Molecular Dynamics* Algorithmus entwickelt hat, der die experimentelle Prozedur simuliert. Man fand heraus, dass selbst niedrige kinetische Anfangsenergie der Cluster zur Bildung von verschiedenen (meta)stabilen Produkten führt. Die Cluster-Moleküle, welche aus dem Kollisionsprozess entstehen, sind relativ kurzlebig, und hängen entscheidend von der ursprünglichen Orientierung der zusammenstoßenden Cluster ab.

Die Deponierung von Clustern auf Oberflächen wurde mithilfe von besonders stabilen, bzw. instabilen Strukturen von Kupfer-Clustern durchgeführt. Diese Ergebnisse zeigen, dass bei niedrigen Anfangsenergien die Struktur des kleinsten deponierten Clusters, $Cu_{13}$, auf der Oberfläche erhalten bleibt. Bei höheren Anfangsenergien von 0.5 eV/Atom bildet das Cluster eine Monoschicht auf der Oberfläche. Ein ähnliches Verhalten wurde mit dem besonders instabilen $Cu_{18}$ Cluster beobachtet. Die Endprodukte der Cluster-Deponierung hängen von allen Parametern des Deponierungsprozesses ab, wie Anfangsenergie, Clustergröße, relativer Orientierung, und Position.

# Zusammenfassung

Seit mehr als 20 Jahren sind Cluster ein Brennpunkt für Experimentalisten und Theoretiker, da sie eine wichtige Rolle in Bereichen wie Nanoindustrie, Katalyse, Informationsspeicherung, Kolloid- und Biophysikalischer Chemie sowie dem Transport von Medikamenten innerhalb des metabolischen Kreislaufes spielen. Die richtige Bestimmung der Strukturen der Cluster ist entscheidend für die erfolgreiche Anwendung, da diese aufgrund ihres großen Oberfläche/Volumen-Verhältnisses Eigenschaften zeigen, die sehr empfindlich sind in Bezug auf Änderungen in der Cluster-Geometrie. Deshalb kann eine ungenaue Bestimmung der Struktur zu falschen Vorhersagen von Cluster-Eigenschaften führen. Gegenwärtig sind selbst die neuesten experimentellen Techniken nicht in der Lage, eine zweifellose Zuordnung von bestimmten Geometrien zu einem untersuchten Cluster durchzuführen. Nur theoretische Untersuchungen können eine vernünftige Grundzustandskonfiguration für eine gegebene Clustergröße ermöglichen. Hier sind die first-principles Methoden auf Berechnungen von vordefinierten Konfigurationen beschränkt, welche 10 - 20 Atome enthalten. Es gibt sehr wenige semiempirische Untersuchungen, die sich auf die global-Minima Strukturen von Metallen mit bis zu 80 Atomen beziehen. Die Strukturen der mittelgroßen und großen Cluster mit 80 - 150 Atomen sind bisher noch nicht gründlich untersucht worden. Selbst für die kleinsten Cluster kann das Problem durch Anwendung der first-principles Methoden nicht gelöst werden. Es wurden jedoch alternative Methoden vorgeschlagen, welche eine Kompromisslösung zwischen Genauigkeit und Effizienz bieten.

Semiempirische Potentiale, welche zu der Embedded-Atom Methode (EAM) Familie gehören sowie das many-body Gupta-Potential wurden erfolgreich auf niedrig-dimensionale Systeme angewandt, unter anderem Nanodrähte, Oberflächendefekte und Legierungen. In vorherigen Arbeiten hat man die Anwendbarkeit der EAM Methoden zur richtigen Beschreibung von kleinsten Ni- und Cu-Clustern bewiesen. Während sowohl die originale Version, die von Daw, Baskes und Foiles vorgeschlagen wurde, als auch die später entwickelte Version von Voter und Chen, die Ni- und Cu-Cluster sehr genau beschreiben, wurde nur die Voter-Chen Version als geeignet für Gold-Cluster betrachtet. Eine alternative Methode, die Eigenschaften der Gold-Cluster zu beschreiben bietet die modifizierte EAM, so wie sie später von Baskes vorgeschlagen wurde.

Die vorliegende Arbeit basiert auf der Anwendung von EAM- und Gupta-Potentialen zur globalen Strukturoptimierung von Übergangs- und Edelmetal Clustern. Es wurde eine globale Strukturoptimierung von kleinen und mittelgroßen Nanoclustern von Cu, Ni, Ag, und Au durchgeführt. Strukturelle und energetische Eigenschaften, wie z.B. Stabilität, Symmetrie, Wachstum, Form der Cluster, Massenträgheitsmoment, Radiale Verteilungsfunktion, Ähnlichkeitsfunktion, und inwiefern ein Cluster bestehend aus $N$ Atomen als ein Cluster aus $N - 1$ Atomen plus ein zusätzliches Atom betrachtet werden kann, wurden quantifiziert.

Für Gold-Cluster mit bis zu 150 Atomen wurden auch die Vibrationsfrequenzen und Wärmekapazitäten berechnet. Die bestimmten Vibrationsfrequenzen vom Gold-Dimer,

$180 \text{cm}^{-1}$, sind in guter Übereinstimmung mit dem experimentellen Wert von 191 $\text{cm}^{-1}$, was darauf hindeutet, dass die anderen Frequenzen auch gut reproduziert werden können. In Übereinstimmung mit früheren experimentellen und theoretischen Untersuchungen erhält man durch die Anwendung jedes einzelnes Potentials die global-minimum-Struktur des $Au_{55}$ Clusters als niedrig symmetrisch. Man fand heraus, dass das globale Minimum vom $Au_{147}$ Cluster deutlich niedrigere Energie besitzt als das vollständige dritte Mackay Ikosaeder $Au_{147}$, was bisher als global-minimum-Struktur für diese Clustergröße betrachtet wurde. Während die Ergebnisse zeigen, dass beide Clustergrößen nicht besonders stabil sind, weisen das unvollständige zweite Mackay Ikosaeder $Au_{54}$ und das 146-Atom Dekaeder hohe Stabilität auf, im Gegensatz zu den Ergebnissen von Silber-Clustern.

Unsere Berechnungen weisen darauf hin, dass sowohl mit dem Gupta- als auch mit dem EAM-Potential die Silber-Cluster energetisch und strukturell den Ni- und Cu-Clustern ähnlicher sind, als den Au-Clustern, zumindest für kleine und mittlere Größen. Letzte theoretische Untersuchungen mit Ag-Clustern mit bis zu 20 Atomen ordnen diese Änlichkeit der mäßigen $s - d$ Hybridisation, die in Cu und Ag existiert. Ein Vergleich zwischen unseren Ergebnissen für Ag-Cluster und Berechnungen mit Cu- und Ni-Clustern lassen ein ähnliches Wachstum für alle 3 Metalle bis zu ungefähr 55 Atomen erkennen. Oberhalb dieser Größe wachsen Ni und Cu ikosaedrisch, während das überwiegende Wachstumsmuster für Ag-Cluster dekaedrisch ist. Parallel zu der Auswertung der Cluster-Eigenschaften wurde eine strukturelle Zuordnung *trapped ion electron diffraction* Daten für ausgewählte Ag-Cluster-Größen. Man fand heraus, dass ikosaedrische Strukturen als besonders stabile Konfigurationen für Cluster mit 19, 38, 55, 59, 75, und 79 Atomen dominieren. Das Gupta-Potential liefert, dass das Clusterwachstum im Größenbereich 65 - 139 Atomen dekaedrisch ist, nur mit Ausnahme von $Ag_{79}$.

In den meisten Experimenten liegen die Cluster weder in Gasphase vor, noch sind sie isoliert. Um dynamische Prozesse in Verbindung mit der Deponierung von Cluster auf Oberflächen zu untersuchen, entwickelten wir einen constant-energy Molecular Dynamics Algorithmus. Indem dieses Programm benutzt wurde, wurden Kollisionsprozesse studiert, welche in der Herstellung von Clustern in der *LECB* experimentellen Technik stattfinden. Die Abhängigkeit des Produktes von der Anfangsenergie, relativer Orientierung der zusammenstoßenden Cluster, und ihrer Größen, wurden untersucht. Dimerbildung der $Cu_4Cu_4$, $Cu_7Cu_7$, $Cu_{10}Cu_{10}$, $Cu_{13}Cu_{13}$, $Cu_{14}Cu_{14}$, und $Cu_{19}Cu_{19}$ Molekülen ähnlich zu früheren Ergebnissen für Na-Cluster wurde nachgewiesen. Das $Cu_4Cu_4$ Molekül besitzt eine Lebenszeit von mehr als 8 Picosekunden, dennoch ist die Dimerbildung für alle Fälle sehr empfindlich gegenüber Änderungen in der Anfangsorientierung der kollidierenden Cluster. Für höhere Stoßenergien wurde eine Dimerbildung nicht beobachtet. Unsere Ergebnisse zeigen, dass man erwarten muß, dass selbst unter extrem guten experimentellen Bedingungen Cluster-Cluster-Kollisionsexperimente zu einem breiten Spektrum von Produkten führen. Die stabilsten Strukturen wurden für sehr niedrige Stoßenergien beobachtet.

Schließlich wurde die Deponierung von kleinen und mittelgroßen Cu-Cluster auf die Cu(111) Ebene simuliert. Es wurde nach einer Beziehung zwischen Deponierungsenergie der Cluster und der strukturellen und energetischen Charakterisierung der Pro-

dukte gesucht. Eine höhere Stoßenergie führte zu einer niedrigeren Energie des gesamten Systems, was mit einer zunehmenden Wechselwirkungsenergie zwischen Oberfläche und Cluster erklärt wurde und nicht mit einer Clusterstruktur von höherer Stabilität. Die kleineren Cluster erreichten höhere maximale innere Temperaturen im Vergleich zu der größeren $Cu_{55}$ Struktur, was auf die niedrigere Anzahl von Atomen zurückzuführen war, welche zu einer zunehmenden Mobilität führte. Die deponierten Cluster zeigten bedeutende strukturelle Umordnungen auf der Oberfläche und verloren schnell die Ähnlichkeit zur Anfangskonfiguration. Die Endprodukte der Clusterdeponierung hingen empfindlich von allen Parametern des Deponierungsprozesses ab, wie Clustergröße, Stoßenergie, relativer Orientierung, und relativer Position.

6

# Chapter 1

# Introduction

Clusters form the link between the microscopic objects considered by the atom- and molecular physics at one extreme and the bulk solids at the other. Their large surface-to-volume ratio gives them unique physical and chemical properties. Transition and noble metal clusters have been recently investigated in connection with the synthesis of nanostructured materials and devices, and diverse applications in the medicinal and colloidal chemistry, as well as in the catalysis. Their growth or aggregation are in close relation with the way they are produced. In the past 20 years, different experimental setups have been developed, like gas aggregation techniques and scanning tunneling microscopy.

However, none of the experimental methods has been capable of unambiguous determination of the cluster structure. Therefore, for both theoreticians and experimentalists, the problem of proper determination of the structures of the small and medium-sized particles remains addressed. Moreover, the quantum-size effects and the evolution from molecule to bulk system have not been thoroughly discussed. It has been extremely difficult to draw a bridge between theory and experiment, as the experimentalists often work with fractions of cluster sizes of relatively large particles (1-2 nm, corresponding to few hundreds of atoms), while even the most powerful first principles studies have difficulties with the global optimizations already at very small cluster sizes. For clusters with more than 10 - 20 atoms unbiased structure determinations are not computationally feasible, only selected structures with chosen geometries are relaxed. This is also due to the very large number ( $10^3$ - $10^4$ ) of local minima already at these cluster sizes.

Alternatively, the global optimizations of larger clusters are all based on semiempirical potentials like the EAM, Sutton-Chen, Murrell-Mottram, or the many-body Gupta potential. With these methods, unbiased calculations have been performed up to the 80-atom cluster. The medium-sized clusters ( $80 \leq N \leq 150$) are still scarcely studied. Besides few first principles studies considering particular structural motifs, there exists no further investigation on the clusters in this size range.

Mass spectra experiments on clusters have shown that some cluster sizes appear very often in the spectra. These especially favored energetically structures were called 'magic'. The magic sizes are different for the different systems. For the transition and noble metal clusters, for example, 'magic-numbered' clusters are those that possess closed electronic

and/or geometric shell. Such clusters have number of atoms $N = 2, 8, 13, 38, 55, 147,$ 309, etc.

In the present work, the structural and energetical stability of various isolated transition and noble metal clusters will be discussed. Some of the studied systems have been extended up to 150 atoms. Therefore, the use of semiempirical approaches is the only choice, if one wants to perform an unbiased structure optimization of clusters with more than several atoms. The applied computational scheme allowed us to optimize thousands of isomers for a cluster with 150 atoms in less than one day with very good energetical and geometrical accuracy.

In the experiment, the clusters remain very seldom isolated, but rather deposited onto different substrates, which has become rapidly an attractive field in the elaboration of nanomaterials and nanodevices. The main problem is if the nanoparticles change significantly their shapes, and how. In order to study the deposition of these small particles, a Molecular Dynamics scheme was developed. The code used the same semiempirical potentials with which the isolated clusters were optimized. Finally, further modifications were implemented in the Molecular Dynamics program in order to study thermodynamical properties, such as melting phenomena.

This work is organized as follows: in Chapter 2 a short introduction to the density functional formalism is given, as well as the potentials based on it used in this study. The algorithms used in the global structure optimization are also described. The most important results for gold clusters with up to 150 atoms are presented in Chapter 3. Their structural and energetical properties are discussed in details, a comparison between the smallest clusters obtained with semiempirical potentials and *ab initio* studies is made. Further, thermodynamical properties, like vibrations and heat capacities are presented. For the same size range, a comparison between different semiempirical approaches is made for silver clusters. The main results, similarities and differences between these clusters and systems we have studied before, are generalized in Chapter 4. In Chapter 5, smaller nickel and copper clusters with up to 60 atoms are studied. Their thermodynamical properties are compared to those of the gold clusters in the same size range. The main features of the developed MD algorithms are described in Chapter 6. Their application in the collision processes between isolated metal clusters existing in the experiment, and the deposition of clusters onto metal surfaces, are discussed in Chapters 7 and 8. Finally, in Chapter 8 we summarise and conclude.

# Chapter 2

# Clusters

The clusters can be considered to constitute a new type of material, since they often have properties which are fundamentally different from those of discrete molecules or the relevant bulk solid. The term *cluster* means an aggregate of a countable number ($2$-$10^n$, where $n$ can be as high as 6 or 7) of particles (i.e atoms or molecules). The constituent particles may be identical, leading to *homo*-atomic, or they can be two or more different species - leading to *hetero*-atomic clusters. These clusters may be studied in the gas phase, in a cluster molecular beam, adsorbed onto a surface or trapped in an inert matrix.

Clusters are formed by most of the elements in the periodic table - even the rare gases. Clusters of the coinage metals copper, silver, gold are to be found in stained glass windows and silver clusters are important in photography. Some clusters, such as water clusters, are even found in the atmosphere. Carbon nanoclusters are now well known, including the famous soccer ball-shaped $C_{60}$ and related fullerenes and the needle-like nanotubes. The clusters can be separated into metallic, semiconductor, ionic, rare gas clusters, and cluster molecules.

Metallic elements from across the periodic table form a wide variety of clusters. These include: the simple $s$-block metals such as the alkali and the alkaline earth metals, where the bonding is metallic, delocalized and non-directional, involving primarily the valence $s$ orbitals; $sp$-metals, where the bonding involves both the $s$ and the $p$ orbitals and has a degree of covalent character; and the transition metals, where the degree of covalency is greater and there is also higher directionality in the bonding, which involves the valence $d$ orbitals. Metal clusters may be composed of a single metallic element or of more than one metal, giving rise to the subclass of intermetallic or nanoalloy clusters.

There is considerable experimental and theoretical interest in the study of elemental clusters in the gas phase and in the solid state. Clusters are of fundamental interest both due to their own intrinsic properties and because of the central position they occupy between molecular and condensed matter science. One of the most compelling reasons for studying clusters is that they span a wide range of particle sizes, from the molecular to the microcrystalline. Clusters also constitute a new type of material, nanoparticles, which may have properties which are distinct from those of either discrete molecules or bulk matter.

Since clusters have a high percentage of their atoms on the surface, there is a strong link between the chemistry and physics of clusters and of the surfaces of bulk matter. As surface atoms have by definition lower coordination numbers than the bulk atoms, there is the possibility of cluster surface rearrangements, analogous to the reconstructions observed for bulk surfaces, which lower the cluster's surface energy by forming additional surface bonds. Clusters may also be stabilized by the coordination of ligands to their surface. The reactivity of under-coordinated surface atoms makes clusters of interest as models for heterogeneous catalysis on bulk metal surfaces. In fact, since metal clusters are small metal particles, clusters (generally supported on an inert oxide substrate) can themselves be used as very finely dispersed metal for catalysis.

A large nanotechnology industry has sprung up on the past decade, motivated by the need to build devices for a variety of electronic, optical, magnetic and even mechanical applications, often using clusters as the basic building blocks. Another rapidly growing area of nanotechnology is the field of organic and bio-organic nanoscience, which encompasses topics such as supramolecular chemistry and molecular recognition, critical for the design of molecular scale machines and computers. At the beginning of the twenty-first century, clusters promise to play a pivotal role as components in novel electronic, magnetic and optical devices.

Since many cluster properties (e.g. cluster geometries, binding energies and energy barriers) are not easily measured directly from experiment, theoretical models and computational methods have been very useful in helping to interpret spectroscopic (e.g. UV-visible and photoelectron spectroscopy) and mass spectrometric data. The field of clusters also serves as an exacting testing ground for theoretical methods - testing the range of validity of theoretical models derived from the extremes of atomic/molecular and solid state physics. One of the challenges for theory is to come up with a theory of cluster structure and bonding which is applicable over and extremely large size range - from a few atoms to millions of atoms.

## 2.1   Cluster experiments

Cluster experiments can be divided into three main stages: *cluster generation*, *cluster investigation*, and *cluster detection*. As the latter constitutes mainly of mass-spectra measurements, here we will concentrate on the first two issues. It is important to note that progress in cluster science has followed closely on the development of new experimental techniques. In particular, the development of molecular beam techniques has enabled the study of free clusters in an interaction-free environment. The study of free clusters, however, presents a number of problems associated with difficulties in measuring physical properties of single particles and with generating intense size-selected cluster beams. Since there are often many cluster isomers with similar energies and low barriers to interconversion, the concept of cluster structure may not always be well defined. Another class of experiments involves the deposition of size-selected clusters on a substrate such as graphite, silicon or an inorganic one, or in an inert gas matrix. While such experi-
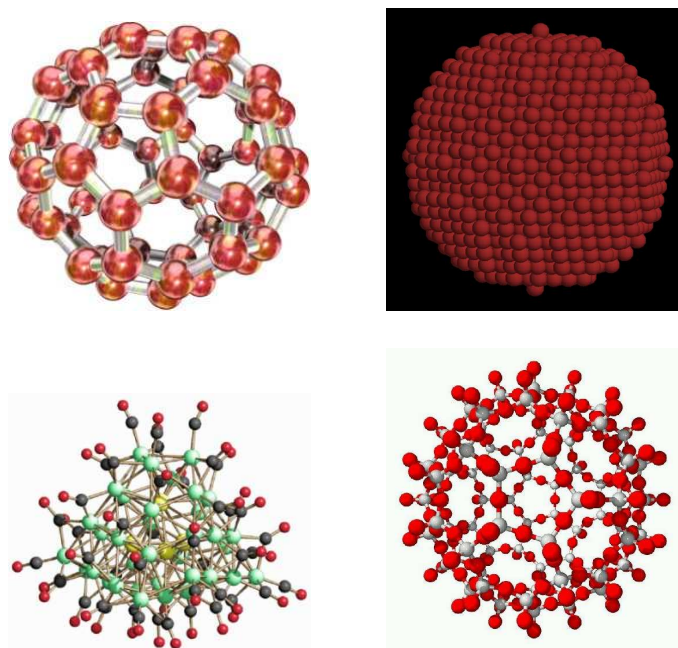
**Figure 2.1:** Examples for fullerene, metal, ionic, and semiconductor clusters.

ments allow individual clusters to be studied by microscopic techniques, it is difficult to infer the geometric or electronic structure of a free cluster from that of the corresponding surface-supported cluster, since such clusters may be perturbed by the substrate. Finally, since clusters in a molecular beam are generally not in thermodynamic equilibrium, the concept of temperature is not well defined in this case.

## 2.1.1 Cluster formation

The first stage in a cluster experiment is the generation of the clusters. They are generated in a *cluster source*, and the generation consists of the processes of *vaporization* (production of atoms or molecules in the gas phase), *nucleation* (initial condensation of atoms or molecules to form a cluster nucleus), *growth* (the addition of more atoms or molecules to the initially formed nucleus), and *coalescence* (the merging of small clusters to form larger clusters). As well as growing, clusters can also shrink by evaporation or fragmentation. Depending on the nature and conditions of the source, different size distributions of clusters may be generated.

In cluster experiments, the extent of clustering depends on many factors - for example, in supersonic beam experiments, important factors are the stagnation pressure, the carrier gas temperature - with lower temperatures and higher pressures leading to larger clusters. If the local thermal energy of the beam is less than the binding energy of the dimer, then a three-atom collision can lead to the formation of a dimeric nucleus, with the third atom removing the excess energy as kinetic energy:

$$A + A + A(KE_1) \rightarrow A_2 + A(KE_2 > KE_1) \tag{2.1}$$

In the presence of an excess of cold, inert carrier or quench gas (B), the nucleation step is more efficient:

$$A + A + B(KE_1) \rightarrow A_2 + B(KE_2 > KE_1) \tag{2.2}$$
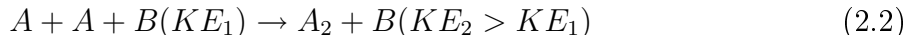
The dimer acts a site for further condensation. By increasing both the nozzle diameter and the stagnation pressure, the average cluster size and density increase. The initially formed cluster nucleus acts as a seed for further cluster growth. Early growth occurs by accretion of atoms one at a time. Subsequently, collisions between smaller clusters can lead to coalescence and the formation of larger clusters:

$$A_N + A \rightarrow A_{N+1} \tag{2.3}$$

$$A_N + A_M \rightarrow A_{N+M} \tag{2.4}$$

In the cluster growth region, the clusters are generally quite hot, so there is competition between growth and decay - i.e clusters shrinking by losing individual atoms (evaporation) and/or fragmentation (splitting into two or more clusters).

It is also difficult to measure and define the cluster temperature accurately. If there is negligible clustering then cluster temperatures are very low. Cluster growth, which is an exothermic process, causes an increase in the temperature (i.e the internal energy increases due to the heat of condensation of the added atoms). In heavily clustered beams, where there is a high ratio of atoms to clusters, and the clusters are larger, the clusters are very hot, possibly molten, when generated.

There are three main mechanisms by which clusters, in a molecular beam can lower their temperature, and these are the *collisional, evaporative*, and *radiative* cooling. In the *collisional* cooling, the collisions with other atoms in the beam remove the excess energy as kinetic energy:

$$A_N(T_1) + B(KE_1) \rightarrow A_N(T_2 < T_1) + B(KE_2 > KE_1), \tag{2.5}$$
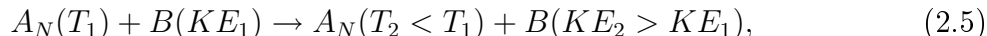
where B may be another atom of element $A$ or an inert carrier gas atom. Using a cold carrier gas leads to more efficient collision cooling. This cooling mechanism is only significant in the condensation and initial expansion regions.

The clusters can lower their internal energies also by evaporation - i.e by losing one or more atoms in an endothermic desorption process. In order for evaporation to occur, internal energy must be channelled into the appropriate cluster vibrational modes, in order to overcome the kinetic activation barrier to bond breaking. After evaporation, this excess energy is imparted as kinetic energy to the escaping atom

$$A_N(T_1) \rightarrow A_{N-1}(T_2 < T_1) + A(KE) \rightarrow A_{N-2}(T_3 < T_2) + A(KE) \rightarrow \dots \tag{2.6}$$

This mechanism is the only cooling mechanism once free flight has been achieved, i.e, when collisions no longer occur. Finally, clusters can lower their internal energies by emitting infrared radiation:

$$A_N(T_1) \rightarrow A_N(T_2 < T_1) + h\nu \tag{2.7}$$

Radiative cooling is an inefficient cooling mechanism, which is slow compared with the time scales of typical cluster experiments. The distribution of cluster sizes produced by a cluster source depends on a number of factors. The distribution is strongly influenced by the particular cluster source being used. The size distribution depends on the way in which the vapor is generated, the initial temperature and pressure, the presence of a carrier or quenching gas, the dimensions and shape of apertures and nozzles.

## 2.1.2 Investigation of clusters

Many experiments involving clusters rely on being able to separate them according to their mass. In order to do this, it is generally necessary to ionize the clusters so that mass selection can be accomplished by deflecting the clusters in a magnetic or electric field. Depending on the material and the type of experiment, either cations or anions may be created. Cations and/or anions may also be formed in the initial cluster generation step.

These charged clusters are easily separated and selected usually by using mass spectrometry. In the *time-of-flight* (TOF) mass spectrometer, cluster ions are accelerated by a succession of homogeneous electric fields into a field-free flight tube, finally impacting on an ion detector. The mass-to-charge ratio $M/Q$ of the cluster is determined from the measured time-of-flight. The mass resolution is limited by the initial conditions and timing accuracy, but the resolution of the analyser is not mass-dependent, and the resolution ($\delta M/M = 10^{-4}$–$10^{-3}$) is good throughout the mass range. One disadvantage of the TOF spectrometer is that it only operates on short cluster pulses and thus low ion intensities are detected.

There are four main media for studying the nature of clusters: molecular beams, inert matrices, supported on surfaces, and in the solid state.

Cluster molecular beams afford the opportunity to study isolated clusters, free from the influence of ligand or supports. While this is clearly desirable, and molecular beam technology has developed tremendously over the past decade, such studies of free clusters present difficulties associated with generating a sufficiently high flux of clusters with a narrow enough size distribution to give definitive information on specific clusters.

Clusters can be also deposited in an inert matrix, which may be liquid, glassy or crystalline, and is generally made up of condensed rare gases or molecules. Matrix isolated clusters may be studied by direct UV-visible and IR spectroscopy, or electron spin resonance.

When clusters are supported on the surface of an inert substrate, such as ionic oxide or a layered semiconductor, it is possible to study the individual clusters using surface microscopy techniques. These include scanning tunneling microscopy, scanning electron

microscopy and atomic force microscopy. For larger particles, X-ray and electron diffraction techniques can be used to study the degree of crystalline order in individual clusters.

Finally, in the recent years, it has proved possible to crystallize solids composed of clusters. In order to prevent cluster coalescence the clusters are generally coated by surfactant molecules - usually organic thiols or thioethers, and these crystals can be studied using X-ray diffraction and microscopy.

If there is an inherent stability associated with a given number of atoms in a neutral cluster then, all other factors being equal, this will give rise to a greater abundance of these clusters and a large peak in the mass spectroscopy intensity, e.g, a *magic number*. Magic numbers are found to be most prominent when cluster generation leads to establishment of a quasi-equilibrium, due to high initial cluster temperatures (e.g. 300-600K for alkali metal clusters) and slow cooling.

In the case of small metal clusters, it is possible to generate high intensity molecular beams of size-selected clusters. In this case the measurement of direct UV-visible and IR absorption spectra are possible. However, experiments on free clusters in molecular beams generally make use of the high sensitivity of mass spectroscopy for the detection of charged particles. Thus, a UV-visible absorption spectrum of a beam of mass-selected ionized clusters can be measured by scanning the frequency of the laser used for photoexcitation. The absorption spectrum is traced out by monitoring the intensity of the mass of the undissociated cluster as a function of laser frequency.

Alternatively, the high sensitivity of detectors for charged particles means that experiments involving charge separation are particularly useful for clusters. Such experiments include the measurement of *photoelectron spectra* of neutral or anionic clusters, as well as the measurement of traditional mass spectral abundances of cationic or anionic clusters. Magnetic or electric fields can be used to deflect or collect cluster cations or anions or the ejected electrons.

Neutral and ionized clusters can be excited either y absorption of light or by electron or ion impact. The excited clusters may then relax by emitting radiation, losing an electron and/or evaporation/fragmentation. This photo fragmentation can also give information as to the cluster binding energy, as can the related *collision-induced fragmentation/dissociation* process.

### Mobility measurements

In the past decade, a cluster ion chromatography, based on the *cluster ion mobility*, was developed. In these experiments, cluster ions are mass selected and injected into a long drift tube, which is filled with an inert buffer gas at a controlled temperature and pressure. The cluster mobilities depend on the number of collisions with the buffer gas and these in turn depend on the collisional cross sectional area, and hence the shape of the cluster. Assuming that the collisions with the buffer gas do not lead to preferential orientation of the clusters, for a given number of atoms, spherical clusters have the smallest collision cross sections and therefore travel fastest through the drift tube. As they rotate in the drift tube, prolate spheroidal clusters (where one dimension or axis of the cluster is appreciably

longer than the other two) carve out a large sphere, and thus have high collision cross sectional areas and slow drift times. Oblate clusters (where one dimension or axis of the cluster is appreciably shorter than the other two) have collisional cross-sectional areas, and hence drift times, intermediate between those of spherical and prolate geometries. In this way cluster isomers, which have the same number of atoms but different shapes, are temporally separated in the drift tube and appear at different times at the detector.

**Electron diffraction**

*Electron diffraction* studies have been performed on rare gas and metal clusters in cluster molecular beams. In such experiments, a well collimated electron beam (with electron energies in the range 30–50 keV) is crossed with a cluster beam. The electrons are scattered by atoms in the cluster and the diffraction pattern (arising from the interference of the scattered electrons) is collected on a photographic film or by an electron detector. Because the information from diffraction experiments is averaged over all clusters that the electron interact with, electron diffraction measurements require a narrow cluster size distribution and a reasonably high cluster intensity. A number of X-ray diffraction studies have also been carried out on metallic clusters deposited on inert substrates. In both electron and X-ray diffraction studies of clusters, the diffraction pattern is interpreted by generating a model of the cluster and adjusting the model so as to maximize the agreement with the experimentally measured pattern. Diffraction experiments can be used to determine the structures and sizes and mean temperatures of the clusters.

**Microscopic techniques**

The most direct way of determining the structure of a cluster is by using microscopy. This necessitates the immobilization of the cluster on a substrate. Because of the small length scales of the order of $10^{-10}$ m of atomic diameters and interatomic distances, traditional optical microscopy cannot be used. Instead, the atomic structure of clusters is imaged by electron microscopy, using electron beams, that can be accelerated to an appropriate energy and can be focused by electrostatic lenses. Electron microscopy techniques, such as *transmission electron microscopy* (TEM), *scanning electron microscopy* (SEM) and *high resolution electron microscopy* (HREM) can now achieve atomic resolution.

In *scanning probe microscopy* (SPM) techniques, the shape of surfaces and clusters are mapped out using a needle tip that is positioned by piezoelectric drives, with an accuracy of $10^{-11}$ m, i.e smaller than the width of a single atom. This enables such techniques to display atomic resolution. The needle tip is tracked backwards and forwards across the substrate and detects atoms in one of two ways. In *scanning tunneling microscopy* (STM) a potential bias is applied between the needle tip and the substrate, causing electrons to tunnel from the surface to the needle. The STM can operate in constant current mode (where the height of the tip above the substrate is varied so as to keep the tunneling current constant) or in constant height mode (where the varying tunneling current is measured). Another variant of scanning probe microscopy is *atomic force microscopy* (AFM), where the repulsive force between the tip and the substrate is measured.
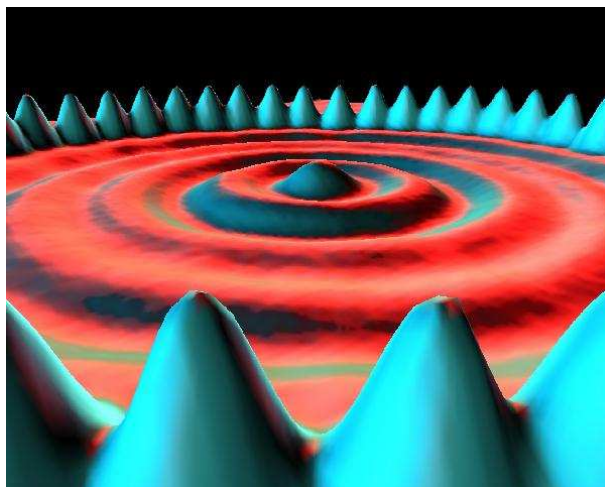
**Figure 2.2:** Image of Iron atoms on Copper (111) obtained with STM techniques. Reproduced from *M. F. Crommie, C.P. Lutz, and D.M. Eigler. Confinement of electrons to quantum corrals on a metal surface. Science 262, 218-220 (1993).*

In summary, although there has been a significant development in the experimental setups and many new techniques have been introduced, the experimental data still can not unambiguously define the structures of the studied clusters. Even the most novel experiments need corresponding computational models which are adjusted in order to achieve best agreement with the experimental results, and the latter have to be compared to prospective candidate structures optimized with *ab initio* or semiempirical methods. Many of the smallest metal clusters with up to 10-15 atoms have been extensively studied by photoelectron spectroscopy combined with density functional calculations[60]. However, the structures of the larger clusters remain still unidentified. In this work, the structural and energetical patterns of clusters of transition and noble metals have been determined by using semiempirical and density functional approaches. Where it was possible, comparison to the experimental data was made. Our aim is to find general trends in the cluster growth and deposition on surfaces, as well as to give further insight into the structural and energetical properties of these unique particles.

# Chapter 3

# Computational methods and algorithms

In this Chapter we will give a short overview of the density functional theory formalism and the semiempirical potentials based on it, and further we will present the main features of the used algorithms for global structure optimization.

## 3.1 Density Functional Theory

The main problem for the theoreticians remain the solution of the Schrödinger's equation

$$\widehat{H}\Psi = E\Psi, \tag{3.1}$$

which is still possible to calculate without any approximation only if we treat the most simple system, e.g, the hydrogen atom. In order to be able to consider multielectron systems, an approximate solution of this fundamental equation is needed. The Born-Oppenheimer approximation that neglects the free motion of the nuclei for the time during which the electrons move, and thus separating the Hamiltonian into electronic and nuclear motion, is the first approximation applied in the *ab initio* methods. Focusing only on time-independent properties within this approximation we can solve Schrodinger's equation for the electrons:

$$\widehat{H}_e\Psi_e = E_e\Psi_e, \tag{3.2}$$

where $\Psi_e$ is the electronic wavefunction depending on all electronic degrees of freedom, e.g., three position-space and one spin coordinate for each electron. For the calculation of experimental observables we need to know the complete N-electron wavefunction $\Psi_e$. The density-functional theory itself is based on the two fundamental theorems by Hohenberg and Kohn published in 1964.

### 3.1.1 Hohenberg-Kohn Theorems

According to Hohenberg and Kohn it is possible to calculate any ground-state property of a given system if we know the distribution of the total electron density $\rho(\mathbf{r})$. Hence, the

total electronic energy of a given system $E_{tot}$ becomes a functional of the electron density $\rho(\mathbf{r})$

$$E_{tot} = E_{tot}[\rho(\mathbf{r})]. \tag{3.3}$$

Then

$$E_e[\rho(\mathbf{r})] = F[\rho(\mathbf{r})] + \int \rho(\mathbf{r}) V_{ext}(\mathbf{r}) d\mathbf{r}. \tag{3.4}$$

Here, $V_{ext}(\mathbf{r})$ is the external electrostatic potential that is determined by the atomic nuclei. $F[\rho(\mathbf{r})]$ is a universal potential that is independent of the external potential and, therefore, also of the geometry of the nuclei of the system. Through the potential, the electron density $\rho(\mathbf{r})$ determines the Hamilton operator and, thereby, all ground state properties. The total number of electrons of the system is also defined by $\rho(\mathbf{r})$:

$$N = \int \rho(\mathbf{r}) d\mathbf{r}. \tag{3.5}$$

According to the second Hohenberg-Kohn theorem, a variation of the ground state electron density

$$\Delta\rho(\mathbf{r}) = \rho(\mathbf{r}) + \delta\rho(\mathbf{r}), \tag{3.6}$$

results in a positive change of the total ground state energy:

$$E_e[\Delta\rho(\mathbf{r})] > E_e[\rho(\mathbf{r})] \tag{3.7}$$

By changing the electron density to $\Delta\rho(\mathbf{r})$ the number of electrons remains unchanged:

$$\int \Delta\rho(\mathbf{r}) d\mathbf{r} = \int \rho(\mathbf{r}) d\mathbf{r}. \tag{3.8}$$

Thus, for calculation of any ground state property of the system it is no longer necessary to calculate the whole $N$-particle wavefunction of the system but simply the electron density.

### 3.1.2   Kohn-Sham Equations

Unfortunately, the Hohenberg-Kohn theorems themselves do not lead to the development of a particular density functional. In 1965 Kohn and Sham published a method for the calculation of the electron density with the so-called Kohn-Sham equations. Alike the Hartree-Fock equations, the Kohn-Sham equations are also split into single particle solutions of the Schrödinger formula. Therefore, one needs to find a solution of this set of single-particle equations, which are depicted as follows:

$$E_e[\rho(\mathbf{r})] = T[\rho(\mathbf{r})] + \int \rho(\mathbf{r}) \left[ V_{ext}(\mathbf{r}) + \frac{1}{2} V_C(\mathbf{r}) \right] d\mathbf{r} + E'_{xc}[\rho(\mathbf{r})]. \tag{3.9}$$

Here $E_e[\rho(\mathbf{r})]$ is the total electronic energy of the system, $T$ is the kinetic energy, $\int \rho(\mathbf{r})V_{ext}(\mathbf{r})d\mathbf{r}$ is the energy resulting from the external potential, and $(1/2)\int \rho(\mathbf{r})V_C(\mathbf{r})d\mathbf{r}$ the Coulomb energy which is resulting from the electron repulsion (the factor 1/2 deletes the double-counted terms). $E'_{xc}$ is the exchange-correlation energy and contains all terms that are not included in the other three add ens.

After exertion of the variational principle using the Lagrange multiplier $\mu$ that is the chemical potential for the electrons, we obtain

$$\frac{\delta T}{\delta \rho} + V_{ext}(\mathbf{r}) + V_C(\mathbf{r}) + \frac{\delta E'_{xc}}{\delta \rho} = \mu, \tag{3.10}$$

where $\mu$ has been introduced to satisfy the condition

$$N = \int \rho(\mathbf{r})d\mathbf{r}. \tag{3.11}$$

The difference between the Hohenberg-Kohn formalism and the last equations is that according to Kohn and Sham the particles are non-interacting. These $N$ non-interacting particles shall move in an external potential $V_{eff}(\mathbf{r})$ that is defined in such a way that the electron density and the energy are equal to the electron density and the energy of the original system of interacting particles. The corresponding relation is embedded in the following formula:

$$E_e[\rho(\mathbf{r})] = T^{KS}[\rho(\mathbf{r})] + \int \rho(\mathbf{r})V_{eff}(\mathbf{r})d\mathbf{r}. \tag{3.12}$$

After applying the variational principle we obtain

$$\frac{\delta T^{KS}}{\delta \rho} + V_{eff}(\mathbf{r}) = \mu \tag{3.13}$$

with

$$V_{eff}(\mathbf{r}) = \frac{\delta T}{\delta \rho} - \frac{\delta T^{KS}}{\delta \rho} + V_{ext}(\mathbf{r}) + V_C(\mathbf{r}) + \frac{\delta E'_{xc}}{\delta \rho}. \tag{3.14}$$

It is important to know that the kinetic energy $T^{KS}$ of the fictive system is not equal to the kinetic energy $T$ of the real system.

The resulting Hamiltonian is significantly simplified and can be written as the sum of $N$ single-particle operators $\hat{h}_{eff}$:

$$\widehat{H} = \sum_{i=1}^{N} \left[ -\frac{1}{2}\nabla_{\mathbf{r_i}}^2 + V_{eff}(\mathbf{r_i}) \right] \equiv \sum_{i=1}^{N} \hat{h}_{eff}(i) \tag{3.15}$$

We can write the many-body wavefunction as a single Slater determinant:

$$\Psi = \mid \psi_1, \psi_2, ..., \psi_N \mid, \tag{3.16}$$

and the single-particle equations are:

$$\hat{h}_{eff}(i)\psi(i) = \epsilon_i \psi_i. \tag{3.17}$$

These determine the single-particle energies $\epsilon_i$. Finally, the electron density is the sum over the $N$ orbitals with the lowest single-particle energies $\epsilon_i$:

$$\rho(r) = \sum_{i=1}^{N} n_i \mid \psi_i(r) \mid^2 \tag{3.18}$$

where $n_i$ is the occupation number of the $i$th orbital. The electron density of the system consisting of non-interacting particles has been constructed in such a way that it is equal to the electron density of the real system. However, the single-particle wave functions of the non-interacting particles $\psi_i$ and energies $\epsilon_i$ are not identical with those of the electrons but practice has shown that they provide a good approximation to them.

## 3.2   The Embedded Atom Method

The Embedded Atom Method is entirely based on the density functional formalism, with the only significant difference that the electron density is calculated numerically for wide range of atom distances, and therefore its recalculation updating the positions of the atoms at each step becomes unnecessary. Therefore, the potential is expected to predict results similar to those obtained with the conventional *ab initio* methods, and to be extremely computationally efficient due to the omission of the Hamiltonian.

### 3.2.1   The EAM of Daw and Baskes

The main idea of the EAM was initially proposed by Daw, Baskes and Foiles (DBF) [1, 2, 3] in 1983-1986 as suitable approach for extended systems with largely delocalized electrons (mainly for early and late transition metals), and since then the generality of the functions of the EAM of DBF has been successfully tested by numerous applications to different problems in metals and alloys, such as defects, surface and interface structures, surface and bulk phonons, etc.

   According to this theory, the energy change associated with placing an atom into a host system of atoms is a functional of the electronic density of the host system before the new atom is embedded [4]. The energy of the host with impurity is then a functional of the unperturbed host electron density and a function of the impurity charge and position. By analogy with the approach of Stott and Zaremba, Daw and Baskes consider each atom of a metal as an impurity embedded in a host provided by all other atoms.

   The principle of the method is to split the total energy of the system into a sum over atomic energies:

$$E_{tot} = \sum_{i}^{N} E_i \tag{3.19}$$

$$E_{tot} = \sum_i^N F_i(\rho_i^h) + \frac{1}{2} \sum_{i,j \neq i}^N \phi_{ij}(r_{ij}) \qquad (3.20)$$

where $\rho_i^h$ is the local electron density at site $i$, $F_i$ is the embedding energy, i.e., the energy required to embed an atom into this density, and the electron-electron interaction $\phi_{ij}$ is modeled as sums of short-ranged, pair potentials between atoms $i$ and $j$ separated by distance $r_{ij}$:

$$\phi_{ij}(R_{ij}) = \frac{Z_i(R_{ij})Z_j(R_{ij})}{R_{ij}}. \qquad (3.21)$$

Adjustable parameters that define $F_i$ and $\phi_{ij}$ have been obtained by fitting to known bulk properties such as sublimation energy, lattice constant, the heat of solution of binary alloys, and, additionally, using the universal equation of Rose [5] that describes the sublimation energy of the most metals as a function of lattice constant. The values for $\rho_i^a$, $F_i$ and $Z_i$ are available in numerical form for Ni, Cu, Ag, Au, Pd, and Pt[6].

## 3.2.2 The EAM of Voter and Chen

Another version of the EAM was proposed by Voter and Chen[7, 8, 9] few years after the original potential appeared. This version of the EAM distinguishes from the version of Daw and Baskes mainly by means of the parameterization and by the form of the pair potential. Furthermore, the version of Voter and Chen takes into account properties of the dimer as well as bulk properties in the fitting procedure, whereas Daw and Baskes use only bulk properties of the metals in their parameterization. In the fitting procedure of Voter and Chen the pairwise interaction is taken to be a Morse potential,

$$\phi(r) = D_M[1 - e^{-\alpha_M(r-R_M)}]^2 - D_M \qquad (3.22)$$

where the three parameters $D_M$, $R_M$ and $\alpha_M$, define the depth, position of the minimum, and a measure of the curvature near the minimum, respectively. The density function, $\rho(r)$, is taken as:

$$\rho(r) = r^6[e^{-\beta r} + 2^9 e^{-2\beta r}] \qquad (3.23)$$

where $\beta$ is an adjustable parameter. To be suitable for use in molecular dynamics, the interatomic potential $\phi(r)$ as well as the electron density $\rho(r)$ should be continuous. This is accomplished by forcing $\phi(r)$ and $\rho(r)$ to go smoothly to zero at a cutoff distance, $r_{cut}$, which is used as a fitting parameter. The five parameters defining $\phi(r)$ and $\rho(r)$: $D_M$, $R_M$, $\alpha_M$, $\beta$, and $r_{cut}$, are optimized by minimizing the root-mean-square deviation ($\chi_{rms}$) between the calculated and experimental values for the three cubic elastic constants, the vacancy formation energy, the bond length and the bond strength of the diatomic molecule. The values of $\rho_i^a$, $\phi_{ij}$ and $F_i(\rho_i)$ that are used by the Voter-Chen version, are also available in numerical form for Ni, Pd, Pt, Cu, Ag, Au and Al.[10]

## 3.3    The Gupta potential

The Gupta potential[11] has been derived from the Gupta's expression for the cohesive energy of a bulk material and can be written in terms of repulsive and attractive many-body terms, which are obtained by summing over all atoms:

$$V_{clus} = \sum_{i=1}^{N} \left[ V^r(i) - V^m(i) \right] \qquad (3.24)$$

where

$$V^r(i) = \sum_{j=1\,(\neq i)}^{N} A(a,b) \exp\left[ -p(a,b)\left( \frac{r_{ij}}{r_0(a,b)} - 1 \right) \right] \qquad (3.25)$$

and

$$V^m(i) = \left\{ \sum_{j=1\,(\neq i)}^{N} \zeta^2(a,b) \exp\left[ -2q(a,b)\left( \frac{r_{ij}}{r_0(a,b)} - 1 \right) \right] \right\}^{\frac{1}{2}} \qquad (3.26)$$

In these three equations $r_{ij}$ is the distance between atoms $i$ and $j$, and $A$, $r_0$, $\zeta$, $p$, and $q$ are fitted to experimental values such as cohesive energy, lattice parameters and independent elastic constants for the reference crystal structure at 0 K. The tight-binding version (TBG) from Ref.[12, 84] uses reduced units for the energy and the coordinates, e.g. the parameters $r_0$ and $\zeta$ are set to 1, additionally, a scaling factor equal to 0.5 is applied to the total energy $V_{clus}$. This does not allow direct structural comparison between the clusters obtained with this version of the Gupta potential (TBG) and those predicted with the EAM and the extended version of the Gupta potential[13] ($n$G). Hence, for structural comparison, the reduced coordinates of the clusters are to be scaled by appropriate factor. In this way, the structural peculiarities of the clusters obtained with the two versions of the Gupta potential can be compared.

## 3.4    Computational scheme

Performing a geometry optimization is often the first step one takes when studying a molecule using computational methods. Geometry optimizations typically attempt to locate a minimum on the potential energy surface (see Fig. 3.1) in order to predict equilibrium structures of molecular systems, although they may also be used to locate transition structures. The potential energy surfaces specify the way in which the energy of a molecular system varies with small changes in its structure. In this way, a potential energy surface is a mathematical relationship linking the molecular structure and the resultant energy. For example, for a diatomic molecule, the potential energy surface can be represented by a two-dimensional plot with the internuclear separation on the X-axis and the energy at that bond distance on the Y-axis; in this case the potential energy surface

is a curve. For larger systems the surface has as many dimensions as there are internal degrees of freedom within the molecule. The potential energy surface illustration depicted at Fig. 3.1 considers only two of the degrees of freedom within the molecule, and plots the energy above the plane defined by them, creating a surface. Each point represents a particular molecular structure, with the height of the surface at that point corresponding to the energy of that structure. Our example surface contains three minima: a minimum is a point at the bottom of a valley, from which motion in any direction leads to a higher energy. Two of them are local minima, corresponding to the lowest point in some limited region of the potential surface, and one of them is the global minimum, the lowest energy point anywhere on the potential surface. Different minima correspond to different conformations or structural isomers of the molecule under investigation. The illustration also shows two maxima and a saddle point (the latter corresponds to a transition state structure).

At both minima and saddle points, the first derivative of the energy, known as the gradient, is zero. Since the gradient is the negative of the forces, the forces are also zero at such points. A point on the potential energy surface where the forces are zero is called a stationary point. All successful optimizations locate a stationary point, although not always the one that was intended. Geometry optimizations usually locate the stationary point closest to the geometry from which they started.

The programs using the following algorithms within the EAM of Daw, Baskes, and Foiles were kindly provided by Dr. V. Grigoryan. Using expression (3.20) one can calculate the total energy of any cluster with any structure as a function of atomic coordinates $\{\vec{R}_i\}$, $E_{\text{tot}}(\vec{R}_1, \vec{R}_2, \ldots, \vec{R}_N)$. In order to obtain the closest local total-energy minimum we use the *variable metric/quasi-Newton* method.[14]

For searching the global minima an *Aufbau/Abbau* algorithm was developed (see Fig. 3.1). It consists of the following steps:

1) We consider two cluster sizes with $N$ and $N + K$ atoms with $K \simeq 5 - 10$. For each of those we study a set of randomly generated structures, $N_{\text{ran}} \simeq 1000$. Using the *quasi-Newton* method the $N_{\text{ran}}$ relaxed structures are identified and the structures of the lowest total energy selected.

Each of the $N_{\text{ran}}$ starting structures for a cluster with $M$ atoms is generated using a random-number generator for positions within a sphere or a cube of volume $V_{cl} = (p \cdot b_{nn})^3 M$, where $b_{nn}$ is the nearest-neighbor distance in the bulk metal and $p = 0.96, 1.0, 1.04$, i.e. we considered slightly compressed, normal, and slightly expanded structures. We included the constraints that the smallest allowed inter-atomic distance was $0.5 b_{nn}$ and each atom has to interact with at least two others.

2) One by one, each of the $M$ atoms is displaced randomly, and the closest local minimum is determined. If the new structure has a lower total energy than the original one, the new one is kept, and the old one discarded. This is repeated approximately $500 - 1000$ times (depending on cluster size).

3) This leaves us with two 'source' metal clusters, $\text{Me}_N$ and $\text{Me}_{N+K}$ with their lowest total energies. One by one an atom is added at a random position to the structure with $N$ atoms (many hundred times for each size), and the structures are relaxed. In parallel, one

by one an atom is removed from the structure with $N + K$ atoms — for each intermediate cluster with $N'$ atoms we consider *all* $N' + 1$ possible configurations, that one can obtain by removing one atom from the $Me_{N'+1}$ cluster. >From the two series of structures for $N \leq M \leq N + K$ those structures of the lowest energies are chosen and these are used as seeds for a new set of calculations. First, when no lower total energies are found, it is assumed that the structures of the global-total-energy minima have been identified, and we proceed to larger clusters. Moreover, we can keep information not only about the single energetically lowest isomer, but more low-lying ones.

When there are no new structures with lower energies, the most stable ones are used as input in a routine that disturbs the cluster structure in order to check for possible lower-energy isomers. In most of the cases it is convenient to generate about 1000 candidate structures. The first structure corresponds to the unchanged geometry of the source cluster. Then the distances between the atoms are expanded consecutively by 1.0, 1.3, 1.6, 1.9, and 2.2 Å, e.g. the bonds of the source cluster are expanded by 1 Å and the structure is optimized. This is repeated approximately 200 times. Then the structure with lowest energy, which could be the initial cluster, is selected and its bonds expanded by 1.3 Å, and this is done again for 200 cluster generations, then it continues with the next disturbance coefficient. This program allows us to check if the lowest-energy structure predicted by the *Aufbau/Abbau* algorithm lies indeed in the global minimum for that cluster size. In some 90% of the cases the global minima clusters have been successfully identified by *Aufbau/Abbau*, however, when a new minimum is found with the disturbance algorithm, this structure is used as an input in new series of *Aufbau/Abbau* calculations, until no lower-energy configurations are found.
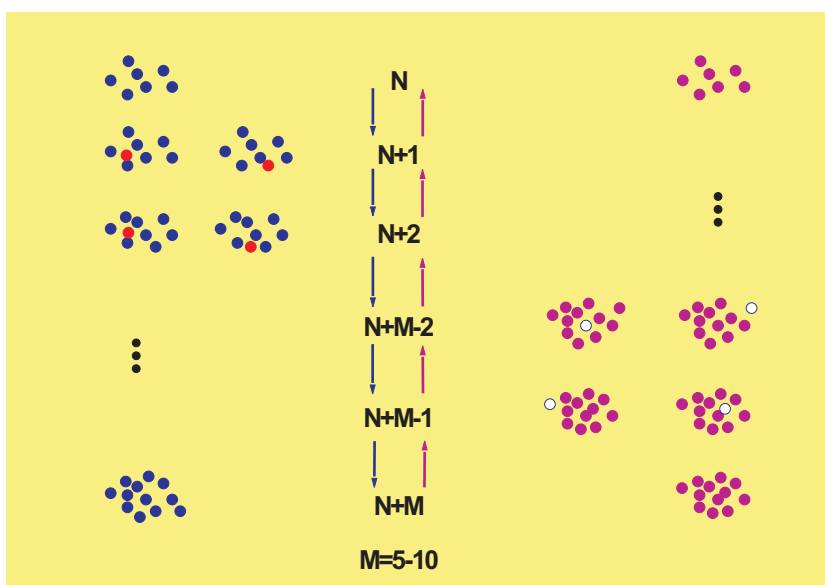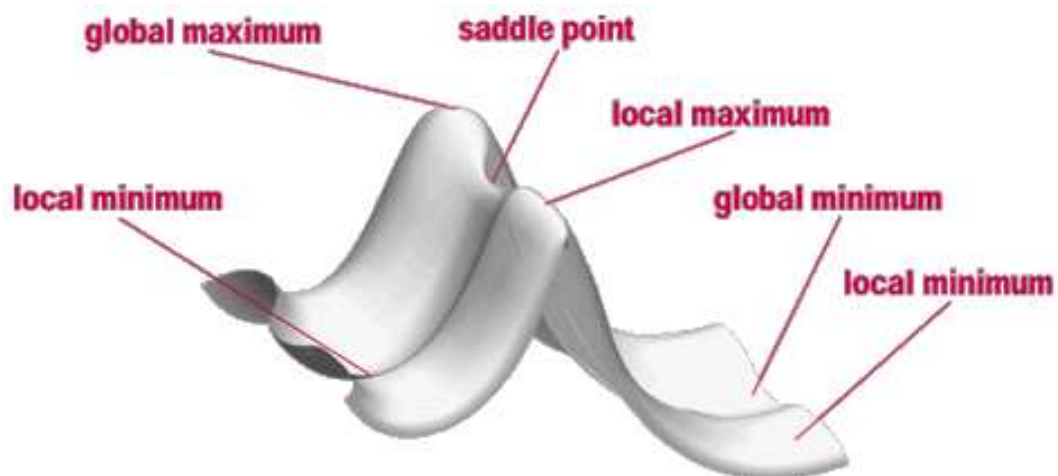
**Figure 3.1:** The Potential Energy Surface (PES) of the clusters and our Aufbau/Abbau algorithm for global structure optimization.

# Chapter 4

# Gold clusters

## 4.1 Introduction

Gold clusters[15, 16] have been recently investigated in connection with the synthesis of nanostructured materials and devices [17, 18, 19, 20, 21]. Their structural and energetic properties have been studied with High-Resolution Electron Microscopy (HREM) and various spectroscopic techniques [22, 23, 24, 25, 26, 27, 28, 29, 30, 31, 32, 33, 34, 35, 36, 37, 38, 39]. Literature concerning small $Au_N$ clusters is enriched with numerous investigations based on density-functional methods [41, 42, 43, 44, 45, 46, 47, 48, 49, 50, 51, 52, 53, 54, 55, 56, 58, 57, 59] that are not yet capable of giving a definite answer to the problem at what cluster size the structural 2D – 3D transition occurs. Recent studies combining theory and experiment [60, 61, 62, 63] show that the gold clusters are planar at least up to $N = 7$ for Ref.[61], or up to $N = 12$, according to Häkkinen[60] and Furche *et al.*[62]. The global optimization is difficult for the *ab initio* methods already at very small cluster sizes. The authors of Ref.[42, 54] performed density functional calculations on clusters containing more than 30 atoms, relaxing selected high-symmetric configurations. Alternatively, the global optimizations of larger clusters are all based on approximate methods like molecular dynamics [64, 65, 66, 67, 68, 69, 70, 71, 72, 73, 74, 75] and semiempirical potentials like the EAM [27, 76, 77], Sutton-Chen [78], Murrell-Mottram [79, 80], or the many-body Gupta potential [81, 82, 83, 84, 85, 86]. Using these methods, unbiased calculations were performed up to the 80-atom cluster. The medium-sized clusters ( $80 \leq N \leq 150$) are still scarcely studied. Besides the first-principles study of Häberlen *et al.* [42], and the EAM calculations by Cleveland *et al.*[27, 76, 77] considering particular structural motifs, there exists no further investigation on the clusters in this size range.

In most of the studies, special attention is paid to the so-called 'magic-numbered' clusters, that possess closed electronic and/or geometric shell. Various calculations on the first 'magic' cluster $Au_{13}$ have pointed to the formation of an icosahedron [41, 42, 78, 79, 84, 86]. Only the authors of Ref.[49, 50] found disordered structure as the lowest-lying isomer of this cluster. On the other hand, the semiempirical potentials [76, 78, 79, 86] and the density functional study by Häkkinen *et al.*[44] on the $Au_{38}$ cluster predicted the truncated octahedron to be the global minimum for this cluster size. However, on the

basis of first-principles and Gupta potential calculations, the authors of Ref.[83, 85] state that a disordered structure is actually lower in energy than the symmetric. It is most probable that the obtained structure depends on the type of the used potential, as by using another form of the same potential, Darby *et al.*[86] found a truncated octahedral structure to be the global minimum of $Au_{38}$. The situation is more clear for the $Au_{55}$ and $Au_{75}$ clusters, where a disordered structure [78, 81, 82, 84, 85, 86] and a Marks decahedron (m-$D_{5h}$) [82, 84] seem to lie in the global minima.

Several groups performed calculations on larger clusters minimizing symmetric initial configurations, hence the structures most probably do not correspond to the global minima. Few clusters were studied - the octahedral $Au_{79}$ [76, 78] and $Au_{140}$ [76], the decahedral $Au_{101}$, $Au_{116}$, and $Au_{146}$ [76], and the icosahedral $Au_{147}$ [42, 76]. The structures and energetics of the clusters between these high symmetrical ones remain scarcely investigated.

In the present Chapter the structure and energetics of the three most stable isomers of small and medium-sized $Au_N$ clusters with $2 \leq N \leq 150$ have been determined for each cluster size by using a combination of the embedded-atom method in the version of Voter and Chen[7, 8, 9] (VC), the *variable metric/quasi-Newton* method, and our own *Aufbau/Abbau* method.

## 4.2   Small gold clusters

First we calculated the bond length of the $Au_2$ dimer with the two versions of EAM. The obtained with the VC approach value of 2.40 Å was in a very good agreement with first-principles studies (2.55 Å) and the experiment (2.47 Å), while the EAM of Daw, Baskes, and Foiles underestimated the bond length (1.80 Å) and overestimated the binding energy of the dimer. For this reason we chose to work with the Voter-Chen version that describes correctly the dimer properties. However, this potential, like all other semiempirical potentials, does not include explicitly the electrons and their orbitals, therefore for the smallest gold clusters, where the spin-orbit interactions play important role, the global minima structures are compact (see Table 4.4.1), and the planar structures only metastable. In the size range $N = 4 - 7$ the first principles studies obtain these 3D configurations as higher-lying isomers, which can serve as example how the inclusion of electronic effects can change the energetic ordering of the isomers. On the other hand, the addition of electrons in the semiempirical potentials would restrict their use only to small and relatively larger clusters. An appropriate choice are the Density Functional Tight-Binding methods (DFTB) that include explicitly the electrons and are computationally more efficient than the common density functionals. In a recent study[91] we showed the important role that the electronic effects play in the values of the binding energy and the stability functions. However, except for $N = 4$, where a rhombus was the lowest-lying isomer according to the DFTB method, all the ground state structures for the smallest gold clusters $Au_5 - Au_9$ had 3D shapes. On the other hand, even the most recent density-functional studies are still not in agreement at which cluster size the structural transition 2D – 3D occurs.

According to the LDA study by Wang *et al.*[50], it is the pentagonal bipyramid that lies in the global minimum of $Au_7$. Remacle and Kryachko[59] suggested that the gold clusters are planar at least up to $N = 9$, while Walker[58] predicts that the transition occurs at $Au_{11}$. Using ion mobility measurements and *ab-initio* molecular dynamics Kappes *et al.*[61, 62] found that the 3D transitions occur at $Au_{12}^-$ and $Au_8^+$. The same group studied the adsorption of CO on isolated gold cluster cations in the size range $N = 1 - 65$. The smallest clusters with $4 \leq N \leq 6$, and $Au_8$ were found to be planar, while for $Au_7$ the global minimum was a 3D structure, but not a bipyramid, in contrast to the results of Wang[50]. In a combined experimental and theoretical study Häkkinen and coworkers[60] confirmed the 2D – 3D transition at $Au_{12}^-$, however, Xiao and Wang[57] suggested that for the neutral clusters this occurs first at $Au_{15}$. In most of the cases the planar structures are competing with 3D isomers, and the energetic differences are insignificant, which in turn means, that the ordering of the isomers depends strongly on the used functional and the starting conditions. For example, Häkkinen *et al.*[48] compared the global minima of relativistic and nonrelativistic $Au_7^-$ clusters and found that for the nonrelativistic gold the lowest-lying isomer was a capped octahedron that corresponds to our second isomer for this cluster size. At larger cluster sizes the potential used in this study yields results in agreement to density functional and experimental studies. The study by Häkkinen *et al.*[44] on the $Au_{38}$ cluster predicted the truncated octahedron to be the global minimum, and a recent experiment[39] shows that the $Au_{55}^-$ cluster most probably is not an icosahedron, but a structure with low symmetry, in agreement to our results.

In summary, we can conclude that although our results for the smallest gold clusters correspond to higher-lying isomers within the first principles methods, due to the lack of electronic effects, our method is sufficiently accurate in describing the larger gold clusters with $N > 9$, where most probably the planar structures begin to compete with 3D configurations.

## 4.3  Comparison to first principles calculations

In order to compare our results for the smallest gold clusters to the ones predicted by the Density Functional formalism, we performed spin-polarized density functional optimizations of gold clusters with up to 10 atoms. For the largest clusters only a few possible structures were considered, due to the very large computational time needed (about a week on a Pentium III computer to optimize only one $Au_{10}$ structure).

The first issue to be addressed is the role of relativity in connection with the proper choice of a density functional in the program package Gaussian 03. All calculations with Au clusters were performed using relativistic effective core potentials developed particularly for systems where the spin-orbit coupling plays important role in the geometric configuration. We calculated the bond length and vibrational frequency of the gold dimer $Au_2$ with various exchange, correlation, and hybrid functionals, the results from which can be seen at Table. 4.1.

Although the *local spin density approximation* LSDA implemented in the Vosko-Wilk-

**Table 4.1:** The $Au_2$ bond length and vibrational frequency as predicted by different functionals and the experiment.

| Method | d[Å] | $\omega[cm^{-1}]$ |
|--------|------|-------------------|
| B3LYP  | 2.58 | 163 |
| BLYP   | 2.59 | 158 |
| PBE    | 2.55 | 169 |
| PW91   | 2.56 | 167 |
| VWN    | 2.49 | 194 |
| *exp*  | 2.47 | 191 |

Nusair (VWN) functional gives the results that best agree with the experimental values, the LSDA functionals are no longer used for optimizations of gold clusters, due to their tendency to overbind and thus predict mainly three dimensional global minima structures, as found by Wang *et al.*[50]. Recent experimental studies[60] unambiguously point to the formation of flat gold clusters up to at least 12 atoms. The results most close to the experimental values, except those from VWN, are predicted by the Perdew-Burke-Ernzerhof (PBE) functional. In our calculations we used a functional containing both exchange and correlation parts modeled by the PBE approximation (PBEPBE). The relativistic CEP-121G basis set is an effective core potential that separates the electrons of the atom into core and valence ones. The 79 electrons of the gold atom are split into 60 core and 19 valence ones, the influence of the core electrons is described by an effective potential, and the Schrödinger equation is solved only for the remaining 19 electrons. Calculations on the dimer were performed also with other basis sets, the LanL2DZ and the Stuttgart/Dresden (SDD) ones, however, the results were worse than those obtained with the CEP-121G basis set.

At Fig. 4.1 to Fig. 4.3 are shown the optimized structures of gold clusters with $3 \leq N \leq 10$ atoms, their symmetries and energy differences are described in Table 4.2. All previous density functional studies denote the obtuse triangle of about $66°$ as the global minimum structure for the $Au_3$ cluster, although the next isomer, an acute triangle, is only about 0.022 eV higher in energy. The other possible configurations, namely the chain and the equilateral triangle, lie significantly higher, especially the latter one, which we were able to optimize only in its triplet electronic configuration. This is the global minimum for this cluster size according to the Voter-Chen potential, however, the inclusion of electronic effects here makes it possible to find a structure with lower symmetry as ground state already for this cluster size, as the semiempirical potential is optimized using spherical, nondirectional electron density.

Again, for $Au_4$, our semiempirical global minimum corresponds to a tetrahedron, which is the energetically most unfavored structure according to the PBEPBE functional. All isomers for this cluster size are already known, only the square has not been widely studied,

however, in this calculations it is the fourth isomer, but when using other functionals or semiempirical methods, it could become a favored structure, close or degenerate with the ground state.

The only one cluster structure for which it is known that it is most probably the global minimum for the according cluster size, is the $Ag_5$ cluster. Almost 10 years ago, Haslett, Bosnik, and Moskovits[110] obtained Raman spectrum of $Ag_5$, mass-selected from a sputtered jet of silver cluster ions, neutralized and matrix isolated in solid argon. In order to assign the spectrum, they performed normal coordinate vibrational analysis for the considered W-shaped cluster and the $C_{2v}$ trigonal bipyramid, as well as a number of other geometries. At least 7 distinct peaks were observed, which ruled out the high-symmetry structures, since they all possess vibrational degeneracies and therefore can not account for the number of peaks observed. The highest symmetry that could be assigned was the $C_{2v}$ one, with all possible modes being non-degenerative and Raman active. To distinguish between the remaining two possible structures, they extended the vibrational analysis to include a rough calculation of the relative Raman intensities of each mode. The results showed that a very strong band at $162cm^{-1}$ corresponded to a very weakly Raman active $B_1$ mode in the bipyramidal structure as opposed to the strongest $A_1$ mode in the planar structure, therefore they could unequivocally assign the spectrum to the trapezoidal planar $Ag_5$. It is very probable that this is also the ground state for the gold cluster, as suggested by various experimental studies[60, 61, 62]. Its third isomer, with trapezoidal shape, and the Y-shaped structure are proposed here for the first time, according to our knowledge. The trapezoid comes immediately after the two popular lowest-energy structures, and has significantly low energy comparing to the next isomers. The high symmetrical trigonal bipyramid lies again rather high in energy, but the most unfavored structure for this cluster size is the capped square, in contrast to the results for the $Au_4$ cluster.

The finding that the trapezoidal shape seems to be energetically advantageous is confirmed by the results for the global minima of $Au_6$ and $Au_7$, which can be considered as capped and bicapped trapezoid. For $Au_6$ the energetical differences between the isomers are significantly large, however, the octahedron and the "boat"-shaped structure correspond to the first and second lowest-lying isomers for this cluster size according to the VC potential. It is not clear why the global minima for these small clusters are all two dimensional according to the density functional formalism. As mentioned before, Häkkinen *et al.*[48] tried to address this question and optimized relativistic and nonrelativistic $Au_7^-$ clusters and found that for the nonrelativistic gold the lowest-lying isomer was a capped octahedron that corresponds to our second isomer for this cluster size. This structure is presented only in Table 4.2, in order to avoid repetition. Hence, the results obtained with the EAM method are comparable to those from nonrelativistic first-principles calculations.

The LDA studies from the past decade established the 2D − 3D crossover for gold at $N = 7$, where the global minimum structure for this cluster size was the pentagonal bipyramid, which is most probably due to the overbinding in LDA leading too early to three dimensional configurations. Wang *et al.*[50] found this structure as global minimum for $Au_7$, followed by the hexagon, while the latter was the preferred configuration accord-
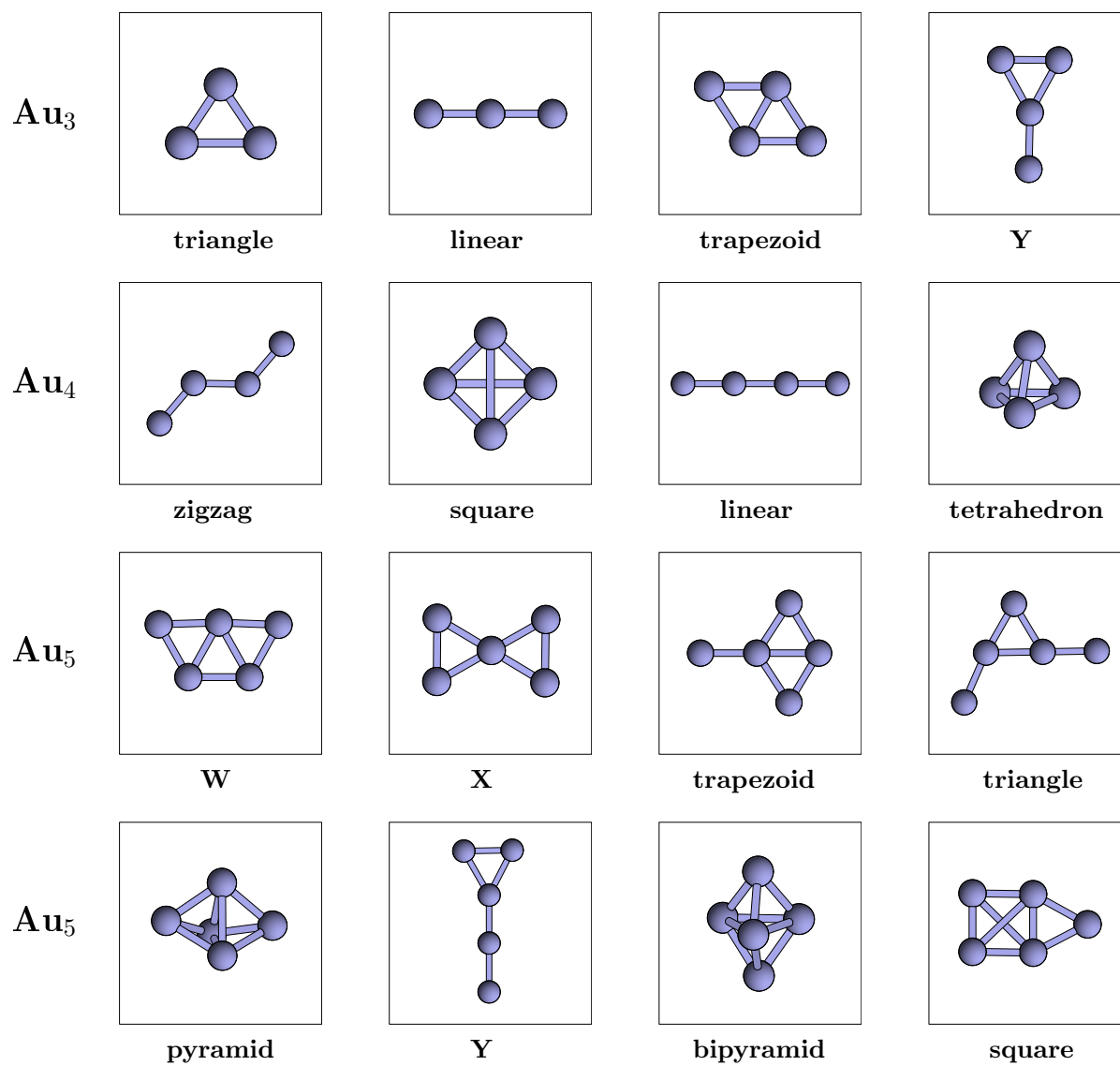
**Figure 4.1:** The optimized candidate structures for Au$_3$, Au$_4$, and Au$_5$. The energy grows from left to the right.
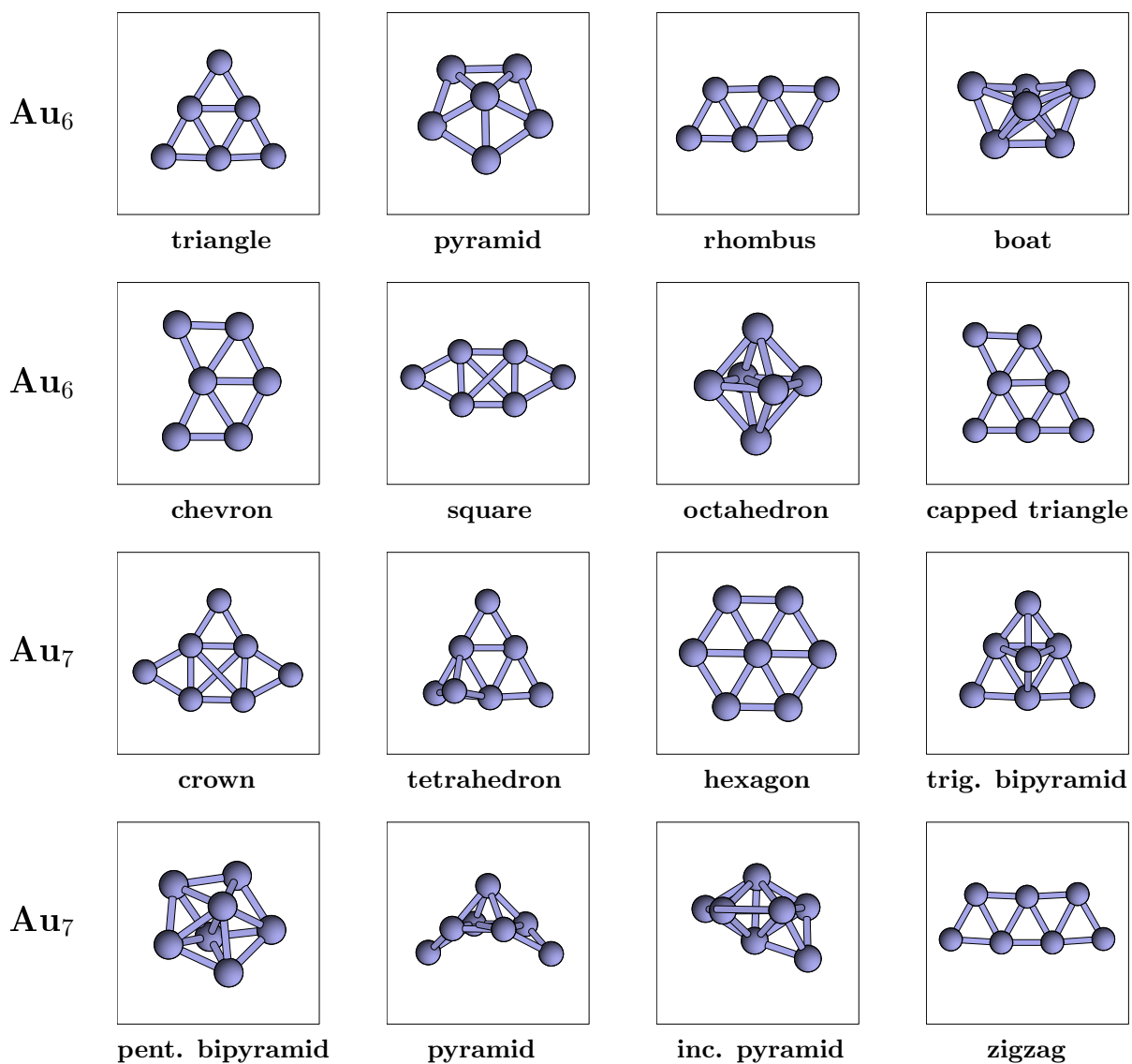
**Figure 4.2:** The same for Au$_6$ and Au$_7$. For optimal presentation, the global minimum of Au$_7$ is shown at the fourth panel in the second row.

**Au$_8$**



capped rhombus



capped hexagon



bicapped oct. I



bicapped oct. II

**Au$_8$**



capped tetrahedron



crown



bicapped oct. III

**Au$_9$**



capped hexagon I



capped hexagon II



trapezoid

**Au$_{10}$**



double hexagon
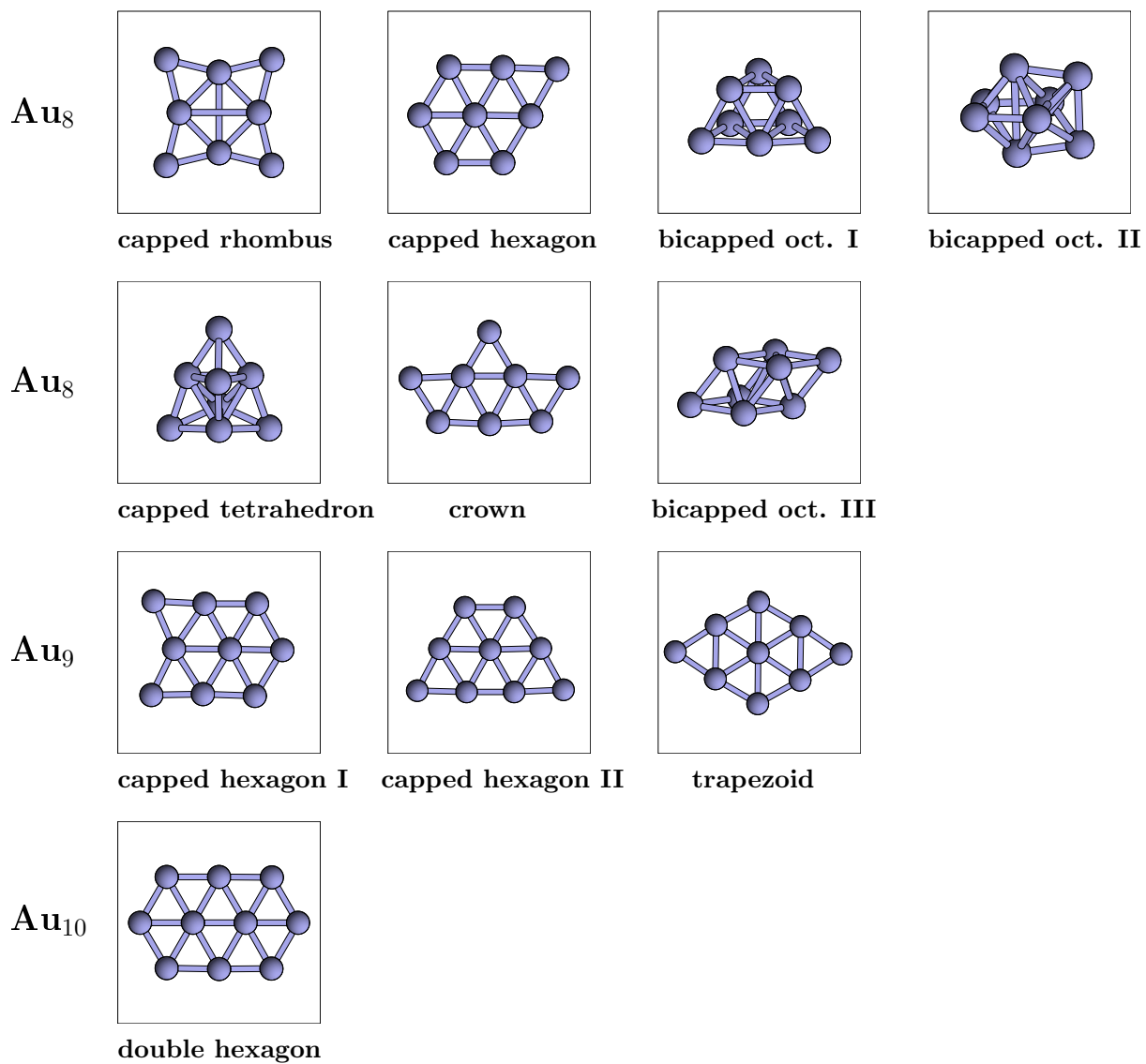
**Figure 4.3:** The same for Au$_8$, Au$_9$, and Au$_{10}$.

**Table 4.2:** Energy separations of isomeric structures from the ground state structure (eV). The calculated lowest-energy structures are marked in bold.

| N | Shape | Sym. | $\Delta$E | N | Shape | Sym. | $\Delta$E |
|---|---|---|---|---|---|---|---|
| 3 | obtuse triangle | $C_{2v}$ | **0.00** | 7 | capped triangle | $C_s$ | **0.00** |
| 3 | acute triangle | $C_{2v}$ | 0.02 | 7 | crown | $C_{2v}$ | 0.13 |
| 3 | chain | $D_{\infty h}$ | 0.04 | 7 | tricapped tetrahedron | $C_{2v}$ | 0.22 |
| 3 | equilateral triangle | $D_{3h}$ | 1.50 | 7 | hexagon | $C_{2h}$ | 0.23 |
| 4 | trapezoid | $D_{2h}$ | **0.00** | 7 | bicapped bipyramid | $C_s$ | 0.29 |
| 4 | Y | $C_{2v}$ | 0.10 | 7 | pentagonal bipyramid | $D_{5h}$ | 0.36 |
| 4 | zigzag | $C_{2h}$ | 0.47 | 7 | bicapped square pyramid | $C_{2v}$ | 0.58 |
| 4 | chain | $D_{\infty h}$ | 0.92 | 7 | incomplete bipyramid | $C_2$ | 0.62 |
| 4 | square | $D_{4h}$ | 0.69 | 7 | zigzag | $C_{2v}$ | 1.48 |
| 4 | tetrahedron | $T_d$ | 2.72 | 7 | capped octahedron | $C_1$ | 1.75 |
| 5 | W | $C_{2v}$ | **0.00** | 8 | capped rhombus | $D_{4h}$ | **0.00** |
| 5 | X | $D_{2h}$ | 0.43 | 8 | capped hexagon | $C_{2v}$ | 0.25 |
| 5 | trapezoid | $C_{2v}$ | 0.63 | 8 | bicapped octahedron I | $C_{2v}$ | 0.27 |
| 5 | triangle | $C_s$ | 0.81 | 8 | bicapped octahedron II | $D_{2d}$ | 0.36 |
| 5 | pyramid | $C_{2v}$ | 0.84 | 8 | capped tetrahedron | $C_s$ | 0.46 |
| 5 | Y | $C_{2v}$ | 1.17 | 8 | crown | $C_{2v}$ | 0.48 |
| 5 | trigonal bipyramid | $D_{3h}$ | 1.35 | 8 | bicapped octahedron III | $D_{3d}$ | 1.79 |
| 5 | square | $C_{2v}$ | 2.05 | 9 | capped hexagon I | $C_{2v}$ | **0.00** |
| 6 | triangle | $D_{3h}$ | **0.00** | 9 | capped hexagon II | $C_{2v}$ | 0.12 |
| 6 | pentagonal pyramid | $C_{5v}$ | 0.79 | 9 | trapezoid | $D_{2h}$ | 0.17 |
| 6 | double rhombus | $D_{2h}$ | 1.32 | 10 | double hexagon | $D_{2h}$ | – |
| 6 | boat | $C_1$ | 1.58 | | | | |
| 6 | chevron | $C_{2v}$ | 1.69 | | | | |
| 6 | square | $D_{2h}$ | 1.78 | | | | |
| 6 | octahedron | $O_h$ | 1.81 | | | | |

ing to a study by Häkkinen and Landman[46] six years ago. The same group found three years later[60] a better configuration than the hexagon, the capped $Au_6$ triangle, and the tricapped square (crown) as the second lowest-lying structure. Nevertheless, the pentagonal bipyramid, our semiempirical global minimum, is only 0.36 eV higher in energy than the PBEPBE ground state, which makes it the only one semiempirical minimum lying so close to the *ab-initio* one. Using other functionals, for example in the *local spin density approximation*, one could determine this configuration as ground state or degenerated with the ground state structure, as reported before.

Few years ago, the global minimum structure of the $Au_8$ cluster was considered to be a distorted bicapped octahedron, however, recent studies[58, 59] reveal that its ground state most probably has the shape of a capped rhombus and is two dimensional. The next isomers are a bicapped hexagon and a series of three dimensional structures. All of them, except for the last isomer, the bicapped octahedron III, lie very close in energy to the ground state and also between themselves. This bicapped octahedron is the global minimum for this cluster size according to the VC potential, however, in the PBEPBE formalism it lies about 1.8 eV higher in energy than the ground state. The sixth isomer, about 0.5 eV higher in energy than the capped rhombus, is also a bicapped hexagon, which according to our knowledge has not been proposed before.

Finally, the number of the considered isomers for the clusters with $N = 9$ and 10 atoms becomes more and more reduced, due to the extremely long computational time needed for the optimization of each structure. The density functional methods could be appropriately used for such heavy systems only up to 10-15 atoms, optimizing chosen structures and using effective core potentials developed especially for these systems. Beyond 10 atoms one needs a computationally efficient method with reasonable compromise between accuracy and capability, and exactly such are the potentials used in the present work - they allow us to optimize thousands of atoms without severe geometrical constraints, and the most important issue is that the calculations remain completely *unbiased*.

At Fig. 4.4 are shown the calculated stability function, the HOMO-LUMO (highest occupied molecular orbital – lowest unoccupied molecular orbital) gap, and the obtained ionization potentials for the global minima structures of the clusters with up to 8 atoms. The stability function, $E_{tot}(N + 1.1) + E_{tot}(N - 1.1) - 2E_{tot}(N.1)$, where $E_{tot}(N.k)$ is the total energy of the energetically $k$-lowest isomer of the $Au_N$ cluster, shows peaks identifying the highly stable structures. Both the stability function and the HOMO-LUMO gap exhibit odd-even oscillations indicating that the even-numbered clusters are relatively more stable than their odd-numbered neighbors. This stabilization is most likely due to spin pairing in these clusters. The HOMO-LUMO gap is particularly larger for $Au_2$ and $Au_6$, and has its minimum at the 3-atom cluster, in contrast to the results by Wang *et al.*[50], who obtained the linear chain, our 3 isomer, as the ground state for this cluster size. Our results are in very good agreement with those from Ref.[46], except for the $Au_5$ cluster, whose HOMO-LUMO gap is more close to the results obtained by Wang, although the lowest-energy structure in all considered studies is the W-shaped trapezoid. Among the smallest clusters, the $Au_6$ one has the highest particular stability. The ionization potentials are calculated as the difference between the total energies of the
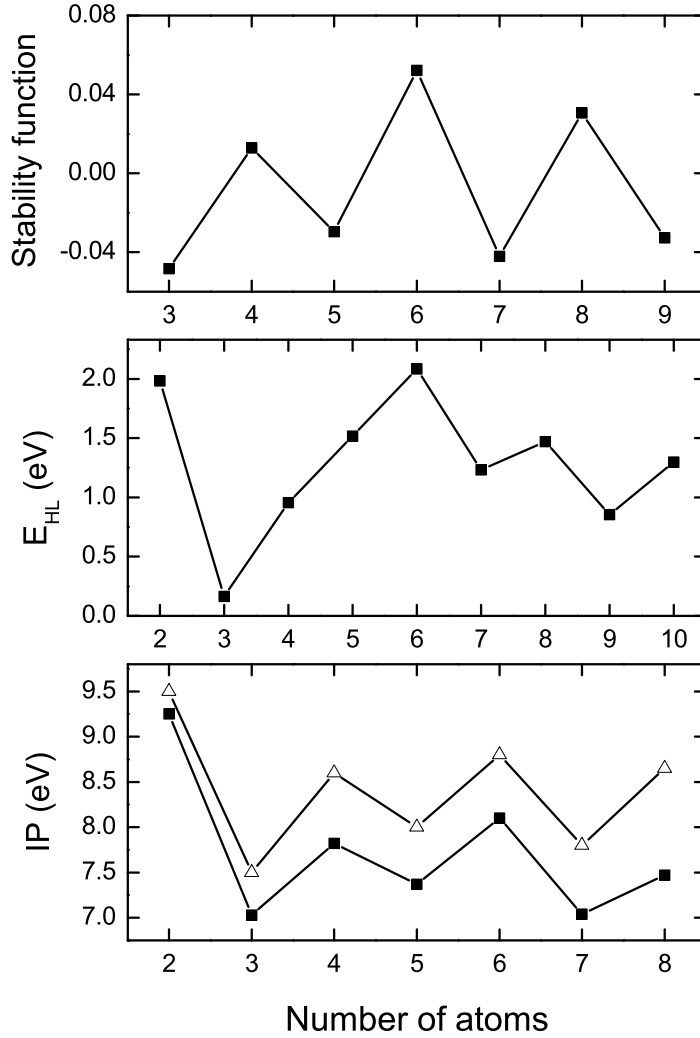
**Figure 4.4:** The stability function, the HOMO-LUMO gap $E_{HL}$, and the calculated (solid squares) and experimental (open triangles) ionization potentials of the gold clusters. The experimental values are from Ref.[95].

positively charged, and those of the neutral clusters. The best agreement between theory and experiment is found for $Au_2$ and $Au_3$, with deviations growing with the number of atoms.

In summary, although the structures predicted by the EAM are not among the first isomers for a given cluster size according to the PBEPBE functional, the omission of the relativistic effects collocates these structures very close or degenerate to the global minima. The EAM formalism has proved its applicability to these small particles[93, 132], therefore, considering the results for the smallest clusters with up to 7 atoms as exhaustively studied by the first principles methods, here we will concentrate on the larger clusters that can be described only by the semiempirical approaches.

## 4.4   Energetic properties

### 4.4.1   Binding energy

The high stability of the so-called 'magic-numbered' clusters has become a subject of great interest in connection with its applicability in the medicinal and the colloidal chemistry, as well as in the production of catalysts and high-tech nanomaterials.

In Fig. 4.5 are presented the binding energy per atom for the global-minima structures, as well as the difference between the total energies of the lowest-lying isomers obtained by us and those found by Sebetci *et al.*[89]. One can see that the difference increases almost linearly with the number of atoms and has its maximum at $N = 79$, where we obtained a truncated octahedron in contrast to the structure with $D_{3h}$ symmetry found by Sebetci and Güvenç. At $N = 52$ they obtained an uncentered icosahedron-like structure with $C_{2h}$ symmetry, that lies energetically between our second and third lowest isomers. As the methods for the global minima optimizations used by these authors and ours are completely different (basin-hopping Monte Carlo algorithm used by Sebetci and Güvenç and the Aufbau/Abbau method developed by us), it is quite possible that the higher-lying isomers found by them would not be found when using our approach, and vice versa. However, having observed the differences in the symmetries of the ground state structures and those in the total energies, we can conclude that our approach performs better in the global-minima search, at least for clusters with up to 80 atoms.

### 4.4.2   Stability

In order to identify the particularly stable clusters we have taken into account the following criteria. The clusters can be considered as very stable if their binding energy per atom is much larger than that of the two neighboring clusters. This can be quantified through the stability function, $E_{\mathrm{tot}}(N+1.1) + E_{\mathrm{tot}}(N-1.1) - 2E_{\mathrm{tot}}(N.1)$, where $E_{\mathrm{tot}}(N.k)$ is the total energy of the energetically $k$-lowest isomer of the $\mathrm{Au}_N$ cluster. This function, that has maxima for particularly stable clusters, is shown in Fig. 4.6.

Here we can identify a large number of particularly stable clusters, i.e., so-called magic clusters. These are found for $N = 4$, 6, 10, 13, 15, 17, 23, 28, 30, 36, 38, 40, 42, 45, 49, 54, 58, 61, 64, 66, 68, 73, 75, 77, 79, 82, 84, 89, 92, 95, 101, 109, 111, 116, 118, 124, 128, 133, 135, 140, 144, and 146. The most pronounced peaks occur at $N = 13$, 30, 40, 54, 75, 79, 82, 124, 133, 140, and 146. In agreement with Sebetci and Güvenç[89], the 54-atom icosahedron without a central atom is found to be more stable than the $\mathrm{Au}_{55}$ cluster. The latter possesses a distorted icosahedral structure with $C_{3v}$ symmetry, lying with 0,374 eV lower than the perfect icosahedron obtained by Sebetci and Güvenç, with 2,9 eV lower than the decahedron, and is with 3,27 eV energetically favored comparing to the cuboctahedron. In our study, all the three lowest-lying isomers of $\mathrm{Au}_{55}$ have lower energy than the symmetric structures, in agreement with previous studies where disordered configurations were found as global minima for $\mathrm{Au}_{55}$[81, 82, 85, 86]. For $\mathrm{Au}_{38}$ and $\mathrm{Au}_{75}$, a cuboctahedron [44, 78, 79, 86, 89] and a Marks decahedron [78, 82, 84, 89]
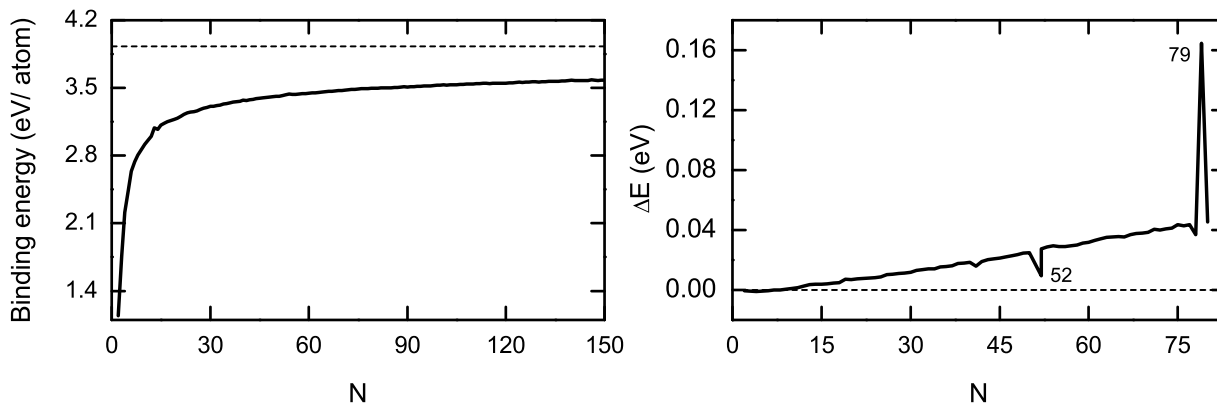
**Figure 4.5:** On the left - the binding energy per atom as a function of size for the energetically lowest isomers of $N$ up to 150, the dashed line shows the *bulk* value; on the right - the difference between the total energies of the lowest-lying isomers with up to 80 atoms obtained by Sebetci *et al.* and those found by us.
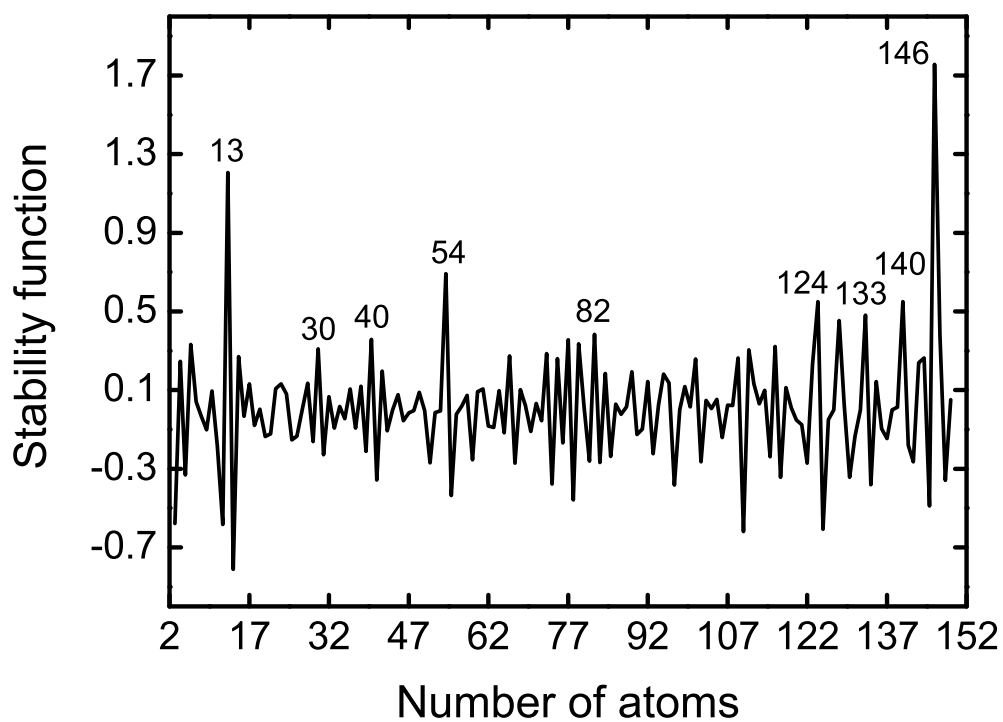


**Figure 4.6:** The stability function as a function of cluster size.
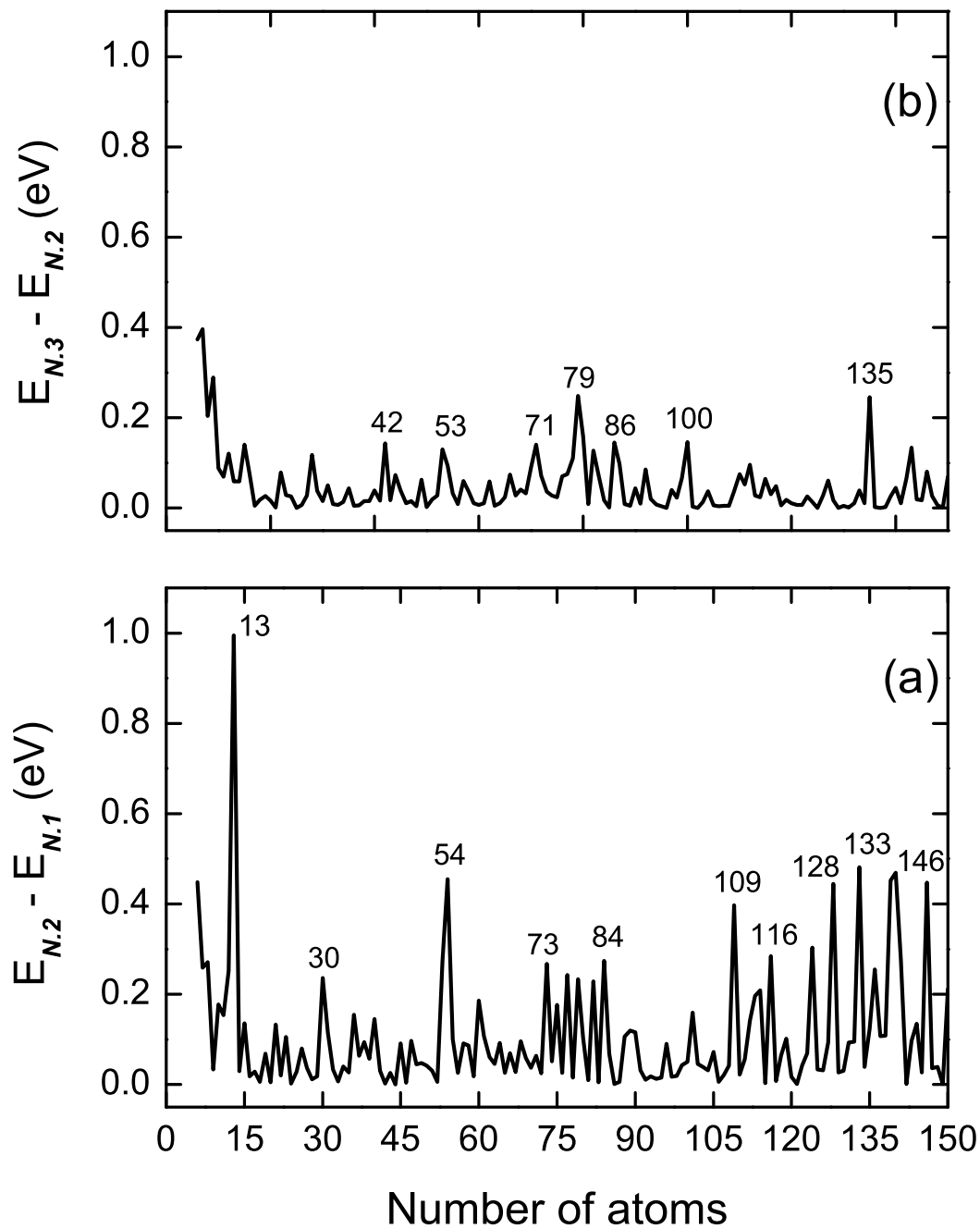
**Figure 4.7:** The total-energy difference between the three energetically lowest neighboring isomers as a function of cluster size.

**Table 4.3:** Point groups of the optimized gold clusters. The lowest-lying isomer is denoted as N.1

| N | N.1 | N.2 | N.3 | N | N.1 | N.2 | N.3 | N | N.1 | N.2 | N.3 | N | N.1 | N.2 | N.3 |
|---|---|---|---|---|---|---|---|---|---|---|---|---|---|---|---|
| 2 | $D_{\infty h}$ | | | 40 | $D_3$ | $C_1$ | $C_2$ | 78 | $C_{2v}$ | $C_s$ | $C_1$ | 116 | $C_s$ | $O_h$ | $C_{3v}$ |
| 3 | $D_{3h}$ | | | 41 | $C_1$ | $C_1$ | $C_1$ | 79 | $O_h$ | $C_s$ | $C_1$ | 117 | $C_s$ | $C_s$ | $C_1$ |
| 4 | $T_d$ | | | 42 | $D_4$ | $T_d$ | $C_1$ | 80 | $C_s$ | $O$ | $C_s$ | 118 | $C_{2v}$ | $C_1$ | $C_1$ |
| 5 | $D_{3h}$ | | | 43 | $D_2$ | $C_1$ | $C_1$ | 81 | $C_{2v}$ | $C_s$ | $C_1$ | 119 | $C_1$ | $C_1$ | $C_1$ |
| 6 | $O_h$ | $C_{2v}$ | | 44 | $C_s$ | $C_2$ | $C_1$ | 82 | $C_s$ | $C_3$ | $C_{2v}$ | 120 | $C_1$ | $C_1$ | $C_1$ |
| 7 | $D_{5h}$ | $C_{3v}$ | $C_2$ | 45 | $C_s$ | $C_1$ | $C_1$ | 83 | $C_s$ | $C_s$ | $C_s$ | 121 | $C_1$ | $C_1$ | $C_1$ |
| 8 | $D_{2d}$ | $C_s$ | $D_{3d}$ | 46 | $C_3$ | $C_s$ | $C_1$ | 84 | $C_s$ | $C_s$ | $C_s$ | 122 | $C_1$ | $C_1$ | $C_1$ |
| 9 | $C_{2v}$ | $D_{3h}$ | $C_s$ | 47 | $C_1$ | $C_2$ | $C_1$ | 85 | $C_s$ | $C_s$ | $C_s$ | 123 | $C_s$ | $C_1$ | $C_1$ |
| 10 | $C_{3v}$ | $D_{4d}$ | $D_{3h}$ | 48 | $C_1$ | $D_{2d}$ | $C_1$ | 86 | $C_s$ | $C_s$ | $C_s$ | 124 | $C_s$ | $C_1$ | $C_s$ |
| 11 | $C_{2v}$ | $C_2$ | $C_2$ | 49 | $C_1$ | $C_1$ | $C_s$ | 87 | $C_2$ | $C_1$ | $C_1$ | 125 | $C_1$ | $C_1$ | $C_1$ |
| 12 | $C_{5v}$ | $C_2$ | $D_{3h}$ | 50 | $C_1$ | $C_1$ | $C_1$ | 88 | $C_1$ | $C_1$ | $C_1$ | 126 | $C_s$ | $C_1$ | $C_1$ |
| 13 | $I_h$ | $C_1$ | $C_s$ | 51 | $C_1$ | $C_1$ | $C_1$ | 89 | $C_2$ | $C_s$ | $C_s$ | 127 | $C_1$ | $C_1$ | $C_1$ |
| 14 | $C_{3v}$ | $C_{2v}$ | $C_s$ | 52 | $D_{5d}$ | $C_{2v}$ | $C_{2v}$ | 90 | $C_1$ | $C_1$ | $C_1$ | 128 | $C_s$ | $C_1$ | $C_s$ |
| 15 | $D_{6d}$ | $C_{2v}$ | $C_s$ | 53 | $C_{5v}$ | $C_{3v}$ | $C_1$ | 91 | $C_1$ | $C_1$ | $C_1$ | 129 | $C_1$ | $C_s$ | $C_s$ |
| 16 | $C_{2v}$ | $D_{3h}$ | $C_{2v}$ | 54 | $I_h$ | $C_1$ | $C_s$ | 92 | $C_1$ | $C_2$ | $C_1$ | 130 | $C_s$ | $C_s$ | $C_s$ |
| 17 | $T_d$ | $D_{4d}$ | $C_s$ | 55 | $C_{3v}$ | $C_s$ | $C_1$ | 93 | $C_1$ | $C_1$ | $C_1$ | 131 | $C_{2v}$ | $C_1$ | $C_1$ |
| 18 | $C_{4v}$ | $C_{2v}$ | $C_s$ | 56 | $C_s$ | $C_{2v}$ | $C_2$ | 94 | $C_1$ | $C_1$ | $C_1$ | 132 | $C_s$ | $C_1$ | $C_1$ |
| 19 | $D_{5h}$ | $D_{4d}$ | $C_{2v}$ | 57 | $C_1$ | $C_1$ | $C_1$ | 95 | $C_1$ | $C_1$ | $C_1$ | 133 | $C_{2v}$ | $C_1$ | $C_1$ |
| 20 | $D_{3d}$ | $D_2$ | $D_{2h}$ | 58 | $C_1$ | $C_s$ | $C_1$ | 96 | $C_1$ | $C_1$ | $C_1$ | 134 | $C_s$ | $C_s$ | $C_s$ |
| 21 | $C_s$ | $C_1$ | $C_s$ | 59 | $C_s$ | $C_1$ | $C_1$ | 97 | $C_2$ | $C_1$ | $C_1$ | 135 | $C_s$ | $C_1$ | $C_1$ |
| 22 | $C_1$ | $C_s$ | $D_{6h}$ | 60 | $C_s$ | $C_s$ | $C_1$ | 98 | $C_1$ | $C_1$ | $C_1$ | 136 | $C_s$ | $C_1$ | $C_1$ |
| 23 | $C_{2v}$ | $C_s$ | $C_s$ | 61 | $C_{3v}$ | $C_s$ | $C_{2v}$ | 99 | $C_2$ | $C_1$ | $C_1$ | 137 | $C_{2v}$ | $C_1$ | $C_1$ |
| 24 | $C_2$ | $C_s$ | $C_{3v}$ | 62 | $C_s$ | $C_1$ | $C_1$ | 100 | $C_1$ | $C_1$ | $C_1$ | 138 | $C_s$ | $C_1$ | $C_1$ |
| 25 | $C_2$ | $C_1$ | $C_{2v}$ | 63 | $C_{2v}$ | $C_s$ | $C_s$ | 101 | $C_2$ | $D_{5h}$ | $C_1$ | 139 | $C_{2v}$ | $C_1$ | $C_1$ |
| 26 | $C_1$ | $C_s$ | $C_s$ | 64 | $C_{2v}$ | $C_1$ | $C_s$ | 102 | $C_1$ | $C_1$ | $C_1$ | 140 | $O_h$ | $C_s$ | $C_s$ |
| 27 | $C_s$ | $C_2$ | $C_s$ | 65 | $C_1$ | $C_1$ | $C_1$ | 103 | $C_2$ | $C_2$ | $C_1$ | 141 | $C_{2v}$ | $C_{2v}$ | $C_s$ |
| 28 | $C_s$ | $C_2$ | $C_{2v}$ | 66 | $C_s$ | $C_2$ | $C_1$ | 104 | $C_1$ | $C_2$ | $C_1$ | 142 | $C_s$ | $C_s$ | $C_s$ |
| 29 | $C_2$ | $C_s$ | $C_2$ | 67 | $C_s$ | $C_1$ | $C_1$ | 105 | $C_2$ | $C_s$ | $C_2$ | 143 | $C_s$ | $C_{2v}$ | $C_s$ |
| 30 | $C_{3v}$ | $C_1$ | $C_2$ | 68 | $C_s$ | $C_1$ | $C_1$ | 106 | $C_{3v}$ | $C_1$ | $C_s$ | 144 | $C_s$ | $C_s$ | $C_s$ |
| 31 | $C_3$ | $C_1$ | $C_{3v}$ | 69 | $C_2$ | $C_1$ | $C_1$ | 107 | $C_s$ | $C_1$ | $C_1$ | 145 | $C_1$ | $C_s$ | $C_1$ |
| 32 | $D_{2d}$ | $C_3$ | $C_{2v}$ | 70 | $C_1$ | $C_1$ | $C_1$ | 108 | $C_s$ | $C_s$ | $C_1$ | 146 | $D_{5h}$ | $C_s$ | $C_1$ |
| 33 | $C_2$ | $C_1$ | $C_1$ | 71 | $C_{2v}$ | $C_{2v}$ | $C_1$ | 109 | $C_{3v}$ | $C_1$ | $C_1$ | 147 | $C_1$ | $C_1$ | $C_1$ |
| 34 | $T_d$ | $C_3$ | $C_s$ | 72 | $C_s$ | $C_s$ | $C_s$ | 110 | $C_{2v}$ | $C_1$ | $C_1$ | 148 | $C_1$ | $C_1$ | $C_1$ |
| 35 | $C_{2v}$ | $D_3$ | $C_{2v}$ | 73 | $C_{2v}$ | $C_1$ | $C_s$ | 111 | $C_1$ | $C_1$ | $C_1$ | 149 | $C_1$ | $C_1$ | $C_1$ |
| 36 | $C_{2v}$ | $C_s$ | $D_2$ | 74 | $C_s$ | $C_{5v}$ | $C_s$ | 112 | $C_{2v}$ | $C_1$ | $C_1$ | 150 | $C_1$ | $C_1$ | $C_1$ |
| 37 | $C_{2v}$ | $C_s$ | $C_2$ | 75 | $D_{5h}$ | $C_{2v}$ | $C_s$ | 113 | $T$ | $C_2$ | $D_2$ | | | | |
| 38 | $O_h$ | $D_{4h}$ | $C_s$ | 76 | $C_s$ | $C_s$ | $C_s$ | 114 | $C_3$ | $C_{2v}$ | $C_2$ | | | | |
| 39 | $D_3$ | $C_s$ | $C_{4v}$ | 77 | $C_{2v}$ | $C_s$ | $C_{2v}$ | 115 | $C_s$ | $C_1$ | $C_s$ | | | | |
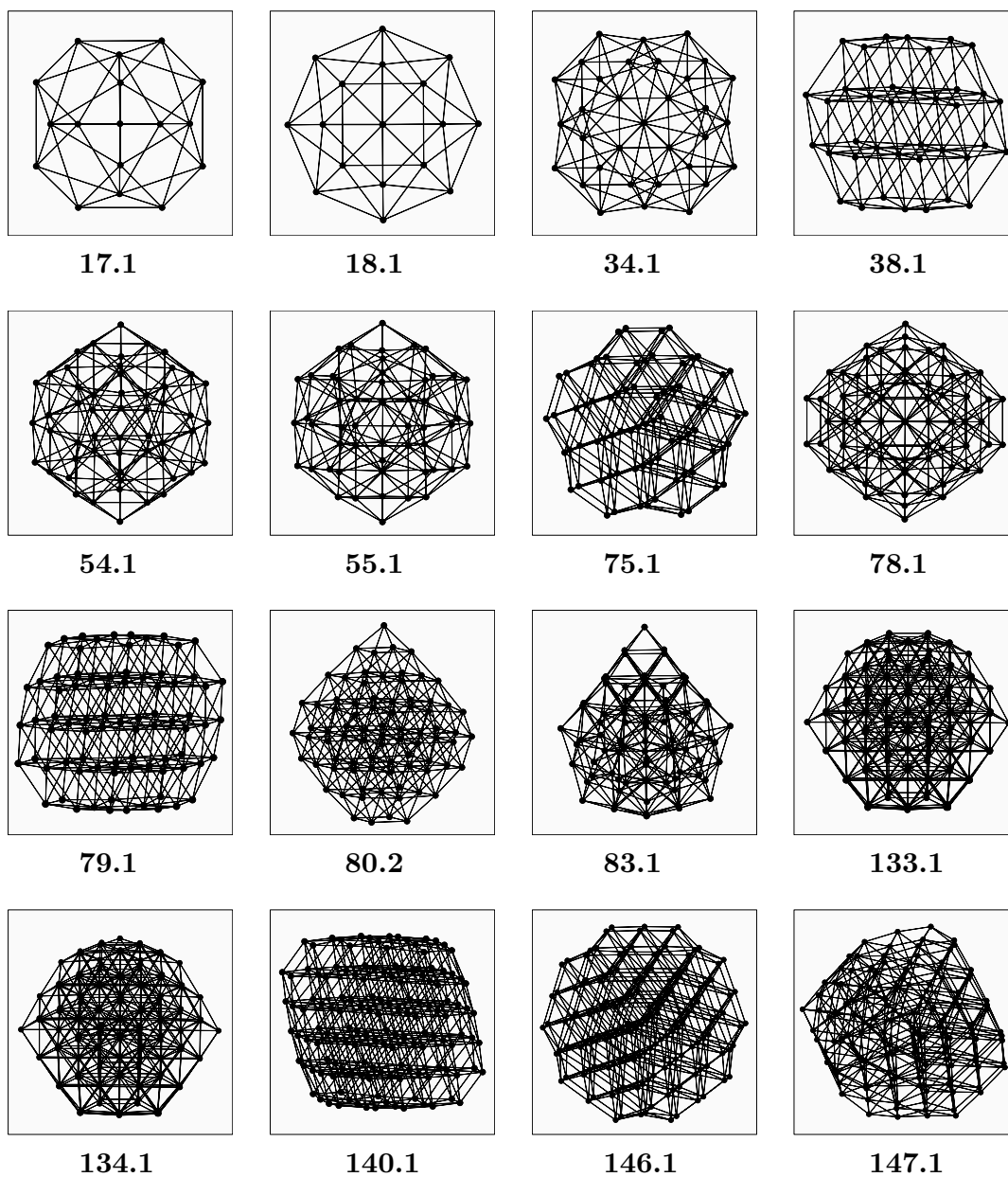
**Figure 4.8:** Some Au$_N$ clusters with high or peculiar symmetry.

were obtained, in agreement with first-principles and semiempirical studies. However, two studies employing the many-body Gupta potential denoted amorphous configurations as global minima of $Au_{38}$ [83, 85], which is most probably due to the parameterization of the potential, as Darby *et al.*[86] found an octahedron as lowest-lying isomer by using another version of the same potential.

The most striking result is that the 146-atom Marks decahedron is more stable than the $Au_{147}$ icosahedron. According to our study, the third Mackay icosahedron lies with 2,89 eV lower than the cuboctahedron, with 2,53 eV lower than the decahedron, but with 0,37 eV higher than a disordered structure with partly decahedral construction. To our knowledge, this is the first study predicting a disordered global minimum for the $Au_{147}$ cluster.

According to our other criterion for a particularly stable cluster, such a cluster occurs if the energy difference between the two energetically lowest isomers $E_{tot}(N.2) - E_{tot}(N.1)$ is large. This energy difference is shown in Fig. 4.7, and comparing to Fig. 4.6 we can see that many of the clusters that are particularly stable according to the first criterion are stable also according to the second one.

## 4.5 Structural properties

In this subsection, instead of discussing in particular the structures of the individual clusters, we shall introduce different quantities that are devised to reduce the available information to some few key numbers. The theoretical background of the descriptors used in the subsection was introduced by us in a previous work.[93]

### 4.5.1 Overall cluster shape

First we shall consider the overall shape of the clusters. As we showed in our earlier report on Ni clusters[93], it is convenient to study the $3 \times 3$ matrix containing the elements

$$I_{st} = \frac{1}{u_l^2} \sum_{n=1}^{N} (R_{n,s} - R_{0,s})(R_{n,t} - R_{0,t}) \tag{4.1}$$

with $u_l = 1\text{Å}$ being a length unit, and $s$ and $t$ being $x$, $y$, and $z$, and with

$$\vec{R}_0 = \frac{1}{N} \sum_{n=1}^{N} \vec{R}_n \tag{4.2}$$

being the center of the cluster. The three eigenvalues of this matrix, $I_{\alpha\alpha}$, can be used in separating the clusters into being overall spherical (all eigenvalues are identical), more cigar-like shaped (one eigenvalue is large, the other two are small), or more lens-shaped (two large and one small eigenvalue). The average of the three eigenvalues, $\langle I_{\alpha\alpha} \rangle$, is a measure of the overall extension of the cluster. For a homogeneous sphere with $N$ atoms, the eigenvalues scale like $N^{5/3}$. Hence, we show in Fig. 4.9 quantities related to $I_{\alpha\alpha}$ but

scaled by $N^{-5/3}$. The shape analysis in Fig. 4.9 separates the clusters into being overall spherical, more cigar-like shaped, or more lens-like shaped. One can see that only few clusters have a spherical shape (these are found for the energetically lowest isomer for $N = 4$, 6, 13, 17, 34, 38, 54, 79, and 140, and for the next one for $N = 42$ and 116), all of them corresponding to high-symmetrical isomers (cf. Table 4.4.1) and, for the lowest-energy isomer most of them to the class of magic clusters. It is interesting that the average value follows more or less the same curve for all the three isomers, with some deviations at $N$ = 130, 146, and 147. Also the largest differences show similar behavior, except for some few cases mainly for $N$ below 40 and between 80 and 85. Therefore, except when the eigenvalues are all very similar (i.e., the largest difference is very small, which occurs for $N$ around 50, 70, 100, 116, and 140), the overall shape (i.e., lens- or cigar-like) is the same for all three isomers.
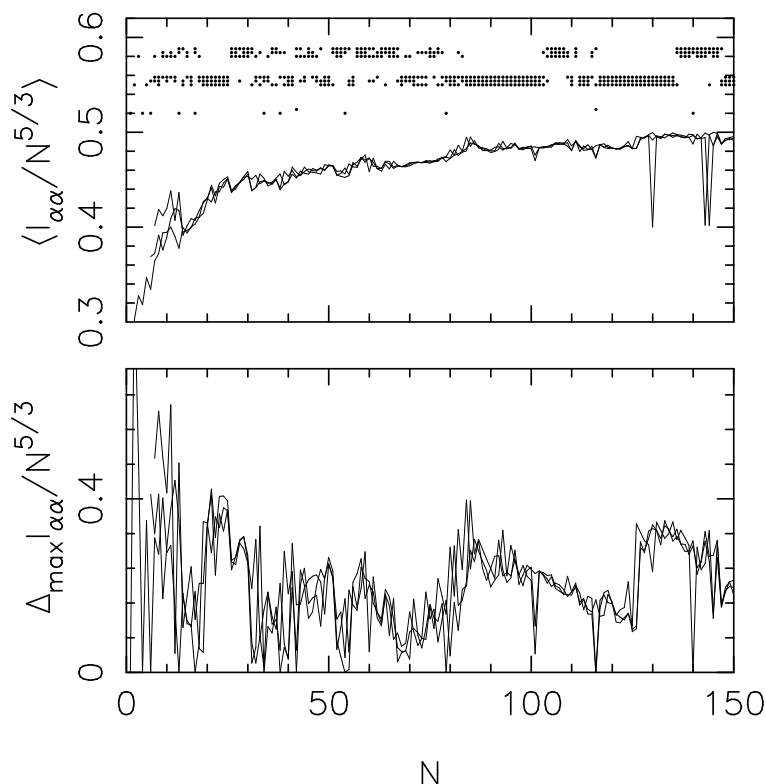


**Figure 4.9:** Different properties related to the eigenvalues $I_{\alpha\alpha}$. In the upper panel we show the average value together with points indicating whether clusters with overall spherical shape (lowest set of rows), overall cigar shape (middle set of rows), or overall lens shape (upper set of rows) are found for a certain size. Moreover, in each set of rows, the lowest row corresponds to the energetically lowest isomer, the second one to the energetically second-lowest isomer, etc. In the lower panel we show the maximum difference of the eigenvalues for the three different isomers.
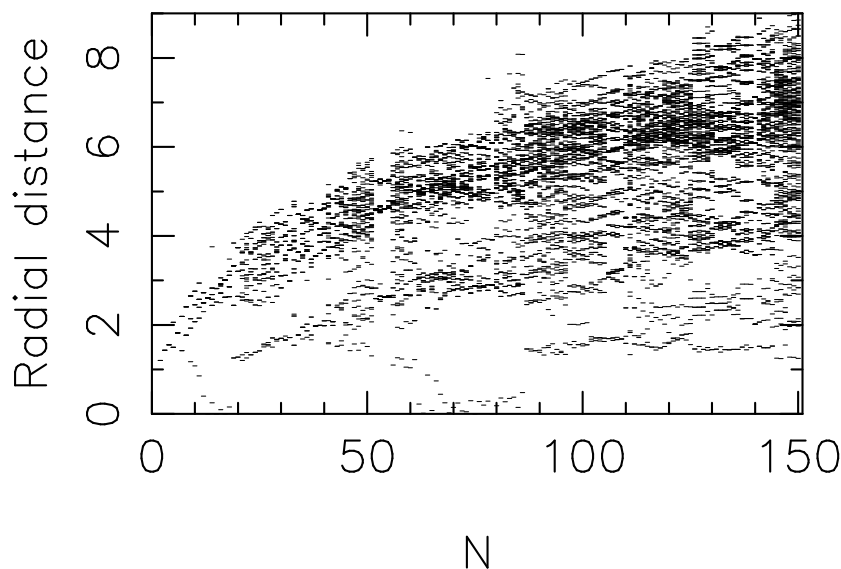
**Figure 4.10:** The distribution of radial distances (in Å) for the lowest-lying isomer as a function of cluster size. Each small line represents (at least) one atom with that radial distance.

The construction of atomic shells can be easily seen from the distribution of radial distances shown in Fig. 4.10 for the ground state structures as function of the cluster size. Up to $N$ around 50, no trends can be identified, but for $N$ just above 50 a clear tendency towards shell construction can be seen for the first isomer. This corresponds to the formation of the $Au_{54}$ icosahedral cluster. Also for $N$ close to 110 and around 140 shell constructions for the lowest-lying isomer are observed. In the latter case, this corresponds to the formation of an octahedron. The radial distributions for the second and the third isomers are not shown, as they are quite similar to that for the first isomer. Particular shell constructions are found only for highly symmetrical clusters corresponding to $N = 42, 48, 80, 101, 116$, and around $Au_{130}$ for the second isomer, and around $N = 40, 60, 116$, and 130 for the third isomer.

## 4.5.2 Similarity functions

We have found earlier[93, 132] that it was useful to monitor the structural development of the isomer with the lowest total energy through the so-called similarity functions. We
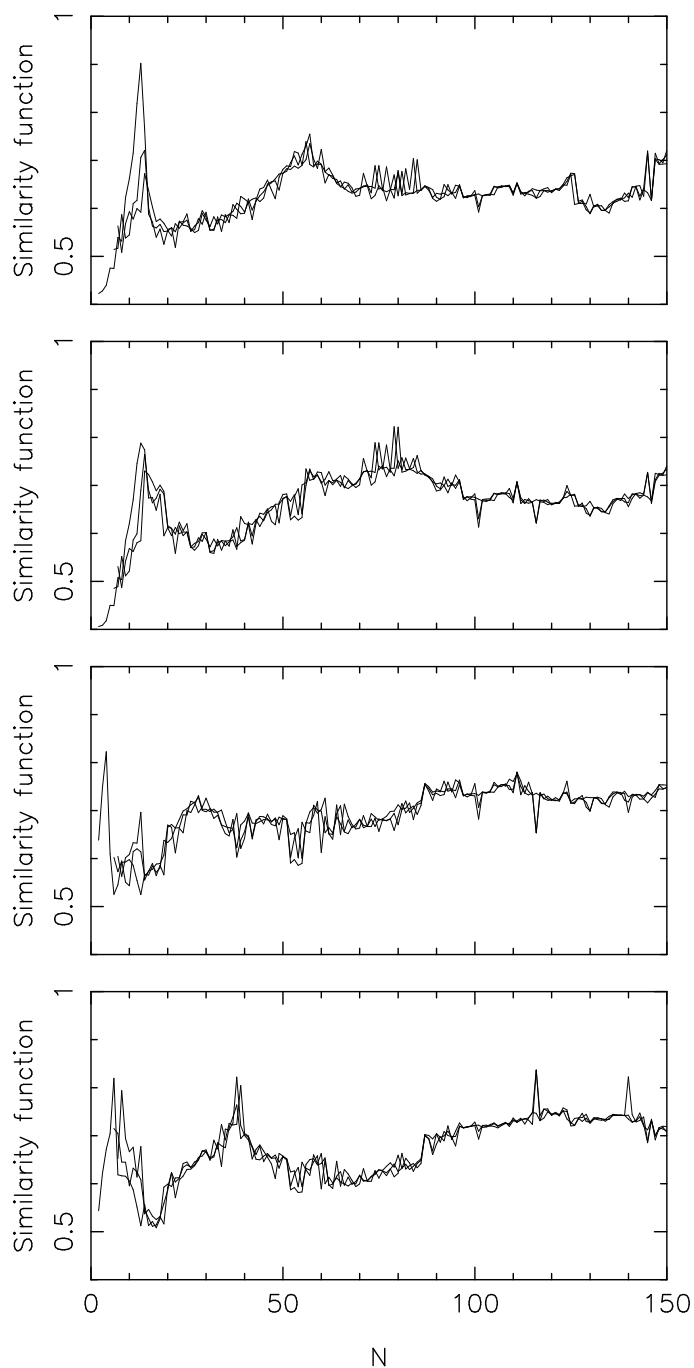
**Figure 4.11:** Each panel shows the similarity function for all the three isomers when comparing to (a) an icosahedral cluster, and (b–d) a spherical fragment of the *fcc* crystal where the center of the fragment is placed at (b) the position of an atom, (c) the middle of a nearest-neighbor bond, and (d) the center of the unit cell, respectively.
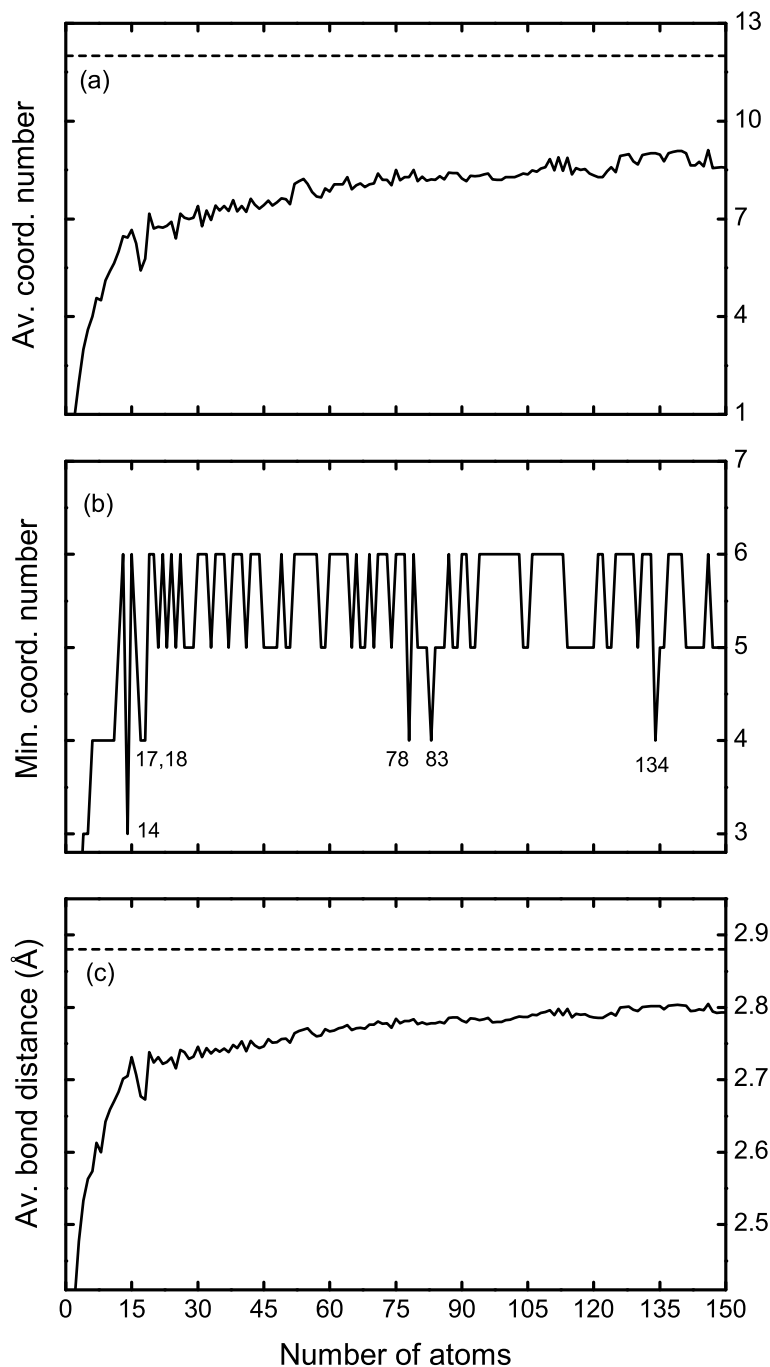
**Figure 4.12:** (a) the average coordination number, (b) the minimum coordination number, and (c) the average bond distances as functions of cluster size. The dashed lines in (a) and (c) show the corresponding bulk values for gold.

define the radial distances from the center for each of the atoms of a given cluster $Au_N$

$$r_n = |\vec{R}_n - \vec{R}_0| \tag{4.3}$$

and sort these in increasing order.

Simultaneously we consider a large spherical fragment of a *fcc* crystal as well as a large cluster of icosahedral symmetry, here $Au_{309}$. Also for these we define a radial distance for each atom, $r'_n$, which also are sorted. In order to compare a given cluster with those two systems we calculate subsequently

$$q = \left[ \frac{1}{N} \sum_{n=1}^{N} (r_n - r'_n)^2 \right]^{1/2}, \tag{4.4}$$

giving the similarity function

$$S = \frac{1}{1 + q/u_l} \tag{4.5}$$

($u_l = 1\text{Å}$). $S$ approaches 1 if the $Au_N$ cluster is very similar to the reference system, i.e., a fragment of the *fcc* crystal or an icosahedral cluster. In Fig. 4.11 we show the resulting functions in four cases, i.e., when comparing with the relaxed $Au_{309}$ cluster, and when comparing with three fragments of the *fcc* crystal differing in the position of the center (i.e., the position of an atom, the middle of a nearest-neighbor bond, and the center of the unit cell, respectively).

One sees both that clusters that clearly resemble *fcc* fragments and that clusters that resemble icosahedral clusters can be identified. The most pronounced peaks for the icosahedral structures correspond to $N = 13$, 55, and 147, the first-, second-, and third-layer Mackay icosahedron, respectively. Clusters with icosahedral structures are also found in the interval between $N = 75$ and $N = 79$, as discussed in the previous subsection. The octahedral ones are found around $N = 6$, 8, 13, 28, 38, and 79. Beyond $N = 135$, the values for the *fcc*-like clusters decrease, whereas an increased similarity with the icosahedral clusters is observed. It is interesting to notice that the structures are built up over a certain range of cluster sizes so that, e.g., the icosahedral structure for $N = 55$ can be seen also for both larger and smaller values of $N$ around this value.

### 4.5.3   Coordination numbers

In Fig. 4.12 are shown the average and minimal coordination numbers, and the average bond lengths of the clusters. We define two atoms as being bonded if their interatomic distance is less than 3.49 Å, which is the average value between the nearest-neighbor distance (2.89 Å) and the next-nearest-neighbor distance (4.08 Å) in bulk Au. Moreover, we distinguish between inner atoms with a coordination number of 12 or larger and surface atoms with a coordination number less than 12.

Fig. 4.12(a) presents the average coordination number as a function of $N$. A saturation towards the bulk limit of 12 is seen, although one has to remember that even for the

largest cluster of our study 94 out of 150 atoms are characterized as surface atoms. Also, the function increases monotonically with the size of the systems, with oscillations in particular for the clusters with $N = 17$ and 18, which is due to the formation of a tetrahedron for $Au_{17}$, and a structure with $C_{4v}$ symmetry at $N = 18$, respectively. The latter is already obtained with the EAM method (see Ref.[89]), but this is the first time when a tetrahedral configuration is found for the $Au_{17}$ cluster. Its second isomer in this study ($D_{4d}$) is already found by Wilson and Johnston[79] as a lowest-lying minimum.

The minimum atomic coordination for each cluster size is shown in Fig. 4.12(b). The existence of low-coordinated atoms, i.e with coordination numbers of 3 or 4, could point to the occurrence of a cluster growth, where extra atoms are added to the surface of the cluster, whereas the higher coordination numbers could indicate a growth where atoms are inserted inside the cluster, or, alternatively, upon a strong rearrangement of the surface atoms. This is the case for the gold clusters, with few exceptions at $N = 14, 17, 18, 78,$ 83, and 134, where lower coordinations are found. The lowest coordination corresponding to $Au_{14}$ is in connection with the formation of an icosahedron plus one additional atom on the surface. At $N = 17$ and 18, some structural changes take place, as discussed above. $Au_{78}$ and $Au_{83}$ correspond to structures with decahedral motif capped with one additional atom. This is also the case for $Au_{134}$ where the $C_{2v}$ symmetry of the decahedral structure corresponding to $N = 133$ is lowered by adding an atom on the surface.

Fig. 4.12(c) shows the average bond length as a function of the cluster size. The dashed line corresponds to the bulk value of 2.89 Å. The average bond length for all the structures is smaller than the bulk value, especially for $Au_{17}$ and $Au_{18}$, where more compact structures are formed. However, this property approaches the bulk value faster than the average coordination number.

### 4.5.4 Cluster growth

The central point in most of the molecular dynamics studies on gold clusters is to identify how the clusters grow and if the cluster with $N$ atoms could be derived from the one with $N-1$ atoms simply by adding one atom. In order to quantify this possible relation, first we consider the structure with the lowest total energy for the $(N-1)$-atom cluster. For this we calculate and sort all interatomic distances, $d_i$, $i = 1, 2, \cdots, \frac{N(N-1)}{2}$. Subsequently we consider each of the $N$ fragments of the $N$-cluster that can be obtained by removing one of the atoms and keeping the rest at their positions. For each of those we also calculate and sort all interatomic distances $d_i'$, and calculate, subsequently,

$$q = \left[ \frac{2}{N(N-1)} \sum_{i=1}^{N(N-1)/2} (d_i - d_i')^2 \right]^{1/2}. \tag{4.6}$$

Among the $N$ different values of $q$ we choose the smallest one, $q_{\min}$ and calculate the similarity function

$$S = \frac{1}{1 + q_{\min}/u_l} \tag{4.7}$$
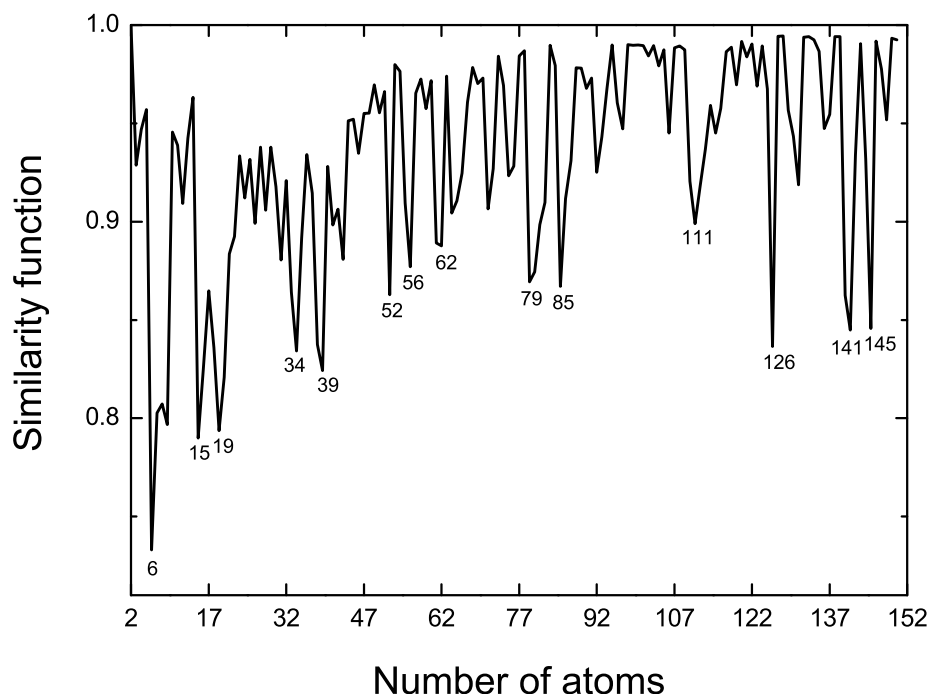
**Figure 4.13:** The similarity function as function of the cluster size. It describes whether the cluster with $N$ atoms is similar to that of $N - 1$ atoms plus an extra atom.

($u_l = 1\text{Å}$) which approaches 1 if the $\text{Au}_N$ cluster is very similar to the $\text{Au}_{N-1}$ cluster plus an extra atom.

The similarity function, shown in Fig. 4.13, approaches 1 if the $\text{Au}_N$ cluster is very similar to the $\text{Au}_{N-1}$ cluster plus an extra atom. We see indeed that for $N$ up to around 50, $S$ is significantly different from 1, confirming that in this range the growth is complicated. The most pronounced peaks occur at $6 < N < 9$, $15 < N < 20$, 34, 38, 39, 52, 56, 79, 80, 85, 111, 126, 140, 141, and $145 < N < 147$. Many of them correspond to high symmetrical clusters, however some of the clusters with larger peaks ($N = 39$, 56, 62, 85, 111, 126, 141, and 145) have lower symmetry. The octahedral $\text{Au}_{38}$ and the low-symmetrical $\text{Au}_{39}$ are structurally very different from their $N$-1-atom neighbors. $\text{Au}_{56}$ marks the end of the icosahedral shell built between $\text{Au}_{52}$ and $\text{Au}_{55}$, and the clusters resume their disordered growth. The octahedral $\text{Au}_{61}$ is followed by the disordered $\text{Au}_{62}$, and the decahedral $\text{Au}_{85}$ comes after the disordered $\text{Au}_{84}$. Between the decahedral $\text{Au}_{110}$ and $\text{Au}_{112}$ lies the disordered $\text{Au}_{111}$. The addition of one atom to the disordered $\text{Au}_{125}$ leads to the formation of an unfinished but regular decahedron at $N = 126$. The decahedral $\text{Au}_{141}$ comes immediately after the octahedron corresponding to $N = 140$. Although $\text{Au}_{144}$ has partly decahedral construction, its $N$+1-atom neighbor is disordered. It seems that for each cluster size there is a rearrangement of the gold atoms, and no a particular growth motif was observed. This in turn means that the cluster growth is very complicated and

it is difficult to consider it as an one-by-one atom addition.

# 4.6 Vibrational spectra and heat capacities

## 4.6.1 Dynamical matrix

We computed the vibrational spectrum of gold clusters with up to 150 atoms using the harmonic approximation. Employing the analytical form of the Hessian matrix, we constructed the $3N$ x $3N$ dynamical matrix

$$D_{ni,mj} = \left( \frac{1}{M} \frac{\partial^2 E_{tot)}}{\partial R_{ni} \partial R_{mj}} \right) \tag{4.8}$$

containing the second derivatives of the total energy with respect to the atomic coordinates in the equilibrium configuration. In this formula $M$ is the atomic mass and $R_{ni}$ denotes the coordinates $(i = x, y, z)$ of atom $n$. We performed the numerical diagonalization of the dynamical matrix

$$|D_{ni,mj} - \omega^2 \delta_{nm} \delta_{ij}| = 0 \tag{4.9}$$

in which $\delta_{nm}$, the Kronecker symbol, equals unity if $n=m$ and is zero otherwise, and $\omega$ is the vibrational frequency. In this study we have determined the vibrational frequencies for each global minima cluster size, however, we will discuss in details only the minimal and maximal vibrational frequencies. These are presented at Fig. 4.14 where one can see the maximal frequencies in the upper panel, and the minimal vibrations are shown in the bottom panel. Even the frequency of the dimer $Au_2$ is well reproduced - the experimental value is 191 cm$^{-1}$, and the obtained with the Voter-Chen EAM is equal to 180 cm$^{-1}$. The small difference is due to the slight contraction of the dimer bond in the EAM (2.40 Å) compared to the experiment (2.47 Å).

## 4.6.2 'Magic numbers' in the spectra

The magnitude of the vibrations is most pronounced up to $N = 31$, then it decreases significantly leaving only one island at $92 < N < 108$, where probably some structural changes take place. The most pronounced peak corresponds to $Au_{19}$ that has $D_{5h}$ symmetry. However, none of the next maxima or minima belongs to a structure of high symmetry, therefore in order to be able to draw a general trend, we proceed to the minimal frequencies. At the bottom panel, the dashed line at 20K corresponds to the temperature for which the heat capacities per vibrational mode were calculated, see Fig. 4.15. In this way, if a particular cluster has vibrations at or below this temperature, there will be most probably also a corresponding peak in the heat capacity. At Fig. 4.15 the values of the heat capacities for $N$ up to 15 are presented separately as they begin with very small values and increase rapidly in this cluster range. The vibrations corresponding to these clusters are also far above the 20 K temperature, therefore the most interesting
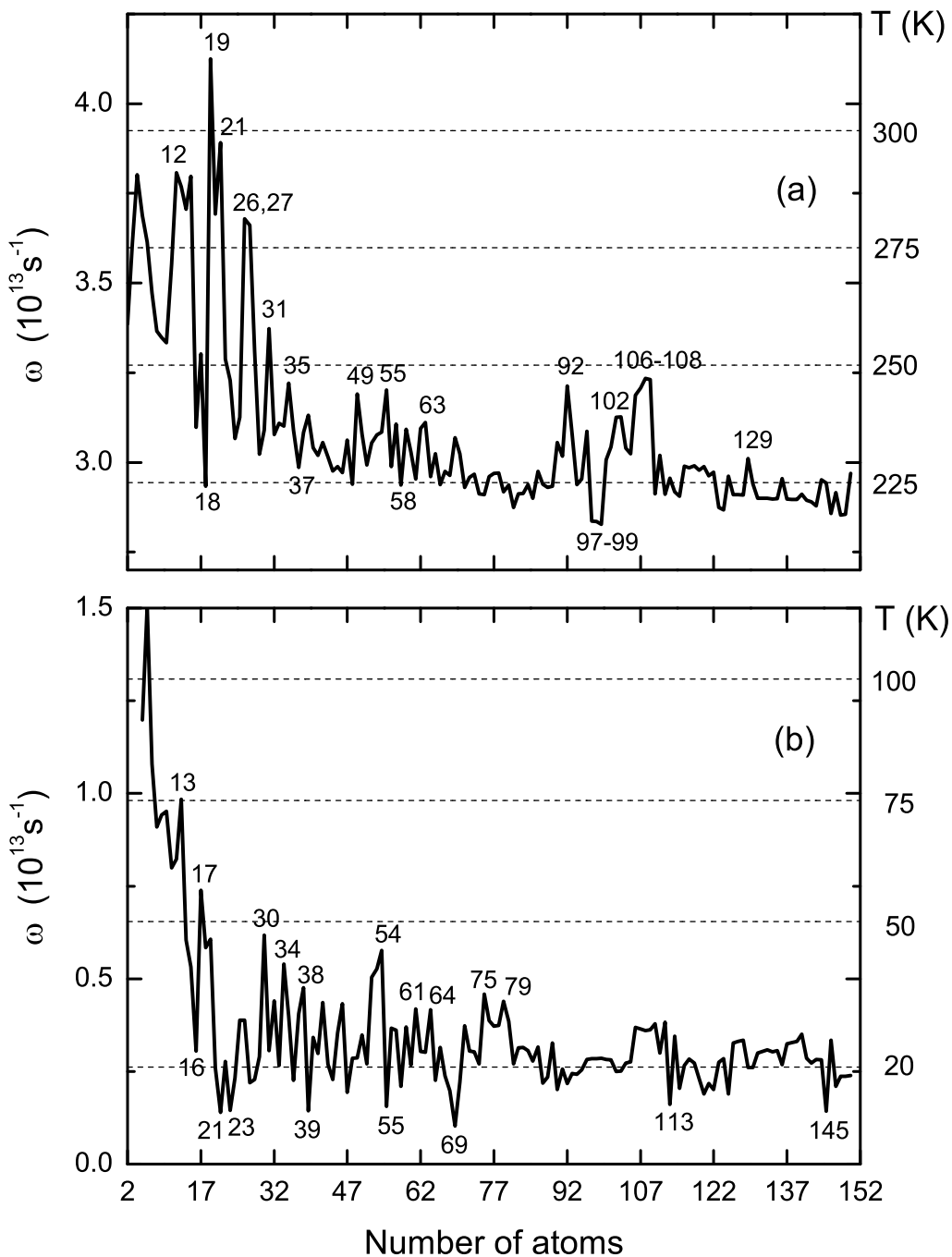
**Figure 4.14:** The maximal (a) and the minimal (b) vibrational frequencies as function of the cluster size.
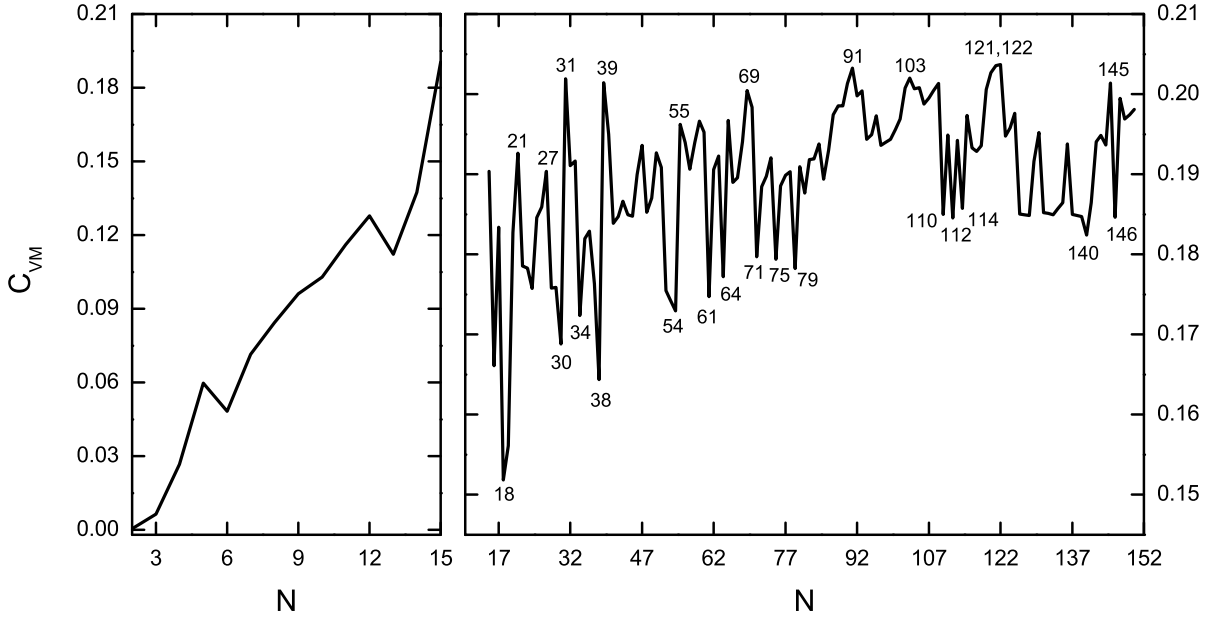
**Figure 4.15:** The calculated heat capacities per vibrational mode at 20 K as function of the cluster size.

contributions will be first beyond $N = 20$. We can see that the clusters whose minimal frequencies are far above the 20 K limit show corresponding low heat capacities - these are found for $N = 18, 30, 38, 54, 61, 64, 75, 79$, many of them belonging to the class of magic clusters. Also the cluster vibrations lying significantly below the 20 K temperature, show corresponding large heat capacities - these are $Au_{21}$, $Au_{39}$, $Au_{55}$, $Au_{69}$, and $Au_{145}$.

### 4.6.3 The low-symmetrical $Au_{55}$ and $Au_{147}$ clusters

For the $Au_{55}$ and $Au_{147}$ clusters a comparison was made between the vibrations of the low-symmetrical clusters obtained as global minima in this study and their icosahedral relatives. The results are shown in Fig. 4.16. In both cases, the spectra of the low-symmetrical clusters decreases monotonically, while, as expected, the icosahedral isomers show very high degeneracy of the vibrations.

To our knowledge, there is not an experimental vibrational spectrum of $Au_{55}$ or $Au_{147}$ to which we could compare our results. There exists an experimental work by Marcus and coworkers[94] on the 55-atom gold cluster made by the Schmid process. They performed optical absorption and temperature-dependent x-ray-absorption fine-structure (EXAFS) measurements on that cluster and the results were consistent with a *fcc* cuboctahedral structure. Another study by Häkkinen *et al.*[39] employing photoelectron spectroscopy and density-functional methods revealed the low-symmetrical nature of the $Au_{55}^-$ cluster. However, there is not a data that undoubtedly engages a theoretically obtained structure
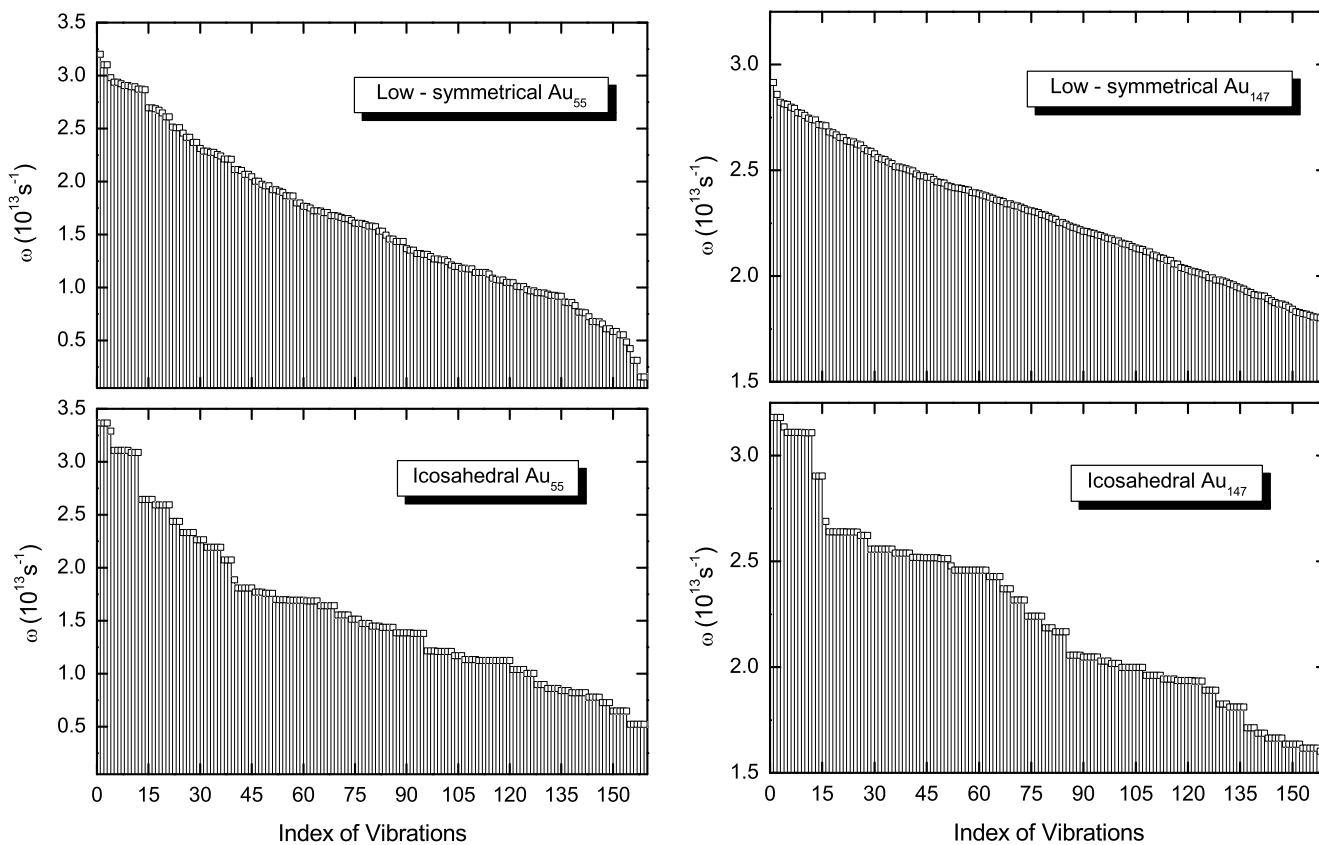
**Figure 4.16:** On the left - the vibrational frequencies of the ground state of $Au_{55}$, and its icosahedral isomer; on the right - the same for $Au_{147}$

to experimental findings, at least not for $Au_{55}$ and $Au_{147}$. These are to be the main point of further studies.

# Chapter 5

# Silver clusters

## 5.1   Introduction

The smallest silver particles remain a subject of great interest to both experimentalists and theoreticians, due to their possible applications in the catalysis, photochemistry, nanoscience. Although various spectroscopic and microscopic techniques have been applied to study the properties of silver clusters[95, 96, 97, 98, 99, 100, 101, 102, 103, 104, 34, 105, 106, 107, 108, 109], none of them could define unambiguously the cluster symmetry. Only one study[110] on the Raman spectrum of $Ag_5$ revealed that the molecule had a planar trapezoidal structure. Much theoretical efforts have been devoted to the determination of the accurate lowest-energy structures, optical and conductive properties of these small particles. Numerous first principles calculations[111, 112, 48, 113, 114, 115, 116] denote $Ag_6$ as the last two dimensional cluster size, while according to the tight-binding methods[117] the smallest three dimensional cluster is more likely to be $Ag_5$. However, both approaches predict the odd-even energy oscillations found from the experiment[95, 96]. According to the spherical jellium model[118, 119], the electronic shell closure is expressed as pronounced peaks in the ionization potentials at cluster size 2, 8, 14, 20, 40, etc. The model successfully interpreted the magic numbers found for alkali metals, and although silver has many $d$-electrons, its $4d$ orbitals are low-lying and this metal is more likely to be also well described. A recent[120] density-functional study on silver clusters in the size range $N = 9$ - 20 atoms predicted that layered structures are the lowest-energy isomers for clusters with less than 16 atoms, while the larger ones most probably are compact with quasispherical shape.

In order to be able to extend their studies beyond the too small silver clusters, many groups have employed (semi-)empirical potentials, in some cases combined with Molecular Dynamics techniques, to investigate static and/or dynamical properties[121, 122, 123, 124, 125]. The authors of Ref.[87, 126] used constant-energy molecular dynamics simulations to study the structures and melting behavior of different *fcc* metal clusters with up to 23 atoms. The model predicted that all clusters had structures based on icosahedral packing and therefore exhibit similar thermodynamic behavior. Another version of the Embedded Atom Method used in [126] was employed by García González and Montejano-

Carrizales[127] to analyze the structural stability and symmetry of nickel, copper, silver and platinum clusters, comparing the cohesive energy of various clusters with the same number of atoms but with different structures. Baletto and coworkers[128, 129, 72] studied the growth of larger silver clusters by means of molecular dynamics simulations, where in one of their works the sizes of the clusters were extended up to 40000 atoms[72]. It was shown that the structures of the clusters depended crucially on the temperatures at which the growth occurred. Investigating three main structural motifs - icosahedral, decahedral, and (truncated) octahedral, they found that icosahedra were favored at small ($N \leq 147$), decahedra at intermediate ($300 \leq N \leq 20000$), and octahedra at large sizes($N > 30000$). Similar trend was obtained by Calvo and Doye[130] in a study on the pressure effects on cluster growth.

In this Chapter we have studied silver clusters with up to 150 atoms using two different versions of the many-body Gupta potential[11], whose parameters are shown in Table 5.1, in order to observe system- and potential-specific as well as -independent properties. We shall here compare part of the results obtained with these two potentials to silver clusters with up to 60 atoms independently studied with two different EAM approaches.

**Table 5.1:** Parameters in the two versions of the Gupta potential used here.

| Parameter | tight-binding[12] | $2^{nd}$ order[13] |
|---|---|---|
| $A$/eV | 0.09944 | 0.1028 |
| $p$ | 10.12 | 10.928 |
| $q$ | 3.37 | 3.139 |
| $r_0$/Å | 1.0 | 2.892 |
| $\zeta$/eV | 1.0 | 1.178 |

## 5.2   Energetical properties

In order to check the accuracy of the chosen potentials, we calculated the dimer bond length with all approaches and compared the results to LDA and experimental values. As can be seen from Table 5.2, all potentials are capable of good description of the shortest cluster bond length, with the VC potential closest to the experimental value, which is due to its parameterization to the dimer properties. As will be discussed below, the global minima structures obtained with the VC potential are identical to those obtained with the other potentials up to cluster size $N=15$.

### 5.2.1   Point groups of the clusters

The point groups of the global-minima structures and the first two isomers with $N$ up to 150 atoms obtained with the two versions of the Gupta potential are shown in Table 5.3

**Table 5.2:** The bond length (in Å) of the Ag dimer as calculated with the tight-binding Gupta (TBG), the extended Gupta potential ($n$G), the Embedded Atom potentials DBF and VC. The dimer bond length obtained in reduced units (TBG) is appropriately scaled. The results are compared with LDA and experimental values.

| System | $n$G | TB | VC | DBF | LDA[116] | exp.[131] |
|--------|------|------|------|------|----------|-----------|
| $Ag_2$ | 2.449 | 2.448 | 2.501 | 2.443 | 2.49 | 2.53 |

and Table 5.4. In order to check the reliability of these approaches, results for the smaller and intermediate silver clusters (up to 60 atoms) obtained with the two versions of the EAM are shown in Table 5.5. In previous works we optimized nickel[93], copper[132] and gold clusters[133] with up to 150 atoms using the DBF and VC EAM potentials. There we proved the applicability of the EAM potential to the smallest nickel and copper clusters. However, the DBF potential was not capable of proper description of the smallest gold clusters[90], especially the dimer molecule, therefore we used only the Voter-Chen version for the calculations of the global minima structures. Here, we aim to find an appropriate method to treat the smaller and intermediate silver clusters, as well as to determine the similarities and differences between the different potentials applied to these systems.

The first differences for the global minima silver clusters can be found in Table 5.3 and Table 5.5 already at cluster size $N = 15$, where the global minimum found for $Ag_{15}$ ($D_{6d}$) exists as second isomer according to the $n$G potential. Likewise, the DBF method also denotes the highly symmetrical structure as a second isomer. The $Ag_{28}$ second isomer obtained with the $n$G potential has T symmetry like the global minimum of this cluster size predicted by VC/DBF, while all isomers for this cluster size found with the TBG potential are disordered. The highly symmetrical $D_{6h}$ structure appears as third isomer at $N = 22$ for the silver clusters obtained with the Gupta potentials, but is not among the three lowest-lying isomers according to the DBF potential. Our results for the global minima structures of silver clusters with $N = 6$, 7, 12, 13, 14, 19, 38, 55, and 75 atoms are consistent with those from Ref.[84]. Up to $N = 22$ our global minima structures obtained with the $n$G potential are identical to those found with the Sutton-Chen potential (SC) by Doye and Wales[78]. The disadvantages of the SC potential such as strong overbinding and resulting short bonds and high binding energies lead to the identification of highly compact structures as global minima. Therefore, it is not surprising that the global minima obtained in Ref.[78] are structurally very different from ours. A detailed discussion is offered in our previous work[132], hence here we will concentrate mainly on the structural comparison between the Gupta and EAM potentials. A symmetrical $D_{2d}$ structure lies in the global minimum of $Ag_{32}$ according to both Gupta potentials, and is a second isomer for the VC potential. Not surprisingly, for all potentials the global minimum of $N = 38$ is a truncated octahedron, the second Mackay icosahedron is most probably the ground state structure at $N = 55$, and the 75-atom Marks decahedron appears to

be the lowest-energy configuration for this cluster size. Growth of silver clusters reveals wide icosahedral windows around $N = 53$ - $55$ and $N = 144$ - $147$. Although the most probable ground state geometry of the 79-atom cluster according to the semiempirical studies is an octahedral one, the TBG potential founds a rather disordered structure with $C_s$ symmetry. It seems that low- and high-symmetrical isomers are indeed close in energy, and the small differences between the potentials lead to various predictions for the ground state configurations. Finally, an icosahedral global minimum is found for the $Ag_{140}$ cluster with the $n$G potential, while the octahedron and the icosahedron are not energetically favored by the DBF potential.

**Table 5.3:** Point groups of the silver clusters with up to 77 atoms optimized with the $n$G and TBG potentials.

| N | N.1 | N.2 | N.3 | N | N.1 | N.2 | N.3 |
|---|---|---|---|---|---|---|---|
| 2 | $D_{\infty h}$ | | | 40 | $C_s/D_{4h}$ | $C_s/D_2$ | $C_1/C_s$ |
| 3 | $D_{3h}$ | | | 41 | $C_s/D_2$ | $C_{3v}/C_{3v}$ | $C_{3v}/C_{3v}$ |
| 4 | $T_d$ | | | 42 | $C_s/C_s$ | $C_s/C_1$ | $C_{2v}/C_1$ |
| 5 | $D_{3h}$ | | | 43 | $C_s/C_1$ | $C_{2v}/C_s$ | $C_1/C_s$ |
| 6 | $O_h$ | $C_{2v}$ | | 44 | $C_s/C_2$ | $C_1/C_1$ | $C_s/C_1$ |
| 7 | $D_{5h}$ | $C_{3v}$ | $C_2$ | 45 | $C_s/C_1$ | $C_s/C_s$ | $C_1/C_1$ |
| 8 | $D_{2d}$ | $C_s$ | $D_{3d}$ | 46 | $C_{2v}/C_s$ | $C_1/C_1$ | $C_1/C_1$ |
| 9 | $C_{2v}/C_{2v}$ | $D_{3h}/C_{2v}$ | $C_{2v}/C_s$ | 47 | $C_1/C_1$ | $C_s/C_1$ | $C_s/C_1$ |
| 10 | $C_{3v}/C_{3v}$ | $D_{2h}/D_{2h}$ | $C_2/C_2$ | 48 | $D_2/D_2$ | $C_s/C_1$ | $C_s/C_s$ |
| 11 | $C_{2v}/C_{2v}$ | $C_2/C_2$ | $C_{2v}/C_2$ | 49 | $C_{3v}/C_{3v}$ | $C_s/C_1$ | $C_s/C_1$ |
| 12 | $C_{5v}/C_{5v}$ | $D_{2d}/D_{2d}$ | $D_{3h}/D_{3h}$ | 50 | $C_s/C_s$ | $C_s/C_s$ | $C_s/C_s$ |
| 13 | $I_h/I_h$ | $C_s/C_s$ | $C_s/C_1$ | 51 | $C_s/C_s$ | $C_s/C_s$ | $C_1/C_1$ |
| 14 | $C_{3v}/C_{3v}$ | $C_{2v}/C_{2v}$ | $C_{6v}/C_2$ | 52 | $C_{2v}/C_{2v}$ | $C_s/C_{3v}$ | $C_s/D_2$ |
| 15 | $C_{2v}/D_{6d}$ | $D_{6d}/C_{2v}$ | $C_{2v}/C_{2v}$ | 53 | $C_{2v}/C_{5v}$ | $C_{2v}/D_2$ | $C_{5v}/D_{5d}$ |
| 16 | $C_s/C_{2v}$ | $C_1/C_1$ | $C_s/C_s$ | 54 | $C_{5v}/I_h$ | $I_h/C_{5v}$ | $C_{2v}/D_2$ |
| 17 | $C_2/C_{2v}$ | $C_2/C_2$ | $C_{2v}/C_s$ | 55 | $I_h/I_h$ | $C_1/C_s$ | $C_s/C_1$ |
| 18 | $C_s/C_2$ | $C_s/C_s$ | $C_2/C_{2v}$ | 56 | $C_{3v}/C_s$ | $C_s/C_{2v}$ | $C_s/C_{3v}$ |
| 19 | $D_{5h}/D_{5h}$ | $C_2/C_s$ | $C_s/C_s$ | 57 | $C_s/C_{3v}$ | $C_s/C_1$ | $C_s/C_s$ |
| 20 | $C_{2v}/C_{2v}$ | $D_2/D_2$ | $D_{3d}/D_{3d}$ | 58 | $C_{3v}/C_{3v}$ | $C_1/C_1$ | $C_1/C_{3v}$ |
| 21 | $C_1/C_1$ | $C_1/C_1$ | $C_{2v}/D_2$ | 59 | $C_{2v}/C_1$ | $C_1/C_{2v}$ | $C_1/C_1$ |
| 22 | $C_s/C_s$ | $C_1/C_1$ | $D_{6h}/D_{6h}$ | 60 | $C_s/C_s$ | $C_s/C_s$ | $C_1/C_1$ |
| 23 | $C_2/D_2$ | $D_{3h}/C_s$ | $C_s/C_s$ | 61 | $C_{2v}/C_{2v}$ | $C_s/C_s$ | $C_1/C_s$ |
| 24 | $C_s/C_s$ | $C_s/D_2$ | $C_2/C_s$ | 62 | $C_s/C_s$ | $C_1/C_s$ | $C_1/C_1$ |
| 25 | $C_3/C_3$ | $C_{3v}/C_1$ | $C_{2v}/C_1$ | 63 | $C_{2v}/C_{2v}$ | $C_1/C_s$ | $C_1/C_1$ |
| 26 | $C_1/C_1$ | $D_{3h}/C_{2v}$ | $C_{2v}/C_s$ | 64 | $C_s/C_s$ | $C_1/C_1$ | $C_1/C_1$ |
| 27 | $C_s/C_s$ | $C_2/C_2$ | $C_1/C_1$ | 65 | $C_{2v}/C_{2v}$ | $C_1/C_s$ | $C_s/C_1$ |
| 28 | $C_1/D_2$ | $T/C_s$ | $C_s/C_1$ | 66 | $C_s/C_s$ | $C_s/C_s$ | $C_1/C_1$ |
| 29 | $C_3/C_2$ | $C_2/C_s$ | $C_s/C_2$ | 67 | $C_{2v}/C_{2v}$ | $C_s/C_s$ | $C_1/C_1$ |
| 30 | $C_s/C_s$ | $C_{2v}/C_1$ | $C_1/C_1$ | 68 | $C_{2v}/C_{2v}$ | $C_s/C_s$ | $C_1/C_1$ |
| 31 | $C_{2v}/C_3$ | $C_3/C_s$ | $C_{2v}/D_2$ | 69 | $C_s/C_s$ | $C_1/C_1$ | $C_1/C_1$ |
| 32 | $D_{2d}/D_{2d}$ | $C_{2v}/C_{2v}$ | $C_2/C_3$ | 70 | $C_s/C_s$ | $C_1/C_1$ | $C_1/C_1$ |
| 33 | $C_{2v}/C_s$ | $C_1/C_2$ | $C_s/C_{2v}$ | 71 | $C_{2v}/C_{2v}$ | $C_1/C_1$ | $C_1/C_1$ |
| 34 | $C_s/C_2$ | $C_s/D_2$ | $C_s/C_s$ | 72 | $C_s/C_s$ | $C_1/C_s$ | $C_1/C_1$ |
| 35 | $C_s/D_3$ | $D_3/C_s$ | $C_{2v}/D_2$ | 73 | $C_s/C_s$ | $C_s/C_s$ | $C_1/D_{5h}$ |
| 36 | $C_s/C_2$ | $C_s/C_1$ | $C_2/D_2$ | 74 | $C_{5v}/C_{5v}$ | $C_1/C_1$ | $C_s/C_s$ |
| 37 | $C_{3v}/C_{2v}$ | $C_s/C_{2v}$ | $C_{2v}/C_s$ | 75 | $D_{5h}/D_{5h}$ | $C_s/C_s$ | $C_1/C_s$ |
| 38 | $O_h/O_h$ | $C_{5v}/D_{4h}$ | $D_{4h}/D_2$ | 76 | $C_{2v}/C_{2v}$ | $C_s/C_s$ | $C_s/C_s$ |
| 39 | $C_{5v}/D_4$ | $C_{4v}/D_3$ | $C_s/C_s$ | 77 | $C_{2v}/C_{2v}$ | $C_1/C_{2v}$ | $C_1/C_{2v}$ |

**Table 5.4:** Point groups of the silver clusters with $77 - 150$ atoms optimized with the $n$G and TBG potentials.

| N | N.1 | N.2 | N.3 | N | N.1 | N.2 | N.3 |
|---|-----|-----|-----|---|-----|-----|-----|
| 78 | $C_s/C_s$ | $C_s/C_s$ | $C_{2v}/C_{2v}$ | 116 | $D_{3d}/T_h$ | $O_h/T$ | $C_1/O_h$ |
| 79 | $O_h/C_s$ | $C_1/C_{2v}$ | $C_1/C_{2v}$ | 117 | $C_1/C_1$ | $C_1/C_1$ | $C_1/C_1$ |
| 80 | $C_s/C_s$ | $C_1/C_s$ | $C_1/C_s$ | 118 | $C_1/C_1$ | $C_1/C_1$ | $C_1/C_1$ |
| 81 | $C_{2v}/C_{2v}$ | $C_s/C_s$ | $C_1/C_s$ | 119 | $C_1/C_1$ | $C_{2v}/C_{2v}$ | $C_1/C_1$ |
| 82 | $C_{2v}/C_{2v}$ | $C_s/C_s$ | $C_s/C_s$ | 120 | $C_s/C_s$ | $C_1/C_1$ | $C_1/C_1$ |
| 83 | $C_{2v}/C_{2v}$ | $C_s/C_s$ | $C_1/C_{2v}$ | 121 | $C_{2v}/C_{2v}$ | $C_1/C_1$ | $C_1/C_1$ |
| 84 | $C_s/C_s$ | $C_{2v}/C_{2v}$ | $C_{2v}/C_s$ | 122 | $C_s/C_s$ | $C_s/C_1$ | $C_1/C_s$ |
| 85 | $C_s/C_s$ | $C_s/C_s$ | $C_s/C_s$ | 123 | $C_{2v}/C_{2v}$ | $C_1/C_1$ | $C_1/C_1$ |
| 86 | $C_{2v}/C_{2v}$ | $C_s/C_s$ | $C_s/C_1$ | 124 | $C_s/C_s$ | $C_1/C_1$ | $C_1/C_1$ |
| 87 | $C_s/C_s$ | $C_s/C_s$ | $C_1/C_s$ | 125 | $C_1/C_1$ | $C_1/C_1$ | $C_1/C_1$ |
| 88 | $C_s/C_s$ | $C_s/C_s$ | $C_1/C_s$ | 126 | $C_s/C_s$ | $C_1/C_1$ | $C_1/C_1$ |
| 89 | $C_s/C_s$ | $C_1/C_s$ | $C_1/C_1$ | 127 | $C_s/C_s$ | $C_s/C_1$ | $C_s/C_s$ |
| 90 | $C_s/C_s$ | $C_1/C_1$ | $C_1/C_1$ | 128 | $C_s/C_s$ | $C_{2v}/C_s$ | $C_1/C_s$ |
| 91 | $C_1/C_1$ | $C_1/C_1$ | $C_s/C_1$ | 129 | $C_s/C_s$ | $C_1/C_1$ | $C_1/C_1$ |
| 92 | $C_1/C_1$ | $C_1/C_1$ | $C_1/C_1$ | 130 | $C_{2v}/D_2$ | $C_1/C_1$ | $C_1/C_s$ |
| 93 | $C_1/C_1$ | $C_1/C_1$ | $C_1/C_1$ | 131 | $C_s/C_s$ | $C_s/C_s$ | $C_s/C_s$ |
| 94 | $C_1/C_1$ | $C_1/C_1$ | $C_1/C_1$ | 132 | $C_s/C_s$ | $C_1/C_1$ | $C_1/C_1$ |
| 95 | $C_1/C_1$ | $C_1/C_1$ | $C_1/C_1$ | 133 | $C_s/C_s$ | $C_1/C_s$ | $C_1/C_s$ |
| 96 | $C_1/C_s$ | $C_1/C_1$ | $C_1/C_1$ | 134 | $C_s/C_s$ | $C_1/C_s$ | $C_1/C_{2v}$ |
| 97 | $C_2/C_2$ | $C_1/C_1$ | $C_1/C_1$ | 135 | $C_s/C_s$ | $C_1/C_s$ | $C_s/C_s$ |
| 98 | $C_s/C_s$ | $T_d/C_1$ | $C_1/C_1$ | 136 | $C_1/C_1$ | $C_1/C_1$ | $C_1/C_1$ |
| 99 | $C_s/C_s$ | $C_1/C_1$ | $C_1/C_1$ | 137 | $C_s/C_s$ | $C_1/C_1$ | $C_1/C_1$ |
| 100 | $C_{5v}/C_s$ | $C_1/C_1$ | $C_s/C_1$ | 138 | $C_s/C_s$ | $C_1/C_1$ | $C_1/C_1$ |
| 101 | $D_{5h}/D_{5h}$ | $C_s/C_s$ | $C_s/C_s$ | 139 | $C_{2v}/D_2$ | $C_s/C_1$ | $C_{5v}/C_s$ |
| 102 | $C_s/C_s$ | $C_s/C_s$ | $C_1/C_{2v}$ | 140 | $C_{5v}/C_s$ | $C_{3v}/O_h$ | $C_{3v}/C_s$ |
| 103 | $C_{2v}/C_{2v}$ | $C_2/C_s$ | $C_s/D_2$ | 141 | $C_s/C_s$ | $C_s/C_{2v}$ | $C_s/C_s$ |
| 104 | $C_1/C_1$ | $C_s/C_1$ | $C_1/C_1$ | 142 | $C_{2v}/D_2$ | $C_s/C_s$ | $C_s/C_s$ |
| 105 | $C_{2v}/C_{2v}$ | $C_2/C_{2v}$ | $C_s/C_1$ | 143 | $C_s/C_{3v}$ | $C_s/C_s$ | $C_s/C_s$ |
| 106 | $C_1/C_1$ | $C_s/C_s$ | $C_s/C_s$ | 144 | $C_{2v}/D_2$ | $D_{5d}/I_h$ | $C_{2v}/D_2$ |
| 107 | $C_{2v}/C_{2v}$ | $C_1/C_{2v}$ | $C_1/C_1$ | 145 | $C_{5v}/I$ | $C_{2v}/D_2$ | $C_s/D_2$ |
| 108 | $C_1/C_1$ | $C_1/C_1$ | $C_1/C_1$ | 146 | $I_h/I_h$ | $C_{5v}/I$ | $D_{5h}/C_s$ |
| 109 | $C_1/C_1$ | $C_1/C_1$ | $C_1/C_1$ | 147 | $I_h/I_h$ | $C_s/C_s$ | $C_s/C_s$ |
| 110 | $C_1/C_1$ | $C_1/C_1$ | $C_1/C_1$ | 148 | $C_s/C_s$ | $C_s/C_s$ | $C_s/C_s$ |
| 111 | $C_1/C_1$ | $C_1/C_1$ | $C_1/C_1$ | 149 | $C_{3v}/C_{3v}$ | $C_{3v}/D_2$ | $C_s/C_{3v}$ |
| 112 | $C_1/C_1$ | $C_1/C_1$ | $C_1/C_1$ | 150 | $C_s/C_s$ | $C_1/C_{3v}$ | $C_1/C_s$ |
| 113 | $C_s/C_s$ | $C_1/C_1$ | $C_1/C_1$ | | | | |
| 114 | $C_1/C_1$ | $C_1/C_1$ | $C_s/C_1$ | | | | |
| 115 | $C_s/C_s$ | $C_1/C_s$ | $C_1/C_1$ | | | | |

**Table 5.5:** Point groups of the silver clusters with up to 60 atoms optimized with the VC and DBF EAM potentials.

| N | N.1 | N.2 | N.3 | N | N.1 | N.2 | N.3 |
|---|---|---|---|---|---|---|---|
| 2 | $D_{\infty h}/D_{\infty h}$ | | | 32 | $D_3/C_{2v}$ | $D_{2d}/D_3$ | $C_{2v}/T_h$ |
| 3 | $D_{3h}/D_{3h}$ | | | 33 | $C_2/C_2$ | $C_s/C_s$ | $C_s/C_1$ |
| 4 | $T_d/T_d$ | | | 34 | $C_s/C_s$ | $C_s/C_s$ | $C_1/C_1$ |
| 5 | $D_{3h}/D_{3h}$ | | | 35 | $D_3/D_3$ | $C_{2v}/C_{2v}$ | $C_{2v}/C_1$ |
| 6 | $O_h/O_h$ | $C_{2v}/C_{2v}$ | | 36 | $C_2/C_1$ | $C_1/C_2$ | $C_s/C_1$ |
| 7 | $D_{5h}/D_{5h}$ | $C_{3v}/C_{3v}$ | $C_2/C_2$ | 37 | $C_{3v}/C_2$ | $D_2/C_{5v}$ | $C_s/C_1$ |
| 8 | $D_{2d}/D_{2d}$ | $C_s/C_s$ | $D_{3d}/D_{3d}$ | 38 | $O_h/O_h$ | $D_{4h}/C_{5v}$ | $D_2/C_{5v}$ |
| 9 | $C_{2v}/C_{2v}$ | $D_{3h}/D_{3h}$ | $C_1/C_{2v}$ | 39 | $C_5/C_{5v}$ | $C_{5v}/C_s$ | $C_{4v}/C_s$ |
| 10 | $C_{3v}/C_{3v}$ | $D_{2h}/D_{2d}$ | $D_{4d}/D_{2h}$ | 40 | $C_s/C_s$ | $D_2/C_s$ | $C_2/C_2$ |
| 11 | $C_{2v}/C_{2v}$ | $C_2/C_2$ | $C_{2v}/C_2$ | 41 | $C_1/C_s$ | $C_3/C_s$ | $C_s/C_1$ |
| 12 | $C_{5v}/C_{5v}$ | $C_1/D_{2d}$ | $D_{3h}/C_1$ | 42 | $C_{2v}/C_s$ | $C_s/C_s$ | $C_1/C_1$ |
| 13 | $I_h/I_h$ | $C_s/C_s$ | $C_s/C_s$ | 43 | $C_s/C_s$ | $C_1/C_s$ | $C_1/C_1$ |
| 14 | $C_{3v}/C_{3v}$ | $C_{2v}/C_{2v}$ | $C_{6v}/C_1$ | 44 | $C_s/C_1$ | $C_2/C_s$ | $C_s/C_1$ |
| 15 | $D_{6d}/C_{2v}$ | $C_{2v}/D_{6d}$ | $C_{2v}/C_{2v}$ | 45 | $C_s/C_s$ | $C_s/C_s$ | $C_s/C_1$ |
| 16 | $C_s/C_s$ | $C_s/C_s$ | $D_{3h}/C_1$ | 46 | $C_{2v}/C_{2v}$ | $C_1/C_1$ | $C_s/C_1$ |
| 17 | $C_2/C_2$ | $C_s/C_s$ | $C_{2v}/C_s$ | 47 | $C_1/C_1$ | $C_1/C_s$ | $C_s/C_s$ |
| 18 | $C_s/C_s$ | $C_2/C_{5v}$ | $C_{2v}/C_s$ | 48 | $C_{2v}/C_s$ | $C_s/C_s$ | $C_s/C_{2v}$ |
| 19 | $D_{5h}/D_{5h}$ | $C_1/C_1$ | $C_s/C_s$ | 49 | $C_{3v}/C_{3v}$ | $C_s/C_s$ | $C_1/C_1$ |
| 20 | $C_{2v}/C_{2v}$ | $D_2/D_{3d}$ | $D_{3d}/D_2$ | 50 | $C_s/C_s$ | $C_{2v}/C_s$ | $C_1/C_s$ |
| 21 | $C_s/C_1$ | $C_1/C_s$ | $C_2/C_s$ | 51 | $C_{2v}/C_s$ | $C_s/C_s$ | $C_s/C_1$ |
| 22 | $C_s/C_1$ | $D_{6h}/C_s$ | $C_1/C_s$ | 52 | $C_{3v}/C_{2v}$ | $C_s/C_{3v}$ | $C_s/C_s$ |
| 23 | $D_{3h}/D_{3h}$ | $C_2/C_2$ | $D_{3h}/C_s$ | 53 | $C_{2v}/C_{2v}$ | $D_{5d}/D_{5d}$ | $C_{2v}/C_{2v}$ |
| 24 | $D_3/C_{2v}$ | $C_{2v}/C_s$ | $C_s/D_3$ | 54 | $C_{5v}/C_{5v}$ | $I_h/I_h$ | $C_{2v}/C_{2v}$ |
| 25 | $C_3/C_3$ | $C_1/C_s$ | $C_{2v}/C_1$ | 55 | $I_h/I_h$ | $C_1/C_s$ | $C_s/C_1$ |
| 26 | $C_1/C_1$ | $C_{2v}/T_d$ | $C_s/C_{2v}$ | 56 | $C_s/C_{3v}$ | $C_{3v}/C_s$ | $C_{3v}/C_s$ |
| 27 | $C_s/C_s$ | $C_s/C_s$ | $C_2/C_2$ | 57 | $C_s/C_s$ | $C_1/C_s$ | $C_s/C_s$ |
| 28 | $T/T$ | $C_1/C_1$ | $C_s/C_{3v}$ | 58 | $C_{3v}/C_{3v}$ | $C_1/C_1$ | $C_1/C_1$ |
| 29 | $C_3/C_3$ | $C_{2v}/C_{2v}$ | $C_s/C_2$ | 59 | $C_1/C_{2v}$ | $C_{3v}/C_1$ | $C_{2v}/C_1$ |
| 30 | $C_s/C_s$ | $C_1/C_{2v}$ | $C_1/C_1$ | 60 | $C_s/C_s$ | $C_s/C_1$ | $C_s/C_{2v}$ |
| 31 | $C_3/C_s$ | $C_s/C_1$ | $C_1/C_s$ | | | | |

## 5.2.2   Stability

The energetical differences between the first and second isomers can give information whether they are energetically very close and most probably exist as a mixture in the experiment, or the global minimum lies very low compared to the next isomers, which is the case of the $Ag_{79}$ cluster obtained with the $n$G potential at Fig. 5.1. The results obtained with the TBG potential are not shown, as they are very similar to these. Here, along with the peaks corresponding to the 'magic' $N = 13, 38, 55$, and 147 clusters, many new peaks appear. They correspond to $N = 63, 71, 79, 95, 101, 115, 120, 121, 126, 130$, and 139. All of them except for the $Ag_{63}$ and $Ag_{79}$ clusters have decahedral structures, the ground state of $Ag_{63}$ has a distorted icosahedral configuration. The energetical peculiarities can be generalized by using the stability function presented at Fig. 5.2 for the silver clusters optimized with the $n$G potential. A comparison with the TBG, DBF, and VC potentials is made for the size range 2-60 atoms (Fig. 5.3).

As already seen at the energy differences between the first isomers, the $Ag_{23}$ and $Ag_{28}$ clusters are not particularly stable. Instead, for the first time the $Ag_{38}$ and $Ag_{61}$ clusters appear to be magic. The $Ag_{61}$ cluster can be viewed as made of the $Ag_{55}$ icosahedron capped with 6 atoms on one of its sides. In comparison to the results for copper clusters[132], here the silver clusters with $N = 86, 92, 116, 119$, and 131 atoms are not particularly stable, while the magic $Ag_{121}$ and $Ag_{130}$ can not be found in the stability function for the copper clusters. The $Ag_{116}$, $Ag_{131}$, and $Ag_{137}$ clusters are not magic in comparison to the nickel ones[93], while the silver structures with $N = 95, 101, 121, 130$, and 139 are absent in the nickel stability function.

At Fig. 5.3 are shown the stability functions for silver clusters with up to 60 atoms obtained with the TB Gupta potential, the DBF and VC versions of the EAM method. One can see that both EAM methods yield very similar results comparing to the TB potential, where the characteristic peaks at $N = 19, 23, 28$, and 49 are missing. Instead, two new magic clusters appear at $N = 48$ and 58. They are also found at the stability function for the $n$G potential. These structures have $D_2$ and $C_{3v}$ symmetries, respectively. Although the global minima for $Ag_{58}$ according to the DBF and VC potentials have the same symmetry, none of them appears as highly stable in the corresponding similarity functions.
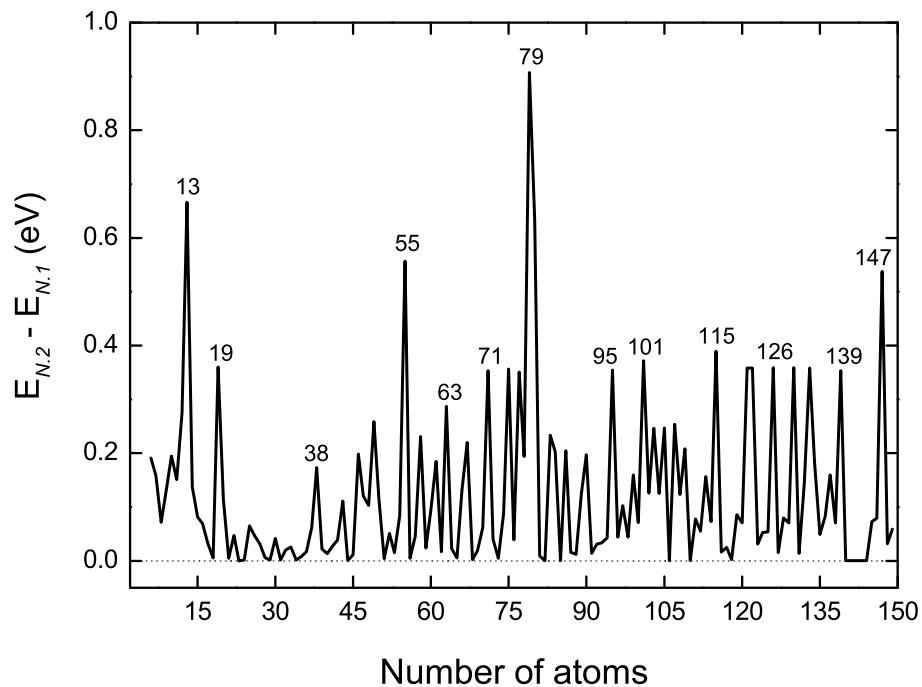
**Figure 5.1:** The energetical difference between the two lowest-lying isomers within the
$n$G potential.
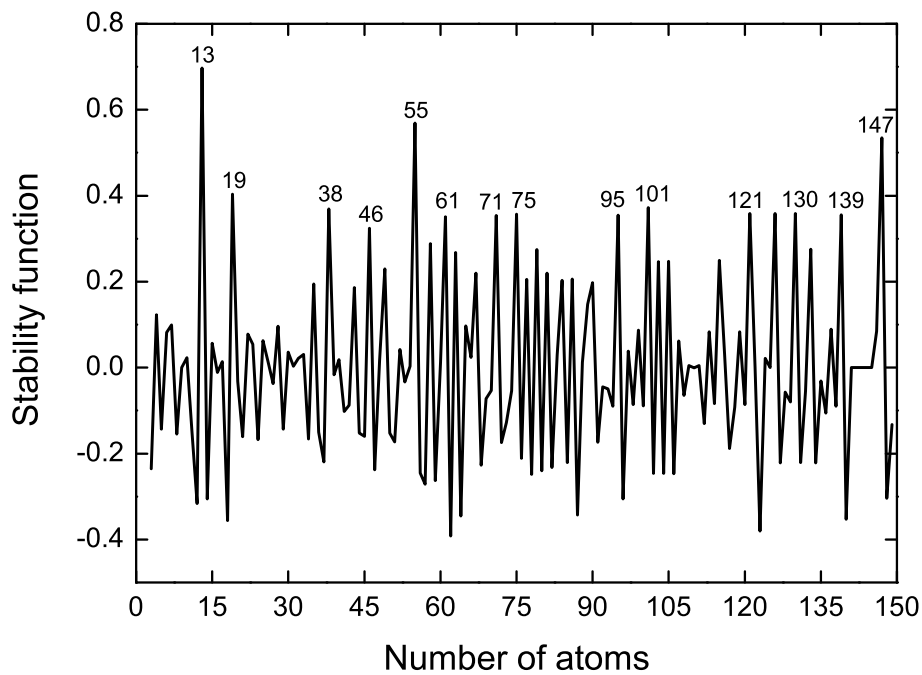


**Figure 5.2:** The stability function for the silver clusters obtained with the same potential.
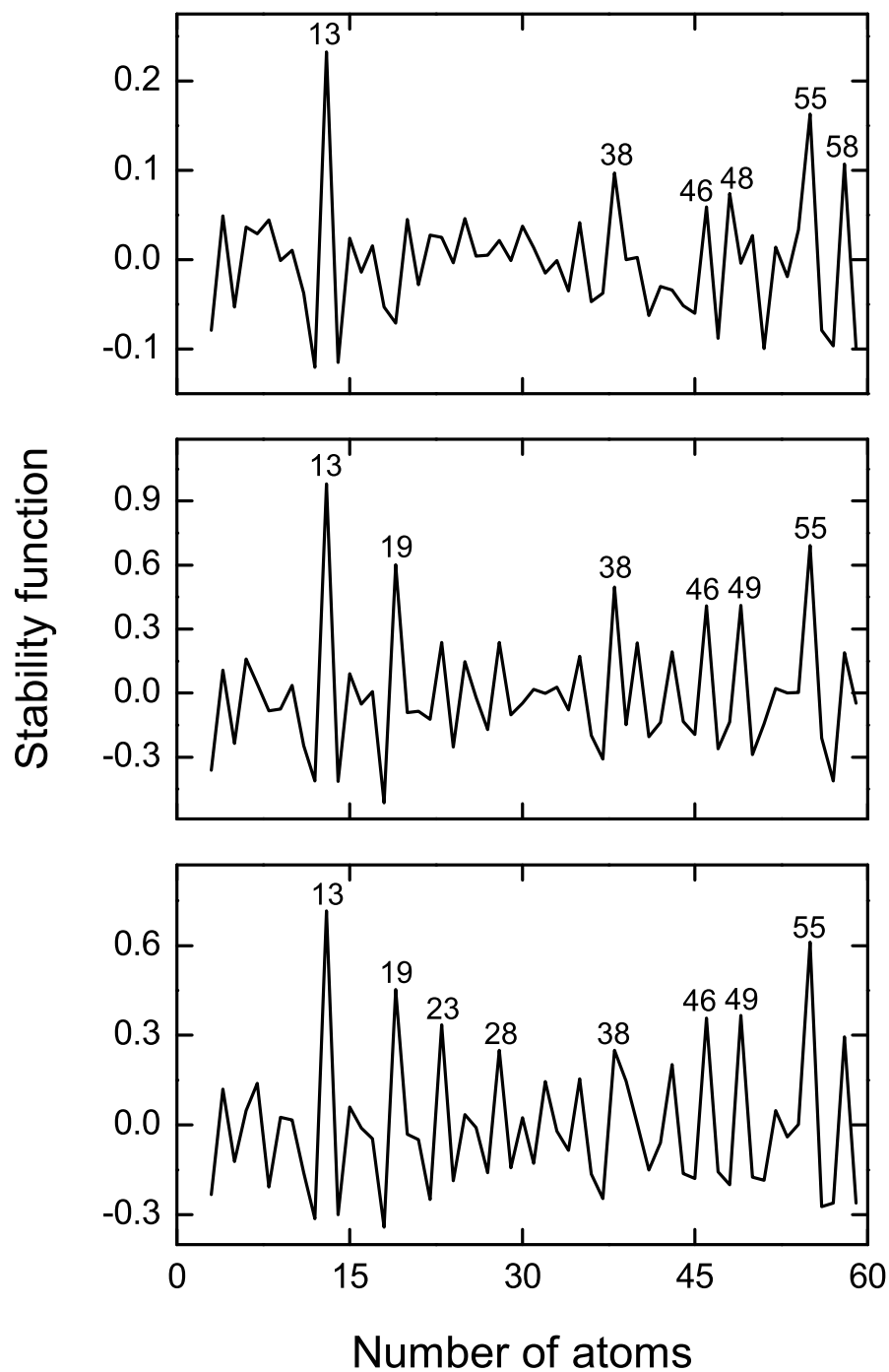
**Figure 5.3:** The stability function for silver clusters with up to 60 atoms with three different potentials: the TBG potential (top), the VC (middle) and DBF (bottom) potentials.

## 5.3 Growth patterns

### 5.3.1 Similarity functions

The similarity functions obtained comparing the $n$G silver clusters to those found with the TBG, DBF, and VC potentials are shown at Fig. 5.4. Although the two Gupta potentials are very similar, they seem to lead to significantly different structures around $N = 15$ and beyond $Ag_{30}$. However, revising Table 5.3 and Table 5.4 we see that for these cluster sizes most of the global minima according to the first potential correspond to higher-lying isomers within the second one, and vice versa, which is also the case for most of the DBF and VC structures.

Surprisingly, the larger silver clusters (Fig. 5.5) obtained with the two Gupta potentials are more similar than the smaller ones with up to 60 atoms. The largest structural differences occur at $N = 140$ and 141, where the global minima of these two clusters have icosahedral constructions according to the $n$G potential. On the other hand, the lowest-lying $Ag_{140}$ and $Ag_{141}$ isomers predicted by the TBG potential have decahedral structures. A previous work[134] using a LDA density functional code predicted icosahedral global minima for the silver clusters with $N = 55$, 135, and 140 atoms. According to all potentials used in this study, the second Mackay icosahedron is most probably the ground state of $Ag_{55}$. However, our three lowest-lying isomers of $Ag_{135}$ obtained with both Gupta potentials have decahedral structures. Moreover, applying the *Abbau* algorithm starting from our icosahedral $Ag_{140}$ global minimum, we were able to obtain an icosahedral isomer for the $Ag_{135}$ cluster size, but it lay around 0.6 eV above our global minimum. Cuboctahedral *fcc* structures, as considered in Ref.[134], are not among our three lowest-lying isomers for the three cluster sizes, except for the second $Ag_{140}$ isomer obtained with the tight-binding Gupta potential.

Further insight into the cluster growth could be obtained if we consider how different a cluster with $N$ atoms could be if it is compared to a $N$-1-atom one plus one additional atom, e.g in this way one can follow the structural changes occurring at the different cluster sizes. These growth patterns could be seen at Fig. 5.6, where we compare the global minima structures obtained with the $n$G potential for each cluster size. A more detailed comparison (for nickel and copper clusters) can be found in our previous works[93, 132]. There are many structural differences to be seen, which indicates an irregular growth of the silver clusters. Comparing to nickel and copper, where also significant differences were observed for the smaller clusters with up to 50 atoms, here there are a few strong peaks for the larger $Ag_{79}$, $Ag_{80}$, $Ag_{97}$, $Ag_{116}$, $Ag_{117}$, and $Ag_{140}$ clusters. The second strongest peak in the figure, corresponding to $Ag_{39}$, is due to the transition from the octahedral global minimum for the 38-atom cluster to an icosahedral ground state, which is also the case for the fcc $Ag_{79}$ and the decahedral $Ag_{80}$. Although the clusters with $N = 115$, 116, and 117 atoms all have decahedral configurations, the last two ones are structurally very different, also between themselves. According to our results, the cluster growth is decahedral in the size range $N = 65$ - 139 atoms, with one exception at the octahedral $Ag_{79}$. Our previous studies on copper and nickel clusters pointed to an icosahedral cluster
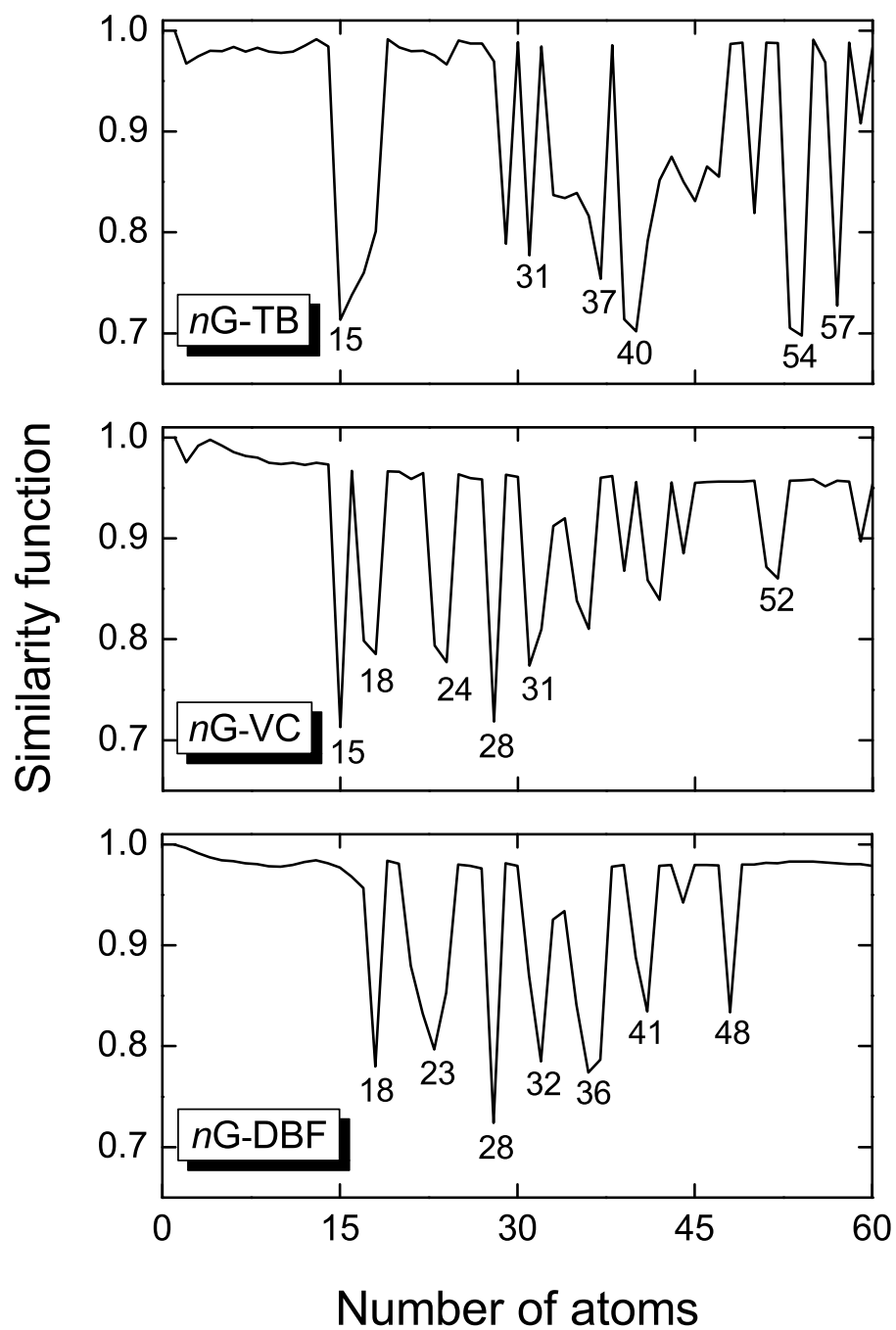
**Figure 5.4:** The similarity functions for the $n$G silver clusters compared to the structures obtained the TB Gupta potential, the DBF and VC potentials.
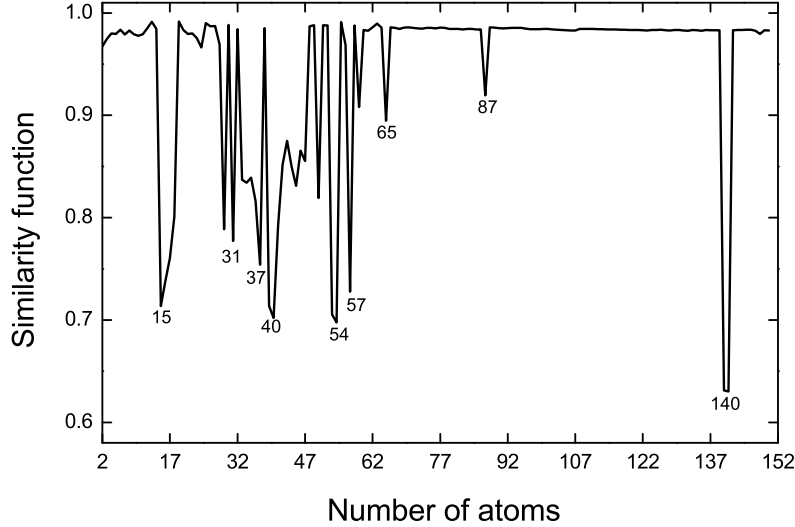
**Figure 5.5:** The similarity functions for the comparison between the $n$G and TBG silver clusters. The structures of the TBG clusters are appropriately scaled.

growth, while the gold clusters showed irregular behavior, forming for each cluster size different, more compact structures. This was also observed at the similarity functions for the different metals - there are significant structural differences between silver and all other studied systems. Although the main 'magic' numbers and structures for $N = 19$, 38, 55, 75, and 147 remain the same for the silver clusters, these seem to be the only few structurally very similar structures to the corresponding copper and nickel ones, except for the smallest clusters with $N$ up to 15.

## 5.3.2 Minimal coordination numbers

Finally, another structural descriptor that can give general information on the cluster configuration is the so-called minimal coordination number that is described elsewhere[93, 132]. Its lower values, 3 and 4, indicate growth by deposition of atoms on the cluster surface, while the large values point to insertion of atoms inside of the cluster, e.g. this leads to the formation of more compact structures. At Fig. 5.7 are presented the calculated coordination numbers for the silver clusters obtained with the two Gupta potentials. They are very similar, with few exceptions, for example at cluster sizes $N = 56$ and 148 that correspond to the second and third Mackay icosahedra plus an additional atom on the surface, with low coordination numbers that are clearly visible within the $n$G potential, but are absent in the corresponding TB Gupta results. Similar absence was found also at the corresponding copper clusters, although the global minima structures had the same configurations. However, most of the copper clusters had predominantly large coordination numbers, with very few clusters with coordination number equal to 4. Here, the low-coordinated structures are significantly more, especially at the smaller
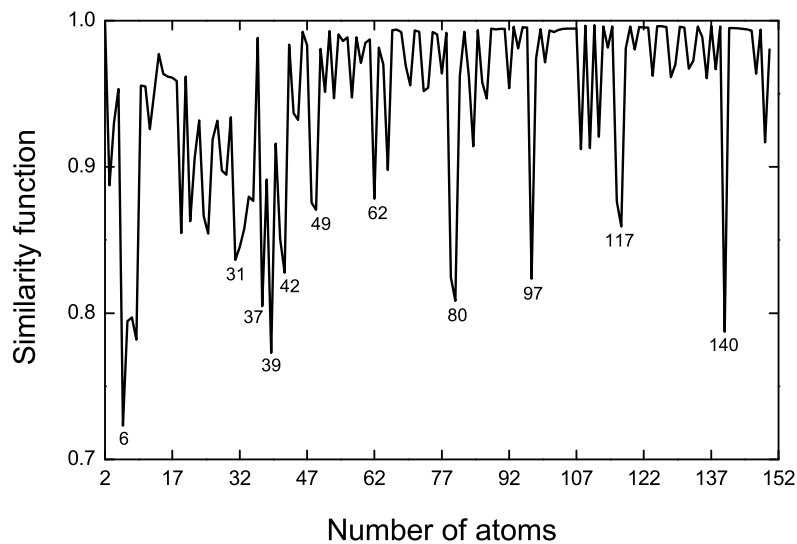
**Figure 5.6:** The similarity function as function of the cluster size. It describes whether the cluster with $N$ atoms is similar to that of $N - 1$ atoms plus an extra atom.
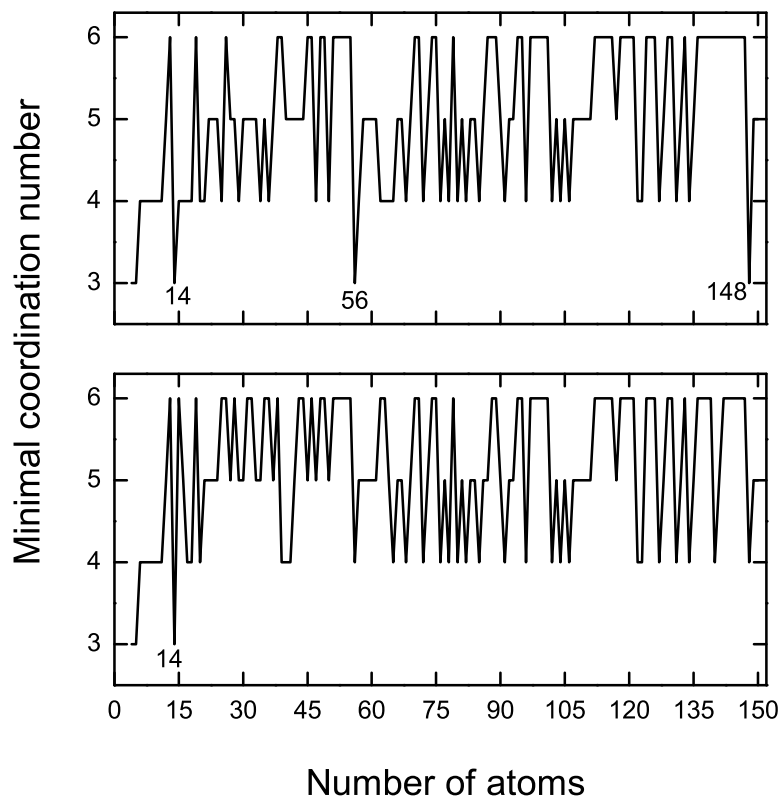


**Figure 5.7:** The minimal coordination number of the $n$G(top) and the TBG clusters(bottom) as function of the cluster size.

cluster sizes - $N = 25, 29, 34, 36, 47, 50$, and 62 - 65 for the $n$G potential in comparison
to the TBG one. On the other hand, the clusters with $N = 39$ - 41 atoms obtained with
the latter potential have low coordination numbers that are connected with the formation
of $Ag_{38}$ fcc-based structures capped with the extra atoms on the surface.

Concluding this section, the structural descriptors used in this work reveal a decahedral
cluster growth, which gives us a further insight into the silver cluster behavior. An atom-
by-atom growth is observed along with preference of compact structures. However, the
silver clusters are structurally not similar to any of the previously studied copper, nickel,
or gold systems.

## 5.4 Comparison to the experiment

In a series of combined experimental and theoretical studies[108, 135] the structures of
mass selected silver cluster cations were probed by trapped ion electron diffraction per-
formed at temperature of 100K. The experimentally obtained scattering intensity was
compared to results from theoretical calculations using proposed structures optimized
with the Turbomole program package. For all cluster sizes, the experimental data was
best described by structures containing the icosahedral motif, also regarding the $Ag_{38}$
and $Ag_{79}$ clusters that have always been considered to be truncated octahedra by the
semiempirical approaches.

In this section we compare our results obtained with the $n$G potential for the cluster
sizes of $N = 19, 38, 55, 59, 75$, and 79 atoms to the experimental results for the electron
diffraction, which were kindly provided by the authors of Ref.[135].

The experimental reduced molecular scattering intensity $sM^{exp}(s)$ as shown in Ref.[135]
is determined from the following formula:

$$sM^{exp}(s) = s\left[\left(\frac{I_{tot}^{exp}}{I_{at}I_{back}}\right) - 1\right], \tag{5.1}$$

where $I_{at}$ is the atomic scattering contribution and $I_{back}$ an unspecific background, ap-
proximated by a flat function of the form:

$$I_{back}(s) = Aexp(-\alpha s) + \sum_i(a_i s^i) \tag{5.2}$$

For a homoatomic cluster, the theoretical reduced molecular scattering function $sM^{theor}$
can be approximated as:

$$sM^{theor}(s') = \frac{S_c}{N}exp\left(\frac{-L^2 s'^2}{2}\right)\sum_i\sum_{j\neq i}\left(\frac{sin(r_{ij}s')}{r_{ij}}\right) \tag{5.3}$$

where $N$ is the number of atoms in the cluster, $s$ is the momentum transfer, and $r_{ij}$
the distance between atoms $i$ and $j$. The mean square vibrational amplitude $L$ and
the amplitude scaling factor $S_c$ are used together with a scaling factor for the $s$ scale,
$k_s$, where $s' = k_s s$. Usually Eq. 5.3 is fitted to the experimental molecular scattering

intensity simultaneously with an unspecific background intensity approximated usually by a flat function of a momentum transfer.[135] Hence, one does not expect an important influence of the background intensity function on the fitting procedure. The parameters $L$, $S_c$, and $k_s$ are calculated by minimizing the difference between $sM^{exp}(s)$ and $sM^{theor}$ by a $\chi^2$ fit. The calculated scattering intensities of our three best-fitting structures for each cluster size are shown in Fig. 5.8 - Fig. 5.13 together with the experimental data.

Most of the semiempirical potentials including the many-body Gupta potential predict the global minimum structure of the neutral $Ag_{19}$ cluster to be a double icosahedron with $D_{5h}$ symmetry. However, the density functional study in Ref.[135] showed that this structure is 0.38 eV higher in energy than a distorted icosahedron capped with six atoms. On the other hand, in our study the difference between the first and the second lowest-lying isomers is 0.36 eV. It seems that the DFT calculations could significantly change the ordering of the isomers, as none of the structures proposed for this cluster size in Ref. [135] except for the double icosahedron corresponds to any of our low-energy isomers. However, our calculations are constrained to neutral systems, and the cations could exhibit different low-energy structures, very probably compact and with lower symmetry, as suggested also by these authors. Here, the structure that shows the best fit to the experimental data is the double icosahedron, followed by the low-symmetrical $C_{2v}$ structure. Our third isomer with partly octahedral construction could be excluded due to its poor description of the experimental results at about 5.2 and 8.5 Å$^{-1}$.

According to previous semiempirical studies, the clusters with 38 atoms possess closed electronic and geometric shell and exhibit particular stability. Many studies have assigned a truncated octahedral symmetry to the $Ag_{38}$ cluster, however, there have been icosahedral and disordered isomers close in energy with the ground state. Our results show an energy gap of 0.17 eV between the *fcc* global minimum and the next isomer, which has icosahedral structure with $C_{5v}$ symmetry. This structure was also considered in Ref.[135] as a successful candidate, where it was obtained as a cation and had a lower $C_1$ symmetry. This configuration together with two isomers of higher energy is presented at Fig. 5.9. The second and the third structures were obtained by simultaneous removal of 17 atoms from the icosahedral $Ag_{55}$ cluster and optimization of the resulting clusters. All possible structures correspond to the binomial coefficients for 55 and 38, which turned out to be about 1 500 000 possible configurations. As it was impossible to optimize this number of structures we restricted the search to 5000 isomers. Surprisingly, the icosahedral cluster with lowest energy corresponded to the already mentioned $C_{5v}$ structure that was the second isomer for this cluster size. The next two isomers have slightly higher energies comparing to the $Ag_{38}$ cuboctahedral cluster and describe very well the experimental scattering intensities, in agreement with a previous study[108], where it was proposed that the ground state of the $Ag_{38}$ cluster is most probably not a single structure, but rather a mixture of low-energy icosahedral isomers. In this case the diffraction experiments encouraged us to search for new ways to calculate the isomers.

For the next cluster sizes, $Ag_{55}$ and $Ag_{59}$, our three lowest-lying isomers give a very good description of the experimental data. Numerous experimental and theoretical studies have denoted the icosahedron as the structure most likely lying in the global minimum

for the first cluster size. Moreover, this cluster is also magic-numbered as seen before, and exhibits particular stability. Its second isomer is separated with more than 0.5 eV from the ground state and differs from the icosahedron only by the rearrangement of one atom. Here, cuboctahedral and decahedral configurations can be eliminated as potential candidates, as according to the $n$G potential the decahedral Ag$_{55}$ cluster lies 0.93 eV higher in energy than the icosahedron and describes very poorly the experiment, and the cuboctahedron was found to be unstable with this potential.

The global minimum and the next two isomers of the Ag$_{59}$ cluster correspond to the Ag$_{55}$ icosahedron capped with four additional atoms. As the three structures are very similar, they give also almost the same scattering intensities as seen in Fig. 5.11. Here the small structural differences between the clusters can not be explicitly seen in the resulting scattering intensities, as many structures having the same growth patterns, but with different configurations, give very similar results. Therefore, it is difficult unequivocally to assign a particular structure to the experimental data. Instead, one can propose a particular structural motif, as in the case of the Ag$_{38}$ cluster, where it has been shown that the octahedral isomer that is always preferred by the semiempirical studies in fact is most probably not seen in the experiment as an energetically favored structure. Here, unambiguous assignment of the structures can not be made, however, it is clearly seen that for all considered cluster sizes icosahedral clusters lie in the global minima, while for the Ag$_{38}$ cluster most probably several icosahedral isomers lie close or degenerate with the global minimum.

The global minima structures for the Ag$_{75}$ and the Ag$_{79}$ clusters according to the semiempirical potentials correspond to a Marks decahedron and a truncated octahedron, respectively. The Marks decahedron describes relatively well the experimental data, showing only one shoulder at 4.8 Å$^{-1}$ and can not be unequivocally excluded as potential low-energy structure. In our study the $n$G potential predicts this structure to be the global minimum for this cluster size, followed by two decahedral isomers with energy separation of 0.36 eV and 0.37 eV from the decahedron, respectively. The same is the situation for the Ag$_{79}$ cluster where the octahedral minimum lies 0.9 eV below the next two isomers that also have octahedral construction. It is clear that the icosahedral isomers will have significantly higher energy than the global minima according to this potential. As seen in Ref.[135], cuboctahedral isomers can be ruled out as possible candidates for both cluster sizes. Therefore, after exhaustive search for icosahedral isomers we were able to obtain configurations that indeed describe significantly well the experimental data, but are energetically unfavored comparing to the global minima structures. Probably *ab initio* calculations may change the energetical ordering, but what becomes obvious is that only icosahedral structures are able of proper description of the experimental findings. Within the Gupta potential the structural factors for larger clusters only can lead to preference of more compact structures with *fcc* or decahedral symmetry. Even more important is that the present calculations were performed for neutral clusters, while the experimental diffraction is obtained using positively charged clusters. Recent experimental studies[60] show that even for the smallest gold clusters the positive or negative charge can lead to different global minima structures, therefore here it is also to expect significant changes in

the energetical ordering of the isomers. Another aspect for speculation why the diffraction experiments do not see *fcc* structures could be connected with the entropy effects. In principle, it is possible that the temperature effects could change the ordering of isomers[177], and, respectively, could make the icosahedral motifs more favorable. All these experiments were taken at a finite temperature of 100 K

The most important results are that for all cluster sizes icosahedral isomers are close or lying in the ground state, with possible mixing with decahedral structures. The *bulk* octahedral construction is not preferred, which reminds us that these small particles are not pieces of the large crystal, but unique systems.
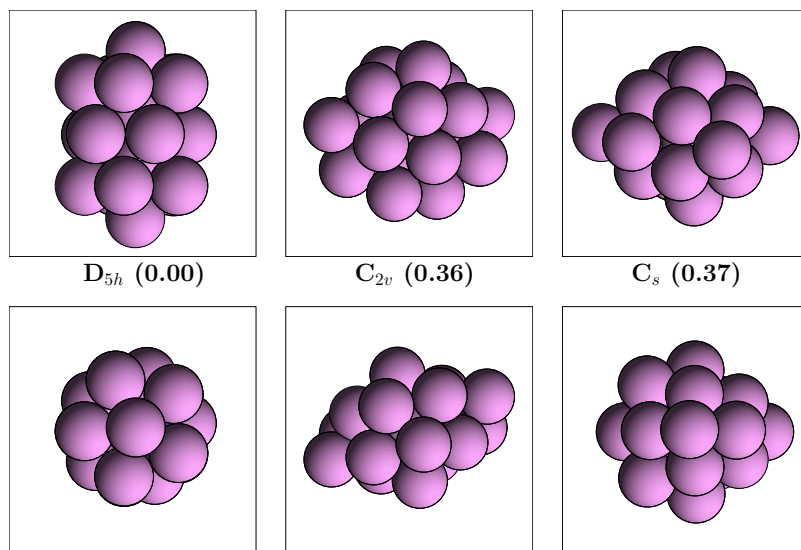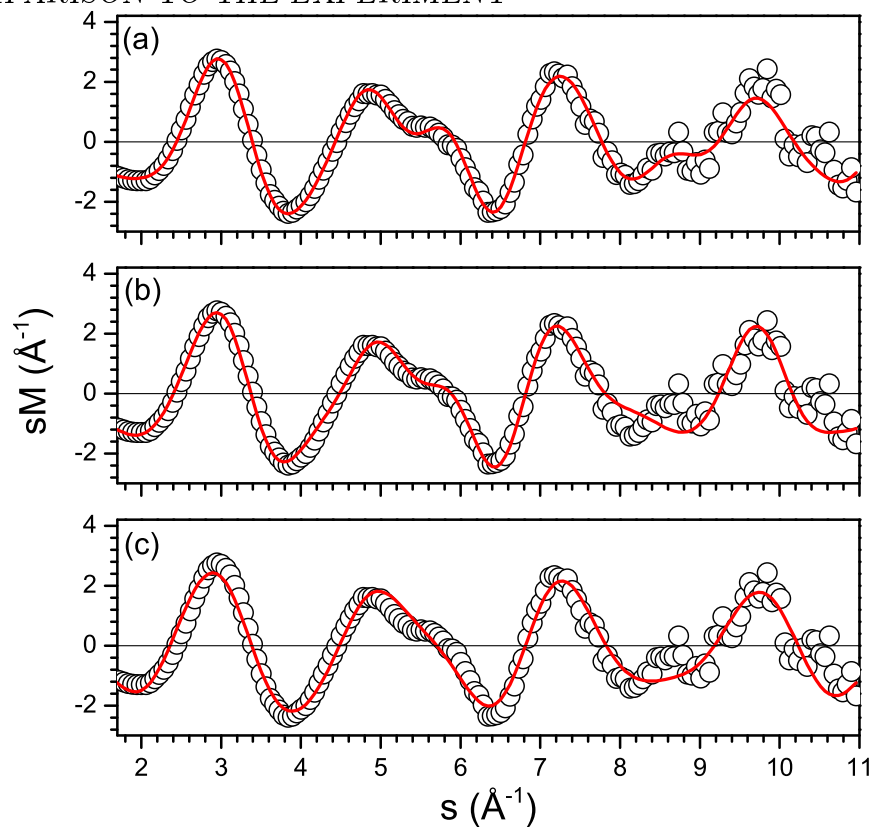
Figure 5.8: Experimental(black circles) and theoretical(red line) reduced molecular scattering intensities for $Ag_{19}$. Our three lowest-lying isomers corresponding to the panels marked with (a), (b), and (c), are presented from left to the right with side and top view. For each structure the point group and the energy separation from the ground state (in eV) are shown.
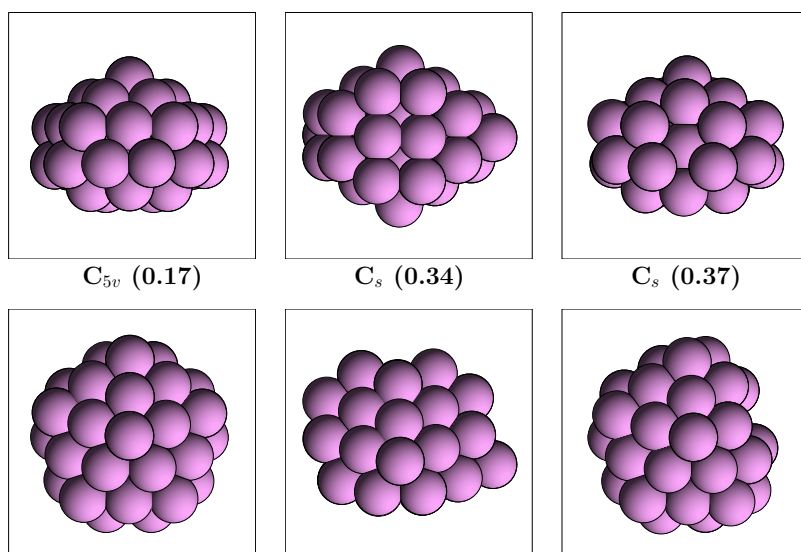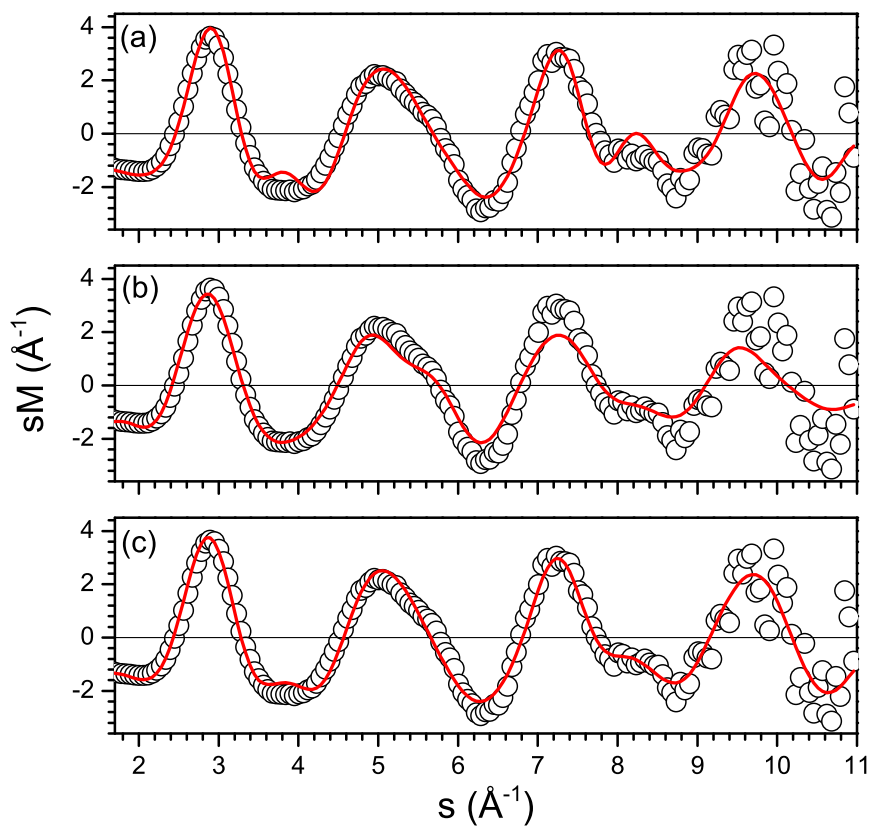
**Figure 5.9:** Comparison between the experimental(black circles) and theoretical(red line) reduced molecular scattering intensities for $Ag_{38}$. Here only the three best-fitting isomers are shown.
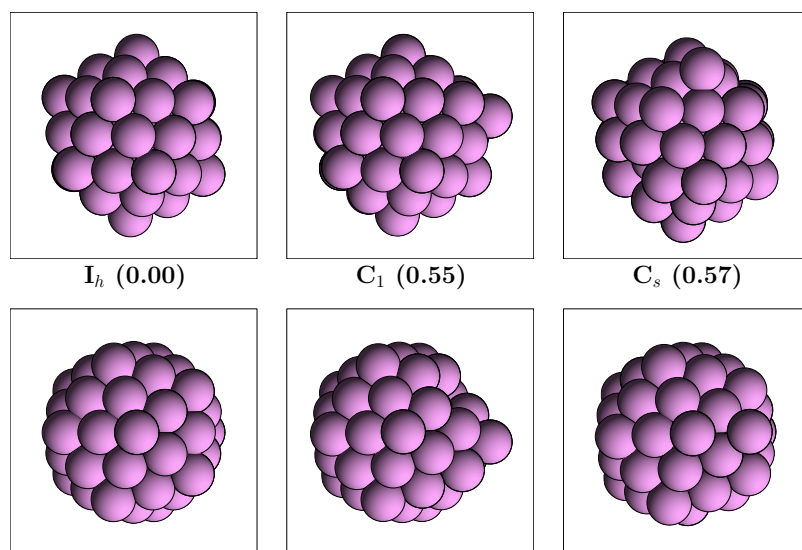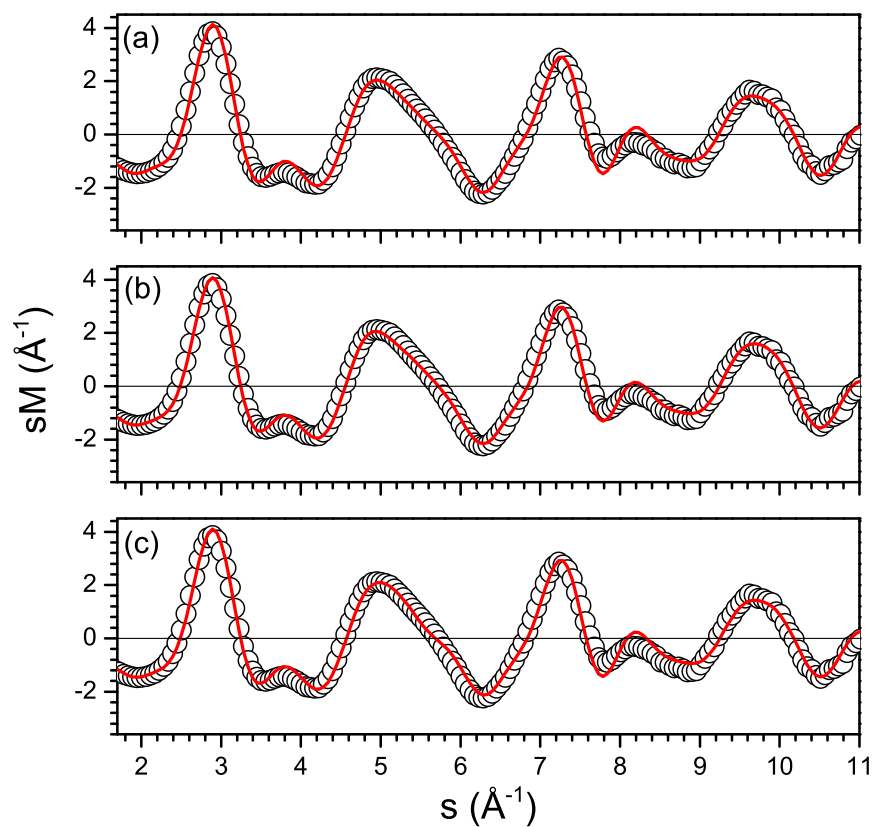
**Figure 5.10:** Comparison between the experimental(black circles) and theoretical(red line) reduced molecular scattering intensities for $Ag_{55}$. The best fit was obtained with our three lowest-lying isomers.
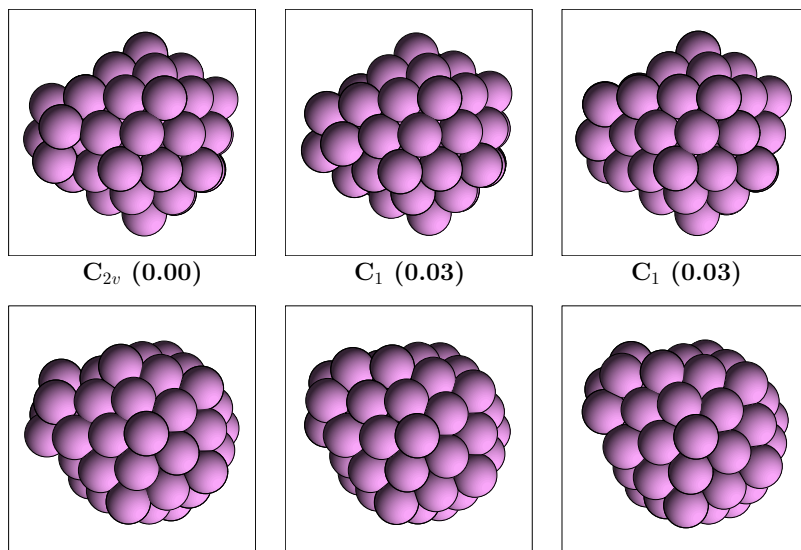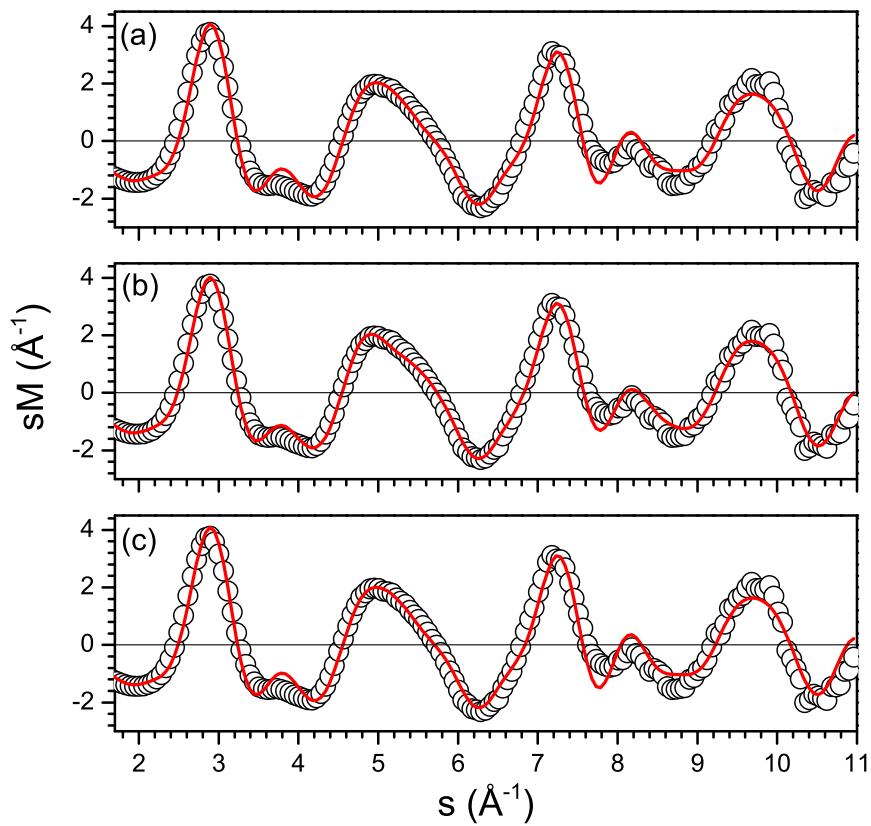
Figure 5.11: The same for $Ag_{59}$.
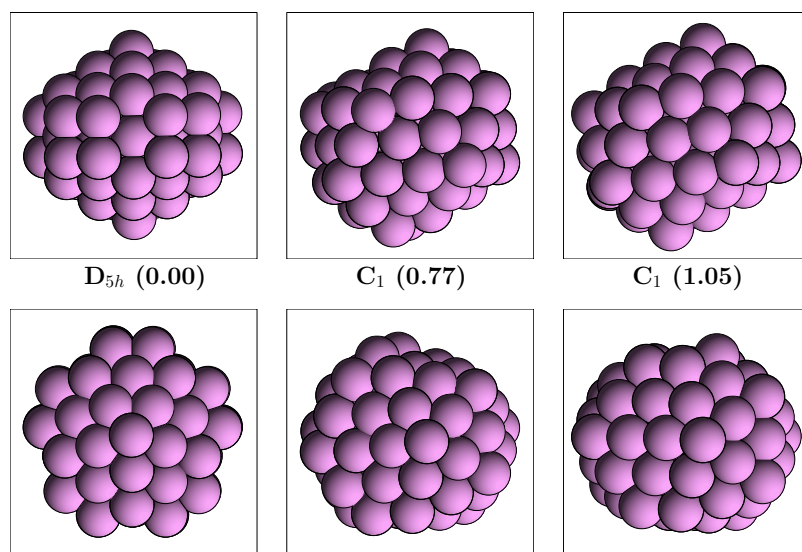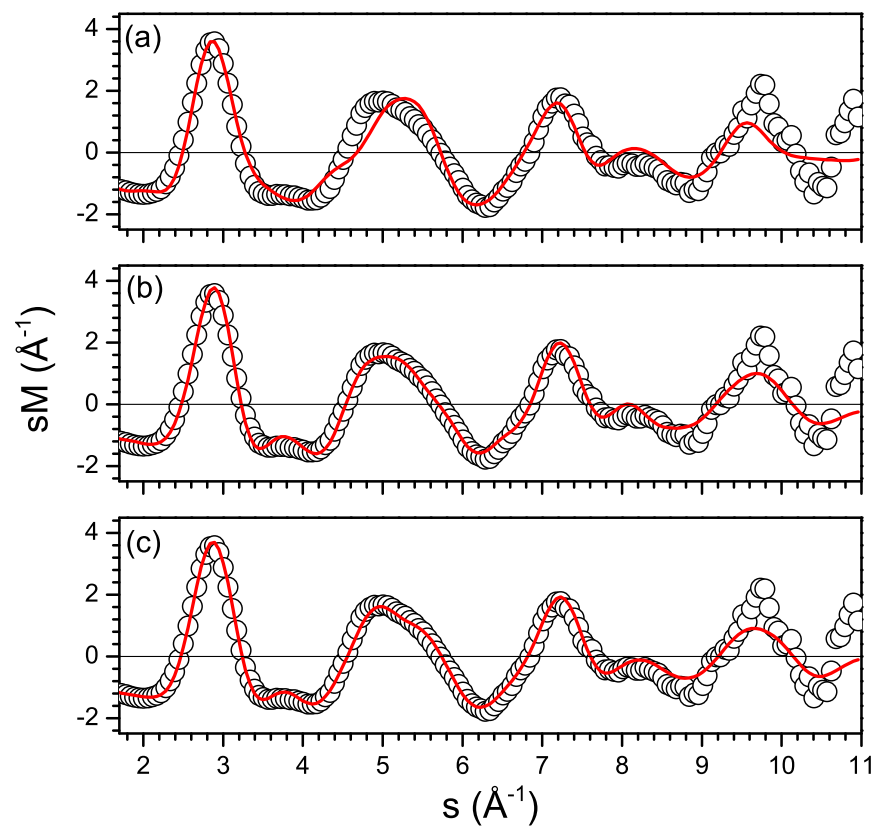
**Figure 5.12:** Experimental(black circles) and theoretical(red line) reduced molecular scattering intensities for Ag$_{75}$. For comparison, our decahedral global minimum structure is also shown.
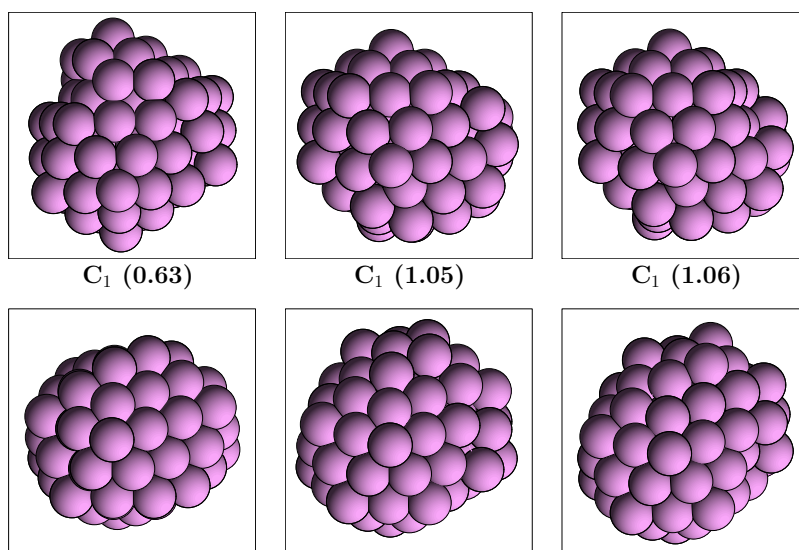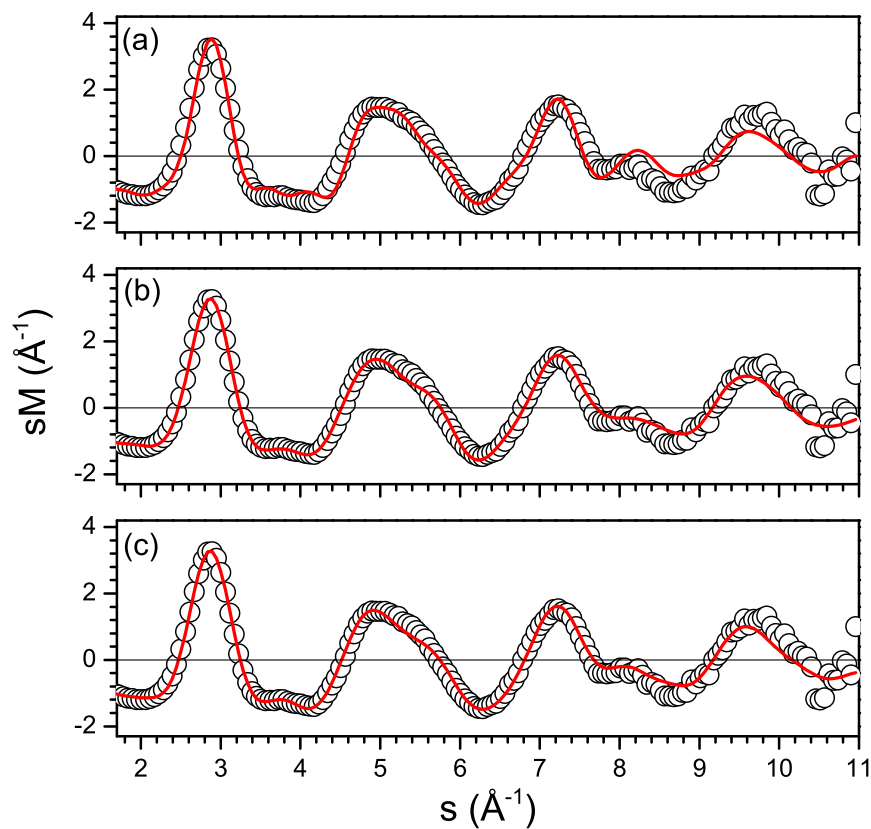
**Figure 5.13:** Experimental(black circles) and theoretical(red line) reduced molecular scattering intensities for $Ag_{79}$. None of the presented structures corresponds to our three lowest-lying isomers.

# Chapter 6

# $Ni_N$, $Cu_N$ and $Au_N$ clusters: $2 \leq N \leq 60$

## 6.1   Introduction

Earlier empirical studies on nickel and copper clusters found that both metals have similar global-minima structures and growth properties, while the properties of the gold clusters may vary from method to method. For example, for $Cu_N$ and $Ni_N$ clusters[78, 86, 92, 93, 136, 137] highly stable structures are the first and second Mackay icosahedra at $N = 13$ and $N = 55$. A *fcc* truncated octahedron was found to be the global minimum for the corresponding $Ni_{38}$ and $Cu_{38}$ clusters. However, Kabir *et al.*[136] found a structure with icosahedral geometry to be most likely the global minimum of the $Cu_{38}$ cluster, which in our study[132] is the second lowest isomer after the octahedron. The gold clusters show a complicated growth, possessing disordered lowest-lying or degenerated with the ground state isomers[81, 82, 83, 84, 85]. Results obtained with first-principles calculations predicted a disordered structure[49, 50] as the global minimum of the first magic-numbered gold cluster, $Au_{13}$, while methods based on empirical many-body potentials denoted the icosahedron as the most stable configuration[73, 78, 79, 86, 89]. For the $Au_{38}$ cluster the empirical potentials[73, 78, 79, 86, 89] as well as the first-principles calculations of Häkkinen *et al.*[46] denoted the *fcc* truncated octahedron to be the most stable structure, while other studies pointed to the formation of either a disordered minimum or amorphous low-lying isomers[82, 83, 84, 85]. Recent experiments and calculations[39, 81, 82, 84, 85, 86] suggest that $Au_{55}$ possesses a low-symmetrical structure, in contrast to the results obtained with the Murrell-Mottram and Sutton-Chen potentials[78, 79]. Accordingly, in order to obtain further insight into the structures of the not-too-small metal clusters, it is highly important both to study the influence of the potential that has been used and to perform unbiased structure optimizations. With this objective we have studied clusters of three metals, Ni, Cu, and Au, using two different versions of the embedded-atom method, and the many-body Gupta potential in order to study system- and potential-specific as well as -independent properties. The results for the gold clusters optimized with the Voter-Chen version of the EAM are taken from Chapter 3.

**Table 6.1:** Parameters[13] defining the Gupta potential for Ni, Cu, and Au clusters.

| Parameter | Ni | Cu | Au |
|---|---|---|---|
| $A$/eV | 0.0376 | 0.0855 | 0.2061 |
| $p$ | 16.999 | 10.960 | 10.229 |
| $q$ | 1.189 | 2.278 | 4.036 |
| $r_0$/Å | 2.491 | 2.556 | 2.884 |
| $\zeta$/eV | 1.070 | 1.224 | 1.790 |

## 6.2   Binding energies

We began with calculation of the bond length of the dimers, $Ni_2$, $Cu_2$, and $Au_2$. Our results together with EAM, *ab initio* and experimental values from Ref.[140] are shown in Table 6.2.

**Table 6.2:** The calculated bond length (in Å) of the dimers in comparison with *ab initio* and experimental values. $n$G denotes the $n$-body Gupta potential, while DBF and VC denote the EAM versions of Daw, Baskes, and Foiles and of Voter and Chen, respectively.

| System | $n$G/DBF/VC | ab initio | exp. |
|---|---|---|---|
| Ni | 2.38/2.13/2.22 | 2.17 | 2.20 |
| Cu | 2.23/2.15/2.23 | 2.17 | 2.22 |
| Au | 2.31/1.81/2.40 | 2.55 | 2.47 |

The bond length of $Cu_2$ calculated with the Gupta potential is equal to the VC value and shows very good agreement with the experiment, while only the latter potential gives reasonable value for gold dimer. However, the $Ni_2$ bond length obtained with the $n$G method shows the largest deviation from the experimental value, which suggests that the results for the small nickel clusters could differ from those obtained with the EAM. From the two version of EAM, the results from the DBF method are very similar to those obtained with the *ab initio* methods, except for Au, where one can see significant differences, which suggests that the DBF version could provide proper geometries of Ni and Cu clusters even for the smallest cluster sizes, but may fail for small Au clusters[90]. On the other hand, the VC version gives an overall good agreement, which is due to its parameterization also to dimer properties.

Our further calculations confirm this statement. On the next figure(Fig. 6.1) is presented the binding energy per atom for the three metals with the three different potentials. One can see that agreement between the calculated binding energies is very good for cop-
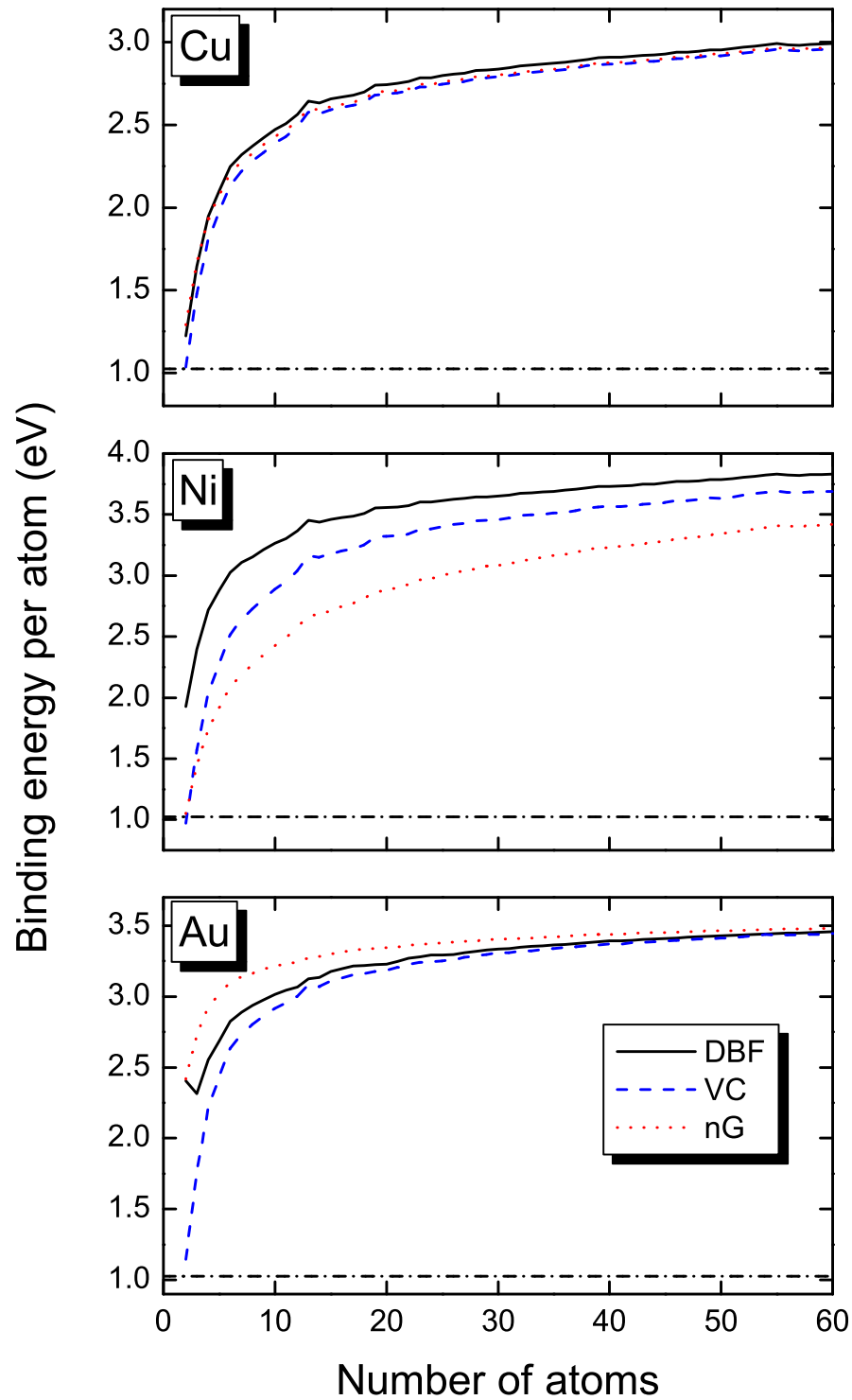
**Figure 6.1:** Binding energy per atom as a function of the cluster size for the three metals with the three different potentials. The dotted lines at the bottom show the experimental dimer values, which for copper and gold are taken from Ref.[138], and for Ni from Ref.[139].

per, for gold the DBF and especially the $n$G-potential overestimate the binding energy of the smaller gold clusters, while for the $Ni_N$ clusters each potential predicts different values. Moreover, while for the other two metals the curves approach each other at larger $N$, for nickel at $N = 60$ the three potentials give binding energies that still differ significantly from each other. The method that gives the best results is again the Voter-Chen potential.

## 6.3    Structural and energetical similarities

The differences in the binding energies per atom for the three metals with the three potentials are presented at Fig. 6.2 to Fig. 6.4 together with the corresponding similarity functions. The best agreement is found for the copper clusters, where the differences between the binding energies are insignificant except for the smallest clusters. On the other hand, the binding energies also for the larger nickel and gold clusters differ for each potential. Here, the VC potential gives the most reasonable values (see Fig. 6.1) due to its parameterization to the dimer properties. The structures of the DBF and VC copper clusters are very similar, and significant disagreements are observed only at $N = 16$, $17$, $27$, $35$, $36$, and $41$, while for the nickel clusters there are more fluctuations, although the agreement is nevertheless reasonable. In contrast to these results, for gold the differences begin already at $N = 12$, moreover, the similarity function approaches 1 only for few values of $N$. The many-body Gupta potential appears to predict structures that are more similar to the DBF potential rather than to the VC version.

More details about the similarities and differences between the three metals and potentials can be obtained through the stability function shown in Fig. 6.5. Here, we find that the $Ni_N$ and $Cu_N$ clusters have very similar stability functions, whereas the properties of the corresponding gold clusters are different. The particularly stable copper clusters within the three potentials have $N = 13$, $19$, $23$, $28$, $43$, $46$, $49$, and $55$ atoms, while only the $n$G and VC methods denote $Cu_{38}$ as a magic-sized cluster. For nickel, the same differences at the middle part of the figure are observed, where, according to the $n$G potential, the $Ni_{26}$, $Ni_{29}$, and $Ni_{38}$ clusters are particularly stable. According to all methods, the global-minimum configuration of $Ni_{38}$ is an octahedron, however, only the $n$G potential points to its high stability, which could be due to the differences between this method and the EAM family of potentials. Except for the particular stability of $Ni_{29}$ within the $n$G potential, representing the only difference between the stability functions of the two metals, the copper and nickel clusters possess the same magic-sized clusters with the same symmetries. The situation is completely different for the case of the gold clusters, where each potential predicts different magic sizes, except for the first Mackay icosahedron $Au_{13}$, where the three potentials are in agreement. The particularly stable clusters according to the DBF method have $N = 13$, $15$, $17$, $22$, $24$, $30$, $40$, and $44$ atoms. The $Au_{22}$ and $Au_{24}$ clusters obtained with this method have higher symmetries ($D_{6h}$ and $C_{3v}$, respectively) than the corresponding global minima obtained with the other two methods. According to the DBF potential, many stable clusters have similar or lower
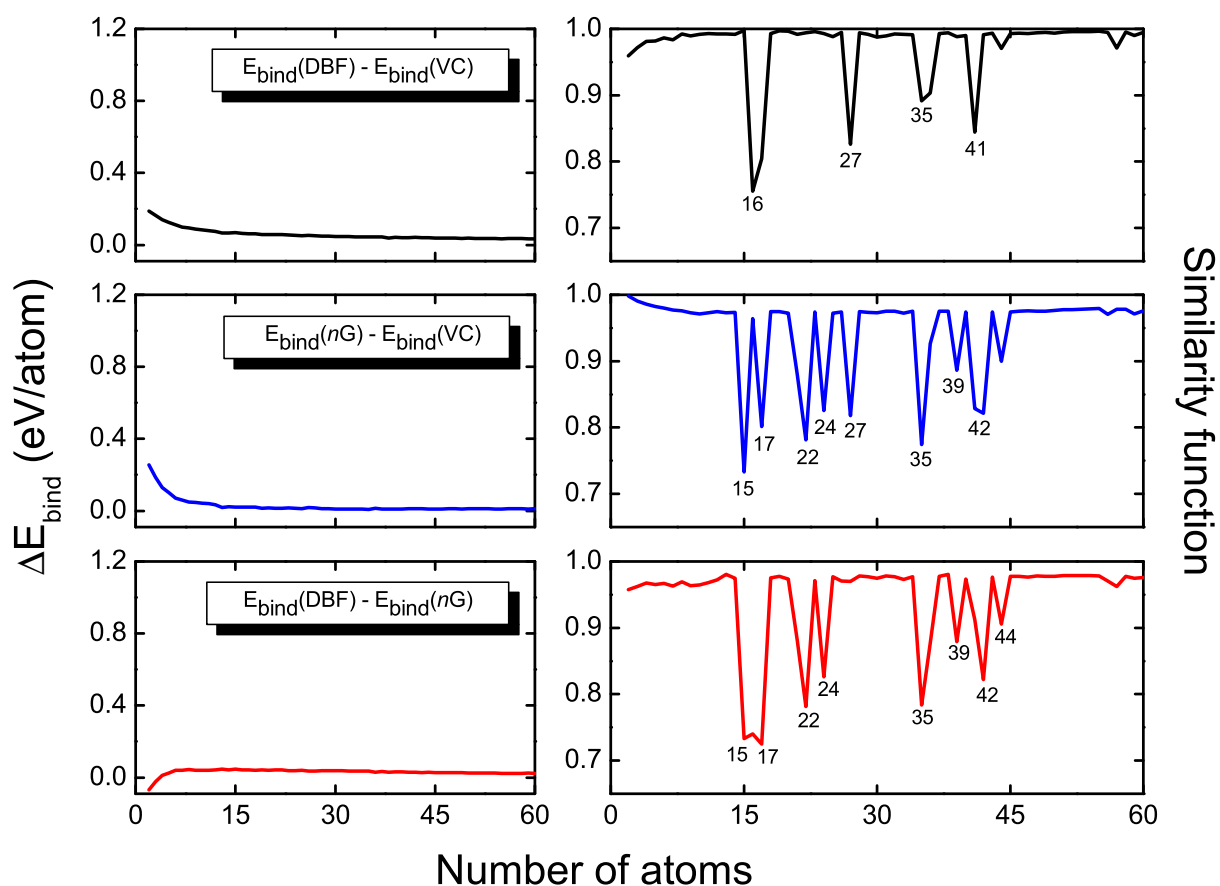
**Figure 6.2:** The left column shows the differences in the binding energies in eV/atom between the copper clusters obtained with the different potentials. The right column shows the similarity function for the comparison between the lowest-lying isomers obtained with the same pairs of potentials.
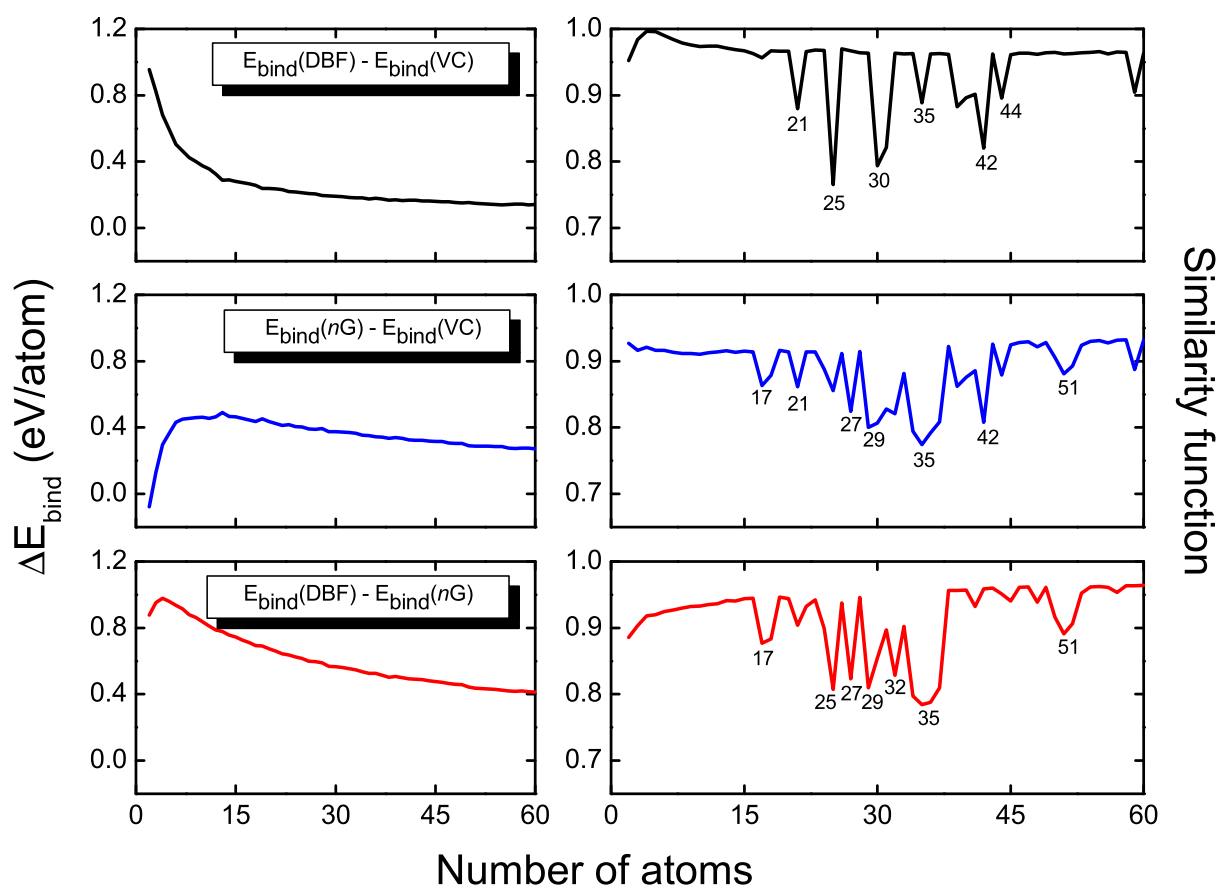
**Figure 6.3:** The same for the nickel clusters.
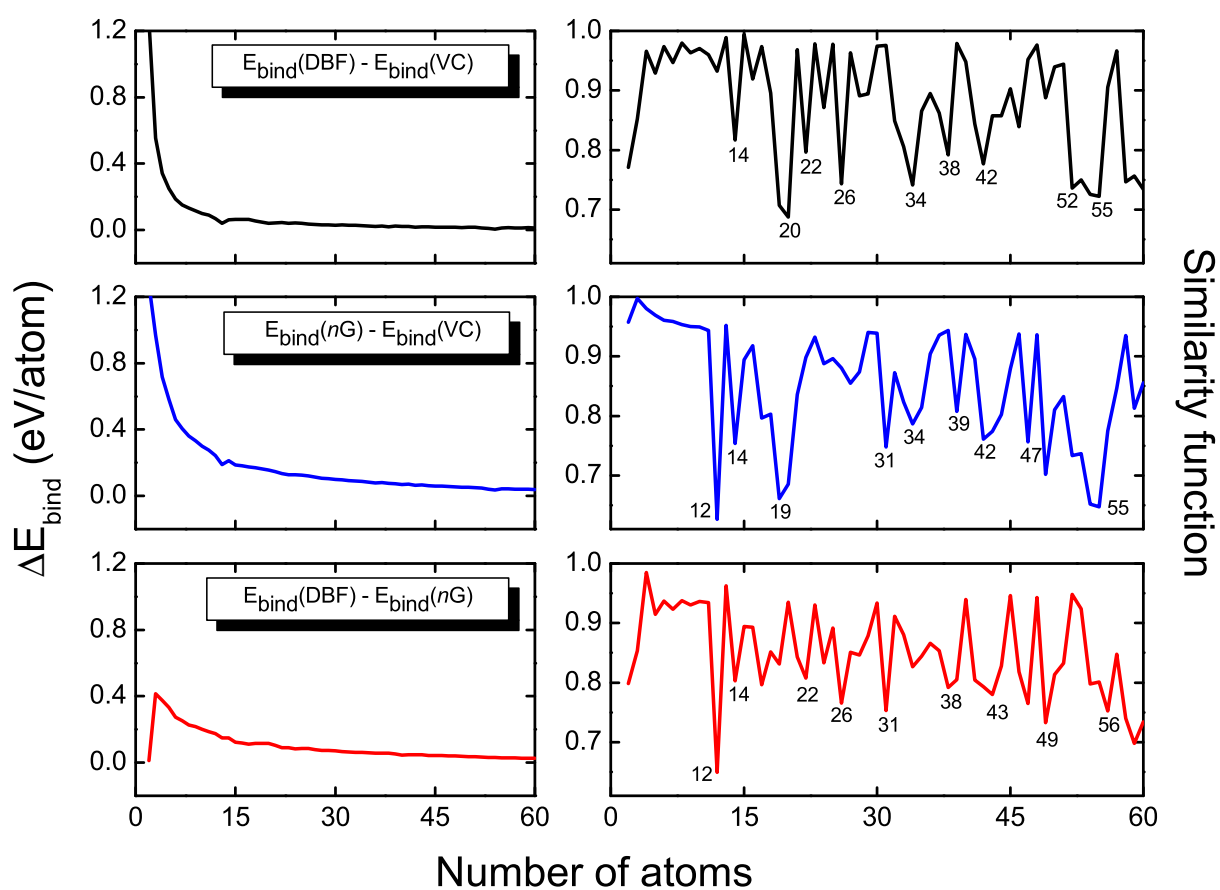
**Figure 6.4:** The same for the gold clusters.
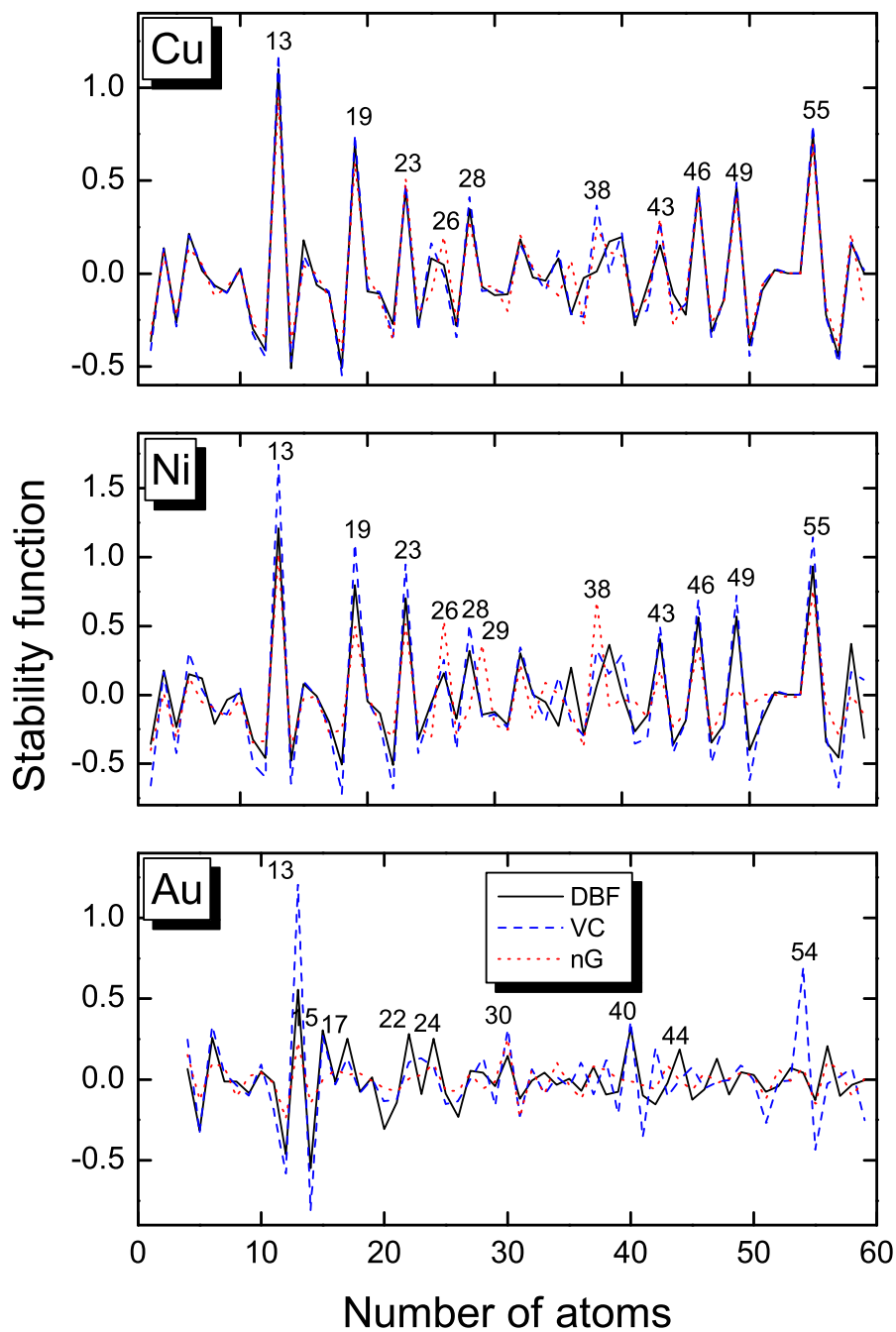
**Figure 6.5:** The stability function as a function of cluster size for the three metals with the three potentials.

symmetries than the corresponding VC and $n$G clusters. The $Au_{38}$ and $Au_{55}$ clusters are not particularly stable, while the $Au_{54}$ icosahedron without a central atom is a magic-sized cluster according to the VC method. In agreement with previous studies on gold clusters with the many-body Gupta potential [81, 82, 84, 85, 86], the lowest-lying isomer of $Au_{55}$ found by us is low-symmetrical (see Table 6.5).

For better understanding of the peculiarities of the small and larger clusters, one has to analyze their symmetries, which for the lowest three isomers with $N$ up to 13 atoms are presented in Table 6.3, and the point groups of the lowest-lying structures with $14 \leq N \leq 60$ atoms obtained with the three potentials are presented in Table 6.4 and Table 6.5. The $Ni_{6.2}$, $Au_{6.2}$, and $Au_{7.3}$ isomers do not exist within the $n$G and DBF potentials.

All small clusters found with the three potentials have the same global minima, except for $Au_{12}$, where the $n$G potential predicts a structure with a $D_{2d}$ symmetry. In agreement with previous semiempirical and molecular dynamics studies, the global minima for the clusters with 13 atoms correspond to the second Mackay icosahedron. On the other hand, Wang *et al.*[50] obtained a disordered structure for the $Au_{13}$ cluster on the basis of first-principles calculations. By using the Generalized Gradient Approximation (GGA) Olviedo and Palmer[49] confirmed this result and found a low symmetrical ground state also for $Cu_{13}$. Observing the second and third isomers, one can determine that the EAM potentials give similar results, while the $n$G potential prefers configurations with higher symmetry. For the nickel clusters, the $n$G potential gives 7 differences in the symmetries compared to the other two potentials, 8 for copper, but only 3 for gold, where in two of the three cases there is not agreement also between the two EAM potentials. It seems that the Gupta potential works well even for the smallest gold clusters, although it slightly overestimates the binding energy, and the differences observed for Cu and Ni could be dependent on the parameterization of the potential.

The results presented in Table 6.4 and Table 6.5 show that the difference between the EAM and the $n$G potentials for copper diminishes at the larger clusters. There are only 7 differences between the $n$G potential and the EAM methods for the copper clusters, 14 for the nickel, but 30 for the gold ones. The differences between the DBF and the VC version of the EAM are 6 cluster sizes for copper, 9 for nickel, and 24 for gold, which in turn means that for a given gold cluster it is hard to find two equal symmetries. For copper and nickel, the EAM and the Gupta potentials predict altogether very similar results, while for the gold clusters all methods lead to different structures, which one more time confirms their complicated growth.

Our results for the copper clusters with the $n$-Gupta potential are completely consistent with those by Darby *et al.*[86], while for gold we found lower-lying minima with different symmetries for the clusters with $N = 47$, 49, 50, 54, 55, and 56 atoms. The energy differences between their and our lowest-lying structures are as follows: 0.047 eV for $Au_{47}$, 0.066 eV for $Au_{49}$, 0.053 eV for $Au_{50}$, 0.025 eV, 0.051 eV, and 0.066 eV for $N = 54$, 55, and 56, respectively. Except for $Au_{55}$, all other structures have high symmetries. Our global minimum structure of $Au_{55}$ according to the $n$G potential is a decahedron capped with one additional atom on one side, and it has a low $C_1$ symme-

try, similar to the results obtained with the EAM and previous studies on gold clusters [81, 82, 84, 85, 86]. Moreover, the next two isomers according to this potential also have $C_1$ symmetry. The icosahedron and cuboctahedron lie above the ground state structure, with energetical differences of 0.304 eV and 0.975 eV, respectively. The global minimum structure obtained with the VC method ($C_{3v}$ symmetry) lies with 0.374 eV below the complete second Mackay icosahedron optimized with the same potential, while the latter is practically unstable within the DBF version.

**Table 6.3:** Point groups of the lowest three isomers of nickel, copper, and gold clusters for $6 \leq N \leq 13$. $n$G denotes the $n$-body Gupta potential, DBF and VC denote the EAM versions of Daw, Baskes, and Foiles and of Voter and Chen, respectively.

| $N$ | Ni $n$G/DBF/VC | Cu $n$G/DBF/VC | Au $n$G/DBF/VC |
|---|---|---|---|
| 6.1 | $O_h/O_h/O_h$ | $O_h/O_h/O_h$ | $O_h/O_h/O_h$ |
| 6.2 | $-/C_{2v}/C_{2v}$ | $C_{2v}/C_{2v}/C_{2v}$ | $C_{2v}/-/C_{2v}$ |
| 7.1 | $D_{5h}/D_{5h}/D_{5h}$ | $D_{5h}/D_{5h}/D_{5h}$ | $D_{5h}/D_{5h}/D_{5h}$ |
| 7.2 | $C_{3v}/C_{3v}/C_{3v}$ | $C_{3v}/C_{3v}/C_{3v}$ | $C_{3v}/C_2/C_{3v}$ |
| 7.3 | $C_{3v}/C_2/C_2$ | $C_{3v}/C_2/C_{3v}$ | $C_2/-/C_2$ |
| 8.1 | $D_{2d}/D_{2d}/D_{2d}$ | $D_{2d}/D_{2d}/D_{2d}$ | $D_{2d}/D_{2d}/D_{2d}$ |
| 8.2 | $C_s/C_s/C_s$ | $C_s/C_s/C_s$ | $C_s/C_s/C_s$ |
| 8.3 | $C_{2v}/D_{3d}/D_{3d}$ | $D_{3d}/D_{3d}/D_{3d}$ | $D_{3d}/D_{3d}/D_{3d}$ |
| 9.1 | $C_{2v}/C_{2v}/C_{2v}$ | $C_{2v}/C_{2v}/C_{2v}$ | $C_{2v}/C_{2v}/C_{2v}$ |
| 9.2 | $D_{3h}/D_{3h}/D_{3h}$ | $D_{3h}/D_{3h}/D_{3h}$ | $D_{3h}/D_{3h}/D_{3h}$ |
| 9.3 | $D_{3h}/C_{2v}/C_{2v}$ | $C_1/C_{2v}/C_s$ | $C_{2v}/C_{2v}/C_s$ |
| 10.1 | $C_{3v}/C_{3v}/C_{3v}$ | $C_{3v}/C_{3v}/C_{3v}$ | $C_{3v}/C_{3v}/C_{3v}$ |
| 10.2 | $D_{4d}/D_{2h}/D_{2h}$ | $C_2/D_{2h}/D_{4d}$ | $D_{2h}/D_{2h}/D_{4d}$ |
| 10.3 | $C_{2v}/C_2/C_2$ | $C_{2v}/C_2/C_2$ | $C_2/C_2/D_{3h}$ |
| 11.1 | $C_{2v}/C_{2v}/C_{2v}$ | $C_{2v}/C_{2v}/C_{2v}$ | $C_{2v}/C_{2v}/C_{2v}$ |
| 11.2 | $C_{2v}/C_2/C_2$ | $C_{2v}/C_2/C_2$ | $C_2/C_2/C_2$ |
| 11.3 | $C_{2v}/C_{2v}/C_{2v}$ | $C_2/C_{2v}/C_{2v}$ | $C_2/C_2/C_2$ |
| 12.1 | $C_{5v}/C_{5v}/C_{5v}$ | $C_{5v}/C_{5v}/C_{5v}$ | $D_{2d}/C_{5v}/C_{5v}$ |
| 12.2 | $D_{3h}/C_1/C_1$ | $D_{3h}/C_1/C_1$ | $C_2/D_2/C_2$ |
| 12.3 | $C_s/D_{2d}/D_{2d}$ | $C_1/D_{3h}/D_{3h}$ | $C_s/D_{2d}/D_{3h}$ |
| 13.1 | $I_h/I_h/I_h$ | $I_h/I_h/I_h$ | $I_h/I_h/I_h$ |
| 13.2 | $C_s/C_s/C_s$ | $C_s/D_{5h}/C_s$ | $C_s/C_s/C_1$ |
| 13.3 | $C_s/C_s/C_s$ | $C_s/O_h/C_s$ | $C_{3v}/C_1/C_s$ |

**Table 6.4:** Point groups of the optimized nickel, copper, and gold clusters for $14 \leq N \leq 40$.

| $N$ | Ni $n$G/DBF/VC | Cu $n$G/DBF/VC | Au $n$G/DBF/VC |
|---|---|---|---|
| 14 | $C_{3v}/C_{3v}/C_{3v}$ | $C_{3v}/C_{3v}/C_{3v}$ | $C_{6v}/C_{2v}/C_{3v}$ |
| 15 | $C_{2v}/C_{2v}/C_{2v}$ | $C_{2v}/D_{6d}/D_{6d}$ | $C_{2v}/D_{6d}/D_{6d}$ |
| 16 | $C_s/C_s/C_s$ | $C_s/D_{3h}/C_s$ | $C_s/D_{3h}/C_{2v}$ |
| 17 | $C_{3v}/C_2/C_2$ | $C_2/T_d/C_2$ | $C_{2v}/T_d/T_d$ |
| 18 | $C_{5v}/C_s/C_s$ | $C_s/C_s/C_s$ | $C_s/C_{2v}/C_{4v}$ |
| 19 | $D_{5h}/D_{5h}/D_{5h}$ | $D_{5h}/D_{5h}/D_{5h}$ | $C_s/C_{2v}/D_{5h}$ |
| 20 | $C_{2v}/C_{2v}/C_{2v}$ | $C_{2v}/C_{2v}/C_{2v}$ | $C_s/C_s/D_{3d}$ |
| 21 | $C_{2v}/C_1/C_s$ | $C_1/C_s/C_s$ | $C_{6v}/C_s/C_s$ |
| 22 | $C_s/C_s/C_s$ | $C_s/D_{6h}/D_{6h}$ | $C_s/D_{6h}/C_1$ |
| 23 | $D_{3h}/D_{3h}/D_{3h}$ | $D_{3h}/D_{3h}/D_{3h}$ | $D_2/C_2/C_{2v}$ |
| 24 | $C_s/C_{2v}/C_{2v}$ | $C_{2v}/D_3/D_3$ | $C_s/C_{3v}/C_2$ |
| 25 | $C_s/C_{2v}/C_3$ | $C_3/C_3/C_3$ | $C_1/D_2/C_2$ |
| 26 | $T_d/T_d/T_d$ | $T_d/T_d/T_d$ | $C_s/D_{3h}/C_1$ |
| 27 | $C_s/C_{2v}/C_{2v}$ | $C_{2v}/C_{2v}/C_s$ | $C_s/C_s/C_s$ |
| 28 | $T/T/T$ | $T/T/T$ | $C_2/C_3/C_s$ |
| 29 | $D_{3h}/C_3/C_3$ | $C_3/C_3/C_3$ | $C_2/C_1/C_2$ |
| 30 | $C_{2v}/C_{2v}/C_s$ | $C_s/C_s/C_s$ | $C_{3v}/C_{3v}/C_{3v}$ |
| 31 | $C_s/C_s/C_3$ | $C_3/C_3/C_3$ | $C_2/C_3/C_3$ |
| 32 | $C_{2v}/D_3/D_3$ | $D_3/D_3/D_3$ | $C_3/C_3/D_{2d}$ |
| 33 | $C_s/C_2/C_2$ | $C_2/C_2/C_2$ | $C_s/C_2/C_2$ |
| 34 | $T/C_s/C_s$ | $C_s/C_s/C_s$ | $C_2/C_2/T_d$ |
| 35 | $D_3/C_{2v}/D_3$ | $D_3/C_{2v}/D_3$ | $C_s/C_{2v}/C_{2v}$ |
| 36 | $C_{2v}/C_s/C_s$ | $C_s/C_s/C_1$ | $C_{2v}/C_{2v}/C_{2v}$ |
| 37 | $C_{3v}/C_2/C_2$ | $C_2/C_2/C_2$ | $C_{2v}/C_1/C_{2v}$ |
| 38 | $O_h/O_h/O_h$ | $O_h/O_h/O_h$ | $O_h/C_2/O_h$ |
| 39 | $C_{5v}/C_{5v}/C_5$ | $C_{5v}/C_5/C_5$ | $C_{4v}/D_3/D_3$ |
| 40 | $C_s/C_s/C_s$ | $C_s/C_s/C_s$ | $D_2/D_2/D_3$ |

**Table 6.5:** Point groups of the optimized nickel, copper, and gold clusters for $41 \leq N \leq 60$.

| $N$ | Ni $n$G/DBF/VC | Cu $n$G/DBF/VC | Au $n$G/DBF/VC |
|---|---|---|---|
| 41 | $C_s/C_s/C_1$ | $C_s/C_1/C_3$ | $C_s/D_2/C_1$ |
| 42 | $C_s/C_s/D_2$ | $C_s/D_2/D_2$ | $C_s/C_2/D_4$ |
| 43 | $C_s/C_s/C_s$ | $C_s/C_s/C_s$ | $C_{2v}/C_1/D_2$ |
| 44 | $C_1/C_1/C_s$ | $C_1/C_s/C_s$ | $C_2/C_1/C_s$ |
| 45 | $C_1/C_s/C_s$ | $C_s/C_s/C_s$ | $C_1/C_1/C_s$ |
| 46 | $C_{2v}/C_{2v}/C_{2v}$ | $C_{2v}/C_{2v}/C_{2v}$ | $C_3/C_1/C_3$ |
| 47 | $C_1/C_1/C_1$ | $C_1/C_1/C_1$ | $C_{2v}/C_1/C_1$ |
| 48 | $C_s/C_s/C_s$ | $C_s/C_s/C_s$ | $C_1/C_1/C_1$ |
| 49 | $C_{3v}/C_{3v}/C_{3v}$ | $C_{3v}/C_{3v}/C_{3v}$ | $D_{5h}/C_1/C_1$ |
| 50 | $C_s/C_s/C_s$ | $C_s/C_s/C_s$ | $D_{3h}/C_1/C_1$ |
| 51 | $C_{2v}/C_{2v}/C_{2v}$ | $C_{2v}/C_{2v}/C_{2v}$ | $C_s/C_1/C_1$ |
| 52 | $C_{3v}/C_{3v}/C_{3v}$ | $C_{3v}/C_{3v}/C_{3v}$ | $C_{2v}/C_{2v}/D_{5d}$ |
| 53 | $C_{2v}/C_{2v}/C_{2v}$ | $C_{2v}/C_{2v}/C_{2v}$ | $C_{3v}/C_{3v}/C_{5v}$ |
| 54 | $C_{5v}/C_{5v}/C_{5v}$ | $C_{5v}/C_{5v}/C_{5v}$ | $C_{2v}/C_1/I_h$ |
| 55 | $I_h/I_h/I_h$ | $I_h/I_h/I_h$ | $C_1/C_1/C_{3v}$ |
| 56 | $C_{3v}/C_{3v}/C_s$ | $C_s/C_s/C_s$ | $D_{2h}/C_2/C_s$ |
| 57 | $C_{2v}/C_s/C_s$ | $C_s/C_1/C_s$ | $C_{2v}/C_1/C_1$ |
| 58 | $C_{3v}/C_{3v}/C_{3v}$ | $C_{3v}/C_{3v}/C_{3v}$ | $C_1/C_1/C_1$ |
| 59 | $C_{2v}/C_{2v}/C_{3v}$ | $C_1/C_1/C_1$ | $C_{2v}/C_1/C_s$ |
| 60 | $C_s/C_s/C_s$ | $C_s/C_s/C_s$ | $C_{2v}/C_s/C_s$ |

## 6.4 Growth

The distribution of radial distances for all metals with all potentials is shown at Fig. 6.6. As discussed already at gold and silver clusters, when only few values are found for a given $N$, the cluster has a high symmetry and contains only few atomic shells. It is interesting to observe how this property is not concentrated to the single values of $N$ but is built up over a larger range of $N$. This is found for all systems and potentials around $N = 13$ and $N = 55$ where the first and second Mackay icosahedra are built, except for the Au$_{55}$ cluster obtained with the VC potential that has an irregular icosahedral structure, and the icosahedral shell is built only up to the incomplete Au$_{54}$ icosahedron. At Fig. 6.6 we also see that the three potentials lead to very similar results for nickel and copper, which is not the case for gold clusters especially with the DBF and $n$G potentials, once again confirming that gold is a material for which small, critical parts of the potential may lead to significantly different results. Moreover, we observe that the results for nickel
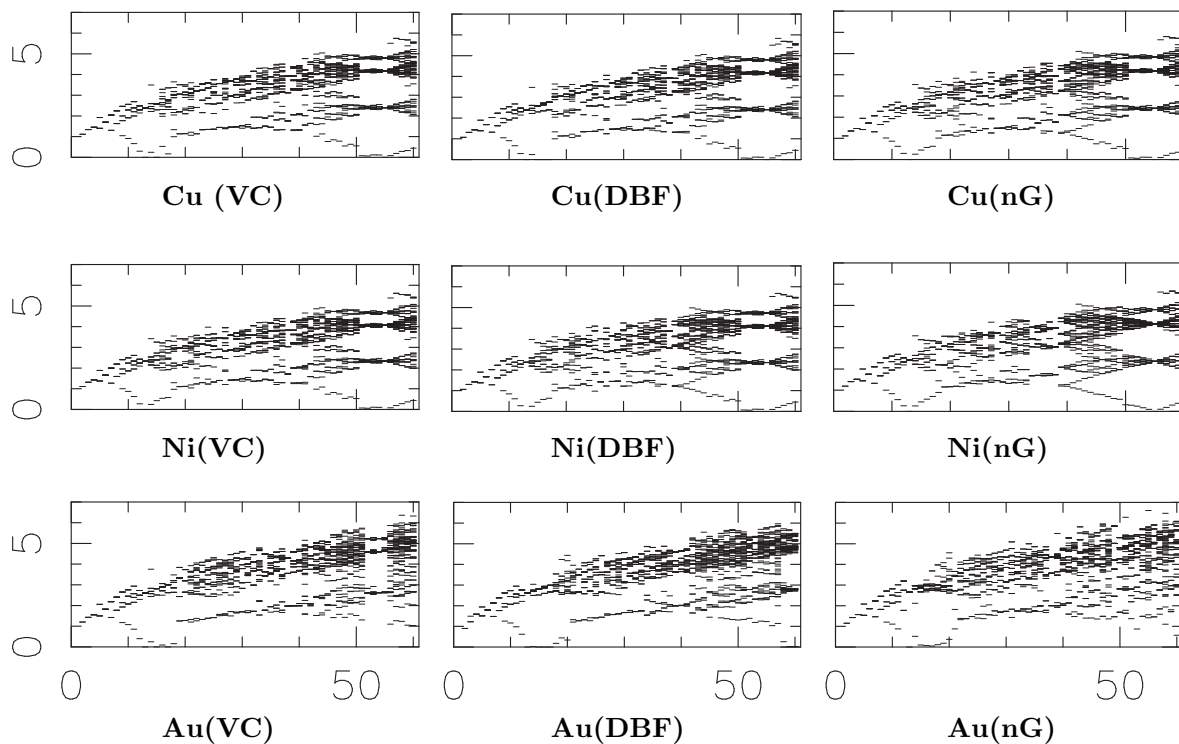
**Figure 6.6:** The radial distribution (in Å) for the energetically lowest isomers. Each small line represents at least one atom with that radial distance.

and copper resemble each other, whereas those for gold are different, with the results from the VC potential being closer to those for the nickel and copper clusters than the ones obtained with the DBF potential that seems to indicate irregular structures of low symmetry.

# Chapter 7

# Molecular Dynamics code

## 7.1  Motivation

Clusters have become an important object in the contemporary nanoscience in conjunction with their potential applications in the computer industry and the catalysis. In the experiments, the clusters are not only investigated in the gas phase, but also deposited on diverse substrates , where the formation of fine monolayers, or cluster islands, respectively, is pursued. Various techniques of cluster deposition have been introduced, from *Electrochemical Scanning Tunneling Microscopy* to *Ionized Cluster Beam Deposition*. There is a growing need of computer simulations which can explain the mechanism of cluster deposition on the surface, predict if the structure of the nanoparticle will be kept unchanged when deposited, and on which kind of substrate this is most likely to happen. Moreover, the theoretical simulations can suggest at what experimental conditions the best results can be obtained.

The first part of this study was concentrated on the global minima optimization of isolated metal clusters. Further, the optimized structures were to be deposited on different metal substrates in order to study the influence of the substrate orientation, impact angle, deposition energy, and different cluster structures, stable and unstable, for each cluster size. The impact cluster energies used in this work are in the range of the experimental *Low Energy Cluster Beam Deposition*, which allows us to compare our results to experimental data when such is available.

To simulate theoretically the experimental process of deposition we need Molecular Dynamics (MD) simulations, as they explicitly describe the molecular system as a function of time, and can directly calculate time-dependent phenomena. In the next two Chapters the cluster interaction is followed from the *Low Energy Cluster Beam* at the beginning of the experiment, where collision processes are studied, up to the deposition and cooling onto the surface, where cluster islands are produced. For the proper description of these events the development of a Molecular Dynamics code becomes essential. Another option to investigate the cluster growth on surface was to extend our Aufbau/Abbau and Random algorithms in order to generate and optimize clusters onto substrates. However, besides that this technique is limited only to studying the cluster growth, the maximal

number of atoms that can be treated will be significantly smaller due to the increased computational demand, especially when the cluster atoms are randomly generated, and many optimization runs are needed, respectively.

As there are typically few thousands of atoms needed in order to model the surface, we were obliged to use a semiempirical potential for the evaluation of energy and forces. Among all potentials used in the present study, the approach that gave the results with best agreement to previous theoretical and experimental data, was the EAM potential as modified by Voter and Chen. We chose to implement the classical MD equations due to the large number of atoms that had to be treated. There exist also *ab initio* MD procedures, such as the *Born-Oppenheimer*[141] and *Car-Parrinello*[142] algorithms. The *Born-Oppenheimer* MD is limited to small metal clusters containing 10-15 atoms, studied in vacuum. As this formalism explicitly solves the Schrödinger equation, it has the same limitations as the modern density functionals. The *Car-Parrinello* program to our best knowledge is used mainly for the simulation of organic molecules. The proper study of gold clusters demands the use of relativistic effective core potentials which would make the *ab initio* MD simulation of larger systems containing these atoms computationally infeasible.

In this Chapter, we will continue by giving a short overview of the basic principles of the classical Molecular Dynamics. The equations of motion and the *Velocity Verlet* algorithm used for their solution here are introduced in Sections 7.2 and 7.3, respectively. The developed MD program is described in Section 7.4, along with the introduction of different routines in the code. Finally, in Section 7.5 the results from some test calculations are discussed.

**Classical Molecular Dynamics**   Based on molecular mechanics, it addresses numerical solutions of Newton's equations of motion i.e. Hamiltonian mechanics on an atomistic or similar model of a molecular system to obtain information about its equilibrium and dynamic properties. The main justification of the MD method is that statistical ensemble averages are equal to time averages of the system. In molecular dynamics, the forces between molecules are calculated explicitly and the motion of the molecules is computed with a suitable numerical integration method. The starting conditions are the positions of the atoms (taken for example, from a known crystal structure) and their velocities (generated from random numbers and scaled to the desired temperature). Following Newton's prescription, from the initial positions, velocities and forces, it is possible to calculate the positions and velocities of the atoms at a small time interval (a time step) later. From the new positions the forces are recalculated and another step in time made. The cycle has to be repeated many times in the course of a full simulation, usually for many thousands of time steps. It is worth noting that a single time step is usually of the order of 1 femtosecond.

Calculation of the atomic forces in a molecular dynamics simulation is usually the most expensive operation. It is normally assumed that the forces between atoms are pair forces; that is, they act exclusively between pairs of atoms. Higher order forces, involving three - or four body terms are also sometimes considered - especially in complex
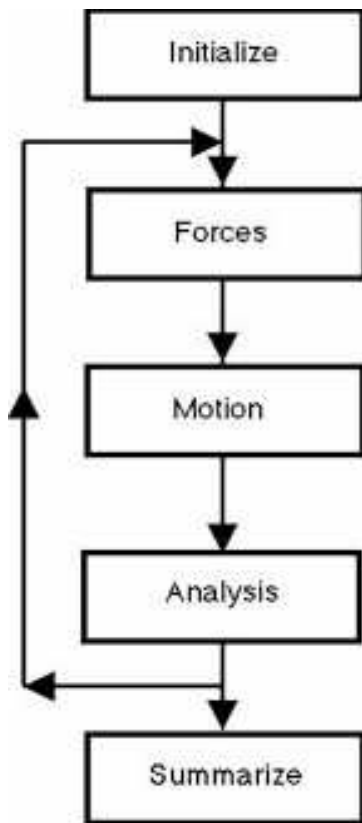
**Figure 7.1:** A generalized scheme of a MD simulation.

molecular structures. If there are $N$ atoms in the system, there will be at most $N(N-1)/2$ unique atom pairs, each with an associated force to compute. The time it takes to perform a molecular dynamics simulation is thus (approximately) proportional to $N^2$. Usually however, a cut-off is applied at a certain interatomic separation, beyond which it is assumed the force is zero. This allows more efficiency in computing the forces, since all atom pairs need no longer be considered. Design of a molecular dynamics simulation should account for the available computational power. Simulation size ($N$ = number of particles), time step and total time duration must be selected so that the calculation can finish within a reasonable time period. However, the simulations should be long enough to be relevant to the time scales of the natural processes being studied. Most scientific publications about the dynamics of proteins and DNA use data from simulations spanning from nanoseconds ($10^{-9}$ s) to microseconds ($10^{-6}$ s). To obtain these simulations, several CPU-days to CPU-years are needed. Parallel algorithms allow the load to be distributed among CPUs.

## 7.2    Equations of motion

The most fundamental form to present the equations of motion is that by Lagrange:

$$\frac{d}{dt}(\partial\mathcal{L}/\partial\dot{q}_k) - (\partial\mathcal{L}/\partial q_k) = 0 \tag{7.1}$$

where the Lagrangian function $\mathcal{L}(q,\dot{q})$ is defined in terms of kinetic and potential energies:

$$\mathcal{L} = \mathcal{K} - \mathcal{V} \tag{7.2}$$

and is considered to be a function of the generalized coordinates $q_k$ and their time derivatives $\dot{q}_k$. The kinetic and potential energies have the following forms:

$$\mathcal{K} = \sum_{i=1}^{N}\sum_{\alpha} p_{i\alpha}^2/2m_i \tag{7.3}$$

where $m_i$ is the molecular mass, and the index $\alpha$ runs over the different (x,y,z) components of the momentum of molecule $i$. The potential energy $\mathcal{V}$ may be divided into terms depending on the coordinates of individual atoms, pairs, triplets, etc.:

$$\mathcal{V} = \sum_{i} v_1(r_i) + \sum_{i}\sum_{j>i} v_2(r_i, r_j) + \sum_{i}\sum_{j>i}\sum_{k>j>i} v_3(r_i, r_j, r_k) + .... \tag{7.4}$$

The $\sum_i\sum_{j>i}$ notation indicates a summation over all distinct pairs $i$ and $j$ without counting any pair twice. The first term, $v_1(r_i)$, represents the effect of an external field on the system. The remaining terms represent particle interactions. The second term, $v_2$, the pair potential, is the most important. The pair potential depends only on the magnitude of the pair separation $r_{ij} = |r_i - r_j|$, so it may be written $v_2(r_{ij})$. Despite the size of three-body terms in the potential, they are only rarely included in computer simulations, because the calculation of any quantity involving a sum over triplets of molecules is very time-consuming. Fortunately, the pairwise approximation gives a remarkably good description of the properties because the average three-body effects can be partially included by defining an effective pair potential in the form:

$$\mathcal{V} \approx \sum_{i} v_1(r_i) + \sum_{i}\sum_{j>i} v_2^{eff}(r_{ij}) \tag{7.5}$$

If we consider a system of atoms, with Cartesian coordinates $r_i$ and the usual definitions of $\mathcal{K}$ and $\mathcal{V}$, then eqn (7.1) becomes

$$m_i\ddot{r}_i = f_i \tag{7.6}$$

where $m_i$ is the mass of atom $i$ and

$$f_i = \nabla_{r_i}\mathcal{L} = -\nabla_{r_i}\mathcal{V} \tag{7.7}$$

is the force on that atom. These equations apply also to the center of mass motion of a molecule. The generalized momentum $p_k$ conjugate to $q_k$ is defined as

$$p_k = \partial \mathcal{L} / \partial \dot{q}_k. \tag{7.8}$$

The momenta feature in the Hamiltonian form of the equations of motion

$$\dot{q}_k = \partial \mathcal{H} / \partial p_k \tag{7.9}$$

$$\dot{p}_k = -\partial \mathcal{H} / \partial q_k. \tag{7.10}$$

The Hamiltonian is strictly defined by the equation

$$\mathcal{H}(p, q) = \sum_k \dot{q}_k p_k - \mathcal{L}(q, \dot{q}) \tag{7.11}$$

where it is assumed that we can write $\dot{q}_k$ on the right as some function of the momenta $p$. For our immediate purposes this reduces to

$$\mathcal{H}(q, p) = \mathcal{K}(p) + \mathcal{V}(q) \tag{7.12}$$

and $\mathcal{H}$ is automatically equal to the energy. For Cartesian coordinates, Hamilton's equations become

$$\dot{r}_i = p_i / m_i \tag{7.13}$$

$$\dot{p}_i = -\nabla_{r_i} \mathcal{V} = f_i \tag{7.14}$$

Computing center of mass trajectories involves solving either a system of 3N second-order differential equations, eqn (7.6), or an equivalent set of 6N first-order differential equations, eqns (7.13) and (7.14).

## 7.3 The Velocity Verlet algorithm

Perhaps the most widely used method of integrating the equations of motion is that initially adopted by Verlet in 1967. This method is a direct solution of the second-order Newtonian equations (7.6). The method is based on positions r(t), accelerations a(t), and the positions r(t-δt) from the previous step. The equation for advancing the positions reads as follows:

$$r(t + \delta t) = 2r(t) - r(t - \delta t) + \delta t^2 a(t) \tag{7.15}$$

Here, the velocities do not appear. They have been eliminated by addition of the equations obtained by Taylor expansion about r(t):

$$r(t + \delta t) = r(t) + \delta t v(t) + (1/2)\delta t^2 a(t) + ... \tag{7.16}$$

$$r(t - \delta t) = r(t) - \delta t v(t) + (1/2)\delta t^2 a(t) - ... \tag{7.17}$$

The velocities are not needed to compute the trajectories, but they are useful for estimating the kinetic energy (and hence the total energy). They may be obtained from the formula:

$$v(t) = \frac{r(t + \delta t) - r(t - \delta t)}{2\delta t} \tag{7.18}$$

A method which stores positions, velocities and accelerations all at the same time $t$, is the *Velocity Verlet* algorithm used in the present work. This algorithm takes the form

$$r(t + \delta t) = r(t) + \delta t v(t) + \frac{1}{2}\delta t^2 a(t) \tag{7.19}$$

$$v(t + \delta t) = v(t) + \frac{1}{2}\delta t[a(t) + a(t + \delta t)] \tag{7.20}$$

Again, the Verlet algorithm may be recovered by eliminating the velocities. The *Velocity Verlet* algorithm involves two stages, with a force evaluation in between. Firstly, the new positions at time $t + \delta t$ are calculated using eqn(7.19), and the velocities at mid-step are computed using

$$v(t + \frac{1}{2}\delta t) = v(t) + \frac{1}{2}\delta t a(t) \tag{7.21}$$

The forces and accelerations at time $t + \delta t$ are then computed, and the velocity move completed.

$$v(t + \delta t) = v(t + \frac{1}{2}\delta t) + \frac{1}{2}\delta t a(t + \delta t) \tag{7.22}$$

At this point, the kinetic energy at time $t + \delta t$ is available. The potential energy at this time will have been evaluated in the force loop. The method uses 9N words of storage, and its numerical stability, convenience, and simplicity make it perhaps the most attractive proposed to date. Alternative method of numerical integration are the predictor-corrector algorithms. According to this formalism, the positions, velocities, and accelerations of the atoms are predicted using their current values, then the forces and the corresponding accelerations are evaluated from the new positions, all old variables are corrected using the new accelerations, and this is repeated about 4-5 times depending on the order of the algorithm until the quantities converge to an accurate solution. However, the numerous iterations make these algorithms slow and memory-consuming, while the *Velocity Verlet* method is fast and allows the use of a long time step, which is not the case for the predictor-corrector techniques.

## 7.4 The developed MD program

Figure 7.2 shows a simplified flow chart of our newly developed Molecular Dynamics algorithm. The following subsections are referring to the characterizations of the processes in the diagram. The important routines will be described in extra sections afterwards.

**Start** By starting the program the input parameters are read, such as number of atoms in the studied systems, simulation time and time step, and also the impact angle between the structures. One option determines if the initial configurations will be optimized. As in our studies, described in the next two Chapters, we have used structures previously optimized with the EAM approach, this option is normally switched off.

**Backup** Maintenance of backup data in long-time simulations is an absolute must. For example, typical MD simulation of clusters requires 30000-50000 time steps, which on a Pentium III computer take between 80 and 100 computer hours depending on the size of the systems. Therefore, in order to use exhaustively the computer time without undesirable restart of the simulation from the beginning, our program generates backup files that contain important information about the cluster coordinates, velocities, coordinates of the center of masses, time step and number of snapshots. Storage of the accelerations is not needed as they can be easily recomputed from the forces, which are recovered from the coordinates. The movement of the center of masses is important for the evaluation of the internal temperature of the cluster, which in this work is defined as relying on the difference between the kinetic energy emerging from the cluster movement and that of its center of masses. This difference in turn eliminates the contribution to the energy arising from the translational and rotational degrees of freedom. As a result of that, we obtain the kinetic energy and the corresponding temperature defined only by the vibrational motion of the particles. As the MD simulations involve explicit movement of the systems, the trajectories of the interacting particles are saved periodically in order to follow the evolution of the systems in time. Normally, it is enough to take snapshots every 5-10 steps, and even in greater intervals for the larger systems. In the present program, a mathematical function defines how often to save the trajectories:

$$if(mod(itime, nprint).eq.0) \qquad (7.23)$$

where *itime* is the current step number, and *nprint* is the total number of simulation steps divided by a rough value of the desired snapshots. For example, if the total number of steps equals 20000, and the desired number of snapshots is given to be 2000, the final number of snapshots according to the *mod* function will be about 1650, which corresponds to a trajectory backup every 12 steps. This is a suitable step also regarding the size of the trajectory file, which for 2000 atoms and 1650 snapshots will be about 150MB large at the end of the simulation. In this way, a "movie" from the particle movements can be created by using common commercial programs like *Molden*. When the program is executed for the first time, the values in the first restart file are all equal to zero. This means that no
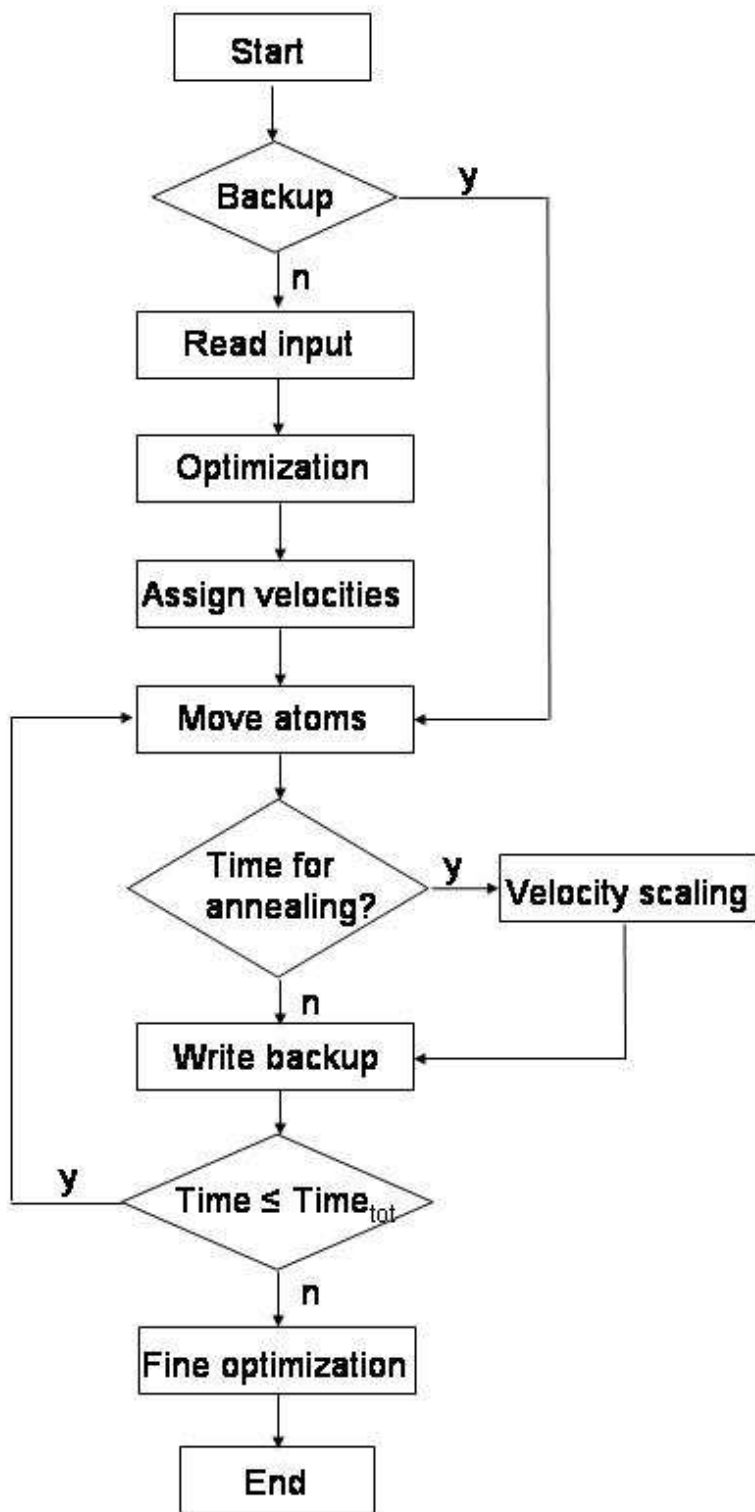
**Figure 7.2:** A scheme of the developed MD program.

backup is created and it moves to the next step, where the input coordinates are read. If there is a backup, after reading it, the program continues from where it had stopped.

**Read input**   The input is read from a single file containing the coordinates of the two interacting systems. The program can be extended so as to treat interactions between more systems. However, for our purposes (cluster depositions on surfaces and cluster-cluster collisions) it was enough to work with two systems. Immediately after reading the coordinates, the program generates an initial graphics file (*pdb*) containing the input data that can be easily visualized with common programs, which is very useful in order to eliminate possible mistakes in the input coordinates.

**Optimization**   If the initial structures are not relaxed, or just randomly generated in a box, there is an option to optimize them using the *Steepest descent* algorithm that relaxes the structure to the next energy minimum. However, we use as input data structures from our previous calculations, which most likely lie in the global minima for these cluster sizes, so this option is switched off by default.

**Assign velocities**   Here, the clusters' center of masses are calculated, and initial velocities are applied along the (x,y,z) directions. The movement is chosen to be along the direction linking the two particles' center of masses. There is also an option for the particles to impact with each other under a defined angle. When a typical cluster deposition on a surface is studied, initial velocity is assigned only to the cluster, perpendicular to the x-y plane defined by the surface atoms. The cluster can also hit the surface in a chosen angle, so as to smear on it [143]. Here, the initial kinetic temperature of the system is evaluated as follows:

$$\frac{mv^2}{2} = \frac{3}{2}Nk_BT \tag{7.24}$$

where $N$ is the number of atoms, $k_B$ is the Boltzmann constant in $eV/K$, and $T$ is the absolute temperature. In this formula, all degrees of freedom are accounted for.

**Move atoms**   The most important part of the simulation begins with the movement of the atoms according to the Newton law. This is the computationally most expensive part of the simulation, therefore it is worth mentioning that the forces are evaluated only twice in a step. Finally, the distance between the particles' centers of masses is evaluated. Its values give important information on the degree of penetration of the cluster in the substrate.

**Annealing**   At the end of the simulation event, a certain number of steps is dedicated to the simulated annealing of the system. Simulated annealing is an essential part of the MD simulation, in which the temperature is gradually reduced, often after an initial heating. This gives the system an opportunity to surmount energetic barriers, and find

non-local minima. As our program uses an *NVE* ensemble, e.g. the total energy, the number of atoms and the volume of the system remain constant, we have to cool down the structures at the end of the simulation, while since the beginning of the event the potential energy of the system decreases as a result of the interaction between the particles. As the total energy is kept constant, this leads to an increase in the kinetic energies of the cluster atoms, thus, in order to obtain reasonable final structures, we perform a simulated annealing consisting of a gradual velocity scaling at each MD step. After experimenting with different techniques we decided to scale the velocities by a factor equal to 0.98. As the results shown in Chapter 9 will confirm, a thermal equilibrium in the system is reached in about 20ps simulation time, and in most of our calculations the simulated annealing begins after 40ps, when the values of the kinetic and potential energies fluctuate insignificantly.

**Write backup**   After a successful MD step is made, it is important to save the progress for the coordinates, velocities, and temperatures. At the end of each step, the backup files for the coordinates and velocities are accessed and overwritten. Unfortunately, we can not keep record for all quantities because of space limitations. The kinetic, potential energies, as well as the instantaneous and internal temperatures of the systems are saved at each step. After the simulation event, the total energy is calculated, and its fluctuations within the microcanonical ensemble divided by the total number of atoms resulted to be of magnitude of $10^{-7}$, which is a significant improvement compared to other results in the literature, where this fluctuation was mentioned to be of order of $10^{-5}$.

**Fine optimization**   Sometimes it is useful to optimize locally the annealed structure in order to obtain more accurate total energy, for example when two large structures have very similar energies and it is not possible to prove visually that they are identical, such local optimization can be very helpful. It is performed again using the *Steepest Descent* technique. It is important to mention that this local optimization will not significantly change the cluster configuration, e.g. it will not find a lower-energy isomer, which is not the case of the global optimization methods. In order to keep the results from the simulation exactly as they are, normally we do not use this procedure, which can be switched on whenever it is needed.

**End**   At the end of the simulation the final geometries of the structures are plotted in "xyz" and "pdb" format. A suitable check if the system has reached an equilibrium are the last values of the forces, which can be compared to the initial ones, saved in a separate file. After the simulated annealing they are normally of magnitude $10^{-3}$ - $10^{-4}$, however, if the structures are consecutively optimized the forces can be of order $10^{-6}$ - $10^{-8}$ depending on what gradient value we choose as a convergence criterion.

## 7.4.1 The *Update* routine

This routine moves the atoms using the *Velocity Verlet algorithm.* Here, a part of it is presented:

call force(n1,ncomp,0)

do 100 i=1,ncomp
do 101 j=1,3
fold(j,i)=fcomp(j,i)
rcomp(j,i)=rcomp(j,i)+vcomp(j,i)*deltat+
+0.5d0*(fold(j,i)/(amu*zmas))*deltat*deltat
101 continue
100 continue

call force(n1,ncomp,0)

avx=0.d0
avy=0.d0
avz=0.d0
do 200 i=1,ncomp
vcomp(1,i)=vcomp(1,i)+0.5d0*((fold(1,i)+
+fcomp(1,i))/(amu*zmas))*deltat
vcomp(2,i)=vcomp(2,i)+0.5d0*((fold(2,i)+
+fcomp(2,i))/(amu*zmas))*deltat
vcomp(3,i)=vcomp(3,i)+0.5d0*((fold(3,i)+
+fcomp(3,i))/(amu*zmas))*deltat
avx=avx+vcomp(1,i)
avy=avy+vcomp(2,i)
avz=avz+vcomp(3,i)
200 continue

avx=avx/float(ncomp)
avy=avy/float(ncomp)
avz=avz/float(ncomp)

do 221 i=1,ncomp
vcomp(1,i)=vcomp(1,i)-avx
vcomp(2,i)=vcomp(2,i)-avy
vcomp(3,i)=vcomp(3,i)-avz
221 continue

The first step is to evaluate the forces ($fold$) before the atom movement. Simultaneously,

the atom positions are updated using these forces, atomic masses and time step. Then the force subroutine is called for a second time, and the new velocities are calculated. A small routine which removes the angular momenta is inserted in the algorithm. Here, the velocities and the positions of the atoms in the whole interacting system corresponding to the value of *ncomp* are evaluated simultaneously.

### 7.4.2   Potential energy and forces

The subroutine for the potential energy consists of three parts which correspond to the potential energy of the two isolated particles, and that of the whole system. In the Voter-Chen EAM potential, a spherical cutoff radius for the potential is used, which for copper corresponds to about 4.96 Å. This makes the potential short ranged, in comparison to other semiempirical potentials like Gupta, or Sutton-Chen. However, the advantage of this cutoff is that the important interactions are included, and the most weak interactions are omitted. This makes the evaluation of the potential energy significantly faster in comparison to other potentials.

The EAM potential is in form of calculated values for the embedding energy, repulsive potential, and density, plotted as function of the distance, e.g, they are not derived analytically. As the cluster interatomic distances most likely do not correspond to particular points in the grid, but very probably lie between them, to ensure that the potential between these points remains continuous, the potential energy is evaluated by using a spline on each of the quantities.

Similarly, the calculation of forces involves the evaluation of the gradient for each atom. Here, besides the spline used for the components of the potential energy, additional spline ensuring that the first derivatives of the energy are continuous, is introduced. Again, the forces acting in the two particles are separately computed, as well as those in the whole system.

The individual computation of energy and forces gives a clear overview of the dynamical processes occurring in the simulation. As the kinetic energy is calculated in the same way, one can distinguish the kinetic and potential energies of the both systems. In this way the exchange from kinetic into potential energy can be followed, and we can determine how and which one of the two particles absorbs it.

## 7.5   Test system

In order to test the developed MD program on our systems of interest, we simulated the deposition of an octahedral $Cu_{38}$ cluster onto a Cu(111) surface consisting of seven layers with each layer containing 267 atoms. The substrate was previously relaxed with the Voter-Chen potential. As seen in Fig. 7.3, the edges of the substrate are not symmetric, which is due to the structure optimization, and not to the MD simulation. The impact energy was chosen to be zero electron volt, and the total simulation time 40ps with included 10ps simulated annealing. Periodic boundary conditions were applied in the x-y

directions. We wanted to determine the optimal width of the substrate, which after test simulations with surface consisting of 9, 8, 7, and 6 atomic layers, respectively, turned out to remain unchanged reduced up to 6 layers. This result is also supported by the short range interactions defined in the used potential. In our further simulations described in Chapter 9, even at high impact energies such as 0.9 eV/atom the bottom layers of the substrate remain unchanged. After reducing the number of layers to 7, we compared the results obtained by "freezing" of the bottom layer atoms to other without restrictions. The results were practically the same, therefore for the final computations we decided not to anneal the bottom substrate layer.

At Fig. 7.3 are shown the structures of the interacting particles at the beginning and at the end of the simulation. For the 40ps simulation time the $Cu_{38}$ configuration remains very compact. As it will be shown in Chapter 9, where the time is extended up to 50ps, during this larger period the cluster rearranges few of its side atoms, which does not happen here. The simulation was repeated with impact energies of 0.1, 0.3, and 0.5 eV/atom.

The potential energies of both cluster and substrate decrease smoothly except for the areas marked with red circles, where the potential energy of the substrate atoms decreases significantly as a result of the attraction to the cluster atoms, while the cluster increases its potential energy due to the energetical barriers which have to be surmounted in order to break the existing bonds in the cluster and establish new ones with the substrate surface. This process is compensated by an increase in the kinetic energy of both systems as seen at the middle right panel of Fig. 7.3. The potential and kinetic energies change mirror-like which is expected to happen in a constant-energy simulation. This ensures the good conservation of the total energy, as seen at the bottom right panel, where the fluctuations in the total energy are of magnitude $10^{-7}$ and are calculated as the difference between the instantaneous total energy and its initial value divided by the number of atoms of the system. This obtained result is very good not only comparing to previous studies, but also taking into account the larger time step of 2fs and the numerical evaluation of energy and forces within the EAM potential.
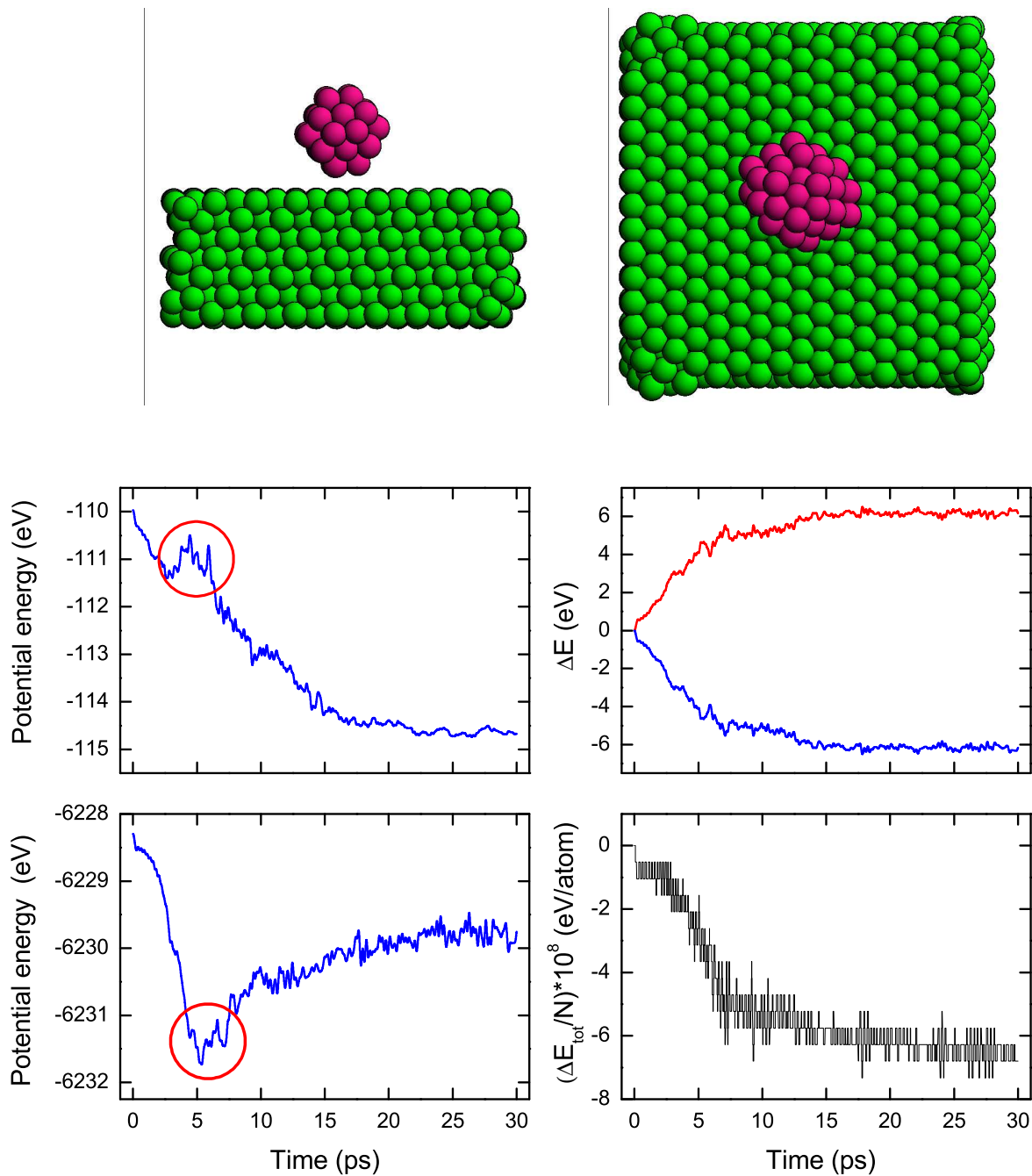
**Figure 7.3:** The initial and final structure of the deposited Cu$_{38}$ cluster and the evolution of the potential energies of the Cu$_{38}$ cluster and the Cu(111) substrate (middle and bottom left panels). On the right panels are shown the changes in the potential (blue line) and kinetic (red line) energy of the whole system and the fluctuations in the total energy multiplied by factor $10^8$.

# Chapter 8

# Collision processes

## 8.1 Introduction

Collisions processes are an important ingredient in nuclear and cluster physics.[144, 145] For instance, cluster-cluster collisions provide an important possibility to study formation of macroscopic aggregates and cluster molecules, collision-induced dissociations, and vibrational energy transfer between two clusters (see, e.g., [146]).

From a theoretical point of view, it is most convenient to study such processes by means of molecular-dynamics simulations, whereby the trajectories, rotations, and dissociation behavior of the particles can be thoroughly studied. Then, there are two approaches, i.e., the *adiabatic* cluster collisions where the reaction channels involve only vibrational and rotational excitations and the *nonadiabatic* collisions where also electronic effects are included.[153] Much interest is paid to the adiabatic collisions, where larger clusters can be studied for a longer simulation time by combining classical molecular dynamics with (semi-)empirical potentials, whereas nonadiabatic simulations like the quantum molecular dynamics (QMD)[154, 155] employing different density functionals, are limited to shorter simulation times and smaller systems.

Experimentally, small copper particles, $Cu_N$, have proven to have an unusual electro-chemical stability,[156] which makes them attractive candidates for electrocatalysts. In order to clarify which cluster sizes are particularly stable, Krückeberg and coworkers[157] studied the decay pathways and dissociation energies of small singly and doubly charged copper clusters by employing the multiple-collision induced dissociation method. For singly charged clusters, an odd-even oscillation in the dissociation energy was observed, with particularly large values for $N = 3$, 9, 15, and 21 cluster sizes, suggesting electronic shell closures for $N = 2$, 8, 14, and 20.

On the other hand, theoretical studies of collision processes between copper clusters have so far not been presented whereas more studies on sodium clusters have been reported. Thus, collision processes between magic sodium clusters with $N = 2$, 8, 20, and 40 atoms were studied by Schmitt and coworkers[150] using a two-center jellium model for the ionic cores. The energetic stability of cluster molecules (i.e., $Na_{N_1}Na_{N_2}$ molecules resulting from $Na_{N_1} + Na_{N_2}$ collision processes and containing the largely unchanged initial
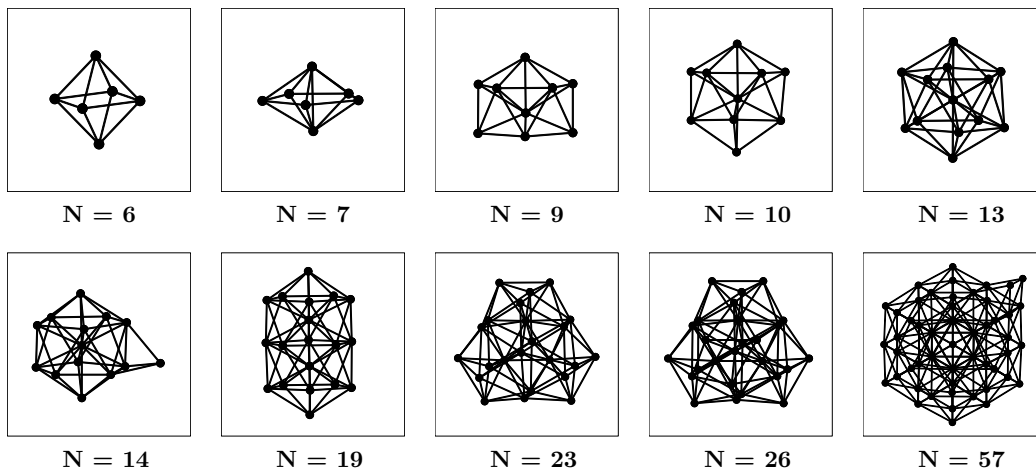
**Figure 8.1:** The initial structures of the copper clusters studied in the collision processes.

entities), as well as the main reaction channels of the cluster-cluster collisions were studied theoretically by Seifert, Schmidt, and Lutz[147, 148] by using MD calculations combined with a density-functional formalism within the local-density approximation (LDA). According to this study, the $Na_9Na_9$ molecule formed in collisions between two $Na_9$ clusters has binding energies close to that of the magic $Na_{18}$ clusters, while the $Na_8Na_8$ molecule was unstable. A study concerning the thermodynamical stability of cluster dimers[152] confirmed that the latter cluster molecule was not a stable structure except when the product happened to get the structure of the stable $Na_{16}$ cluster. This was found also by Häkkinen and Manninen[151] using *ab initio* molecular dynamics. This issue was further investigated by Zhang *et al.*[149] using a tight-binding approximation, where, in addition, the possibilities of formation of the $Na_{19}Na_{19}$ and $Na_{20}Na_{20}$ cluster dimers were studied.

The purpose of the present work is to study collision processes between two Cu clusters with $N_1$ and $N_2$ atoms for low impact energies. Special emphasis is put on the characterization of the products as a function of impact energy and size of the colliding clusters. In particular, we shall explore whether the product resembles either the initial clusters, $Cu_{N_1}$ and $Cu_{N_2}$, or the most stable larger $Cu_{N_1+N_2}$ cluster. In the former case, one may consider the product as being a cluster molecule, whereas the latter case corresponds to a fusion process. A study with a similar aim was recently presented by Rogan *et al.*[73] who investigated collision processes between small gold clusters using a parameterized potential for the inter-atomic interactions similar to the one we shall use, i.e., the Voter and Chen[7, 9] version of the embedded-atom method.[1] Rogan *et al.*[73] varied the collision energy and the impact parameter in order to cover the complete fusion, scattering, and fragmentation regimes. Here, however, we are interested in fusion processes in the low collision-energy range.

## 8.2   Dimer Formation

In the simulation of the reaction paths we use classical constant-energy molecular dynamics in order to investigate larger structures over longer simulation time. The Newtonian equations of motion are integrated by using the Velocity Verlet algorithm with time steps of $1 \times 10^{-15}$ s. The integration time in most of the simulations was 35 ps, while for the larger clusters some of the calculations were extended up to 50 ps. In order to identify the products of the collision processes, the simulations include a final simulated-annealing period of 5 ps.

We simulated the collision events between various (non)magic copper clusters at center-of-masses incident energies of $E = 0.0$, 0.038, 0.1, 0.3, and 0.5 eV/atom, and chose in all simulations the impact parameter $b = 0$, as our study is concerned entirely with possible fusion processes between the clusters. In most cases the initial orientation of the clusters contained parallel principal axes of inertia, although also some additional calculations with different relative orientations were performed.

In all cases, we find that the total energy of the final product of the $Cu_{N_1} + Cu_{N_2}$ collision process is very close to that of the global-minimum structure of the $Cu_{N_1+N_2}$ cluster. This is illustrated in Fig. 8.2. It is seen that there is an overall tendency for the total energy of the final product to decrease as a function of increasing impact energy, although smaller deviations occur. An interesting exception is that of $(N_1, N_2) = (6, 7)$, which is the lowest curve in the figure. In this case, the relative total energy shows the largest deviations from that of the globally optimized structure with $N = 13$ atoms, in particular for an impact energy around 0.3 eV/atom. A possible reason is that the $Cu_{13}$ cluster is particularly stable, having the icosahedral symmetry, and that this structure corresponds to a global total-energy minimum with a narrow basin, i.e., even smaller deviations from this structure will lead to structures of other local total-energy minima. In that case, it is quite unlikely that the structures that result from a collision process will relax to the icosahedron. On the other hand, the overall decrease in the relative total energy can be explained through the total-energy hypersurface that has an essentially exponentially growing number of local minima with cluster size so that it becomes very likely that the product cluster gets trapped in not the global, but in an energetically higher-lying local total-energy minimum.

It turned out that longer simulation times in some cases lead to lower total energies of the products, i.e., to different structures. This finding may be due to the fact that systems at a non-zero temperature have the possibility to overcome energy barriers between different local total-energy minima, and it implies that in experiment slow and fast cooling rates may lead to different products.

For an impact energy of 0.0 eV/atom the simulations for which the main axes of the colliding clusters were aligned, led to the following product structures. The final structure for $N_1 = N_2 = 6$ collision constituted of two octahedra with a common side and two additional atoms lying next to each other on one of the sides. Therefore, it can be considered as a 'double octahedron' bridged by two atoms. The $N_1 = N_2 = 13$ system has a symmetrical, oblate shape suggesting the formation of a dimer. This cluster
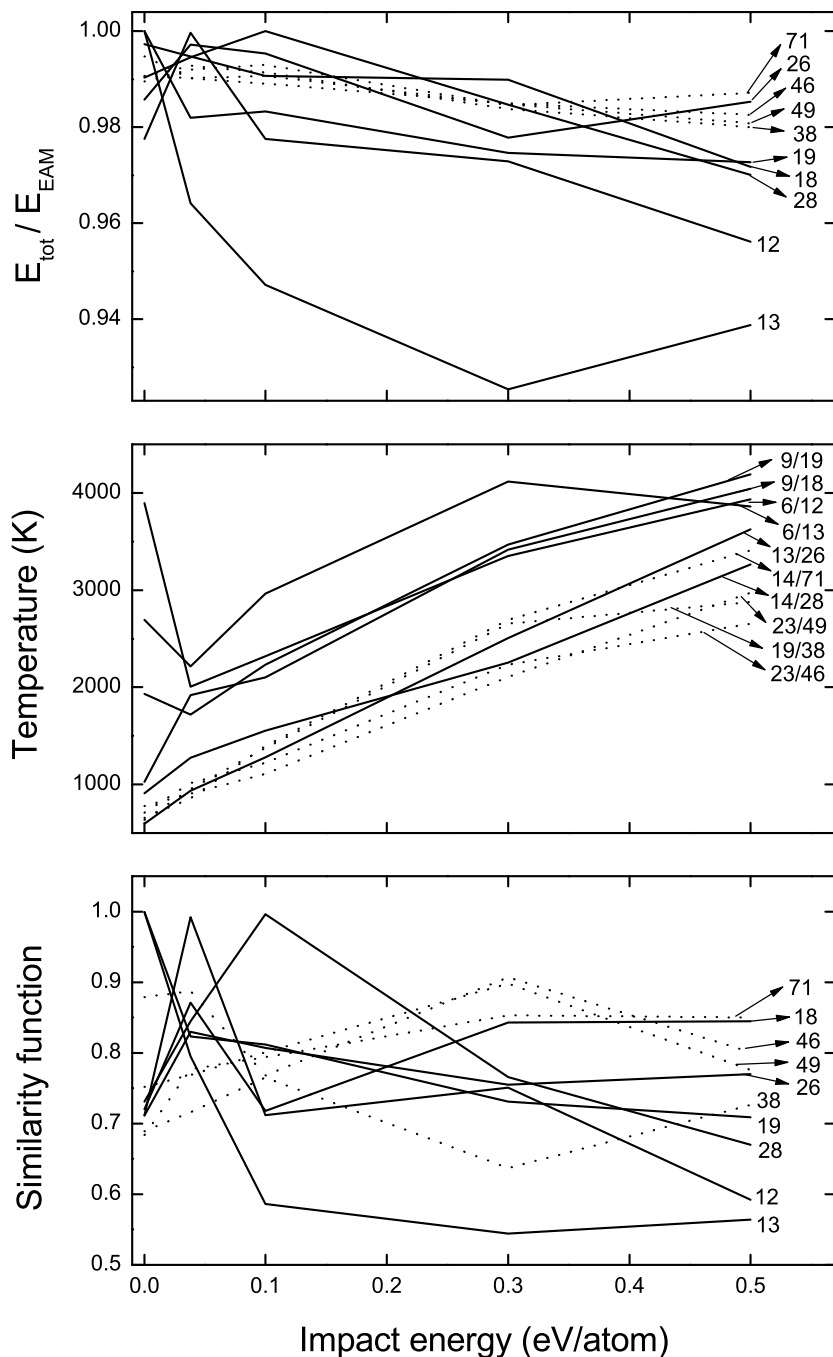
**Figure 8.2:** Various properties quantifying the end product of the $Cu_{N_1}+Cu_{N_2}$ collision process compared to the cluster with $N = N_1 + N_2$ atoms. The top panel shows the total energy of the final product relative to that of the $Cu_N$ cluster, whereas the middle panel shows the maximal internal temperature of some of the reacting clusters. Here, the labels on the right show $N_1/N$ or $N_2/N$. In the lowest panel the similarity function quantifying whether the structure of the final product of the collision resembles the structure of the global total-energy minimum for the $Cu_N$ cluster. The labels show $N$. In each panel, the solid curves represent the results for $N \le 28$ and the dashed curves those for $N \ge 38$.
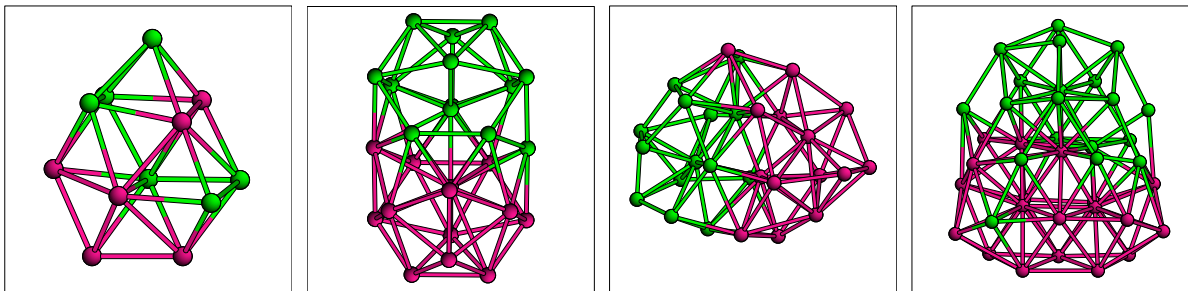
**Figure 8.3:**  The product of a $Cu_{N_1}$ + $Cu_{N_2}$ collision process for zero impact energy. From left to right: $(N_1, N_2)$ equals (6,6), (13,13), (14,14), and (19,19).

possesses the $D_{3d}$ symmetry, in contrast to the $C_1$ low-symmetrical $N_1 = N_2 = 6$ and $N_1 = N_2 = 19$ cases. On the other hand, the $N_1 = N_2 = 14$ system (with $D_2$ symmetry) contains elements of tetrahedral symmetry and can be considered a fusion product. These four systems are shown in Fig. 8.3.

Repeating the simulation for the $N_1 = N_2 = 6$ cluster, but for other relative spatial orientations, the structure of the global total-energy minimum for $Cu_{12}$ was found at impact energies of 0.038 eV/atom and higher. The formation of a dimer molecule was not observed in any of the simulations for this cluster size. On the other hand, for the $Cu_{13}$ + $Cu_{13}$ interaction at an impact energy of 0.0 eV and with aligned main axes a stable cluster dimer was formed for around 2.45 ps simulation time, at which time a final rearrangement led to the highly symmetrical product $Cu_{26}$. For the $Cu_{19}$+$Cu_{19}$ and $Cu_{14}$+$Cu_{14}$ systems short-living dimers were observed for the first 1.75 ps, and 1.4 ps of the simulations, respectively.

In Fig. 8.4 we show the $Cu_{13}Cu_{13}$ dimer structures at different stages of the simulation. After rotating one of the $Cu_{13}$ colliding clusters by a 90° angle around an axis perpendicular to the collision direction and repeating the collision, a dimer formation was not observed even at the beginning of the event, but the clusters rapidly fused resulting in a low-symmetry product. The same behavior was observed for the simulations leading to the $Cu_{28}$ and $Cu_{38}$ products. Therefore, the formation of dimers seems to be strongly dependent on the initial cluster orientation.

Calculations for colliding clusters with 4, 7, and 10 atoms all led to dimer formations at different stages of the simulations. For $Cu_7Cu_7$, the dimer existed between 0.7 ps and 2.1 ps, the $Cu_{10}Cu_{10}$ molecule lived for 1.2 ps, and, finally, the $Cu_4Cu_4$ dimer turned out to be highly stable, having a lifetime of 8.4 ps. At the end of the simulations the $Cu_4Cu_4$ system had reached the geometry of the global total-energy minimum for $N = 8$ whereas the $Cu_{14}$ and $Cu_{20}$ clusters had low-symmetry structures, corresponding to higher-lying isomers for those cluster sizes. The fact that the number of local total-energy minima grows essentially exponentially with the size of the system is most likely the explanation for why the collisions for the larger systems do not result in the structures of the global total-energy minima.

**t = 1225fs (side and top view)**



**t = 2450fs (side and top view)**
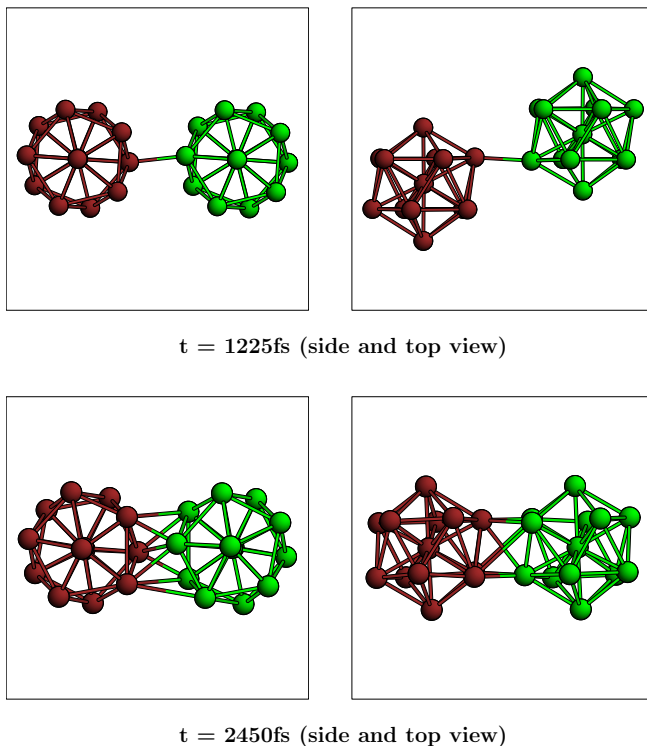
**Figure 8.4:** The formation of a $Cu_{13}Cu_{13}$ dimer.

In order to check the influence of the relative orientation of the clusters, we performed calculations on the same set of clusters but with other initial orientations of the colliding particles. The results did not indicate any dimer formation, again implying that the outcome of the collision processes depends very sensitively on all details of the process.

## 8.3   Internal temperature

One interesting issue in connection with the behavior of the colliding clusters is the variation of the internal temperatures of each cluster during the collision process. We define these as follows. For each of the two clusters we determine its center of mass,

$$\vec{R}_{0,j} = \frac{1}{N_j} \sum_{i=1}^{N_j} \vec{R}_{i,j}, \tag{8.1}$$

where $\vec{R}_{i,j}$ is the position of the $i$th atom of the $j$th cluster and $N_j$ is the number of atoms in the $j$th cluster. Subsequently, the internal temperature of the $j$th cluster, $T_j$, is defined as

$$\frac{3}{2} N_j k T_j = \frac{1}{2} m \sum_{j=1}^{N_j} \left[ |\dot{\vec{R}_{i,j}}|^2 - |\dot{\vec{R}_{0,j}}|^2 \right] \tag{8.2}$$

where $m$ is the mass of a Cu atom and the dots represent time derivatives.

The highest internal temperatures that are reached in a collision process are shown in the middle panel in Fig. 8.2, where each curve corresponds to the value for one of the two colliding clusters. The results show a clear difference between the smaller clusters with up to 9 atoms and the larger ones. For three of the four cases including smaller clusters, the temperature possesses minima at 0.038 eV/atom impact energy, which, comparing to the zero impact energy, can be explained with the lower mobility of the cluster center of masses of the latter, leading to a higher internal temperature. Moreover, except for the case of energy of 0.0 eV/atom for the smallest structures, the relation between impact energy and temperature is almost linear for all clusters. However, again the case of $N = 13$ and an impact energy of 0.3 eV/atom is different, with a particularly high maximal internal temperature. The high internal temperature suggests that the atoms are moving much, which, therefore, may result in a final structure of an unusual low total energy, cf. Fig. 8.2.

## 8.4   Structural similarity

We shall now study how the structural properties of the collision product depend on the properties of the individual properties of the colliding clusters. In particular, we shall explore whether both or at least one of the colliding clusters experience significant structural changes, i.e., whether one may talk about a 'harder' and a 'softer' cluster. To this end we shall use the concept of similarity functions.[132] These can be used also to quantify to which extent the products are more *fcc*- or *icosahedral*-like, and whether the product resembles one or the other of the two colliding clusters.

For the $Cu_{N_1}+Cu_{N_2}$ collision process we compared the final structure with the two initial structures of the non-interacting clusters. We considered all subsets of $N_1$ ($N_2$) atoms of the product cluster and compared each of those with the isolated cluster of $N_1$ ($N_2$) atoms. However, the results (not shown) did not indicate a correlation between size or impact energy on the one hand and similarity function on the other. Thus, although the total energy of the products in general decreases as a function of impact energy, cf. the upper panel in Fig. 8.2, this does not imply that the structure of the clusters gets increasingly different from those of the colliding clusters before impact.

Instead we compare the final structure of the $Cu_{N_1}+Cu_{N_2}$ collision process with the structure of the global total-energy minimum of the $Cu_N$ ($N = N_1+N_2$) cluster. One may imagine that for a larger impact energy, the atoms of the colliding clusters are so mobile that they are able to avoid getting trapped in local total-energy minima and, therefore, will be able to obtain the structure of the global total-energy minimum. Alternatively, for smaller impact energies it may be possible that the clusters do not break up into smaller fragments that are not able to relax to the structure of the global total-energy minimum. The lowest panel in Fig. 8.2 shows the results. There is at most a weak tendency for a decreasing similarity function with increasing impact energy. Moreover, the smaller clusters tend to obtain structures that are most different from those of the
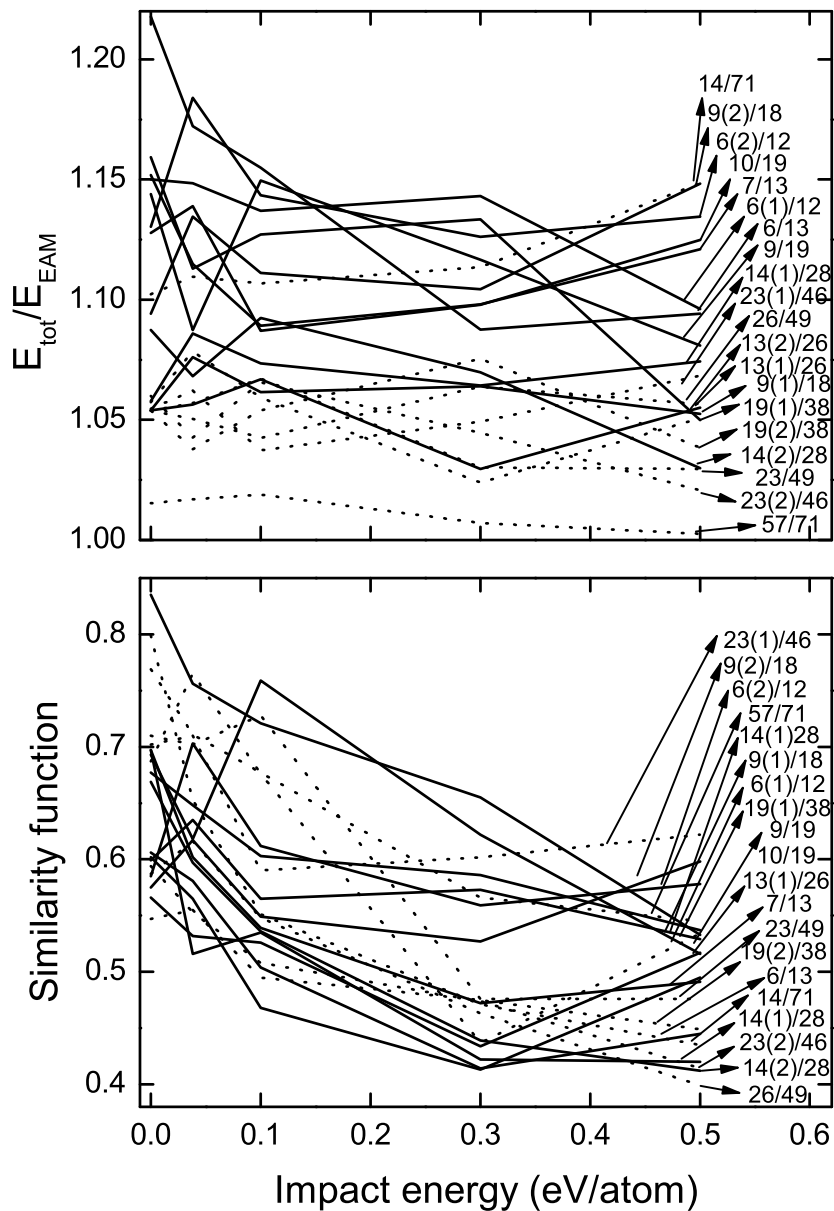
**Figure 8.5:** Various properties used in comparing the final and initial structures of the $Cu_{N_1}$ and $Cu_{N_2}$ clusters. The top panel shows the total energy of the final structures relative to that of the initial one, and in the bottom panel we compare the structures themselves using the similarity functions. For details, see the text. Moreover, the labels show $N_1/N$ or $N_2/N$ ($N = N_1 + N_2$). In each panel, the solid curves represent the results for $N \leq 28$ and the dashed curves those for $N \geq 38$.

global total-energy minima for slightly larger impact energies. The latter may surprise as one may expect that the smaller clusters are less 'rigid' so that the atoms easier can find the structure of the global total-energy minimum and, furthermore, these systems have a smaller number of total-energy minima. On the other hand, the larger clusters may contain an inner, core, part that is somewhat independent of the size of the cluster and, therefore, is identified in the clusters both before and after the collision process.

When using the similarity functions in comparing the product clusters and different *fcc* and *icosahedral* structures (not shown) fairly low values are found. This may not surprise, as also the structures of the global total-energy minima in this size range only for few special sizes (e.g., $N = 13$ for which an icosahedron is found) resemble *fcc* of *icosahedral* fragments.

We may use Eqs. (3.19) and (3.20) in analyzing the energy distribution of the final products. Eq. (3.20) allows to ascribe each atom a certain part of the total energy and by adding the contributions from the $N_1$ or $N_2$ atoms of the colliding clusters after the collision, we can split the total energy of the final structure into contributions from the two initial clusters. Finally, these can be compared with the total energies of the two clusters before they start interacting. The results are shown in the upper panel in Fig. 8.5. Since the atoms of the final structures interact with more atoms, the total energy goes down (becomes more negative), i.e., the relative total energies are in all cases above 1. Moreover, the smallest part ($N_1 = 14$) of the largest system ($N_1 + N_2 = 71$) is of that reason the system for which the relative total energy is the largest. Furthermore, the figure indicates an overall decrease in the relative total energy as a function of impact energy with some deviations for the absolutely smallest impact energies, i.e., as we have seen above the larger impact energies make the systems get trapped in energetically higher-lying structures.

Also when comparing the final structures of the $N_1$ and $N_2$ atoms with those of the initial structures (using the similarity functions above) we see, cf. the lower panel in Fig. 8.5, that in general the structures become increasingly different from the initial structures when increasing the impact energy. But from the discussion above it is clear that this change is not accompanied with a trend towards more stable final structures.

Finally, we shall study the structure and the overall shape of a collision process by varying the relative orientation of the two colliding clusters as well as the impact energy. We shall consider the single case of $N_1 = N_2 = 19$. The initial orientations of the colliding particles are shown in Fig. 8.6.

For a structure with $N$ atoms we calculate the $3 \times 3$ matrix with the components $\sum_{i=1}^{N} s_i t_i$ with $s_i$ and $t_i$ being the $x$, $y$, or $z$ component of the $i$th atom relative to the center of mass. The eigenvalues of this matrix give information on the overall shape. In particular, compact structures have a small average value and spherical systems have three identical values.

In the upper panel in Fig. 8.7 we show the results of this analysis. It is interesting to observe that for impact angles of 30° and 60° the overall shape depends only weakly on the impact energy. Moreover, situations can be identified (i.e., impact angle of 30° and impact energy of 0.3 eV/atom as well as impact angle of 60° and impact energy of
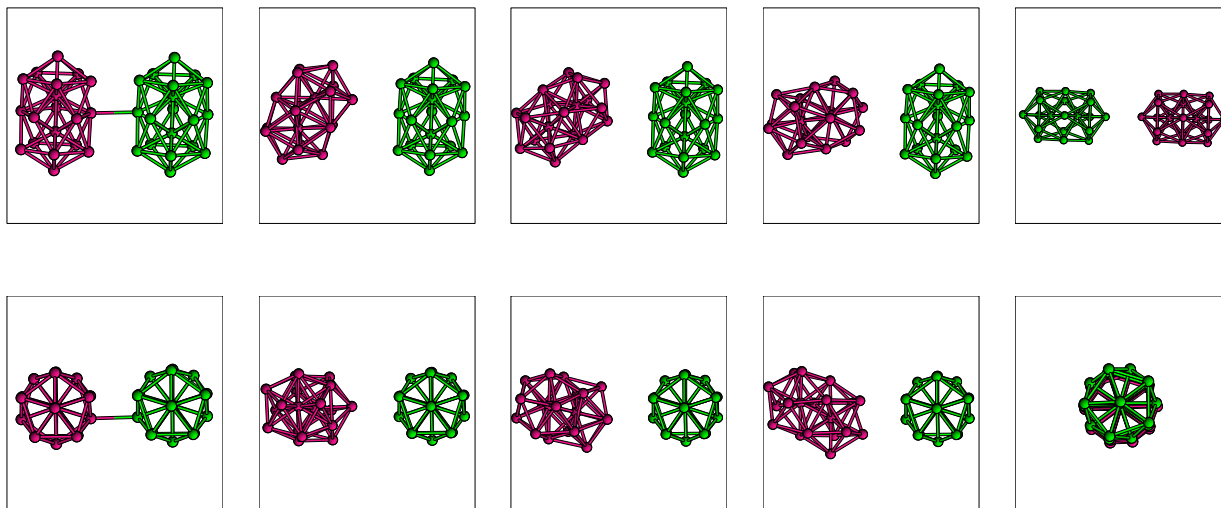
**Figure 8.6:** Side and top view of the initial orientations of the two interacting $Cu_{19}$ clusters. From left to the right the impact angle corresponds to 0, 30, 60, and 90 degrees. The configuration in which the principle axes of inertia of both clusters are aligned (right) is also considered.

0.1 eV/atom) where the product cluster is essentially spherical. On the other hand, for other impact angles (e.g. 0° and 180°) the final structure depends strongly on the impact energy.

Also when comparing the initial and final structure of the colliding clusters it becomes clear that the results depend sensitively on the impact angle. This is illustrated in the lower panel in Fig. 8.7.
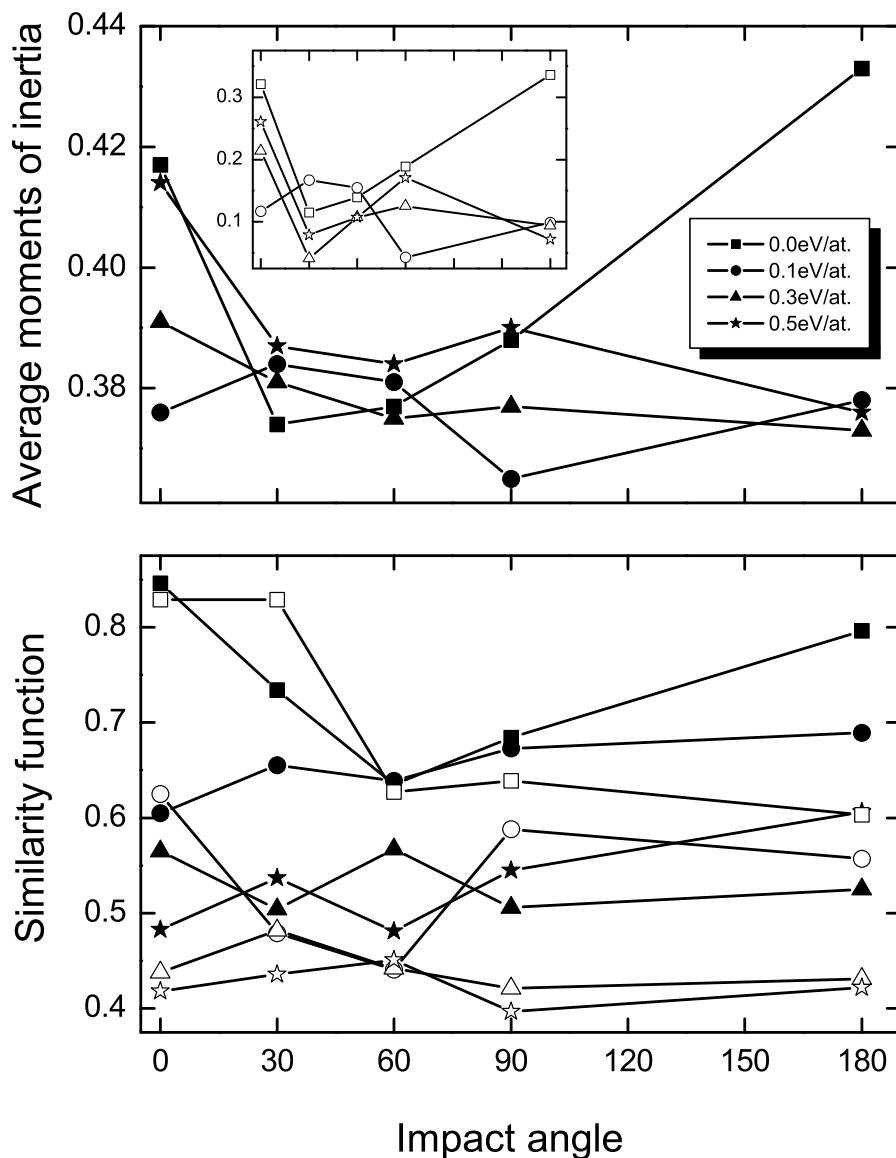
**Figure 8.7:** Various properties used in comparing the final structures of the $Cu_{19}+Cu_{19}$ collision process. The top panel shows quantities related to the overall shape. Here, the average value of the eigenvalues of the matrix containing $\sum_i s_i t_i$ is shown (for details, see the text) and the insert shows the largest difference of those. In the bottom panel the similarity function between the initial and final structures of the colliding clusters is shown. Squares, circles, triangles, and stars mark results for impact energies of 0.0, 0.1, 0.3, and 0.5 eV/atom, respectively. Here, open and closed symbols are used in distinguishing the two clusters.

# Chapter 9

# Deposition of magic clusters on Cu(111)surfaces

## 9.1    Introduction

The deposition of atomic clusters on metal surfaces has become an active field in the past decades, since it opens up new opportunities for applications in the nano- and biotechnologies.[158, 159, 160] As a consequence of the growing need for ways of depositing a cluster on a surface, new techniques like Low Energy Cluster Beam Deposition (LECBD)[161] and Ionized Cluster Beam Deposition (ICBD)[162, 163] have been developed. By using scanning tunneling microscopy (STM)[164, 165] on the deposited clusters one may obtain information on the cluster shape and stability, as well as possible coagulation of the clusters.[33]

The experimental processes can be simulated by using Monte Carlo or Molecular Dynamics calculations. Since the computational requirements for such simulations can be quite large, it is most convenient to combine the calculations with (semi-)empirical potentials for describing the interatomic interactions. Depending on the initial velocity of the clusters, one may distinguish between three different kinds of molecular dynamics simulations, which lead to different products: the soft landing[123, 166] of clusters with kinetic energy less than 1 eV/atom leads to the formation of islands on the surface and in most cases does not damage the substrate; the energetic cluster impact,[167, 168] especially when using larger clusters (some 300-3000 atoms)[169] is of importance for understanding the formation of thin films,[170, 171] and the bombardment with high-energetic clusters (from eV to some few keV per atom)[172, 173, 101] leads to crater formations, sputtering and even radiation damages.

For the applications in the microelectronics, reliable methods for the soft deposition or growth of metal clusters on different substrates are sought.[174] However, experiments can only provide information about the size and the approximate distribution of the clusters on the surface, but not on the mechanism of their deposition. It is known that when a sufficiently small cluster lands on a single-crystalline substrate, it will align epitaxic with the substrate, and as the cluster grows in size it will react more slowly due to the lowering

of the surface-to-volume ratio.

This Chapter addresses the question how fast the deposited cluster reaches epitaxy, what is the influence of the initial velocity on the rearrangement of the cluster atoms and the stability of the product on the surface, how much does the structure of the deposited cluster change, and how similar is the deposited cluster to a *fcc* or an *icosahedral* fragment. In particular, we have varied the impact energy and the size of the deposited cluster, and defined different tools for a quantitative description of our results.

## 9.2   Simulation conditions

As substrate we consider a Cu(111) fragment consisting of seven atomic layers (in the $z$ direction) with dimensions $10a_0 \times 10a_0$ ($a_0$ being the lattice constant, in this case 3.615 Å). A cutoff for the potential (4.96 Å) allows us to use a relatively thin slab, making it possible to consider a larger surface area in the two other directions. Periodic boundary conditions are applied in the $(x, y)$ plane.

For the collision processes we orient the first and the second Mackay icosahedra ($Cu_{13}$ and $Cu_{55}$) relative to the surface so that the $S_6$ axis remains perpendicular to the $(x, y)$ plane, while for the $Cu_{38}$ cluster the truncated side with the smaller surface is placed towards to the substrate.

The Newtonian equations of motion of the microcanonical ($NVE$) ensemble are integrated by using the velocity Verlet algorithm with a time step of $2 \times 10^{-15}$ s. For the smaller clusters, i.e., $Cu_{13}$, $Cu_{18}$, and $Cu_{38}$, the total integration time is 50 ps, while for the larger $Cu_{55}$ cluster the calculations are extended up to 90 ps. In the computational scheme are included 10 ps simulated annealing in order to relax the final structures to their total-energy minima. The starting velocities of the clusters correspond to 0.0, 0.1, 0.3, 0.5, 0.7, and 0.9 eV per atom, the range in which the Low Energy Cluster Beam Deposition is performed. Both the clusters and the substrates are initially relaxed to equilibrium at 0 K. Then an initial velocity in direction perpendicular to the substrate is assigned only to the cluster, whereas the substrate remains cold. It could be interesting to compare these calculations using different substrate temperatures, however, a previous study[175] has shown that increasing the temperature leads to a more rapid spreading of the cluster on the surface which is compensated by a lower degree of epitaxy due to the movements of the surface and the cluster.

## 9.3   Energetic properties

For each simulation a relaxed structure from the ones shown in Fig. 9.1 is released in the vicinity of the Cu(111) substrate with a velocity perpendicular to the surface ranging from 0.0 to 0.9 eV/atom. The kinetic energies of the cluster and the substrate grow rapidly, and for the first few hundred femtoseconds their potential energies decrease due to the attractive interactions between the atoms of the cluster and those of the surface. Later,
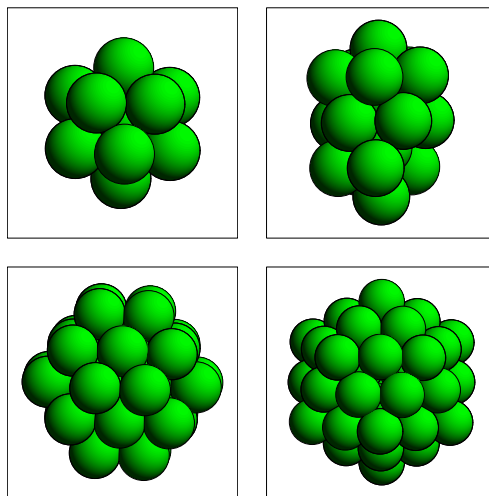
**Figure 9.1:** The optimized structures of $Cu_{13}$, $Cu_{18}$, $Cu_{38}$, and $Cu_{55}$.

when the cluster reaches the surface and begins to rearrange its atoms, the potential energy of the surface increases and ultimately the complete system reaches an equilibrium structure, which in our calculations is determined through a simulated-annealing procedure at the end of the simulation. Thereby, we model the energy uptake of a much larger surface than the one of the simulation.

## 9.3.1 Kinetic temperature

Fig. 9.3 presents the translational kinetic temperatures for various combinations of clusters and impact energies. This is calculated from the mass of the cluster and the speed of the center of mass of the cluster. We compare this temperature with that of the substrate, calculated from the kinetic energy of all the atoms forming the substrate.

In the upper left panel we show the results for the $Cu_{13}$ cluster released with zero kinetic energy in the proximity of the surface. The kinetic temperature grows rapidly during the first picoseconds and then abruptly drops, but possessing some few further peaks around $t = 10$ ps that correspond to the adsorption of the cluster on the surface. On the other hand, the kinetic temperature of the substrate reaches a maximal temperature of only 17 K, which shows that the large crystal acts well as a thermal reservoir. Already after around 20 ps the system is close to the equilibrium, and at $t = 40$ ps, the two curves have almost converged to the same temperature. As the last 10 ps constitute the simulated annealing of the system, they are not shown here. When increasing the impact energy, the time needed for the system to reach thermal equilibrium decreases, and for $Cu_{38}$ and $Cu_{55}$ the system thermalizes in only 20 ps.
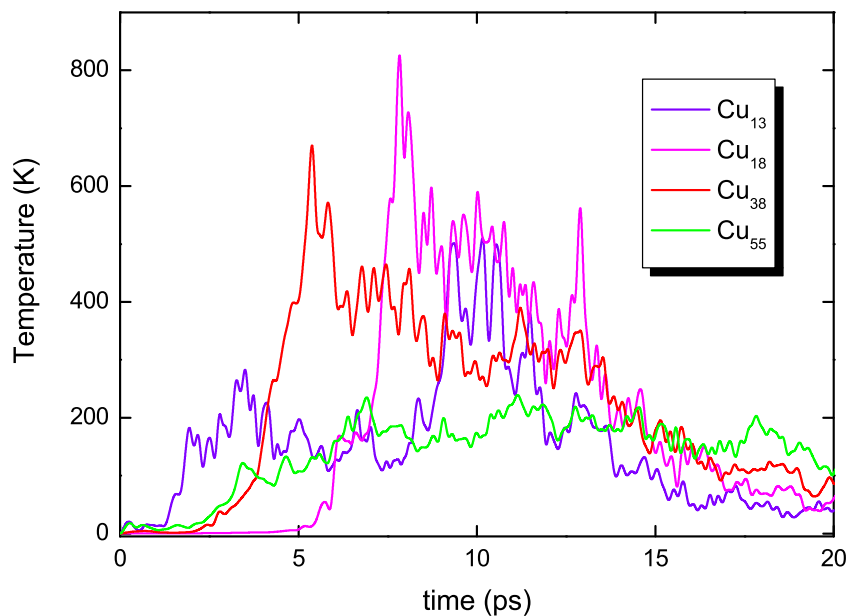
**Figure 9.2:** The internal temperatures of $Cu_{13}$, $Cu_{18}$, $Cu_{38}$, and $Cu_{55}$ at impact energy 0.0 eV/atom as functions of the time.
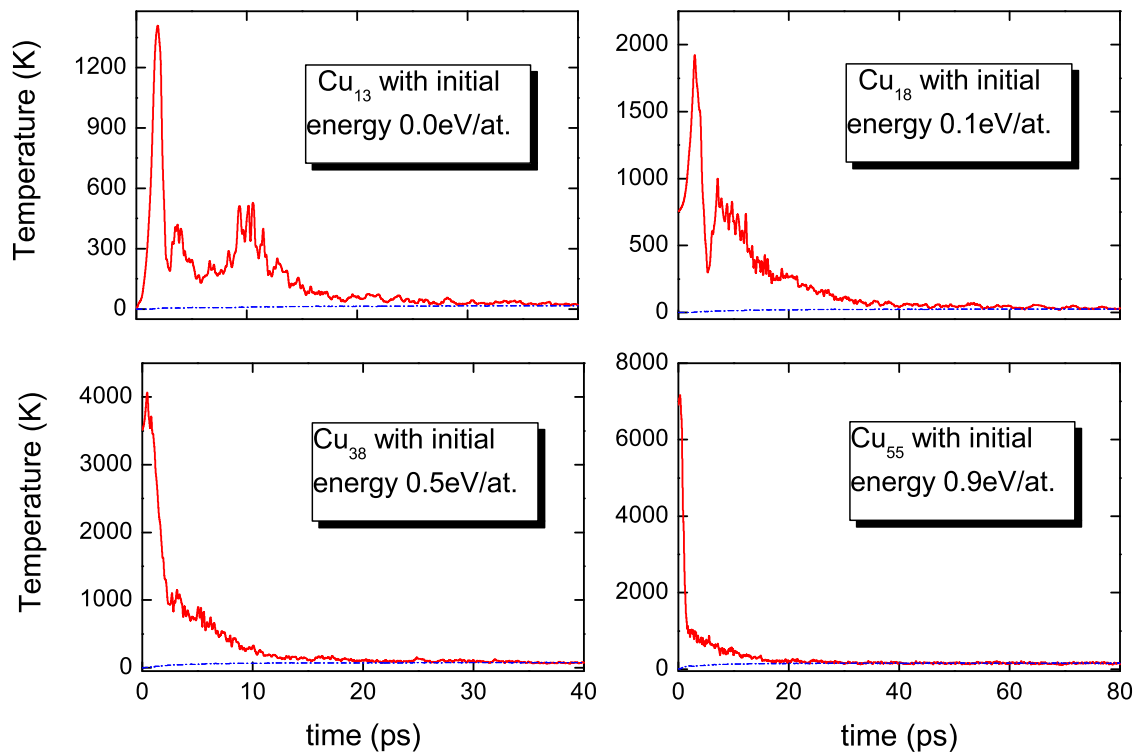


**Figure 9.3:** The translational temperatures of the $Cu_{13}$, $Cu_{18}$, $Cu_{38}$, and $Cu_{55}$ clusters and the belonging substrates at different impact energies.

### 9.3.2 Internal temperature

The translational, 'kinetic' temperature measures only the velocity of the colliding clusters, but not their internal temperatures. In Fig. 9.2 we show the evolution of the internal temperature with the cluster size in the case that the clusters are released with zero kinetic energy. The internal temperature is obtained from the velocities of the individual atoms relative to that of the center of mass. As expected, the clusters with the most fluctuating temperatures are those with smaller number of atoms, namely $Cu_{13}$ and $Cu_{18}$. The slower heating of $Cu_{18}$ compared to the $Cu_{13}$ icosahedron can be explained from the 'cigar-like' shape of the former cluster, while the icosahedron is relatively compact, and therefore most of its atoms more rapidly come into contact with the substrate. The larger clusters, $Cu_{38}$ and $Cu_{55}$, have more atoms and a smaller surface-to-volume ratio, so that the energy can be better distributed among the atoms, which results in an overall smaller heating, except for the first 5 ps for the $Cu_{38}$ octahedron. At around 15 ps all four clusters are already close to thermal equilibrium.

It is interesting to compare the total energies of the products of the different simulations, since they give information on the relative stability of the structures. Table 9.1 lists the total energies of all products together with the energies of the optimized clusters in the gas phase. In all cases, the attractive interactions between the substrate and the cluster leads to a lowering of the total energy of the cluster when being deposited on the substrate. For $Cu_{13}$ the deposition driven only by the attraction to the substrate gives the highest total energy, but increasing the deposition energy we obtain lower values with a minimum at an impact energy of 0.5 eV/atom. The situation is different for the $Cu_{18}$ cluster, where the impact energies 0.3 and 0.7 eV/atom give more stable structures. For the larger clusters with $N = 38$ and 55 the most stable structures are obtained for the lowest impact energies, with one exception for $Cu_{55}$ at an impact energy of 0.9 eV/atom.

In conclusion, the energetically more stable products of the smaller clusters are obtained with higher deposition energies, whereas lower deposition energies are used for the larger clusters.

## 9.4 Structural patterns

### 9.4.1 Monolayer formation

The final structures of the collisions of the four clusters on the substrates at different impact energies are presented in Figs. 9.4, 9.5, 9.6, and 9.7.

The shape of the $Cu_{13}$ icosahedron stays almost unchanged for the lowest impact energies. But for a deposition energy of 0.5 eV/atom the cluster spreads out on the surface forming a slightly deformed monolayer involving also two atoms from the substrate. This rearrangement of the atoms of both the substrate and the cluster is not observed for the larger deposition energies. Instead, the structure becomes a symmetrical pyramid for the impact energy equal to 0.7 eV/atom and a double layer for an energy of 0.9 eV/atom. It has been found[176] that the relatively small (i.e., 55 − 125 atoms) three-dimensional

**0eV/atom**          **0.1eV/atom**          **0.3eV/atom**

**0.5eV/atom**          **0.7eV/atom**          **0.9eV/atom**
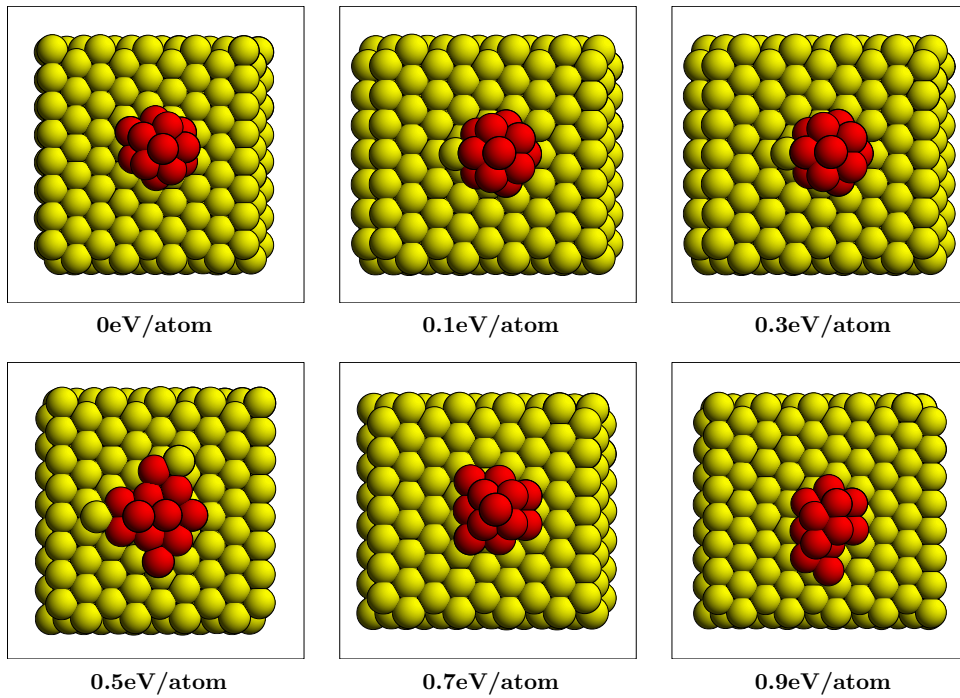
**Figure 9.4:** The final products of $Cu_{13}$ clusters with different deposition energies, colliding on substrates.



**0eV/atom**          **0.1eV/atom**          **0.3eV/atom**

**0.5eV/atom**          **0.7eV/atom**          **0.9eV/atom**
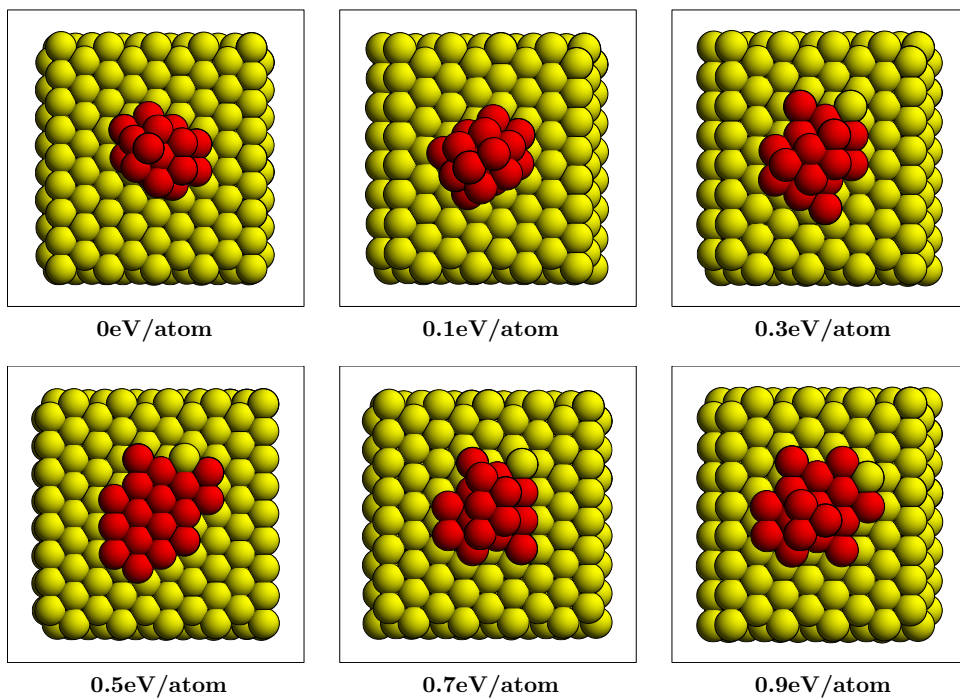
**Figure 9.5:** The same for $Cu_{18}$.
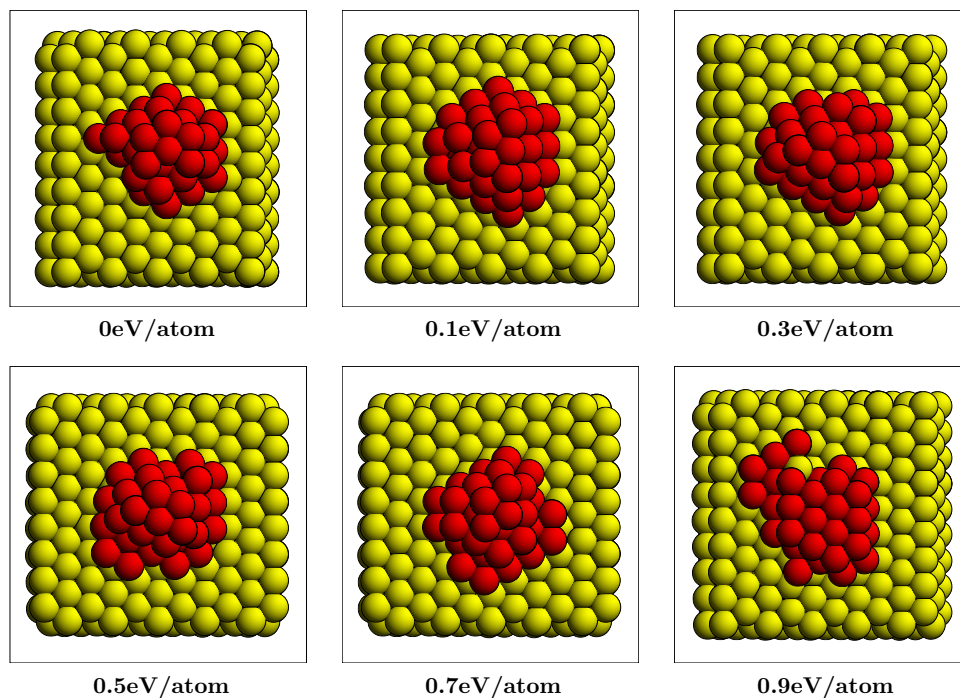
**Figure 9.6:** The final products of $Cu_{38}$ clusters with different deposition energies, colliding on substrates.
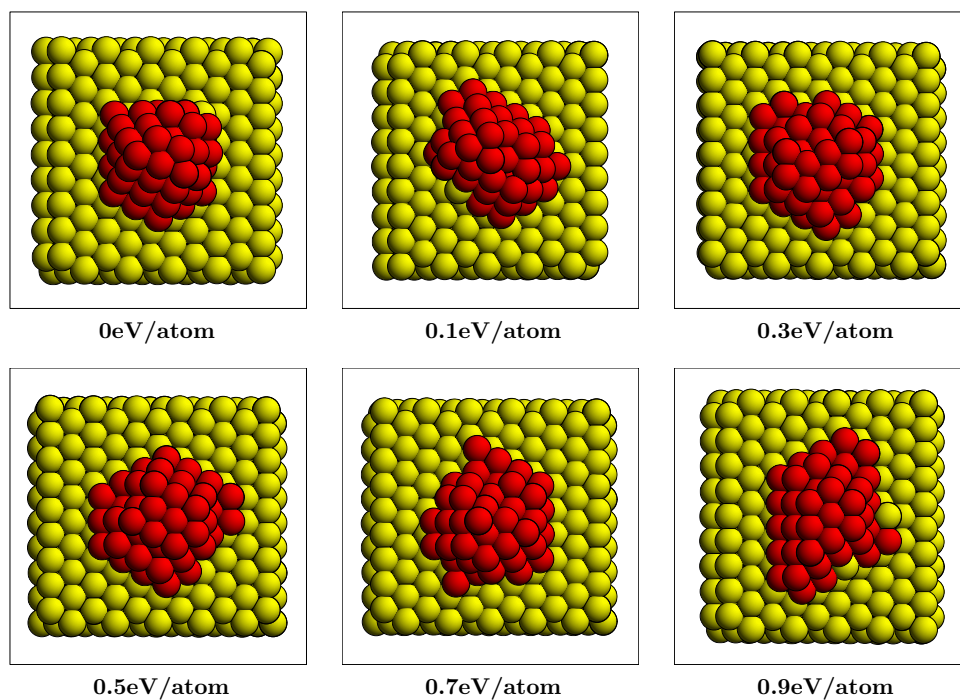


**Figure 9.7:** The same for $Cu_{55}$.

clusters tend to have the shape of a pyramid, with sides oriented in the directions of small surface energy, when being deposited on a surface.

The behavior of the $Cu_{13}$ icosahedron spreading into a monolayer at impact energy 0.5 eV/atom is also found in the simulation for the $Cu_{18}$ cluster. This cluster was chosen as the energetically most unstable, for comparison with the behavior of the magic clusters with $N = 13$, 38, and 55. Moreover, it possesses a not completely closed 'double-icosahedral' shell that becomes closed at the next cluster size, $N = 19$. In our simulations we find that the monolayer obtained at energy 0.5 eV/atom is more regular than that of $Cu_{13}$, but, in general, the behavior of this cluster is very similar to that of the icosahedron.

In contrast to the results obtained for the smaller clusters, we do not find monolayer products in the simulations with the $Cu_{38}$ and $Cu_{55}$ clusters. For $Cu_{38}$ all products consist of three layers except the one obtained with the highest initial velocity, where one atom from the cluster penetrates the surface of the substrate, but later in the simulation this atom becomes substituted by an atom from the substrate, thus giving a double-layered product. Like above, at a deposition energy of 0.7 eV/atom a symmetric product is formed, and at the highest impact energy there are substitutions with atoms from the surfaces for both cluster sizes. One interesting observation is made for the $Cu_{55}$ icosahedron for an impact energy of 0.7 eV/atom where we see the formation of a fourth layer and where also the number of atoms constituting the bottom layer of the product decreases, in comparison with the case of 0.5 eV/atom impact energy.

In total, our simulations suggest that for impact energies in the range 0.5–0.7 eV/atom one obtains products that consist of more layers or have a particularly high symmetry compared with those that are found at lower deposition energies. Hence, this impact energy range could be attractive for the production of monolayers of small clusters.

## 9.4.2   Similarity functions

In previous studies[93, 132] we have demonstrated the ability of the similarity functions to give very good qualitative and quantitative estimation of the cluster growth and the structural differences between two clusters with the same number of atoms, but structurally different.

In Table 9.2 we show the resulting functions in five cases, i.e., when comparing the products of the collisions with the initial $M_N$ clusters, with the icosahedral $Cu_{309}$, and when comparing with three fragments of the *fcc* crystal differing in the position of the center [i.e., either at the position of an atom (marked with '1'), at the middle of a nearest-neighbor bond (marked with '2'), or at the center of the cubic unit cell (marked with '3'), respectively], where from the last case only the largest value of the similarity function is shown.

The results suggest an epitaxic rearrangement of the cluster atoms on the *fcc* Cu(111) surface, since all the product clusters have values of the similarity function when comparing to *fcc* fragments that are similar or higher than those to the *icosahedral* cluster. It is not surprising that the similarity functions between the original and product structures for the larger $Cu_{38}$ and $Cu_{55}$ clusters decrease relatively smoothly when increasing the impact
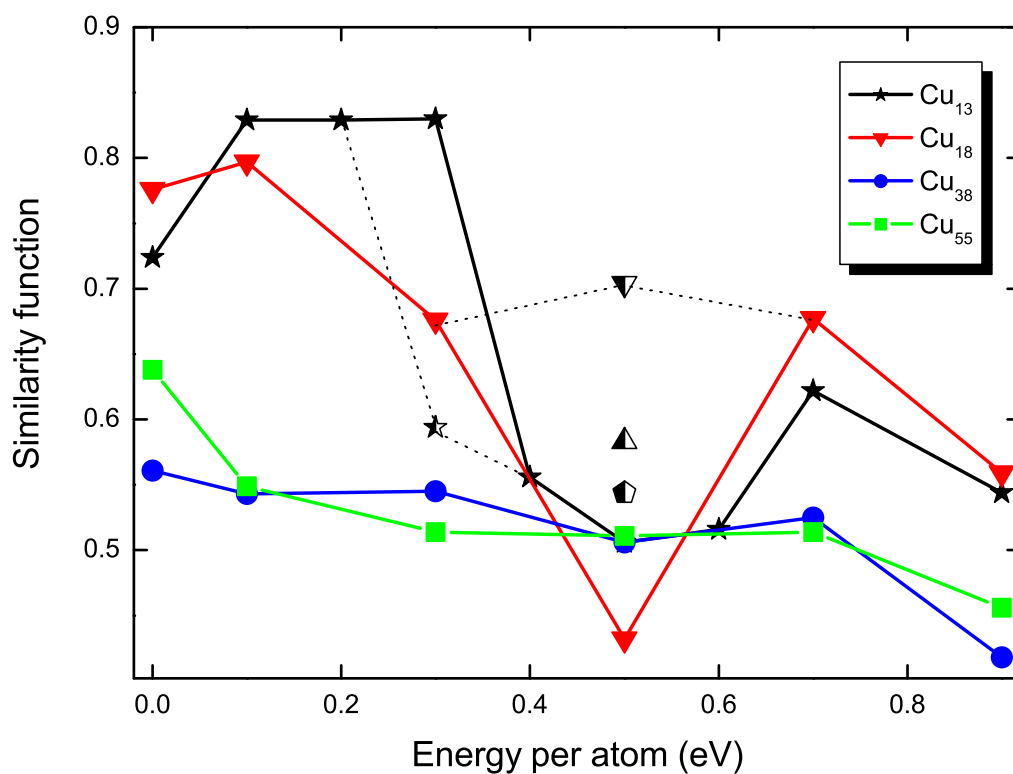
**Figure 9.8:** The similarities between the original clusters and the products at different impact energies. The half-filled star and the triangle turned upside-down correspond to the cases when the $Cu_{13}$ and $Cu_{18}$ deposited clusters were translated by 0.9 Å from their initial position in order to study the influence of the substrate-surface orientation. The half-filled pentagon and triangle at 0.5eV/atom deposition energy correspond to the final similarity functions for the rotated by 90 degrees $Cu_{13}$ and $Cu_{18}$, respectively.

**Table 9.1:** The total energy of the cluster after the collision with the surface as a function of the impact energy per atom. The results from the calculations with translated (tr.) or rotated (rot.) initial structures are also shown. The total energies of the initial structures obtained with the EAM are shown for comparison.

| Cluster | 0eV | 0.1eV | 0.3eV | 0.5eV | 0.7eV | 0.9eV | EAM |
|---------|-----|-------|-------|-------|-------|-------|-----|
| 13 | -36.66 | -37.67 | -37.67 | -37.79 | -36.80 | -36.96 | -33.50 |
| 18 | -52.02 | -51.91 | -52.89 | -52.53 | -52.79 | -52.15 | -47.47 |
| 38 | -115.04 | -115.63 | -115.54 | -114.84 | -115.16 | -114.83 | -108.62 |
| 55 | -169.79 | -169.66 | -169.49 | -169.62 | -168.48 | -170.62 | -162.62 |
| 13(tr.) | | -37.67 | -37.71 | | | | |
| 13(rot.) | | | | -36.96 | | | |
| 18(tr.) | | | | -53.29 | | | |
| 18(rot.) | | | | -52.09 | | | |

**Table 9.2:** Each panel from top to the bottom shows the similarity function when comparing with (top) the optimized with the EAM structure corresponding to this cluster size, an icosahedral cluster (middle), and a spherical fragment of the *fcc* crystal (bottom) when the center of the fragment is placed at (1) the position of an atom, (2) the middle of a nearest-neighbor bond, and (3) the center of the cube, respectively. From the latter only the highest value and its corresponding fragment are shown.

| Cluster | 0eV | 0.1eV | 0.3eV | 0.5eV | 0.7eV | 0.9eV | EAM |
|---------|-----|-------|-------|-------|-------|-------|-----|
| 13 | 0.724 | 0.829 | 0.830 | 0.506 | 0.622 | 0.544 | - |
| | 0.739 | 0.847 | 0.848 | 0.513 | 0.635 | 0.554 | 0.966 |
| | 0.741 [1] | 0.843[1] | 0.844 [1] | 0.664 [2] | 0.696 [3] | 0.679[3] | 0.858[1] |
| 18 | 0.776 | 0.797 | 0.676 | 0.432 | 0.677 | 0.559 | - |
| | 0.659 | 0.699 | 0.603 | 0.451 | 0.650 | 0.604 | 0.607 |
| | 0.725 [3] | 0.744 [1] | 0.720 [3] | 0.481 [3] | 0.721[3] | 0.611 [3] | 0.706[2] |
| 38 | 0.561 | 0.543 | 0.545 | 0.506 | 0.525 | 0.418 | - |
| | 0.570 | 0.548 | 0.549 | 0.519 | 0.530 | 0.441 | 0.656 |
| | 0.694 [2] | 0.676[2] | 0.671 [2] | 0.615 [2] | 0.632 [2] | 0.487[2] | 0.906[3] |
| 55 | 0.638 | 0.549 | 0.514 | 0.511 | 0.514 | 0.456 | - |
| | 0.648 | 0.555 | 0.518 | 0.515 | 0.519 | 0.459 | 0.963 |
| | 0.727 [2] | 0.657 [2] | 0.607 [2] | 0.604 [3] | 0.597[2] | 0.541 [3] | 0.770[1] |
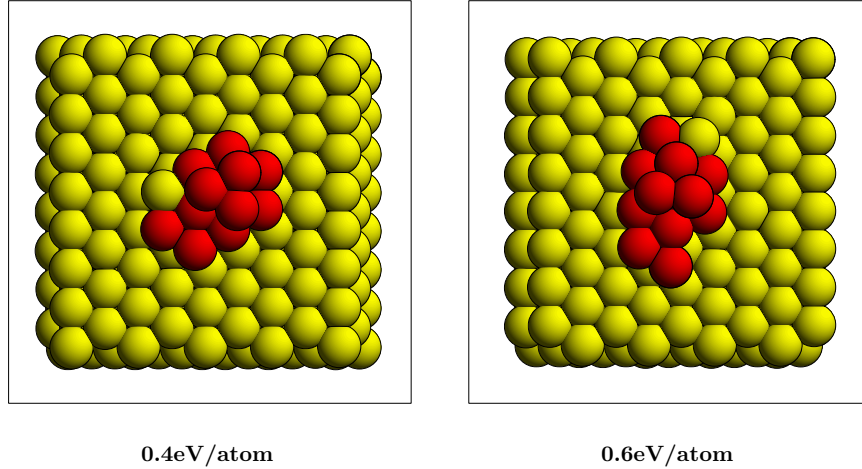
<div align="center">0.4eV/atom            0.6eV/atom</div>

**Figure 9.9:** The final products of $Cu_{13}$ clusters with deposition energies 0.4 and 0.6eV/atom.

energy. For both clusters, the 0.9 eV/atom impact energy seems to be critical and the similarity functions decrease abruptly, which corresponds to the large deformation of the clusters shown in Figs. 9.6 and 9.7. However, the small $Cu_{13}$ and $Cu_{18}$ clusters maintain high similarity to their original structures at lower impact energies, and for $Cu_{13}$ there is even an increase in the similarity for 0.1 eV/atom and 0.3 eV/atom impact energies.

The similarity functions from the structural comparison between the original and the product clusters are shown in Fig. 9.8. At energy 0.5 eV/atom the similarity functions for both the two smaller clusters have deep minima, and increase at higher impact energies. This corresponds to the formation of the monolayers on the copper substrates, as discussed above. The peaks in the similarity functions at 0.7 eV/atom can be explained with the formation of symmetrical structures, that at even higher energies not are found where, instead, flat structures occur.

In order to investigate the reasons for the increase in the similarity function for the $Cu_{13}$ cluster, we performed simulations also with impact energy 0.2, 0.4, and 0.6 eV/atom, which results are included in Fig. 9.8. The products of the collision of these clusters with Cu(111) substrates are shown in Fig. 9.9, except for the case of $Cu_{13}$ with deposition energy 0.2 eV/atom, for which the final structure is very similar to the ones obtained at energies 0.1 and 0.3 eV/atom. From the figure it can be seen that a small change in the deposition energy away from 0.5 eV/atom for $Cu_{13}$ leads to the formation of double-layered structures, and the monolayered product is found only at an energy of 0.5 eV/atom.

Subsequently, for $N = 13$ and $N = 18$ for impact energies in the range 0.1–0.3 eV we studied further collision processes where we varied either orientation of the cluster or its position on the surface both for $N = 13$ and for $N = 18$. The results are included in the figure, and it is clearly seen that the similarity function depends very sensitively on the

**Table 9.3:** The height of the cluster (in Å) after the collision with the surface as a function of the impact energy per atom. The results for the rotated/translated copper clusters are also shown.

| Cluster | 0eV | 0.1eV | 0.3eV | 0.5eV | 0.7eV | 0.9eV |
|---------|-----|-------|-------|-------|-------|-------|
| 13 | 5.365 | 5.295 | 5.349 | 3.609 | 5.564 | 4.042 |
| 18 | 5.999 | 5.980 | 4.062 | 2.061 | 3.992 | 3.943 |
| 38 | 6.331 | 5.929 | 5.626 | 5.696 | 5.734 | 4.122 |
| 55 | 8.174 | 8.049 | 6.659 | 6.652 | 8.071 | 6.443 |
| 13(tr.) |  | 5.288 | 4.103 |  |  |  |
| 13(rot.) |  |  |  | 4.078 |  |  |
| 18(tr.) |  |  |  | 4.077 |  |  |
| 18(rot.) |  |  |  | 4.209 |  |  |

details of the collision process. We propose the following explanation.

When the cluster starts interacting with the substrate, the interactions can lead to the excitation of vibrations, both of the substrate and of the cluster. If the vibrational amplitudes of the cluster are sufficiently large, the cluster may be deformed. Which vibrations are excited is also determined by the symmetry properties of the complete system, cluster+substrate. Thus, if the cluster arrives at a high-symmetry position of the surface and, in addition, so that the cluster itself shares many symmetry properties with the substrate, only few vibrations can be excited and in that case it is much less likely that the cluster is deformed through the deposition. On the other hand, a high-symmetry collision may also lead to resonances between cluster and surface which, in turn, amplify the vibration amplitudes of the cluster, so that the cluster becomes more deformed. We suggest that the results for $N = 13$ and $N = 18$ for the first, high-symmetry deposition processes can be explained through those two scenarios. For impact energies below 0.4 eV the first effect can explain our findings, whereas the second one can be held responsible for the particularly low value of the similarity function for an impact energy of 0.5 eV. When the collision process has a lower symmetry, neither effect is pronounced.

### 9.4.3   Time evolution of similarity and epitaxy

In order to get further information on the structural rearrangements of the clusters during the deposition, we shall study the temporal development of the similarity function, when comparing with the original structure. The results are presented in Fig. 9.10. Only the cases of impact energy of 0.0, 0.3, and 0.5 eV/atom are shown, since the results for higher energies are similar to those for an impact energy of 0.5 eV/atom.

The larger clusters show a more smooth structural change with the time, and form the final product faster when increasing the deposition energy. The occurrence of steps for

the lowest impact energies suggest that certain meta-stable structures have been formed during the deposition. Not so simple are the similarity functions for the smaller $Cu_{13}$ and $Cu_{18}$, where there are significant fluctuations in the values with larger periods of time. We interpret these fluctuations as indications of the large vibration amplitudes, mentioned above, that ultimately may, or may not, lead to a change in the structure of the cluster. The case of the $Cu_{18}$ cluster deposited on the surface with zero kinetic energy is interesting because the similarity function decreases smoothly at the beginning of the simulation, and rapidly drops at around 7.2 ps, when the kinetic energy of the $Cu_{18}$ cluster is around 0.038 eV/atom. This cluster has a cigar-like shape and is in our simulation deposited with the long axis perpendicular to the surface. Therefore, it takes some time after the touching of the cluster with the surface before the most distant atoms start moving.

As the last issue we shall study quantitatively whether the atoms of the deposited cluster possess a structure that is dictated by the underlying *fcc* substrate, i.e., to which extent the deposition can be classified as being epitaxic. To this end we shall introduce a parameter, the 'index of epitaxy', $I$, through

$$q = \sum_i^N |\vec{R}_i - \vec{R}_c|^2$$
$$I = \frac{1}{1 + q/u_l^2}, \tag{9.1}$$

where $|\vec{R}_i - \vec{R}_c|$ is the distance between the positions of the $i$th atom and the closest-lying fictitious atom in the infinite, periodic crystal that is obtained by continuing the structure of the substrate periodically. $I = 1$ if perfect epitaxy is obtained.

The results are shown in Fig. 9.11 for three different impact energies of the clusters. The calculations for the $Cu_{55}$ clusters were expanded over a longer period of time. It is surprising that an increased impact energy does not necessarily lead to an increased value of $I$. Moreover, the fact that in most cases $I$ is well below 1 implies that the interatomic forces within the clusters are sufficiently strong to influence the final structure of the clusters significantly. Among all simulations only the $Cu_{18}$ cluster for an impact energy of 0.5 eV/atom achieves a high epitaxy index which can be related to its monolayered arrangement on the surface.

The height of the product clusters as a function of the deposition energy is shown in Table 9.3. It can be seen that at a deposition energy 0.5 eV/atom there is a minimum in the height of the clusters, except for the $Cu_{38}$ cluster that has the same height also for an impact energy of 0.3 eV/atom. This fact suggests once again that the deposition energy of 0.5 eV/atom could be favorable for the production of monolayers.
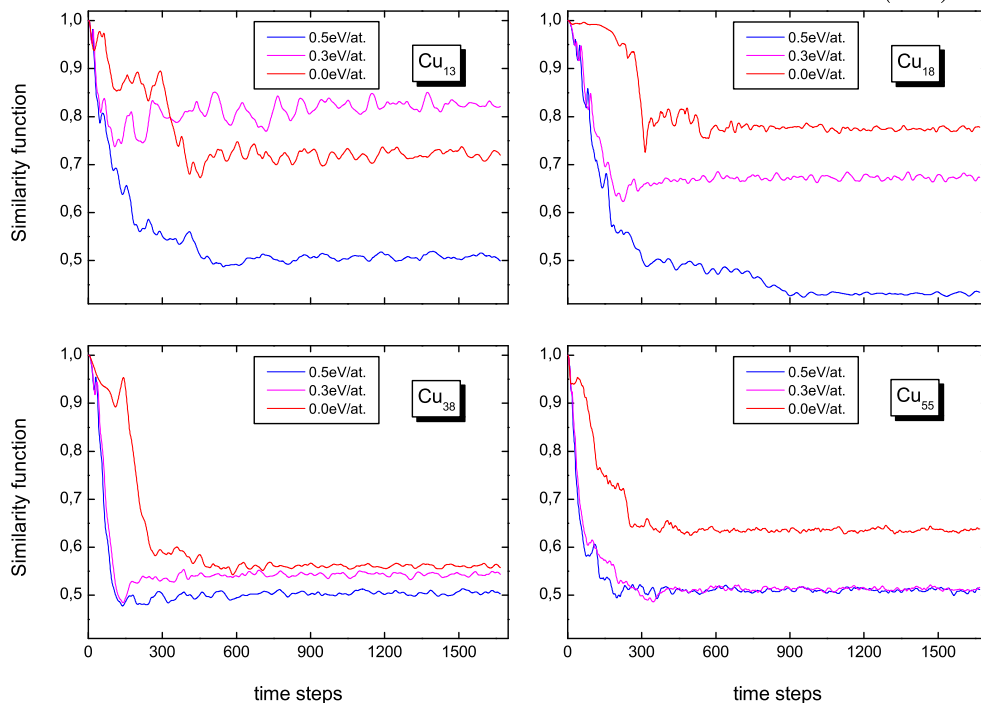
**Figure 9.10:** The evolution of the similarity functions with the time for the simulations with cluster energies of 0.0, 0.3, and 0.5eV/atom. The similarity functions corresponding to energy 0.0eV are solid lines, the ones for 0.3 and 0.5eV/atom are dot-dashed, and dotted lines, respectively.
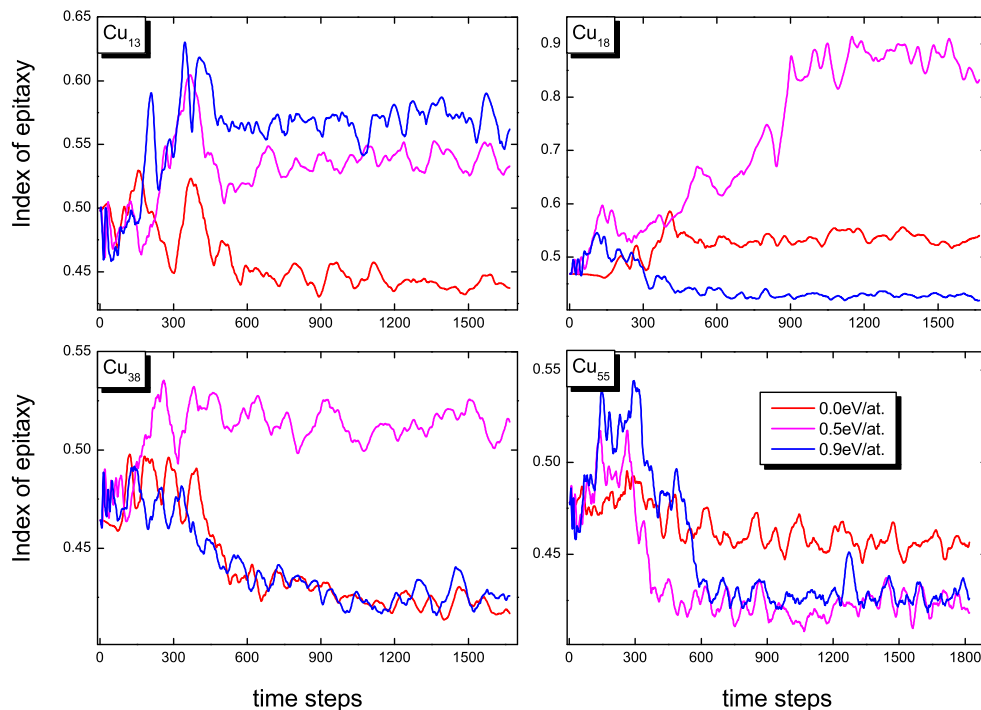


**Figure 9.11:** The evolution of the index of epitaxy with the time for the simulations with cluster energies of 0.0, 0.5, and 0.9eV/atom.

# Chapter 10

# Summary and Conclusions

In the present work we have investigated structural and energetic properties of different transition and noble metal clusters. The global optimization of the isolated particles was carried out using our *Random*, *Aufbau/Abbau*, and *Disturbance* algorithms in combination with the *variable metric/quasi-Newton* method.

Within this formalism, using the EAM potential as developed by Voter and Chen for the expressions of the total energy and forces, we have determined the three energetically lowest isomers of gold clusters in the range $2 \leq N \leq 150$. Although the calculations provide a large amount of information for each individual cluster, instead of discussing each cluster separately, we focused on identifying general trends such as total energy per atom, overall symmetry and shape, average bond length and coordination number, similarity with $N-1$-atom clusters, vibrational spectra and heat capacities.

The version of EAM used in these calculations is parameterized to bulk, as well as to the dimer properties, which allows it to describe properly the properties of the smaller gold clusters. We have performed[90] calculations on smaller gold clusters with $2 \leq N \leq 60$ atoms comparing the EAM of Daw, Baskes, and Foiles (DBF) and the version used in this work, and we found that the DBF overestimated the binding energy of the dimer by 209% and underestimated the bond distance by 37%. For comparison, the EAM of Voter and Chen gives dimer binding energy corresponding to 99,6% of the experimental, and bond distance that is 92,2% of the experimental value. Therefore, we decided to expand our studies by applying the Voter-Chen version of the EAM method.

The calculations predicted a number of particularly stable clusters, i.e., 'magic-numbered' clusters that in many cases are in agreement with results obtained by first principles and other semiempirical studies when such exist, but the advantage of our study is that the structures were obtained by using a completely unbiased approach. These magic numbers were clearly visible both in the 'stability function' and in the total-energy difference between the energetically lowest and higher-lying isomers.

We also found that even for our largest cluster the binding energy per atom has still not converged to the bulk limit. Similarly, the average coordination number is far from the bulk value, but higher than for nickel clusters, where several structures with shell constructions and corresponding low coordination numbers were formed [93]. The

average bond distance for gold has not reached the bulk value, due to the rearrangement of the atoms for each cluster size that leads to the formation of very compact structures.

The shape analysis showed that roughly spherical clusters corresponded mainly to the energetically lowest isomer, but in some cases also to the second-lowest one, and that these often belong to particularly stable structures.

By analysing the distribution of radial distances as a function of the cluster size we could identify a region with $N$ around 55, where a shell construction was formed. Comparing to previous results for nickel clusters [93], where clear shell constructions were formed at $N$ around 13, 55, and 147, here the atoms rearrange for each global minimum, and therefore particular shell constructions can not be observed. The similarity function also points to the lack of regular growth.

The most central results are the calculated vibrational spectra and heat capacities. Many of the "magic" clusters, identified with the stability function, have particularly high or low vibrational frequencies or heat capacities, respectively. The $Au_{19}$ cluster possesses the highest vibrational frequency among all cluster sizes, and the second lowest heat capacity in the size range $16 \leq N \leq 150$. The vibrational spectra and the heat capacities appear to oscillate with the cluster size without tendencies to form "islands" at which typical vibrations could take place, which is the case for copper and nickel clusters[177]. It seems that the word "disordered" describes most accurately the growth of the smallest gold particles.

For the silver clusters with up to 150 atoms we chose to use two different many-body Gupta potentials for the evaluation of the energy and forces. According to numerous previous studies, the Gupta potential has been successfully applied to metal clusters. However, for silver we were able to find only one work, which considered particular cluster sizes. For those cluster sizes, our minima are completely consistent with the results obtained in Ref[84]. Up to 60 atoms, an energetical and structural comparison was made to our independent results from two Embedded Atom Method approaches. Although the small silver clusters obtained with all potentials are very similar, significant structural differences occur already at $Ag_{15}$. The potential that predicts the structures most similar to the obtained with the extended Gupta potential is not the tight-binding Gupta approach, but the EAM of Daw, Baskes, and Foiles. Along with the peaks for the magic $N = 13$, 38, 55, and 147 clusters, many new peaks appear, all of them except for the $Ag_{63}$ and $Ag_{79}$ clusters revealing decahedral structures, the ground state of $Ag_{63}$ having a distorted icosahedral configuration. The peaks corresponding to the particular stability of $Ag_N$ with $N = 23$, 28, and 137 atoms are missing, in contrast to previously studied nickel[93] and copper[132] structures. The similarity functions and the minimal coordination numbers show complicated growth, especially at $N = 31 - 42$, $N = 62$, 80, 97, 117 and 140 atoms, where significant structural changes take place. The cluster growth is predominantly decahedral, e.g., in the size range 65 - 139 atoms, with islands of icosahedral and *fcc* structures, in contrast to the results for copper and nickel clusters, where the main structural motif is the icosahedral construction.

The comparison to the experimental scattering intensities unambiguously shows that icosahedral structures lie in the global minima or are degenerate with it, however, three

out of the six experimentally suggested systems could not be described properly by the $n$G potential, which predicts the octahedral $Ag_{38}$ and $Ag_{79}$ clusters and the 75-atom Mark decahedron to lie in the ground state for those cluster sizes. The latter one could not be unequivocally excluded as a potential candidate, which could lead to a ground state containing a mixture of decahedral and icosahedral isomers. Regarding the $Ag_{38}$ and $Ag_{79}$ clusters, we suppose that the parameterization of the Gupta potential leads to a preference of compact structures such as the octahedral ones. The experimental data was obtained using cationic silver clusters that can have different global minima geometries than the neutral clusters optimized in this work. However, the unbiased structure optimization of many candidate configurations is still computationally infeasible for the density functional methods, and only by using semiempirical potentials one can select prospective candidates lying close to the global minima.

In order to compare the results from the EAM and Gupta potentials used in this work we performed also unbiased structure optimization of Ni, Cu, and Au clusters with up to 60 atoms using the two EAM potentials and the second-moment approximated Gupta potential. Regarding the binding energies, the best agreement between the three potentials was found for copper, and the poorest for nickel, with the Voter-Chen potential giving the most reasonable results. As expected, the corresponding differences between the binding energies obtained with the different potentials were most insignificant at the copper clusters, while for the smallest gold clusters they reached deviations of about 1.2eV/atom. Again, the copper clusters optimized with the three potentials are structurally most similar except for some cluster sizes, where the global minima obtained with one potential corresponded to higher-energy isomers according to other potential, and vice versa. The similarity functions for nickel and gold reveal significant structural differences, especially pronounced for the gold clusters, where there are more differences than similarities, as also suggested by the point groups of the global minima. We found that the sequence of magic numbers is very similar for Ni and Cu clusters, but markedly different for gold, where each potential predicts different magic clusters, and the only one agreement between the three potentials is that the clusters with $N = 19, 23, 38, 46, 49$, and 55 atoms are not particularly stable in contrast to the results for copper and nickel. Similar trend has been obtained with the Sutton-Chen potential[78]. In accordance with these results, the distribution of radial distances clearly shows the formation of large icosahedral windows ending at the complete second Mackay icosahedron at $N = 55$ for nickel and copper, while for gold the distribution is more scattered, with a small shell for the icosahedral $Au_{54}$ within the Voter-Chen potential, while the global minima for $Au_{55}$ obtained with all potentials point to a low-symmetry structure, in agreement with previous theoretical and experimental studies. It is very clear that the structures of $Au_N$ clusters depend critically on the used potential which may be an explanation for the large scattering in the results that have been obtained for this system. On the other hand, the weak sensitivity of the results for copper clusters on the potential makes us propose that this may be a more general property for those systems, i.e., also other theoretical approaches should give results that only differ little from those presented here. Finally, whereas both EAM potentials gave realistic results for Ni and Cu, only the VC parameterization was considered useful

for Au.

The next issue in the present work was to investigate the cluster deposition on a surface. This has become a subject of interest for many experimentalists and theoreticians over the past 20 years. In order to be able to follow the processes occurring from the cluster generation in the *Low Energy Cluster Beam* up to the cooling onto the substrate surface, we developed a Molecular Dynamics program working with a constant-energy ensemble. The program was successfully tested on copper clusters described with the Voter-Chen potential.

We have studied collision processes between smaller copper clusters at different impact energies in order to find possible relations between the initial energies and the energetic and structural stability of the products. A main finding of the computations is that with increasing impact energy the final products of the $Cu_{N_1} + Cu_{N_2}$ collision become increasingly different from the structure of the global total-energy minimum of the $Cu_N$ ($N = N_1 + N_2$) cluster. The maximal internal temperature showed an essentially linear dependence on the impact energy, i.e., the atoms become increasingly mobile, which most likely is the reason for why the final structures of the collision processes depend sensitively on all parameters of the collision process, i.e., size of the clusters, impact energy, relative orientation, and impact parameter. We have demonstrated this with the exception of the dependence on the impact parameter that was not varied.

A further outcome of the calculations was the prediction of the possible formation of the cluster molecules $Cu_4Cu_4$, $Cu_7Cu_7$, $Cu_{10}Cu_{10}$, $Cu_{13}Cu_{13}$, $Cu_{14}Cu_{14}$, and $Cu_{19}Cu_{19}$ similar to the earlier findings for sodium clusters.[149] In all cases we have studied, the stability of the cluster molecules (including their lifetime) shows a strong dependence on the initial orientation of the clusters. For larger impact energies dimer formation was not observed. The structural comparison between the product clusters and different *fcc* and *icosahedral* structures shows that all collision products have only marginal similarity with *fcc*-like and *icosahedral*-like structures. In total, our results show that even at extremely well-defined experimental conditions, cluster-cluster collision experiments should be expected to lead to a broad spectrum of resulting structures. The most stable structures are obtained for low, although not almost vanishing, impact energies.

Then the clusters were deposited onto Cu(111) surfaces previously relaxed with the EAM potential. The source $Cu_N$ clusters ($N = 13, 18, 38,$ and $55$) were taken from our previous calculations with the Voter-Chen potential described in Chapter 6, and corresponded to the global minima for these cluster sizes according to the used potential. The reason we chose these clusters is that we wanted to compare the deposition behavior of particularly stable particles such as the first and second Mackay icosahedra, and the octahedral $Cu_{38}$ to that of a particularly unstable structure, such as the incomplete double icosahedron $Cu_{18}$. The main issue was the relation between deposition energy of the cluster and the structural and energetic characteristics of the products. As shown in Table 9.1, a higher impact energy leads to a lower total energy of the complete system, which first of all is due to an increased interaction energy between substrate and cluster, and not to a cluster structure of larger stability. The larger clusters reach rapidly and smoothly the thermal equilibrium at higher impact energies, while for the small $Cu_{13}$ and $Cu_{18}$ clusters

there are many secondary peaks in the kinetic temperatures at low energies. The slower increase in the internal temperature of the $Cu_{18}$ cluster could be related to its 'cigar-like' shape with the long axis perpendicular to the surface. The smaller clusters reach higher maxima in their internal temperatures in comparison to the larger $Cu_{55}$ structure, which is due to the smaller number of atoms and their increased mobility, respectively. However, the surface heats very smoothly, without fluctuations, to constant temperatures during the simulations, which shows that it successfully acts as a thermal reservoir.

Another important issue, is the problem how similar are the original and the product clusters at different deposition energies, and how these similarity functions propagate with the time. A structural descriptor, similar to one of those used in this study, was previously introduced by Palacios *et al.*[175] It is remarkable that the deposited clusters have values of this function that indicate a significant structural rearrangement, so that even softly deposited clusters change their structure markedly from the ones in the gas phase.

Through these descriptors we are able to formulate our main conclusion: Clusters deposited on surface, even at low impact energies, are not simply gas-phase clusters on a substrate, but form a different system consisting of both cluster and substrate. The structure of this system depends very sensitively on all parameters of the deposition process, i.e., cluster size, impact energy, relative orientation, and relative position.

Further insight into the structure and dynamics of these small particles can provide the modification of the existing software in order to describe deposition of homoatomic and/or bimetallic clusters on diverse (non)metallic substrates.

# Bibliography

[1] M. S. Daw and M. I. Baskes, Phys. Rev. Lett. **50**, 1285 (1983).

[2] M. S. Daw and M. I. Baskes, Phys. Rev. B **29**, 6443 (1984).

[3] S. M. Foiles, M. I. Baskes, and M. S. Daw, Phys. Rev. B **33**, 7983 (1986).

[4] M. J. Stott and E. Zaremba, *Phys. Rev. B*, **22**, 1564, (1980)

[5] J. H. Rose, J. R. Smith, F. Guinea, *Phys. Rev. B*, **29**, 2963, (1984)

[6] Internet address: 146.246.250.1

[7] A. F. Voter and S. P. Chen, in *Characterization of Defects in Materials*, edited by R. W. Siegal, J. R. Weertman, and R. Sinclair, MRS Symposia Proceedings No. 82 (Materials Research Society, Pittsburgh, 1987), p. 175.

[8] A. Voter, Los Alamos Unclassified Technical Report No LA-UR 93-3901 (1993).

[9] A. F. Voter, in *Intermetallic Compounds*, edited by J. H. Westbrook and R. L. Fleischer (John Wiley and Sons, Ltd, 1995), Vol. 1, p. 77.

[10] A. F. Voter, private communication.

[11] R. P. Gupta, Phys. Rev. B **23**, 6265 (1981).

[12] V. Rosato, M. Guilope, and B. Legrand, Philos. Mag. A **59**, 321 (1989).

[13] F. Cleri and V. Rosato, Phys. Rev. B **48**, 22 (1993).

[14] W. H. Press, S. A. Teukolsky, W. T. Vetterling, B. P. Flannery, in *Numerical Recipes in FORTRAN: the Art of Scientific Computing*, (Cambridge University Press, Cambridge, 1992), p. 387.

[15] P. Pyykkö, Angew. Chem. Int. Ed. **43**, 4412 (2004).

[16] F. Baletto and R. Ferrando, Rev. Mod. Phys. **77**, 371 (2005).

[17] R. L. Whetten, J. T. Khoury, M. M. Alvarez, S. Murthy, I. Vezmar, Z. L. Wang, P. W. Stephens, C. L. Cleveland, W. D. Luedtke, and U. Landman, Adv. Mater. **8**, 428 (1996).

[18] A. Sanchez, S. Abbet, U. Heiz, W. -D. Schneider, H. Häkkinen, R. N. Barnett, and U. Landman, J. Phys. Chem. A **103**, 9573 (1999).

[19] H. Häkkinen, S. Abbet, A. Sanchez, U. Heiz, and U. Landman, Angew. Chem. Int. Ed. **42**, 1297 (2003).

[20] L. D. Socaciu, J. Hagen, T. M. Bernhardt, L. Wöste, U. Heiz, H. Häkkinen, and U. Landman, J. Am. Chem. Soc. **125**, 10437 (2003).

[21] U. Heiz and E. L. Bullock, J. Mater. Chem. **14**, 564 (2004).

[22] K. J. Taylor, C. L. Pettiette-Hall, O. Cheshnovsky, and R. E. Smalley, J. Chem. Phys. **96**, 4 (1992).

[23] H. Handschuh, G. Ganteför, P. S. Bechthold, and W. Eberhardt, J. Chem. Phys. **100**, 7093 (1994).

[24] A. Pinto, A. R. Pennisi, G. Faraci, G. D'Agostino, S. Mobilio, and F. Boscherini, Phys. Rev. B **51**, 5315 (1995).

[25] M. M. Alvarez, J. T. Khoury, T. G. Schaaff, M. Shafigullin, I. Vezmar, and R. L. Whetten, Chem. Phys. Lett. **266**, 91 (1997).

[26] T. G. Schaaff, M. N. Schafigullin, J. T. Khoury, I. Vezmar, R. L. Whetten, W. G. Cullen, P. N. First, C. Gutiérrez-Wing, J. Ascensio, and M. J. Jose-Yacamán, J. Phys. Chem. B **101**, 7885 (1997).

[27] C. L. Cleveland, U. Landman, M. N. Shafigullin, P. W. Stephens, and R. L. Whetten, Z. Phys. D **40**, 503 (1997).

[28] K. Koga, H. Takeo, T. Ikeda, and K. Ohshima, Phys. Rev. B **57**, 4053 (1998).

[29] B. Palpant, B. Prével, J. Lermé, E. Cottancin, M. Pellarin, M. Treilleux, A. Perez, J. L. Vialle, and M. Broyer, Phys. Rev. B **57**, 1963 (1998).

[30] L. E. Harrell, T. P. Bigioni, W. G. Cullen, R. L. Whetten, and P. N. First, J. Vac. Sci. Technol. B **17**, 2411 (1999).

[31] V. A. Spasov, Y. Shi, and K. M. Ervin, Chem. Phys. **262**, 75 (2000).

[32] M. Vogel, K. Hansen, A. Herlert, and L. Schweikhard, Eur. Phys. J. D **16**, 73 (2001).

[33] N. Vandamme, G. Verschoren, A. Depuydt, M. Cannaerts, W. Bouwen, P. Lievens, R. E. Silverans, C. V. Haesendonck, Appl. Phys. A **72**, 177 (2001).

[34] H. Hövel, Appl. Phys. A **72**, 295 (2001).

[35] V. Torma, O. Vidoni, U. Simon, and G. Schmid, Eur. J. Inorg. Chem. 1121 (2003).

[36] R. Salvati, A. Longo, G. Carotenuto, L. Nicolais, S. De Nicola, and G. P. Pepe, Eur. Phys. J. B **41**, 43 (2004).

[37] G. Mills, B. Wang, W. Ho, and H. Metiu, J. Chem. Phys. **120**, 7738 (2004).

[38] B. K. Min, W. T. Wallace, A. K. Santra, and D. W. Goodman, J. Phys. Chem. B **108**, 16339 (2004).

[39] H. Häkkinen, M. Moseler, O. Kostko, N. Morgner, M. A. Hoffmann, and B. v. Issendorff, Phys. Rev. Lett. **93**, 093401 (2004).

[40] J. M. Seminario and J. M. Tour, Int. J. Quant. Chem. **65**, 749 (1997).

[41] L. Lamare and F. Michel-Calendini, Int. J. Quant. Chem. **61**, 635 (1997).

[42] O. D. Häberlen, S. - C. Chung, M. Stener, and N. Rösch, J. Chem. Phys. **106**, 5189 (1997).

[43] G. Bravo-Pérez, I. L. Garzón, and O. Novaro, J. Mol. Str. (Theochem) **493**, 225 (1999).

[44] H. Häkkinen, R. N. Barnett, and U. Landman, Phys. Rev. Lett. **82**, 3264 (1999).

[45] H. Grönbeck and W. Andreoni, Chem. Phys. **262**, 1 (2000).

[46] H. Häkkinen and U. Landman, Phys. Rev. B **62**, 2287(R) (2000).

[47] J. M. Soler, M. R. Beltrán, K. Michaelian, I. L. Garzón, P. Ordejón, D. Sánchez-Portal, and E. Artacho, Phys. Rev. B **61**, 5771 (2000).

[48] H. Häkkinen, M. Moseler, and U. Landman, Phys. Rev. Lett. **89**, 033401 (2002).

[49] J. Olviedo and R. E. Palmer, J. Chem. Phys. **117**, 9548 (2002).

[50] J. Wang, G. Wang, and J. Zhao, Phys. Rev. B **66**, 035418 (2002).

[51] J. Wang, G. Wang, and J. Zhao, Chem. Phys. Lett. **380**, 716 (2003).

[52] J. Zhao, J. Wang, and J. G. Hou, Phys. Rev. B **67**, 085404 (2003).

[53] B. Yoon, H. Häkkinen, and U. Landman, J. Phys. Chem. A **107**, 4066 (2003).

[54] M. P. Johansson, D. Sundholm, and J. Vaara, Angew. Chem. Int. Ed. **43**, 2678 (2004).

[55] S. Chrétien, M. S. Gordon, H. Metiu, J. Chem. Phys. **121**, 3756 (2004).

[56] R. M. Olson, S. Varganov, M. S. Gordon, H. Metiu, S. Chretien, P. Piecuch, K. Kowalski, S. A. Kucharski, and M. Musia, J. Am. Chem. Soc. **127**, 1049 (2005).

[57] L. Xiao and L. Wang, Chem. Phys. Lett. **392**, 452 (2004).

[58] A. V. Walker, J. Chem. Phys. **122**, 094310 (2005).

[59] F. Remacle and E. S. Kryachko, J. Chem. Phys. **122**, 044304 (2005).

[60] H. Häkkinen, B. Yoon, U. Landman, X. Li, H.-J. Zhai, and L.-S. Wang, J. Phys. Chem. A **107**, 6168 (2003).

[61] S. Gilb, P. Weis, F. Furche, R. Ahlrichs, and M. M. Kappes, J. Chem. Phys. **116**, 4094 (2002).

[62] F. Furche, R. Ahlrichs, P. Weis, C. Jacob, S. Gilb, T. Bierweiler, and M. M. Kappes, J. Chem. Phys. **117**, 6982 (2002).

[63] M. Neumaier, F. Weigend, and O. Hampe, J. Chem. Phys. **122**, 104702 (2005).

[64] F. Ercolessi, W. Andreoni, and E. Tosatti, Phys. Rev. Lett. **66**, 911 (1991).

[65] H. Arslan and M. H. Güven, Springer-Verlag, ARI (1998) **51**, 145

[66] W. D. Luedtke and U. Landman, J. Phys. Chem. B **102**, 6566 (1998).

[67] C. L. Cleveland, W. D. Luedtke, and U. Landman, Phys. Rev. Lett. **81**, 2036 (1998).

[68] C. L. Cleveland, W. D. Luedtke, and U. Landman, Phys. Rev. B **60**, 5065 (1999).

[69] Y. Chushak and L. S. Bartell, Eur. Phys. J. D **16**, 43 (2001).

[70] S. M. Paik, S. M. Yoo, M. Namkung, and R. A. Wincheski, NASA/CR-2001-211014, ICASE Report No. 2001-17

[71] S. -C. Lee, K. -R. Lee, J. -G. Lee, and N. M. Hwang, Nanotech Vol. 2 (2002).

[72] F. Baletto, R. Ferrando, A. Fortunelli, F. Montalenti, C. Mottet, J. Chem. Phys. **116**, 3856 (2002).

[73] J. Rogan, R. Ramírez, A. H. Romero, and M. Kiwi, Eur. Phys. J. D **28**, 219 (2004).

[74] U. Landman and W. D. Luedtke, Faraday Discuss. **125**, 1 (2004).

[75] Y. Wang, S. Teitel, and C. Dellago, J. Chem. Phys. **122**, 214722 (2005).

[76] C. L. Cleveland, U. Landman, T. G. Schaaff, M. N. Shafigullin, P. W. Stephens, and R. L. Whetten, Phys. Rev. Lett. **79**, 1873 (1997).

[77] R. N. Barnett, C. L. Cleveland, H. Häkkinen, W. D. Luedtke, C. Yannouleas, and U. Landman, Eur. Phys. J. D **9**, 95 (1999).

[78] J. P. K. Doye and D. J. Wales, New J. Chem. **22**, 733 (1998).

[79] N. T. Wilson and R. L. Johnston, Eur. Phys. J. D **12**, 161 (2000).

[80] N. T. Wilson and R. L. Johnston, Phys. Chem. Chem. Phys. **4**, 4168 (2002).

[81] I. L. Garzón and A. Posada-Amarillas, Phys. Rev. B **54**, 11796 (1996).

[82] I. L. Garzón, K. Michaelian, M. R. Beltrán, A. Posada-Amarillas, P. Ordejón, E. Artacho, D. Sánchez-Portal, and J. M. Soler, Phys. Rev. Lett. **81**, 1600 (1998).

[83] I. L. Garzón, K. Michaelian, M. R. Beltrán, A. Posada-Amarillas, P. Ordejón, E. Artacho, D. Sánchez-Portal, and J. M. Soler, Eur. Phys. J. D **9**, 211 (1999).

[84] K. Michaelian, N. Rendón, and I. L. Garzón, Phys. Rev. B **60**, 2000 (1999).

[85] T. X. Li, S. Y. Yin, Y. L. Ji, B. L. Wang, G. H. Wang, and J. J. Zhao, Phys. Lett. A **267**, 403 (2000).

[86] S. Darby, T. V. Mortimer-Jones, R. L. Johnston, and C. Roberts, J. Chem. Phys. **116**, 1536 (2002).

[87] C. Rey, L. J. Gallego, J. García - Rodeja, J. A. Alonso, and M. P. Iñiguez, Phys. Rev. B **48**, 8253 (1993).

[88] J. García - Rodeja, C. Rey, L. J. Gallego, and J. A. Alonso, Phys. Rev. B **49**, 8495 (1994).

[89] A. Sebetci and Z. B. Güvenç, Modelling Simul. Mater. Sci. Eng. **13**, 683 (2005).

[90] V. G. Grigoryan, D. Alamanova, and M. Springborg, Eur. Phys. J. D **34**, 187 (2005).

[91] D. Alamanova, Y. Dong, H. ur-Rehman, M. Springborg, and V. G. Grigoryan, Computing Letters **1**, 319 (2005).

[92] V. G. Grigoryan and M. Springborg, Chem. Phys. Lett. **375**, 219 (2003).

[93] V. G. Grigoryan and M. Springborg, Phys. Rev. B **70**, 205415 (2004).

[94] M. A. Marcus, M. P. Andrews, J. Zegenhagen, A. S. Bommannavar, and P. Montano, Phys. Rev. B **42**, 3312 (1990).

[95] C. Jackschath, I. Rabin, and W. Schulze, Ber. Bunsenges. Phys. Chem. **96**, 1200 (1992).

[96] C. Jackschath, I. Rabin, and W. Schulze, Z. Phys. D **22**, 517 (1992).

[97] G. Alameddin, J. Hunter, D. Cameron, and M. M. Kappes, Chem. Phys. Lett. **192**, 122 (1992).

[98] K. Bromann, C. Félix, H. Brune, W. Harbich, R. Monot, J. Buttet, and K. Kern, Science **274**, 956 (1996).

[99] S. Fedrigo, W. Harbich, and J. Buttet, Phys. Rev. B **58**, 7428 (1998).

[100] M. Yeadon, M. Ghaly, J. C. Yang, R. S. Averback, and J. M. Gibson, Appl. Phys. Lett. **73**, 3208 (1998).

[101] S. J. Carroll, S. G. Hall, R. E. Palmer, and R. Smith, Phys. Rev. Lett. **81**, 3715 (1998).

[102] S. Krückeberg, G. Dietrich, K. Lützenkirchen, L. Schweikhard, C. Walther, and J. Ziegler, J. Chem. Phys. **110**, 7216 (1999).

[103] U. Busolt, E. Cottancin, H. Röhr, L. Socaciu, T. Leisner, and L. Wöste, Appl. Phys. B. **68**, 453 (1999).

[104] Y. Shi, V. A. Spasov, and K. M. Ervin, J. Chem. Phys. **111**, 938 (1999).

[105] F. Reinert, G. Nicolay, S. Schmidt, D. Ehm, and S. Hüfner, Phys. Rev. B **63**, 115415 (2001).

[106] R. E. Palmer, S. Pratontep, and H.-G. Boyen, Nature Materials **2**, 443 (2003).

[107] H. Häkkinen, M. Moseler, O. Kostko, N. Morgner, M. A. Hoffmann, and B. v. Issendorff, Phys. Rev. Lett. **93**, 093401 (2004).

[108] X. Xing, R. M. Danell, I. L. Garzón, K. Michaelian, M. N. Blom, M. M. Burns, and J. H. Parks, Phys. Rev. B **72**, 081405(R) (2005).

[109] A. Fielicke, I. Rabin, and G. Meijer, J. Phys. Chem. A **110**, 8060 (2006).

[110] T. L. Haslett, K. A. Bosnick, and M. Moskovits, J. Chem. Phys. **108**, 3453 (1998).

[111] Z. F. Liu, W. L. Yim, J. S. Tse, and J. Hafner, Eur. Phys. J. D **10**, 105 (2000).

[112] V. Bonačić-Koutecky, V. Veyret, and R. Mitrić, J. Chem. Phys. **115**, 10450 (2001).

[113] M. N. Huda and A. K. Ray, Phys. Rev. A **67**, 013201 (2003).

[114] B. K. Agrawal, S. Agrawal, P. Srivastava, and S. Singh, J. Nanopart. Res. **6**, 363 (2004).

[115] Y. Wang and X. G. Gong, Eur. Phys. J. D **34**, 19 (2005).

[116] J. C. Idrobo, S. Öğüt, and J. Jellinek, Phys. Rev. B **72**, 085445 (2005).

[117] J. Zhao, Y. Luo, and G. Wang, Eur. Phys. J. D **14**, 309 (2001).

[118] W. A. de Heer, Rev. Mod. Phys. **65**, 611 (1993).

[119] M. Brack, Rev. Mod. Phys. **65**, 677 (1993).

[120] M. Yang, K. A. Jackson, and J. Jellinek, J. Chem. Phys. **125**, 144308 (2006).

[121] C. Massobrio and P. Blandin, Phys. Rev. B **47**, 13687 (1993).

[122] G. Vandoni, C. Félix, and C. Massobrio, Phys. Rev. B **54**, 1553 (1996).

[123] B. Nacer, C. Massobrio, and C. Félix, Phys. Rev. B **56**, 10590 (1997).

[124] C. Massobrio, J. Phys. Chem. B **102**, 4374 (1998).

[125] H. Arslan and M. H. Güven, New J. Phys. **7**, 60 (2005).

[126] J. García-Rodeja, C. Rey, L. J. Gallego, and J. A. Alonso, Phys. Rev. B **49**, 8495 (1994).

[127] L. García González and J. M. Montejano-Carrizales, Phys. Stat. Sol. (A) **220**, 357 (2000).

[128] F. Baletto, C. Mottet, and R. Ferrando, Phys. Rev. Lett. **84**, 5544 (2000).

[129] F. Baletto, C. Mottet, and R. Ferrando, Phys. Rev. B **63**, 155408 (2001).

[130] F. Calvo and J. P. K. Doye, Phys. Rev. B **69**, 125414 (2004).

[131] B. Simard, P. A. Hackett, A. M. James, and P. R. R. Langridge-Smith, Chem. Phys. Lett. **186**, 415 (1991); V. Beutel, H.-G. Krämer, G. L. Bhale, M. Kuhn, K. Weyers, W. Demtröder, J. Chem. Phys. **98**, 2699 (1993).

[132] V. G. Grigoryan, D. Alamanova, and M. Springborg, Phys. Rev. B **73**, 115415 (2006).

[133] D. Alamanova, V. G. Grigoryan, and M. Springborg, Z. Phys. Chem. **220**, 811 (2006).

[134] D. R. Jennison, P. A. Schultz, and M. P. Sears, J. Chem. Phys. **106**, 1856 (1997).

[135] M. N. Blom, D. Schooss, J. Stairs, and M. M. Kappes, J. Chem. Phys. **124**, 244308 (2006).

[136] M. Kabir, A. Mookerjee, and A. K. Bhattacharya, Phys. Rev. A **69**, 043203 (2004).

[137] V. G. Grigoryan and M. Springborg, Phys. Chem. Chem. Phys. **3**, 5125 (2001).

[138] K. P. Huber and G. Hertzberg, in *Constants of Diatomic Molecules* (Van Nostrand Reinhold, New York, 1979).

[139] J. O. Noell, M. D. Newton, P.J. Hay, R.L. Martin, and F. W. Bobrowicz, J. Chem. Phys. **73**, 2360 (1980).

[140] M. D. Morse, Chem. Rev. 1986, **86**, 1049 (1986).

[141] R. N. Barnett and U. Landman, Phys. Rev. B **48**, 2081 (1993).

[142] R. Car and M. Parrinello, Phys. Rev. Lett. **55**, 2471 (1985).

[143] F. Palacios, R. Méndez, and M. P. Iñiguez, Eur. Phys. J. D **24**, 319 (2003).

[144] R. Bock, *Heavy Ion Collisions* (North-Holland, Amsterdam, 1980).

[145] B. H. Bransden, *Atomic Collision Theory* (Benjamin-Cummings, Reading, 1983).

[146] N. Andersen *et al.*, Physics Reports **165**, 1 (1988), *ibid.* **278**, 107 (1997), *ibid.* **279**, 251 (1997).

[147] R. Schmidt, G. Seifert, and H. O. Lutz, Phys. Lett. A **158**, 231 (1991).

[148] G. Seifert, R. Schmidt, and H. O. Lutz, Phys. Lett. A **158**, 237 (1991).

[149] F. S. Zhang, F. Spiegelmann, E. Suraud, V. Fraysé, R. Poteau, R. Glowinski, and F. Chatelin, Phys. Lett. A **193**, 75 (1994).

[150] U. R. Schmitt, E. Engel, and R. M. Dreizler, Phys. Rev. B **50**, 14674 (1994).

[151] H. Häkkinen and M. Manninen, Phys. Rev. Lett. **76**, 1599 (1996).

[152] F. Calvo and F. Spiegelmann, Phys. Rev. B 54, 10949 (1996).

[153] U. Saalmann and R. Schmidt, Phys. Rev. Lett. **80**, 3213 (1998).

[154] O. Knospe, A. V. Glotov, G. Seifert, and R. Schmidt, J. Phys. B: At. Mol. Opt. Phys. **29**, 5163 (1996).

[155] R. Schmidt, O. Knospe, and U. Saalmann, Il Nuovo Cimento **110 A**, 1201 (1997).

[156] D. M. Kolb, G. E. Engelmann, and J. C. Ziegler, Andew. Chem. Int. Ed. **39**, 1123 (2000).

[157] S. Krückeberg, L. Schweikhard, J. Ziegler, G. Dietrich, K. Lützenkirchen, and C. Walther, J. Phys. Chem. **114**, 2955 (2001).

[158] U. Heiz and W.-D. Schneider, J. Phys. D: Appl. Phys. **33**, R85 (2000).

[159] P. Jensen *et al.*, Chpt. **4** in *Nanoclusters and Nanocrystals*, ed. by H. S. Nalwa (2003).

[160] R. E. Palmer, S. Pratontep, and H.-G. Boyen, Nature Materials **2**, 443 (2003).

[161] P. Melinon et al., Int. J. Mod. Phys. B **9**, 339 (1995).

[162] T. Takagi, I. Yamada, and A. Sasaki, J. Vac. Sci. Technol. **12**, 1128 (1975).

[163] T. Takagi, *Ionized-Cluster Beam Deposition and Epitaxy* (Materials Science and Process Technology Series, Noyes Publications, 1989)

[164] K. Bromann, C. Félix, H. Brune, W. Harbich, R. Monot, J. Buttet, and K. Kern, Science **274**, 956 (1996).

[165] X. Hu and P. von Blanckenhagen, Appl. Phys. A **68**, 137 (1999).

[166] M. Hou, Nucl. Instr. Meth. B **135**, 501 (1998.)

[167] H.-P. Cheng and U. Landman, J. Phys. Chem. **98**, 3527 (1994).

[168] H. Haberland, Z. Insepov, and M. Moseler, Phys. Rev. B **51**, 11061 (1995).

[169] Y. Xu, Z. Y. Pan, and Y. X. Wang, Mod. Phys. Lett. B **15**, 455 (2001).

[170] S.-C. Lee, N. M. Hwang, B. D. Yu, and D.-Y. Kim, J. Cryst. Growth **223**, 311 (2001).

[171] J. Frantz, M. Rusanen, K. Nordlund, and I. T. Koponen, J. Phys.: Condens. Matter **16**, 2995 (2004).

[172] L. Rongwu, P. Zhengying, and H. Yukun, Phys. Rev. B **53**, 4156 (1996).

[173] M. Hou, R. W. Lee, and Z. Y. Pan, Nucl. Instr. Meth. B **115**, 536 (1996).

[174] Q. Hou, M. Hou, L. Bardotti, B. Prével, P. Mélinon, and A. Perez, Phys. Rev. B **62**, 2825 (2000).

[175] F. J. Palacios, M. P. Iñiguez, M. J. López, and J. A. Alonso, Phys. Rev. B **60**, 2908 (1999).

[176] M. G. Del Pópolo, E. P. M. Leiva, and W. Schmickler, J. Electroanal. Chem. **518**, 84 (2002).

[177] V. G. Grigoryan and M. Springborg, unpublished results

# List of publications

1. *Structure and Magnetic Interaction in Organic Radical Crystals. 6. Spin-Transfer Crystals: A Theoretical study*
N. Tyutyulkov, M. Staneva, A. Stoyanova, D. Alaminova, G. Olbrich, and F. Dietz,
J. Phys. Chem. B *106*, 2901 (2002).

2. *Structure and energetics of nickel, copper, and gold clusters*
V. G. Grigoryan, D. Alamanova, and M. Springborg,
Eur. Phys. J. D **34**, 187 (2005).

3. *Structural and Electronic Properties of Gold Clusters*
D. Alamanova, Y. Dong, H. ur-Rehman, M. Springborg, and V. G. Grigoryan,
Computing Letters **1**, 319 (2005).

4. *Structural and Electronic Properties of Metal Clusters*
M. Springborg, V. G. Grigoryan, Y. Dong, D. Alamanova, H. ur-Rehman, and V. Tevekeliyska,
Lecture Series on Computer and Computational Sciences **4**, 1026 (2005).

5. *Structure and energetics of $Cu_N$ clusters with ($2 \leq N \leq 150$): An embedded-atom-method study*
V. G. Grigoryan, D. Alamanova, and M. Springborg,
Phys. Rev. B **73**, 115415 (2006).

6. *Theoretical Study of Structure and Energetics of Gold Clusters with the EAM Method*
D. Alamanova, V. G. Grigoryan, and M. Springborg,
Z. Phys. Chem. **220**, 811 (2006).

7. *Deposition of magic copper clusters on Cu(111) surfaces*
D. Alamanova, V. G. Grigoryan, and M. Springborg,
Phys. Rev. B (submitted)

8. *Formation of stable products from cluster-cluster collisions*
D. Alamanova, V. G. Grigoryan, and M. Springborg,
Phys. Rev. B (submitted)

9. *Theoretical study of structure and energetics of silver clusters*
D. Alamanova, V. G. Grigoryan, and M. Springborg,
in preparation